Lumineszente Farbstoffe in Metall-organischen Gerüstverbindungen – Untersuchungen zu Struktur, Photophysik und Wirt-Gast-Wechselwirkungen

Inaugural-Dissertation

zur Erlangung des Doktorgrades
Dr. rer. nat.
der Mathematisch-Naturwissenschaftlichen Fakultät
der Heinrich-Heine-Universität Düsseldorf

vorgelegt von

Annette Vollrath
aus Neuss

Düsseldorf, August 2026

Aus dem Institut für Anorganische Chemie und Strukturchemie I – Nanoporöse und nanoskalierte Materialien
der Heinrich-Heine-Universität Düsseldorf

Gedruckt mit der Genehmigung der
Mathematisch-Naturwissenschaftlichen Fakultät der
Heinrich-Heine-Universität Düsseldorf

Berichterstatter:

1. Prof. Dr. Christoph Janiak

2. Prof. Dr. Christian Ganter

Tag der mündlichen Prüfung: 09.10.2026

Eidesstattliche Erklärung

Ich, Annette Vollrath, versichere an Eides statt, dass ich die vorliegende Dissertation selbstständig und ohne unzulässige Hilfe angefertigt habe. Ich habe keine anderen als die von mir angegebenen Quellen und Hilfsmittel benutzt. Alle Stellen der Arbeit, die wörtlich oder sinngemäß aus veröffentlichten oder unveröffentlichten Arbeiten anderer übernommen wurden, sind als solche kenntlich gemacht. Die Dissertation wurde in gleicher oder ähnlicher Form keiner anderen Prüfungsbehörde vorgelegt. Ich versichere, dass ich nach bestem Wissen die reine Wahrheit erklärt und nichts verschwiegen habe unter Beachtung der „Grundsätze zur Sicherung guter wissenschaftlicher Praxis“.

_____ _____

Ort, Datum Unterschrift

Danksagung

An dieser Stelle möchte ich all den Personen meinen herzlichen Dank aussprechen, die mich während meiner Promotionszeit begleitet und auf vielfältige Weise unterstützt haben.

Mein Dank gilt zunächst meinem Doktorvater, Herrn Prof. Dr. Christoph Janiak, für die Möglichkeit, diese Arbeit in seiner Arbeitsgruppe anzufertigen. Ich danke ihm für seine fachliche Unterstützung, sowie die Freiräume, die er mir während der gesamten Promotionszeit eingeräumt hat.

Ebenso danke ich Herrn Prof. Dr. Christian Ganter herzlich für die Übernahme des Zweitgutachtens meiner Arbeit.

Darüber hinaus möchte ich mich bei meinen Co-Autorinnen und Co-Autoren für die gute Zusammenarbeit und ihre wertvollen Beiträge bedanken, die wesentlich zum Erfolg unserer gemeinsamen Publikationen beigetragen haben. Herrn Jun.-Prof. Dr. Markus Suta danke ich darüber hinaus für viele wertvolle Beiträge und Hilfestellungen bei Fragen.

Ein herzliches Dankeschön geht auch an die Festangestellten des Arbeitskreises Jutta Bourgeois, Birgit Tommes, Annette Ricken und Marcell Demandt, für Ihre Unterstützung und Bereitschaft bei Fragen aller Art.

Meinen Bachelorstudenten Lara Szukat, Xiang Liu und Nikolas Jansen danke ich für ihre engagierte Mitarbeit und wertvollen Beiträge zu meiner Forschung. Eure Arbeit hat die behandelten Forschungsthemen maßgeblich vorangebracht und dazu beigetragen, dass daraus erfolgreiche Publikationen entstanden sind. Für euren weiteren beruflichen und privaten Weg wünsche ich euch alles Gute und viel Erfolg.

Ein großes Dankeschön gilt allen aktuellen und ehemaligen Mitgliedern unseres Arbeitskreises: Nabil Assahub, Lukas Eisenhuth, Jonas Fabrizi, Peter Ferber, David Geller, Quang-Dien Hoang, Sven Hößel, Brenda Flore Kenyim, Vivian Küll, Ayşenur Limon, Sarah Merzenich, Julia Overhoff, Varvara Ryabuhina, Philipp Seiffert, Till Strothmann und Imene Ziani-Cherif. Auch weiterhin die bereits promovierten Alumni Dr. Dustin Jordan, Dr. Marilyn Kaul, Dr. Daniel Komisarek, Dr. Takin Haj Hassani Sohi, Dr. Linda Sondermann, Dr. Alex Spieß und Dr. Dennis Woschko. Vielen Dank für die angenehme Arbeitsatmosphäre, den wissenschaftlichen Austausch, die gegenseitige Unterstützung und die vielen gemeinsamen Kaffeepausen, Besuche in der Cafeteria und Gespräche. Auch die gemeinsamen Aktivitäten außerhalb der Universität haben meine Promotionszeit bereichert. Ihr habt dazu beigetragen, dass diese Jahre nicht

nur fachlich lehrreich, sondern auch persönlich unvergesslich geworden sind. Ich wünsche euch allen für die Zukunft alles Gute und weiterhin viel Erfolg.

Danke auch an Gülsüm Kinik, Lukas Träger, Benedikt Bendel und Tom Förster für viele Gespräche und lustige Stunden bei dem „letzten Freitag“ im Monat. Und auch an Theresa Ott für die schöne Zeit in den Japanisch Sprachkursen.

Ein besonderer Dank gilt meinen ehemaligen Bürokollegen Dr. Thi Hai Yen Beglau, Dr. Dietrich Püschel und Dr. Marcus N. A. Fetzer. Ich habe die Zeit mit euch im Büro immer sehr geschätzt. Wir haben unzählige fachliche und persönliche Gespräche geführt, gemeinsam gelacht und viele schöne Erinnerungen geschaffen. Rückblickend bin ich sehr dankbar, diese Zeit mit euch im wunderschönen Büro verbracht zu haben.

Ich danke außerdem meinen Freunden Johannes Gierling, Mathieu Kippes, Dr. Ann-Kathrin Scherer, Lysander Presser und Michelle Rademacher, die ich während meines Studiums kennenlernen durfte und die mich begleitet haben. Eure Unterstützung und eure Fähigkeit, mich auch in stressigen Phasen immer wieder zum Lachen zu bringen, haben dazu beigetragen, diese Zeit erfolgreich zu meistern.

Ganz besonders möchte ich mich bei meinem ehemaligen Masterarbeitsbetreuer Dr. Marcus N. A. Fetzer bedanken. Ich bin bis heute sehr froh und dankbar, dass ich meine Masterarbeit bei dir anfertigen durfte. Du hast mich fachlich und persönlich geprägt und mir unglaublich viel beigebracht. Vor allem die vielen langen Abende in der Universität mit unseren Gesprächen und Diskussionen werden mir immer in besonderer Erinnerung bleiben.

Ein ganz besonderer Dank gilt meinem Freund Tim. Danke, dass du mich in allen Phasen meiner Promotion (auch in den stressigen und emotional herausfordernden Momenten) immer unterstützt, ermutigt und aufgebaut hast. Ich bin unendlich froh, dich im Arbeitskreis kennengelernt zu haben und gemeinsam mit dir so viele schöne Erinnerungen geschaffen zu haben. Danke, dass du an meiner Seite bist.

Der größte Dank gilt meiner Familie. Ihr wart von Anfang an an meiner Seite, habt mich auf meinem Weg begleitet, mir in schwierigen Momenten Kraft gegeben und mich stets darin bestärkt, meinen eigenen Weg zu gehen. Eure Geduld, euer Vertrauen und eure bedingungslose Unterstützung haben mir den Rückhalt gegeben, den ich in all den Jahren gebraucht habe. Ohne euch wäre dieser Weg nicht möglich gewesen.
Diese Arbeit ist euch gewidmet.

Von ganzem Herzen danke ich euch allen und wünsche euch nur das Beste!

Unterschätze nie ruhige Menschen.

Sie bemerken mehr, als du glaubst,

denken sich mehr, als sie sagen

und wissen mehr, als sie preisgeben.

– Verfasser unbekannt

Inhaltsverzeichnis

Kurzzusammenfassung I

Abstract III

Publikationsliste V

Abkürzungsverzeichnis VIII

1 Einleitung 1

1.1 Metall-organische Gerüstverbindungen 1

1.2 Lumineszenz 6

1.2.1 TADF 9

1.2.2 MR-TADF 12

1.3 Einlagerungsmethoden 13

1.4 Verwendete Farbstofftypen 15

1.4.1 Flavine 15

1.4.2 Phenazine 17

1.4.3 DiKTa 18

2 Zielsetzung und Motivation 20

3 Kumulativer Teil 22

3.1 Cobalt Coordination Networks Based on the Linker (Phenazine-5,10-diyl)di- and Tetrabenzoate 23

3.2 Investigations on the Luminescence Behavior of a Flavin Derivative Incorporated into Al-based Metal-Organic Frameworks for the Sensing of Aromatic Nitro Compounds 80

3.3 From Aggregation to Isolation: Preserving MR-TADF Emission of DiKTa in MOF-5 110

3.4 Beiträge an weiteren Veröffentlichungen als Co-Autor 184

3.4.1 Encapsulation of Phosphorescent Pt(II) Complexes in Zn-Based Metal-Organic Frameworks toward Oxygen-Sensing Porous Materials 184

3.4.2 Novel Re(I) Complexes as Potential Selective Theranostic Agents in Cancer Cells and In Vivo in Caenorhabditis elegans Tumoral Strains 186

3.4.3 Mechanochemical synthesis and application of mixed-metal copper–ruthenium HKUST-1 metal–organic frameworks in the electrocatalytic oxygen evolution reaction 187

3.4.4 Comparison of In Situ and Postsynthetic Formation of MOF-Carbon Composites as Electrocatalysts for the Alkaline Oxygen Evolution Reaction .. 188

3.4.5 Synthesis and characterization of lignin-modified geopolymer composites for aqueous phase sequestration of methyl orange dye in a fixed-bed column 189

3.4.6 Eco-friendly energy storage: optimizing alfalfa biomass for advanced supercapacitor materials 190

4 Zusammenfassung 192

5 Unveröffentlichte Ergebnisse 195

6 Experimentalteil 205

6.1 Chemikalien 205

6.2 Geräte 205

6.3 Synthesevorschriften 207

7 Anhang 208

8 Literaturverzeichnis 210

Kurzzusammenfassung

Die vorliegende kumulative Dissertation befasst sich mit der Entwicklung und Untersuchung funktionaler Metall-organischer Gerüstverbindungen als strukturierte Wirtsmaterialien für lumineszente organische Farbstoffe und deren Wechselwirkungen innerhalb der porösen Wirtsstrukturen. Ziel der Arbeit ist es, den Einfluss der Gerüststruktur auf die Photophysik organischer Chromophore aufzuklären und grundlegende Struktur-Eigenschafts-Beziehungen sowie Wirt-Gast-Wechselwirkungen in hybriden MOF-basierten Materialsystemen zu analysieren. Hierzu werden sowohl neuartige Koordinationsnetzwerke auf Basis phenazinhaltiger Linker entwickelt als auch funktionelle Lumineszenzfarbstoffe und multiresonante TADF-Emitter gezielt in Metall-organische Gerüstverbindungen eingebracht.

Der erste Teil der Arbeit beschäftigt sich mit der Synthese neuer phenazinbasierter Dicarboxylat- und Tetracarboxylat-Linker sowie deren Einsatz zum Aufbau koordinativer Netzwerke. Es zeigt sich, dass bereits geringe Änderungen der Linkergeometrie und des Substitutionsmusters zu unterschiedlichen Sekundärbaueinheiten und Gerüsttopologien führen, obwohl identische Metallzentren und vergleichbare Synthesebedingungen verwendet werden. Die Ergebnisse verdeutlichen den entscheidenden Einfluss der molekularen Struktur auf die Ausbildung koordinativer Netzwerke und deren strukturelle Eigenschaften.

Im zweiten Teil wird ein Flavinderivat erfolgreich in aluminiumbasierte Metall-organische Gerüstverbindungen eingebracht und hinsichtlich seiner strukturellen sowie photophysikalischen Eigenschaften untersucht. Die erhaltenen Hybridmaterialien zeigen eine selektive Fluoreszenzlöschung gegenüber nitroaromatischen Verbindungen sowie eine Fluoreszenzverstärkung gegenüber elektronenreichen nicht-nitrohaltigen Aromaten. Diese Effekte lassen sich auf unterschiedliche Wirt-Gast-Wechselwirkungen und photoinduzierte Elektronentransferprozesse zurückführen und verdeutlichen das Potenzial der Komposite als anpassbare fluoreszenzbasierte Sensormaterialien.

Der dritte Teil der Dissertation widmet sich der Einlagerung des multiresonanten TADF-Emitters DiKTa in MOF-5-Einkristalle. Mithilfe komplementärer Charakterisierungsmethoden, darunter Einkristall- und Pulverröntgendiffraktometrie,

Gassorptionsmessungen sowie verschiedene spektroskopische Verfahren, wird die erfolgreiche Einlagerung der Emittermoleküle in die Poren des MOFs nachgewiesen. Gleichzeitig bleiben die charakteristischen photophysikalischen Eigenschaften des MR-TADF-Emitters erhalten, während aggregationsbedingte Veränderungen des Lumineszenzverhaltens weitgehend unterdrückt werden.

Insgesamt zeigt die Arbeit, dass Metall-organische Gerüstverbindungen vielseitige Plattformen zur gezielten Immobilisierung lumineszenter Farbstoffe darstellen und deren strukturelle sowie photophysikalische Eigenschaften maßgeblich durch Wirt-Gast-Wechselwirkungen beeinflusst werden. Die gewonnenen Erkenntnisse erweitern das Verständnis des Zusammenspiels von Struktur, Photophysik und Wirt-Gast-Wechselwirkungen in hybriden Materialsystemen und bilden eine Grundlage für die Entwicklung neuer lumineszenter Materialien für Anwendungen in der chemischen Sensorik und der organischen Optoelektronik.

Abstract

This cumulative dissertation focuses on the development and investigation of functional metal-organic framework compounds as structured host materials for luminescent organic dyes and their interactions within the porous host structures. The aim of this work is to elucidate the influence of the framework structure on the photophysics of organic chromophores and to analyze fundamental structure-property relationships as well as host-guest interactions in hybrid MOF-based material systems. To this end, novel coordination networks based on phenazine-containing linkers are being developed, and functional luminescent dyes and multi-resonant TADF emitters are being specifically incorporated into metal-organic frameworks.

The first part of the work focuses on the synthesis of new phenazine-based dicarboxylate and tetracarboxylate linkers and their use in constructing coordination networks. It has been shown that even minor changes in the linker geometry and substitution pattern lead to different secondary building units and framework topologies, even though identical metal centers and comparable synthetic conditions are used. The results highlight the decisive influence of molecular structure on the formation of coordination networks and their structural properties.

In the second part, a flavin derivative is successfully incorporated into aluminum-based metal-organic frameworks and investigated with respect to its structural and photophysical properties. The resulting hybrid materials exhibit selective fluorescence quenching toward nitroaromatic compounds and fluorescence enhancement toward electron-rich non-nitroaromatic compounds. These effects can be attributed to various host-guest interactions and photoinduced electron transfer processes and highlight the potential of the composites as tunable fluorescence-based sensor materials.

The third part of the dissertation focuses on the incorporation of the multiresonant TADF emitter DiKTa into MOF-5 single crystals. Using complementary characterization methods, including single-crystal and powder X-ray diffraction, gas sorption measurements, and various spectroscopic techniques, the successful incorporation of the emitter molecules into the pores of the MOF is demonstrated. At the same time, the characteristic photophysical properties of the MR-TADF emitter are preserved, while aggregation-induced changes in luminescence behavior are largely suppressed.

Overall, this work demonstrates that metal-organic framework compounds serve as versatile platforms for the targeted immobilization of luminescent dyes, and that their structural and photophysical properties are significantly influenced by host-guest interactions. The findings expand our understanding of the interplay between structure, photophysics, and host-guest interactions in hybrid material systems and lay the foundation for the development of new luminescent materials for applications in chemical sensing and organic optoelectronics.

Publikationsliste

Im Rahmen der vorliegenden Dissertation wurden mehrere Publikationen angefertigt und veröffentlicht, darunter drei Erstautorenschaften und weitere Co-Autorenschaften, welche nachfolgend aufgelistet werden.

Erstautorenschaften:

Annette Vollrath, Xiang Liu, Nikolas Jansen, Philipp Seiffert, David Geller, Christoph Janiak:
„Cobalt Coordination Networks Based on the Linker (Phenazine-5,10-diyl)di- and Tetrabenzoate“

Crystals **2026**, *16*, 185. DOI: 10.3390/cryst16030185

Annette Vollrath, Vasily Gvilava, Philipp Seiffert, Constantin Czekelius, Christoph Janiak:
„Investigations on the Luminescence Behavior of a Flavin Derivative Incorporated into Al-based Metal-Organic Frameworks for the Sensing of Aromatic Nitro Compounds”

Z. Anorg. Allg. Chem. **2026**, e70183. DOI: 10.1002/zaac.70183

Annette Vollrath,‡ Marcus N. A. Fetzer,‡ Jennifer Kremper,‡ Benedikt Bendel, Ralf Kühnemuth, Markus Suta, Jan Meisner, Oliver Weingart, Christoph Janiak :
„From Aggregation to Isolation: Preserving MR-TADF Emission of DiKTa in MOF-5”

Eingereicht in: *Adv. Opt. Mater.* **2026**.
‡ Diese Autoren haben zu gleichen Teilen an dieser Publikation beigetragen.

Co-Autorenschaften:

Tim-Oliver Knedel, Stefan Buss, Iván Maisuls, Constantin G. Daniliuc, Carsten Schlüsener, Philipp Brandt, Oliver Weingart, Annette Vollrath, Christoph Janiak, Christian A. Strassert:
„Encapsulation of Phosphorescent Pt(II) Complexes in Zn-Based Metal–Organic Frameworks toward Oxygen-Sensing Porous Materials"

Inorg. Chem. **2020**, *59*, 7252-7264. DOI: 10.1021/acs.inorgchem.0c00678

Alicia Marco, Pezhman Ashoo, Samanta Hernández-García, Pedro Martínez-Rodríguez, Natalia Cutillas, Annette Vollrath, Dustin Jordan, Christoph Janiak, Fernando Gandía-Herrero, José Ruiz:
„Novel Re(I) Complexes as Potential Selective Theranostic Agents in Cancer Cells and In Vivo in Caenorhabditis elegans Tumoral Strains"

J. Med. Chem. **2024**, *67*, 7891-7910. DOI: 10.1021/acs.jmedchem.3c01869

Linda Sondermann, Quentin Smith, Till Strothmann, Annette Vollrath, Thi Hai Yen Beglau, Christoph Janiak:
„Mechanochemical synthesis and application of mixed-metal copper–ruthenium HKUST-1 metal–organic frameworks in the electrocatalytic oxygen evolution reaction"

RSC Mechanochem. **2024**, *1*, 296-307. DOI: 10.1039/D4MR00021H

Linda Sondermann, Laura Maria Voggenauer, Annette Vollrath, Till Strothmann, Christoph Janiak:
„Comparison of In Situ and Postsynthetic Formation of MOF-Carbon Composites as Electrocatalysts for the Alkaline Oxygen Evolution Reaction (OER)"

Molecules **2025**, *30*, 208. DOI: 10.3390/molecules30020208

Idriss Kamdem Taquieteu, Hermann Dzoujo Tamaguelon, Victor Shikuku, Sylvain Tome, Donald Kamdem Njouond, Manelle Fouetfack Dongmo, Hanibal Othman,

Annette Vollrath, Abdulrahman Mohabbat Christoph Janiak, Charles Banenzouéa, David Joh Daniel Dina:

„Synthesis and characterization of lignin-modified geopolymer composites for aqueous phase sequestration of methyl orange dye in a fixed-bed column”

Mater. Adv. **2025**, *6*, 5074-5088. DOI: 10.1039/d5ma00248f

---

Zohreh Asadi Ghare Jeloo, Sakineh Ghasemzadeh, Hassan Hosseini-Monfared, Mehran Javanbakht, Philipp Seiffert, Annette Vollrath, Robert Oestreich, Julia Michalski, Leila Naji, Mitra Najafloo, Christoph Janiak:

„Eco-friendly energy storage: optimizing alfalfa biomass for advanced supercapacitor materials”

Mater. Sci. Eng. B **2026**, *324*, 118944. DOI: 10.1016/j.mseb.2025.118944

Abkürzungsverzeichnis

1D	eindimensional
2D	zweidimensional
3D	dreidimensional
ACQ	Aggregation-caused quenching (*dt.* aggregationsbedingte Fluoreszenzlöschung)
BET	Brunauer, Emmett, Teller
Bpy	Bipyridin
bzw.	beziehungsweise
°C	Grad Celsius
CCDC	Cambridge Crystallographic Data Centre
DA	Donor-Akzeptor(-Gruppe/Substituent)
DABCO	1,4-Diazabicyclo[2.2.2]octan
DCM	Dichlormethan
DEF	*N,N*-Diethylformamid
DiKTa	Chinolin[3,2,1-*de*]acridin-5,9-dion
DMF	*N,N*-Dimethylformamid
dt.	deutsch
DUT	Dresden University of Technology
ΔE_{ST}	Energiedifferenz zwischen Singulett- und Triplett-Zuständen
EDX	Energy dispersive X-ray spectroscopy (*dt.* Energiedispersive Röntgenspektroskopie)
engl.	englisch
et al.	et alii (*dt.* und andere)
FAD	Flavinadenindinukleotid
FMN	Flavinmononukleotid
FWHM	Full width at half maximum (*dt.* Halbwertsbreite)
HBTC	1,3,5-Benzoltricarbonsäure
HKUST	Hong Kong University of Science and Technology

HOMO	Highest occupied molecular orbital (*dt*. Höchstes besetztes Molekülorbital)
IC	Internal conversion (*dt*. Innere Umwandlung)
IQE	Internal quantum efficiency (*dt*. interne Quantenausbeute)
IR	Infrarotspektroskopie
ISC	Intersystem crossing (*dt*. Interkombination)
IUPAC	International Union of Pure and Applied Chemistry (*dt*. Internationale Union für reine und angewandte Chemie)
LUMO	Lowest Molecular Unoccupied Orbital (*dt*. Niedrigstes unbesetztes Molekülorbital)
MIL	Matériaux de l'Institut Lavoisier
MOF	Metal organic framework (*dt*. Metall-organische Gerüstverbindung)
MR-TADF	Multi-resonance thermally activated delayed fluorescence (*dt*. Multiresonante thermisch aktivierte verzögerte Fluoreszenz)
NMR	Nuclear magnetic resonance spectroscopy (*dt*. Kernspinresonanzspektroskopie)
OLED	Organic light emitting diode (*dt*. Organische Leuchtdiode)
PXRD	Powder X-Ray Diffraction (*dt*. Pulverröntgendiffraktometrie)
Py	Pyridin
Ref.	Referenz
REM	Rasterelektronenmikroskopie
rISC	Reverse intersystem crossing (*dt*. Rück-Interkombination)
RT	Raumtemperatur
SBU	Secondary Building Unit (*dt*. Sekundäre Baueinheit)
TADF	Thermally activated delayed fluorescence (*dt*. Thermisch aktivierte verzögerte Fluoreszenz)
TFA	Trifluoressigsäure
TGA	Thermogravimetrische Analyse
UiO	Universitetet i Oslo
UV/Vis	Ultraviolet/Visible (*dt*. Ultraviolett/sichtbar)

1 Einleitung

1.1 Metall-organische Gerüstverbindungen

Metall-organische Gerüstverbindungen (*engl*. metal-organic frameworks, MOFs) bilden eine vielseitige Klasse kristalliner, potenziell poröser Hybridmaterialien, die aus anorganischen und organischen Strukturbausteinen aufgebaut sind.[1] Sie bestehen aus Metallionen oder Metallclustern als Knotenpunkten, welche die sogenannten sekundären Baueinheiten (*engl*. secondary building unit, SBU) bilden, und werden über organische Liganden, welche aufgrund ihrer verbrückenden Eigenschaften oft als Linker bezeichnet werden, durch koordinative Bindungen zu periodischen dreidimensionalen Netzwerkstrukturen verbunden. Neben klassisch anorganischen Materialien, wie Zeolithen oder Silica-Gel, und organischen Materialien, wie Aktivkohle, können MOFs deutlich höhere innere Oberflächen von teilweise bis zu mehreren tausend Quadratmetern pro Gramm aufweisen.[2-3] Auf der Grundlage der Brunauer-Emmett-Teller-(BET-)Theorie[4] können die Größe dieser spezifischen Oberflächen bestimmt und mithilfe von Sorptionsmessungen zusätzlich die Porendurchmesser und das Porenvolumen der MOFs gemessen werden.

Um diese meist hochporösen Architekturen von verwandten Materialklassen abzugrenzen, bedarf es einer klaren Definition. Nach der Terminologie der International Union of Pure and Applied Chemistry (IUPAC) werden poröse koordinationschemische Festkörper anhand ihrer strukturellen Dimension und Topologie klassifiziert.[5] Ein Koordinationspolymer ist demnach ein Festkörper, der aus Metallzentren und organischen oder anorganischen Liganden aufgebaut ist, die durch koordinative Bindungen zu einer unendlichen Struktur verknüpft sind.[1] Entscheidend ist hierbei die periodische Wiederholung der Koordinationseinheiten in mindestens einer Raumrichtung, sodass eindimensionale (1D), zweidimensionale (2D) oder dreidimensionale (3D) Strukturen entstehen können. Ein Koordinationsnetzwerk stellt eine Unterklasse der Koordinationspolymere dar und bezeichnet speziell solche Systeme, die sich durch eine verzweigte, mehrdimensionale Vernetzung auszeichnen. Während lineare oder kettenartige Polymere ebenfalls als Koordinationspolymere klassifiziert werden, impliziert der Begriff „Netzwerk“ eine topologisch erweiterte Struktur mit mindestens zwei- oder dreidimensionaler Ausdehnung. Der Begriff Metall-

organische Gerüstverbindung ist nach IUPAC eine weitere Spezifizierung innerhalb der Koordinationsnetzwerke.[5] MOFs sind demnach Koordinationsnetzwerke mit potenzieller Porosität, bei denen die Struktur so aufgebaut ist, dass zugängliche Hohlräume oder Kanäle vorhanden sind. Diese Porosität unterscheidet MOFs von anderen Koordinationsnetzwerken und ist entscheidend für ihre Anwendung als Wirtsmaterialien. Daraus ergibt sich, dass alle MOFs Koordinationsnetzwerke und damit auch Koordinationspolymere sind, jedoch nicht jedes Koordinationspolymer oder -netzwerk die strukturellen Voraussetzungen eines MOFs erfüllt. Die Klassifikation erfolgt somit hierarchisch von allgemeinen Koordinationspolymeren über Netzwerke hin zu porösen MOF-Strukturen (Abbildung 1).

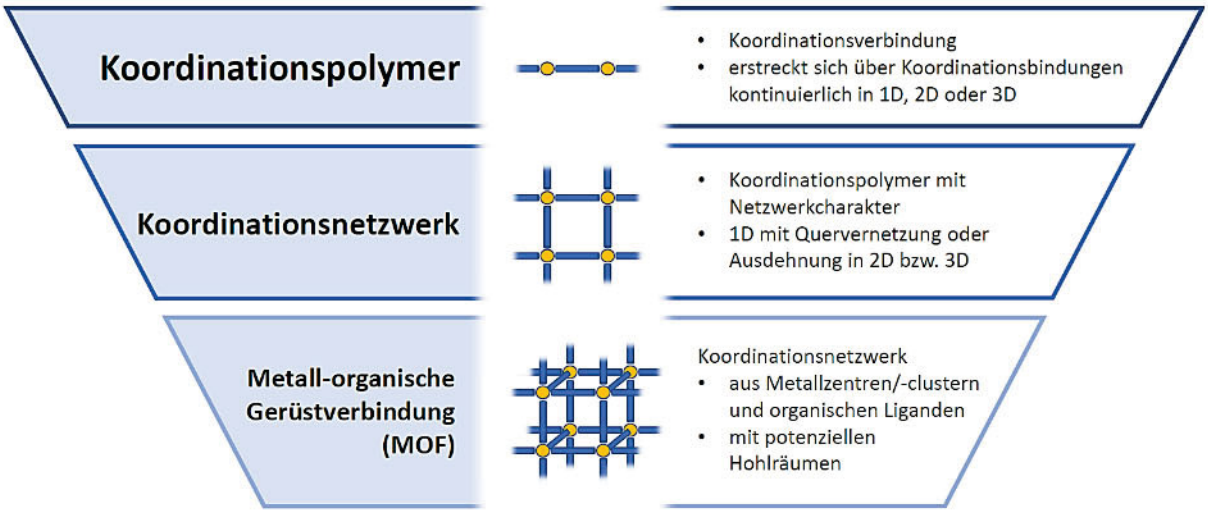


Abbildung 1: Schematischer Überblick über die hierarchische Terminologie von Koordinationspolymer, Koordinationsnetzwerk und Metall-organische Gerüstverbindung (MOF) mit zugehöriger Definition dieser Begriffe nach der IUPAC von 2013.[5]

Historisch geht die Entwicklung von MOFs auf Arbeiten zur Koordinationschemie und zur porösen anorganischen Festkörperchemie zurück.[6] Frühe Beispiele strukturell definierter poröser Koordinationspolymere wurden in den 1990er Jahre beschrieben, wobei insbesondere die von Yaghi *et al.* eingeführten Systeme als wegweisend gelten.[7] In deren Publikationen aus dem Jahr 1995 haben sie die Strukturen $[Cu(I)(4,4'\text{-bpy})_{1,5}NO_3]\cdot(H_2O)_{1,25}$ (bpy = Bipyridin) und $[Co(II)(HBTC)(Py)_2]\cdot(Py)_{2/3}$ (HBTC = 1,3,5-Benzoltricarbonsäure; Py = Pyridin) beschrieben und verwendeten darin zum ersten Mal den Begriff „Metal-Organic Framework“. Diese frühen Materialien zeigten, dass sich hohe spezifische Oberflächen und geordnete Porensysteme auch in rein koordinationschemisch aufgebauten Gerüsten realisieren lassen. Die damit einhergehende Erkenntnis führte zu einem stark wachsenden Interesse an diesem

Forschungsfeld, sodass die Entwicklung von MOFs in den darauffolgenden Jahren erheblich an Dynamik gewann. Dies spiegelt sich auch in der kontinuierlich steigenden Anzahl wissenschaftlicher Veröffentlichungen der letzten Jahre wider (Abbildung 2).[8] Die besondere Bedeutung dieser Materialklasse wurde zudem durch die Verleihung des Chemie-Nobelpreises 2025 an Susumu Kitagawa, Richard Robson und Omar M. Yaghi für die Entwicklung Metall-organischer Gerüstverbindungen hervorgehoben.[9]

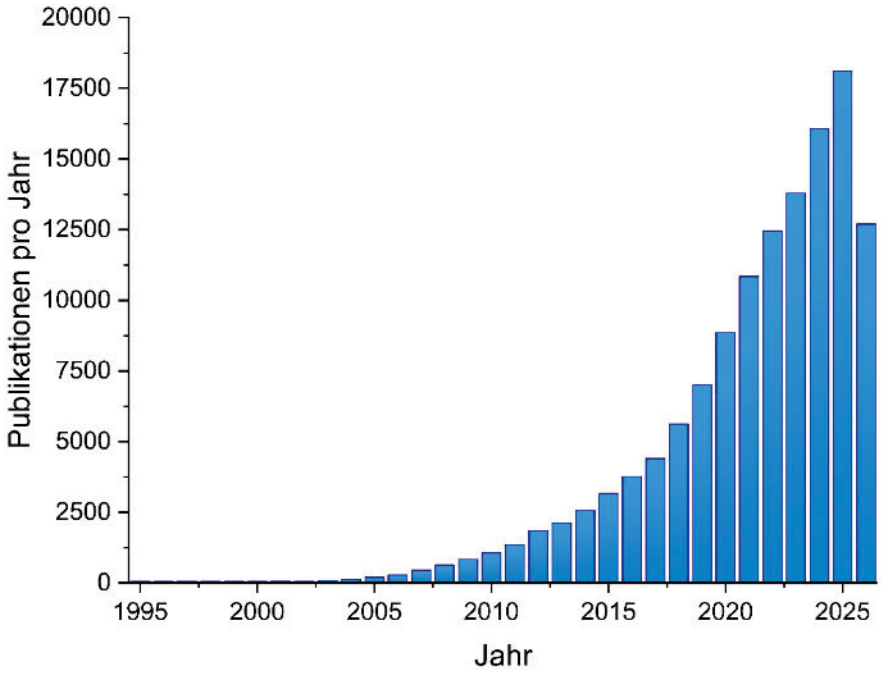


Abbildung 2: Anzahl an Publikationen pro Jahr (begrenzt auf veröffentlichte Journals und Reviews) im Zeitraum von 1995 bis 2026, die unter dem Begriff „Metal-organic framework“ auf der Plattform SciFinder gefunden wurden. Stand vom 13.08.2026.

Im Vergleich zu Zeolithen, deren Zusammensetzung und Topologie relativ begrenzt sind, bieten MOFs eine deutlich größere strukturelle und chemische Gestaltungsfreiheit, da sowohl die Metallknoten als auch die organischen Linker synthetisch variiert werden können.[10] Durch die Kombination verschiedener SBUs mit linearen oder verzweigten organischen Linkern können gezielt unterschiedliche Netzwerktypen sowie Porengeometrien und -größen realisiert werden.[11-13] Zur Verdeutlichung hierfür werden im nachfolgenden einige bekannte Beispiele dargestellt. Darunter fallen die MOFs HKUST-1, MOF-5, MIL-53 und UiO-66, die sich sowohl in ihrer SBU-Struktur als auch in ihren strukturellen und chemischen Eigenschaften deutlich unterscheiden.

HKUST-1 basiert auf Kupfer(II)-Schaufelrad-SBUs, bei denen jeweils zwei Kupferionen durch Carboxylatgruppen verbrückt sind.[14] Diese Struktur führt zu einem

dreidimensionalen, stark porösen Netzwerk mit offenen Metallzentren, die für Adsorptions- und katalytische Anwendungen von besonderer Bedeutung sind. MOF-5, eines der frühesten intensiv untersuchten MOF-Systeme, besteht aus Zn_4O-Cluster-SBUs, die über Terephthalat-Linker verbunden sind.[15] Das resultierende kubische Netzwerk zeichnet sich durch große, gut zugängliche Poren und eine hohe spezifische Oberfläche aus, weist jedoch, aufgrund der Anfälligkeit der Zink-Sauerstoff-Koordinationsbindungen gegenüber Hydrolyse, eine vergleichsweise geringe Stabilität gegenüber Feuchtigkeit auf. MIL-53 basiert auf Metall-Oxo-Ketten (typischerweise mit Aluminium, Chrom oder Eisen), die durch lineare Dicarboxylat-Linker verbunden sind und ein eindimensionales Kanalnetzwerk bilden.[16] Charakteristisch für dieses Material ist seine „Breathing"-Fähigkeit, bei der sich die Porenstruktur in Abhängigkeit von Temperatur, Druck oder Gastmolekülen reversibel verändern kann. UiO-66 hingegen basiert auf hochstabilen Zirkonium(IV)-Oxo-Clustern ($Zr_6O_4(OH)_4$), die mit Terephthalat-Linkern ein dreidimensionales Netzwerk bilden.[17] Aufgrund der starken Zr-O-Bindungen weist UiO-66 eine außergewöhnlich hohe thermische und chemische Stabilität auf und gilt als eines der robustesten MOF-Systeme. Die unterschiedlichen SBUs dieser Materialien sind in der folgenden Abbildung 3 vergleichend dargestellt.

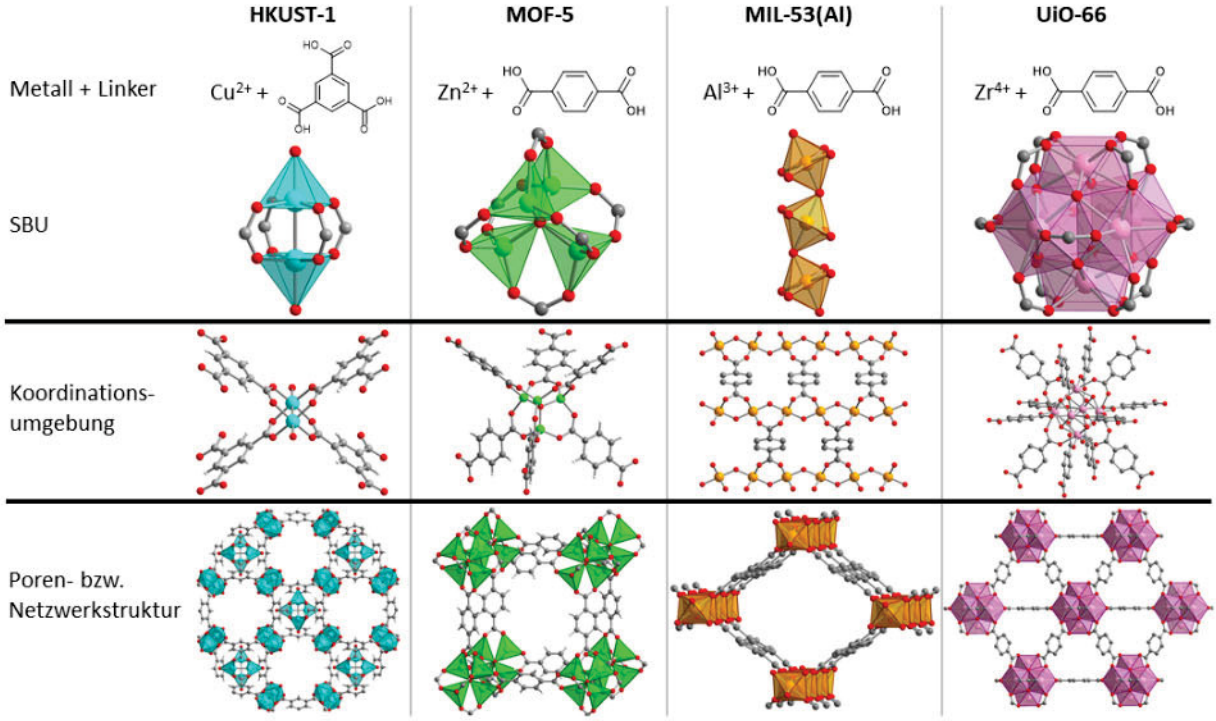


Abbildung 3: Übersicht über die Zusammensetzungen aus Metall und Linker, SBUs, Koordinationsumgebungen und Poren- bzw. Netzwerkstrukturen der MOFs HKUST-1, MOF-5, MIL-53(Al) und UiO-66. Die Strukturen wurden aus den bei CCDC hinterlegten cif-Dateien 112954 für HKUST-1[14], 256965 für MOF-5[15], 220476 für MIL-53(Al)[16] und 752051 für UiO-66[18] erstellt.

Durch synthetische Kontrollmöglichkeiten lassen sich nicht nur die Porenstruktur, sondern auch spezifische physikalisch-chemische Funktionalitäten gezielt maßschneidern. In den letzten Jahren haben insbesondere lumineszente MOFs und Wirt-Gast-Konzepte an Bedeutung gewonnen.[19-21] Hierbei kann entweder das Gerüst selbst emissiv sein, etwa durch geeignete metallische Knoten oder organische Liganden, oder es dient als strukturierter Wirt für eingelagerte Farbstoffe und andere optisch aktive Gastmoleküle.[22-25] Die periodische Porenarchitektur ermöglicht eine definierte räumliche Verteilung der Gastmoleküle und trägt dadurch zur Unterdrückung von Aggregation, Fluoreszenzlöschung (*engl*. Quenching) sowie nichtstrahlenden Relaxationsprozessen bei.[26] Gleichzeitig ermöglichen spezifische Wirt-Gast-Wechselwirkungen – etwa π-π-Wechselwirkungen, Wasserstoffbrückenbindungen oder koordinative Kontakte – eine gezielte Beeinflussung der elektronischen Zustände und Emissionseigenschaften.

Diese Möglichkeit zur gezielten Synthese von MOFs mit bestimmten Eigenschaften macht diese Materialien interessant für ein breites Anwendungsspektrum. Darunter fallen vor allem die Gasadsorption, -speicherung und -trennung.[27-29] Neben diesen klassischen Anwendungsfeldern finden MOFs ebenfalls Einsatz in der heterogenen Katalyse, der Wirkstofffreisetzung und der Sensorik.[30-34] Auch die Wahl der Synthesemethode kann Morphologie und Eigenschaften des herzustellenden MOFs beeinflussen. Im Laufe der Zeit haben sich hierfür verschiedene Syntheserouten etabliert. Die am weitesten verbreitete Methode stellt die Solvothermalsynthese dar, bei der Metallsalze mit bi-, tri- oder multifunktionalen Liganden in einem Solvens bei hohen Temperaturen und Drücken zu MOFs umgesetzt werden. Als Solvens kommen dabei häufig Alkohole oder Dialkylformamide zum Einsatz.[12, 35] Eine weitere Methode ist die Hydrothermalsynthese, welche im wässrigen Medium bei Temperaturen und Drücken oberhalb von 100 °C und 1 bar stattfindet. Weitere Herstellungsverfahren, neben der Raumtemperatursynthese, sind die Mikrowellensynthese, elektrochemische, mechanochemische und sonochemische Synthese. Eine Übersicht der verschiedenen Synthesemethoden ist in Abbildung 4 dargestellt.[12]

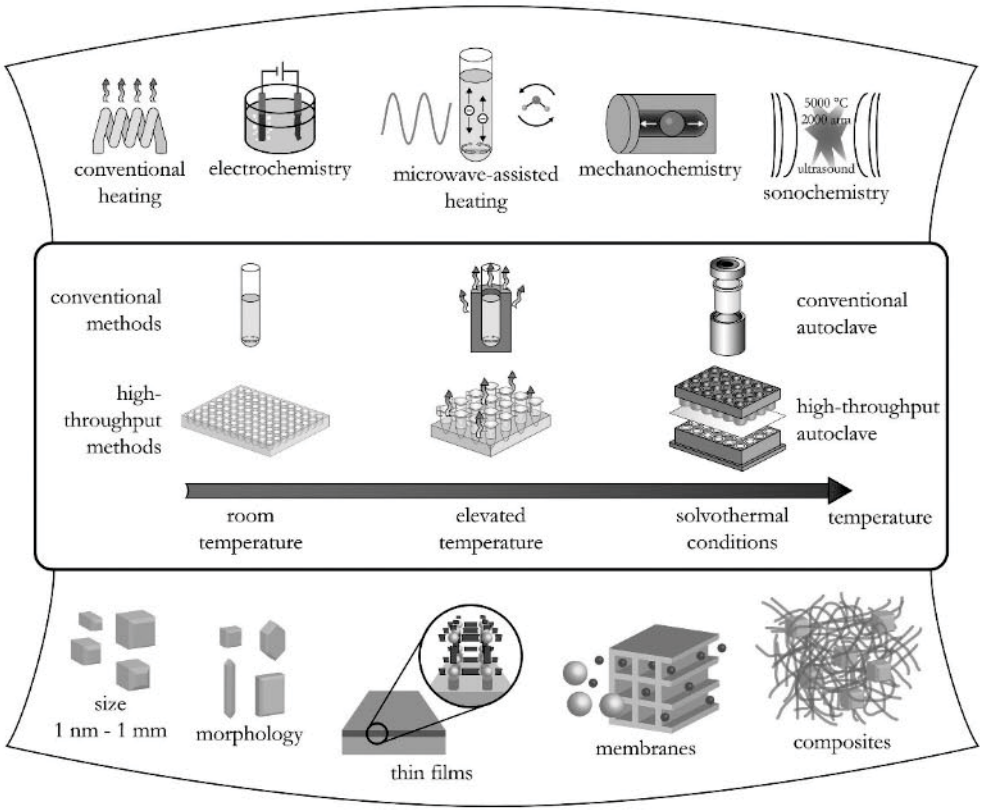


Abbildung 4: Übersicht über verschiedene Synthesemöglichkeiten von MOFs. Nachdruck mit Genehmigung von Ref. [12] © 2011 American Chemical Society.

MOFs stehen damit an der Schnittstelle zwischen klassischer porenstruktureller Festkörperchemie, Koordinationschemie und funktionalen optischen Materialien. Die Kombination aus designbasierter Synthese, struktureller Ordnung und chemischer Variabilität bildet eine Grundlage für die Entwicklung lumineszenter Wirt-Gast-Systeme, in denen photophysikalische Prozesse gezielt gesteuert und im Zusammenhang mit der Gerüststruktur untersucht werden können.

1.2 Lumineszenz

Lumineszenz bezeichnet die Emission von Licht, die nicht auf thermische Anregung (Glühen), sondern auf elektronische Anregungsprozesse zurückgeht.[36-38] In molekularen Systemen entsteht Lumineszenz typischerweise nach Absorption von Photonen oder nach elektronischem Ladungstransfer, wodurch ein oder mehrere Elektronen aus dem Grundzustand (S_0) in angeregte Zustände (S_1–S_n) überführt werden. Die anschließende Rückkehr in energetisch tiefere Zustände kann strahlend (unter Emission von Licht) oder nichtstrahlend (unter Freisetzung von Wärme) erfolgen.[36] Die beobachtete Emission ist das Resultat einer Konkurrenz zwischen

Strahlungsprozessen und verschiedenen nichtstrahlenden Relaxationskanälen wie interner Konversion (*engl.* Internal Conversion, IC), Interkombination (*engl.* Intersystem Crossing, ISC) oder Vibrationsrelaxation. Es wird zwischen den zwei verschiedenen Emissionsprozessen Fluoreszenz und Phosphoreszenz unterschieden.[39] Fluoreszenz bezeichnet die strahlende Relaxation aus einem angeregten Singulettzustand S_1 in den elektronischen Grundzustand S_0 und ist typischerweise durch kurze Lebenszeiten im Bereich von Nanosekunden gekennzeichnet. Gemäß der Kasha-Regel stammt die Emission in der Regel ausschließlich aus dem niedrigsten schwingungsrelaxierten Zustand des S_1-Niveaus, da Elektronen aus höher angeregten Zuständen durch sehr schnelle interne Konversion und Vibrationsrelaxation zunächst strahlungslos in den S_1-Zustand übergehen, bevor eine Emission stattfinden kann.[40] Phosphoreszenz geht dagegen von einem angeregten Triplettzustand T_1 aus, der durch Intersystem Crossing aus einem Singulettzustand hervorgeht. Aufgrund der spinverbotenen Natur des Triplett-Singulett-Übergangs sind die Phosphoreszenzlebenszeiten deutlich länger und können von Mikrosekunden bis hin zu Sekunden reichen. Eine vereinfachte Darstellung der beschriebenen energetischen Prozesse der Fluoreszenz und Phosphoreszenz können mithilfe des Jabłoński-Diagramms veranschaulicht werden (Abbildung 5).[41-42]

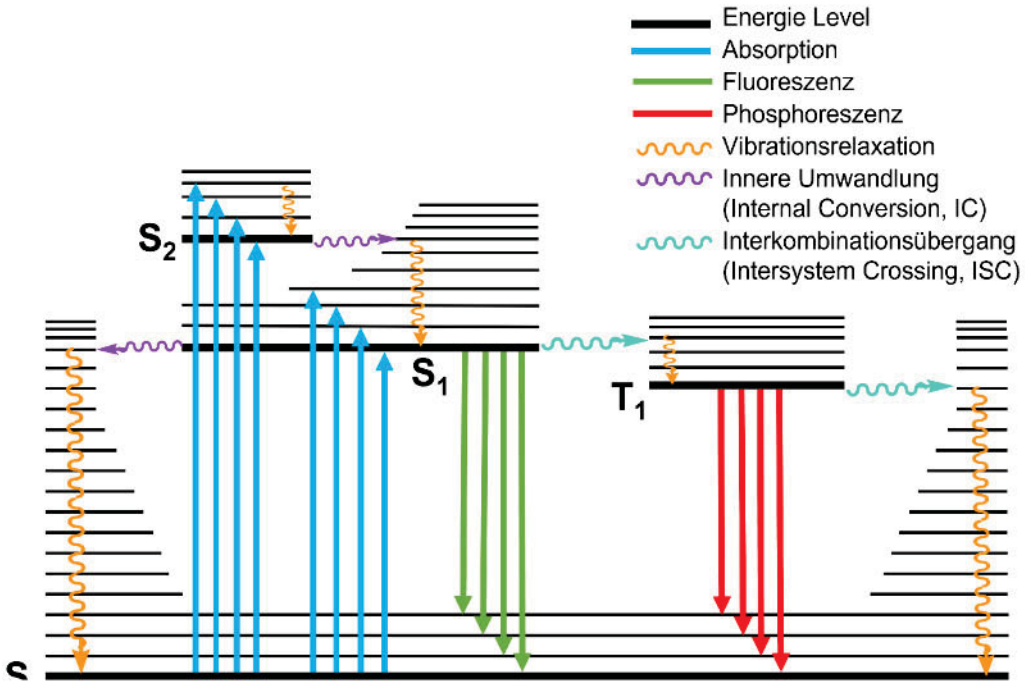


Abbildung 5: Vereinfachtes Jabłoński-Diagramm. Die Abbildung wurde in Anlehnung an Ref. [43] erstellt.

Einen Anwendungsfall auf dieser Grundlage bildet eine organische Leuchtdiode (*engl.* Organic light-emitting diode, OLED), welche ein mehrschichtig aufgebautes Bauelement ist, das aus Anode, Kathode sowie organischen Transport- und Emissionsschichten besteht.[44-46] In diesen Schichten werden die injizierten Ladungsträger (Elektronen und Elektronenlöcher) transportiert und rekombinieren im Emissionsbereich unter Lichtemission. Dabei werden angeregte Zustände, sogenannte Exzitonen, gebildet, deren Spinverteilung statistisch im Verhältnis von etwa 1:3 auf Singulett- (S_1) und Triplettzustände (T_1) erfolgt.[47-49] Diese Spin-Statistik ergibt sich aus den möglichen Kombinationen der Elektronenspins bei der Rekombination. Ein schematischer Aufbau einer organischen Leuchtdiode ist in Abbildung 6 abgebildet.

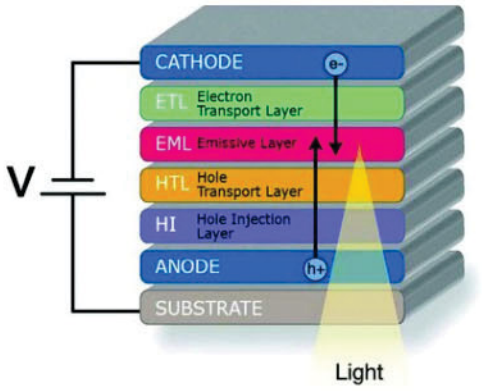


Abbildung 6: Schematischer Aufbau einer organischen Leuchtdiode (OLED). Nachdruck mit Genehmigung von Ref. [50] © 2018 WILEY-VCH Verlag GmbH & Co. KGaA, Weinheim.

Konventionelle fluoreszierende Emitter, wie beispielsweise Derivate von Anthracen oder Coumarin, emittieren Licht ausschließlich aus Singulettzuständen nach elektronischer Anregung.[36] Der Übergang vom angeregten Singulettzustand in den Grundzustand ($S_1 \rightarrow S_0$) ist Spin-erlaubt und daher effizient, während Triplettzustände aufgrund ihres Spin-verbotenen Charakters nur sehr langsam oder gar nicht zur Emission beitragen. Die Triplettpopulation geht stattdessen überwiegend durch nichtstrahlende Prozesse verloren, wodurch die maximale interne Quantenausbeute solcher Systeme auf etwa 25 % begrenzt ist.[51]

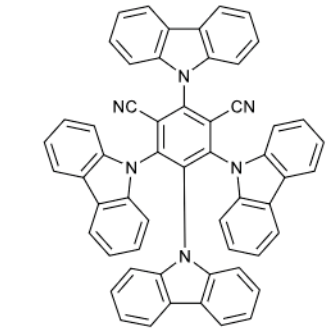
Phosphoreszierende Emitter überwinden die auf etwa 25 % begrenzte interne Quantenausbeute (*engl.* Internal Quantum Efficiency, IQE) konventioneller fluoreszierender OLEDs durch die Nutzung schwerer Metallzentren, insbesondere Iridium(III) oder Platin(II).[52] Bekannte Beispiele sind der grün emittierende Komplex

$Ir(ppy)_3$ und der rot emittierende Porphyrinkomplex PtOEP.[53-54] Die durch die schweren Metallatome hervorgerufene starke Spin-Bahn-Kopplung führt zu einer Mischung von Singulett- und Triplettzuständen und lockert dadurch die Spin-Auswahlregeln. Auf diese Weise wird der strahlende Übergang vom niedrigsten Triplettzustand in den Singulettgrundzustand ($T_1 \rightarrow S_0$) ermöglicht und sowohl Singulett- als auch Triplett-Exzitonen können zur Lichtemission beitragen.[44] Theoretisch können phosphoreszierende OLEDs daher interne Quantenausbeuten von nahezu 100 % erreichen.[55] Nachteile dieser Emittermaterialien ergeben sich insbesondere aus der Verwendung seltener und kostenintensiver Metalle wie Iridium und Platin. Darüber hinaus stellen vor allem die Entwicklung stabiler blau phosphoreszierender OLEDs und die begrenzte Betriebsstabilität weiterhin Herausforderungen dar.[56] Langlebige Triplettzustände können zudem bei hohen Anregungsdichten die Wahrscheinlichkeit von Löschprozessen erhöhen. Prozesse wie Triplet-Triplet Annihilation tragen zum Effizienzabfall bei hohen Stromdichten und zur Degradation phosphoreszierender OLEDs bei.[57] Die Entwicklung neuer lumineszenter Materialien ist daher von zentraler Bedeutung für die Optimierung der Leistungsfähigkeit organischer Leuchtdioden.

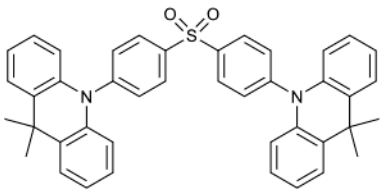
1.2.1 TADF

Die vorbeschriebenen Limitierungen – kostenintensive Ressourcen, begrenzte Stabilität, eingeschränkte Umweltverträglichkeit und vor allem geringe Effizienz – haben zur Entwicklung alternativer Konzepte geführt, insbesondere organischer thermisch aktivierte verzögerte Fluoreszenz- (*engl*. Thermally Activated Delayed Fluorescence, TADF-)Emitter, die ohne Schwermetalle und langen Lebenszeiten der Phosphoreszenz auskommen und dennoch eine effiziente Nutzung von Triplettzuständen ermöglichen. Das Konzept der verzögerten Fluoreszenz ist bereits seit den 1960er Jahren bekannt und wurde ursprünglich im Zusammenhang mit organischen Farbstoffen wie Eosin beschrieben.[58] Eine breite Anwendung in der organischen Optoelektronik erlangte TADF jedoch erst deutlich später, insbesondere seit der gezielten molekularen Entwicklung effizienter Emitter ab etwa 2012 durch Chihaya Adachi und Mitarbeitende.[46] Zu den frühen und häufig zitierten Beispielen zählen Donor-Akzeptor-(DA-)Verbindungen wie 4CzIPN (2,4,5,6-Tetra(9*H*-carbazol-9-yl)isophthalonitril), die als prototypische TADF-Moleküle gelten (Abbildung 7).[46]

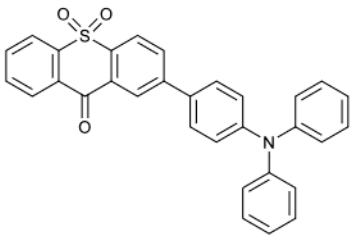
Neben 4CzIPN wurden zahlreiche weitere Vertreter dieser Klasse entwickelt, darunter DMAC-DPS (9,9-Dimethyl-9,10-dihydroacridin-diphenylsulfon), TXO-TPA sowie PXZ-TRZ, die sich durch unterschiedliche Donor- und Akzeptoreinheiten sowie variierende Emissionsfarben auszeichnen (Abbildung 7).[59-61]



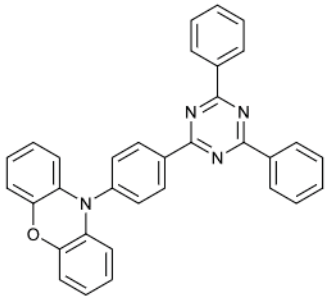
2,4,5,6-Tetra(9*H*-carbazol-9-yl) isophthalonitril
(4CzIPN)



10,10'-(Sulfonylbis(4,1-phenylen)) bis(9,9-dimethyl-9,10-dihydroacridin)
(DMAC-DPS)



2-(4-(diphenylamino)phenyl)-9*H*-thioxanthen-9-on-10,10-dioxid
(TXO-TPA)



10-(4-(4,6-diphenyl-1,3,5-triazin-2-yl) phenyl)-10*H*-phenoxazin
(PXZ-TRZ)

Abbildung 7: Strukturformeln von 4CzIPN, DMAC-DPS, TXO-TPA und PXZ-TRZ.

In diesen Molekülen bezeichnet der Begriff Donor-Akzeptor-Struktur typischerweise eine kovalent verknüpfte Elektronendonator-Elektronenakzeptor-Architektur mit einem ausgeprägten Charge-Transfer-Charakter, die den Singulett-Triplett-Abstand ΔE_{ST} verringert. TADF basiert auf diesem kleinen energetischen Abstand zwischen dem niedrigsten angeregten Singulettzustand S_1 und dem entsprechenden Triplettzustand T_1. Nach der Anregung entstehen zunächst Singulett-Exzitonen, aus denen gemäß Kashas Regel zunächst prompt fluoreszierende Emission aus dem S_1-Zustand mit kurzen Lebensdauern im Nanosekundenbereich erfolgen kann.[40] Gleichzeitig kann ein Teil der angeregten Population durch Intersystem Crossing in den Triplettzustand T_1 überführt werden, von wo aus sie bei hinreichend kleinem ΔE_{ST} thermisch aktiviert wieder zurück in den Singulettzustand zurückgelangt (reverse Intersystem Crossing, rISC) und so zur verzögerten Fluoreszenz beiträgt.[62] Abbildung 8 zeigt den

vereinfachten Vergleich zwischen den Elektronentransferprozessen in einer konventionellen OLED und einer TADF-basierten OLED.

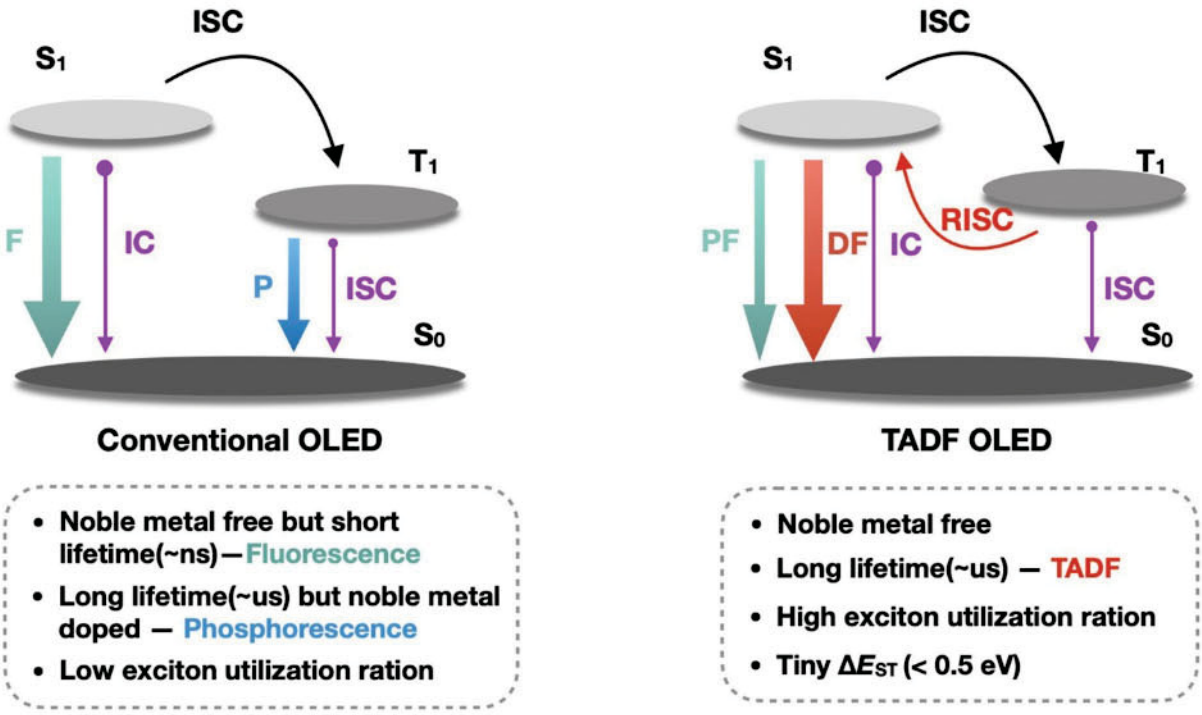


Abbildung 8: Vergleich der Elektronentransfermechanismen in einer konventionellen OLED (links) mit einer TADF-basierten OLED (rechts). Nachdruck mit Genehmigung von Ref. [63] © 2020 Frontiers in Chemistry.

Diese sogenannte *delayed fluorescence* weist typischerweise Lebensdauern im Mikrosekundenbereich auf und zeigt eine deutliche Temperaturabhängigkeit, da der rISC-Prozess thermisch aktiviert ist. Die effiziente Realisierung kleiner ΔE_{ST}-Werte wird häufig durch eine gezielte räumliche Trennung von den höchsten besetzten Molekülorbitalen (*engl*. Highest occupied molecular orbital, HOMO) und den niedrigsten unbesetzten Molekülorbitalen (*engl*. Lowest unoccupied molecular orbitals, LUMO) erreicht, wie sie in klassischen Donor-Akzeptor-Systemen vorkommt. In stark verdrehten DA-Molekülen ist das höchste besetzte Molekülorbital überwiegend am Donor lokalisiert, während das niedrigste unbesetzte Molekülorbital vorwiegend am Akzeptor zentriert ist. [64] Dies führt zwar zu einer Reduktion des Austauschintegrals und verringert damit den Singulett-Triplett-Abstand, erleichtert jedoch zugleich nichtstrahlende Prozesse und resultiert in zu breiten Emissionsbanden.

Die Effizienz von TADF-Emittern wird durch das Zusammenspiel von promptem und verzögertem Fluoreszenzanteil bestimmt. Die Gesamtquantenausbeute hängt damit sowohl von der Geschwindigkeitskonstante des strahlenden Zerfalls aus dem

Singulettzustand als auch von der rISC-Rate und der Minimierung nichtstrahlender Zerfallsraten ab.[44] Umgebungseffekte wie Matrixsteifigkeit, Polarität oder Aggregation beeinflussen diese Prozesse maßgeblich. Daher spielt die Einbettung von TADF-Emittern in geeignete Wirtsmaterialien eine zentrale Rolle, um die Vorteile des TADF-Mechanismus in praktischen Anwendungen, insbesondere in OLED-Strukturen, auszuschöpfen.

1.2.2 MR-TADF

Multiresonante TADF-(MR-TADF-)Emitter zeichnen sich insbesondere durch ihre typischerweise schmalbandige Emission, geringe Stokes-Verschiebung und hohe Farbreinheit aus (Abbildung 9).[62, 65] Diese Eigenschaften machen sie besonders attraktiv für Anwendungen, bei denen eine präzise Farbkontrolle und enge Emissionsbanden erforderlich sind, beispielsweise in hochauflösenden OLED-Displays.[66] Im Vergleich zu klassischen Donor-Akzeptor-TADF-Emittern ermöglichen MR-TADF-Systeme somit eine deutlich stärkere spektrale Eingrenzung der Emission.

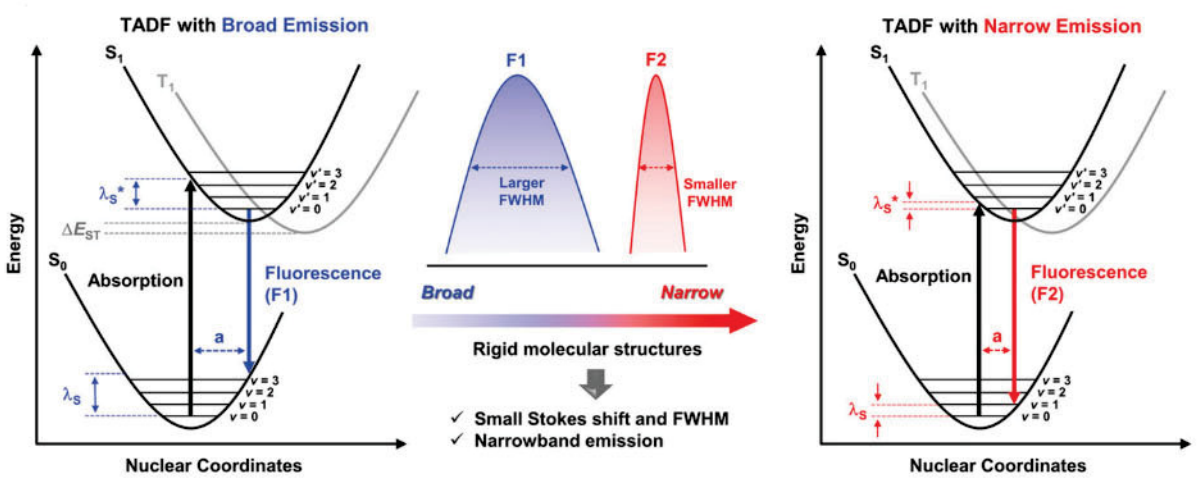


Abbildung 9: Schematische Darstellung des Grundprinzips für schmalbandige Emission. Nachdruck mit Genehmigung von Ref. [62] © 2022 The Authors. Advanced Optical Materials published by Wiley-VCH GmbH.

Die Ursache hierfür liegt in ihrem besonderen molekularen Aufbau. Während bei klassischen, häufig verdrehten Donor-Akzeptor-TADF-Molekülen die Trennung von HOMO und LUMO überwiegend durch die räumliche Separation von Donor- und Akzeptoreinheiten erreicht wird, beruht das MR-TADF-Konzept auf einer alternierenden Elektronendichte innerhalb eines starren aromatischen Gerüsts (Abbildung 10).[67] Dadurch entsteht eine lokal begrenzte Ladungstrennung mit

Charge-Transfer-Charakter, wobei zugleich eine hohe lokale Übergangsdichte erhalten bleibt. Die starre Molekülstruktur reduziert zudem geometrische Relaxationen im angeregten Zustand, was wesentlich zur geringen Stokes-Verschiebung und zur schmalen Emissionsbandbreite beiträgt.[62]

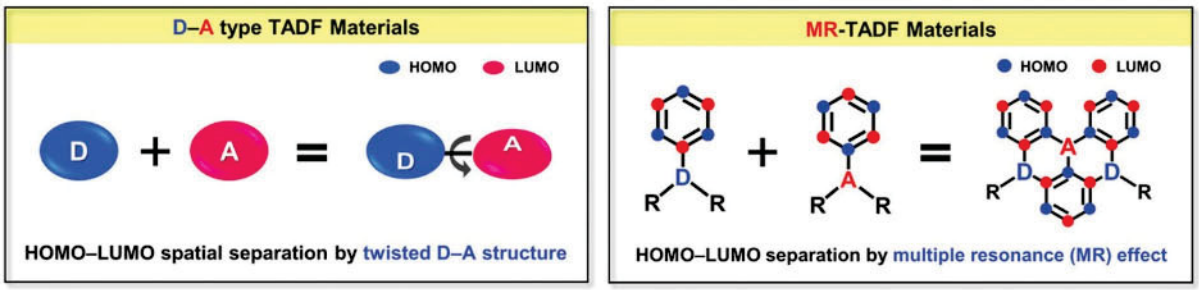


Abbildung 10: Design-Konzepte für Donor-Akzeptor TADF Materialien (links) und Multiresonante TADF Materialien (rechts). Nachdruck mit Genehmigung von Ref. [62] © 2022 The Authors. Advanced Optical Materials published by Wiley-VCH GmbH.

Der TADF-Mechanismus in solchen Systemen unterscheidet sich von dem klassischer Donor-Akzeptor-Emitter, da die effiziente Triplett-Singulett-Konversion weniger auf einer starken räumlichen Orbitaltrennung beruht. Stattdessen spielen vibronische Kopplungen zwischen energetisch nahe beieinanderliegenden Singulett- und Triplettzuständen eine zentrale Rolle.[68]

Trotz der vorteilhaften Eigenschaften von MR-TADF-Emittern bestehen weiterhin Herausforderungen. Dazu zählen die Kontrolle der Stabilität unter Betriebsbedingungen, sowie die Vermeidung von Degradationspfaden im angeregten Zustand. Eine mögliche Lösung dieser Herausforderungen liegt in der Einbettung der Emittermoleküle in geeignete Wirtsmaterialien. Die Wechselwirkung mit der Matrix kann Energieniveaus, rISC-Raten und Emissionsbandbreiten beeinflussen und verlangt eine sorgfältige Abstimmung von Emitter- und Wirtsdesign.

1.3 Einlagerungsmethoden

Die Einlagerung funktionaler Gastmoleküle in Metall-organische Gerüstverbindungen stellt eine zentrale Strategie dar, um gezielt hybride Materialsysteme mit maßgeschneiderten Eigenschaften zu erzeugen.[69] Durch die Kombination des kristallinen, porösen Wirtsgerüsts mit molekularen Gästen lassen sich Komposite realisieren, deren physikalische, chemische und optische Eigenschaften über die Einzelkomponenten hinausgehen. Eine Vielzahl unterschiedlicher Spezies kann in MOFs immobilisiert werden, darunter Metall-Nanocluster[70], pharmazeutische

Wirkstoffe[71], Enzyme[72], Fullerene[73] sowie (lumineszente) Farbstoffe[74]. Die erfolgreiche Einlagerung kann sich bereits makroskopisch, beispielsweise durch Farbänderungen, bemerkbar machen und wird typischerweise durch eine Kombination analytischer Methoden wie Pulverröntgendiffraktometrie (*engl*. Powder X-Ray Diffraction, PXRD), Sorptionsmessungen sowie Rasterelektronenmikroskopie (REM) mit energiedispersiver Röntgenanalyse (EDX), UV/Vis-, Fluoreszenz-, Infrarot- (IR) und Raman-Spektroskopie, thermogravimetrischer Analyse (TGA) oder Elementaranalyse verifiziert.

Die Integration von Gastmolekülen erfolgt dabei auf verschiedene Art und Weise, bei denen entweder das Gerüst um das Molekül herum aufgebaut wird (*in situ*) oder das bereits gebildete MOF nachträglich beladen wird (post-synthetisch).[69] Unabhängig vom konkreten Vorgehen resultiert die Einlagerung in einer räumlichen Fixierung der Moleküle innerhalb der Porenstruktur, wodurch deren Beweglichkeit, Orientierung und lokale Umgebung gezielt beeinflusst werden. Dies ist insbesondere für empfindliche oder reaktive Spezies von Bedeutung. So können beispielsweise Enzyme oder pharmazeutische Wirkstoffe innerhalb des Gerüsts vor äußeren Einflüssen geschützt und gleichzeitig kontrolliert freigesetzt werden, wie es für Systeme etwa von MIL-100 oder UiO-66 gezeigt wurde.[75-77] Auch die Stabilität vieler Gastmoleküle kann durch die Einbettung signifikant erhöht werden, was sich in einer verbesserten thermischen und chemischen Beständigkeit sowie einer verlängerten Lebensdauer äußert.

Für optisch aktive Moleküle wie Farbstoffe oder TADF-Emitter spielt die Einlagerung eine besonders wichtige Rolle, da deren Emissionseigenschaften stark von der molekularen Umgebung abhängen. Ein zentrales Problem vieler organischer Chromophore ist das sogenannte „Aggregation Caused Quenching“ (ACQ), bei der intermolekulare Wechselwirkungen wie π-π-Stapelung zu einer Abschwächung oder vollständigen Unterdrückung der Lumineszenz führen.[78-79] Die definierte Porenstruktur von MOFs ermöglicht eine effektive räumliche Trennung einzelner Moleküle und kann somit Aggregationsprozesse gezielt unterbinden. Gleichzeitig bietet die kristallographisch geordnete Struktur im Vergleich zu amorphen Matrizen eine wohldefinierte Umgebung, in der Struktur-Eigenschafts-Beziehungen systematisch untersucht werden können. Neben der reinen räumlichen Isolation tragen auch Wechselwirkungen zwischen Wirtsgerüst und Gastmolekülen wesentlich zur Modulation der chemischen, photophysikalischen und optischen Eigenschaften bei.

Wasserstoffbrückenbindungen, elektrostatische Effekte, koordinative Bindungen oder π-π-Wechselwirkungen mit den organischen Linkern können die energetische Lage angeregter Zustände sowie strahlende und nichtstrahlende Übergangsprozesse beeinflussen.[80] Darüber hinaus bestimmen Porengröße und -geometrie die Freiheitsgrade der Gastmoleküle. Eine eingeschränkte Rotation oder Konformationsänderung kann nichtstrahlende Relaxationsprozesse reduzieren und strahlende Übergänge begünstigen.

Insgesamt stellen MOFs somit nicht nur passive Wirtsmaterialien dar, sondern fungieren als aktiv gestaltbare Plattformen zur Kontrolle molekularer Eigenschaften. Die in dieser Arbeit untersuchten Systeme nutzen dieses Konzept, indem Farbstoffe gezielt in MOF-Strukturen eingebracht werden, um den Einfluss von Wirt-Gast-Wechselwirkungen und struktureller Ordnung auf die unterschiedlichen Emissionsverhalten zu untersuchen.

1.4 Verwendete Farbstofftypen

1.4.1 Flavine

Flavine stellen eine Klasse stickstoffhaltiger, aromatischer Heterozyklen dar, die auf einem trizyklischen Isoalloxazin-Grundgerüst basieren. Dieses besteht aus einem kondensierten Ringsystem mit mehreren Stickstoff- und Carbonylfunktionen, wodurch sich eine ausgeprägte Elektronendelokalisierung sowie vielseitige Wechselwirkungsmöglichkeiten ergeben. Zu den bekanntesten Vertretern zählen Riboflavin (Vitamin B_2), Flavinmononukleotid (FMN) und Flavinadenindinukleotid (FAD), die in biologischen Systemen als Cofaktoren weit verbreitet sind (Abbildung 11).

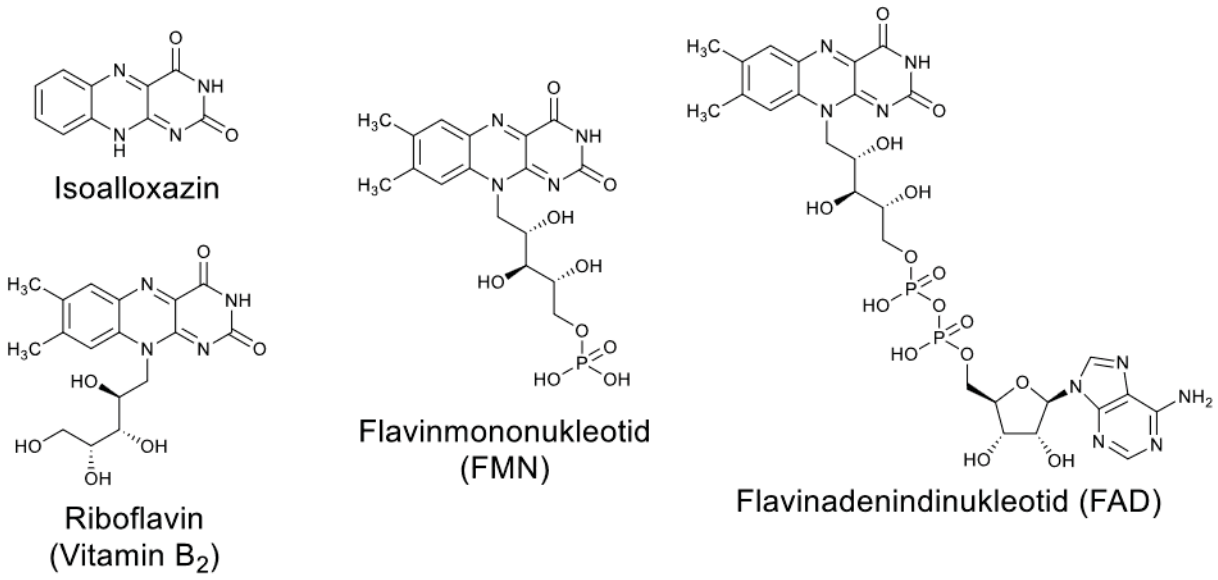


Abbildung 11: Strukturformeln von Isoalloxazin (links oben), Riboflavin (Vitamin B_2) (links unten), Flavinmononukleotid (FMN) (mittig) und Flavinadenindinukleotid (FAD) (rechts).

Ein charakteristisches Merkmal von Flavinen ist ihre strukturelle und chemische Variabilität. Durch Substitution an verschiedenen Positionen des Isoalloxazin-Gerüsts können sowohl elektronische Eigenschaften als auch Löslichkeit und intermolekulare Wechselwirkungen gezielt beeinflusst werden. Insbesondere die funktionellen Gruppen im Ringsystem ermöglichen Wasserstoffbrückenbindungen sowie Wechselwirkungen mit polaren und koordinierenden Umgebungen, was Flavine zu geeigneten Bausteinen für supramolekulare Systeme macht.

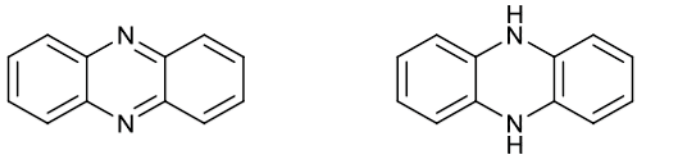
Die photophysikalischen Eigenschaften von Flavinen sind stark von ihrem Oxidationszustand abhängig. Während oxidierte Flavine typischerweise intensive Absorptionsbanden im blauen Bereich zeigen und gelb fluoreszieren, weisen reduzierte Formen deutlich veränderte elektronische Strukturen und Emissionseigenschaften auf.[81] Charakteristisch ist zudem die Empfindlichkeit gegenüber der Umgebung, insbesondere hinsichtlich Polarität, pH-Wert und Wasserstoffbrückenbindungen, wodurch sich ihre spektralen Eigenschaften gezielt modulieren lassen. Aufgrund dieser Eigenschaften finden Flavine nicht nur in biologischen Systemen Anwendung, sondern werden zunehmend auch in synthetischen Materialien eingesetzt. Beispiele hierfür sind ihre Verwendung als Photokatalysatoren oder als Bausteine für sensorische Systeme.[82] Ihre Fähigkeit, definierte nichtkovalente Wechselwirkungen einzugehen, macht sie insbesondere für

die Integration in strukturierte Wirtssysteme wie poröse Materialien oder koordinative Gerüste interessant.

Insgesamt stellen Flavine somit vielseitige, strukturell gut modifizierbare Moleküle dar, deren Kombination aus konjugiertem π-System, funktionellen Gruppen und Redoxflexibilität sie zu attraktiven Kandidaten für die Entwicklung funktionaler Materialsysteme macht.

1.4.2 Phenazine

Phenazine bilden eine Klasse planarer, aromatischer Stickstoffheterozyklen, die aus zwei kondensierten Benzolringen mit zwei gegenüberliegenden Stickstoffatomen an den Positionen 5 und 10 bestehen (Abbildung 12). Sie zeichnen sich durch ihre ausgedehnte π-Konjugation und ihre ausgeprägte Redoxaktivität aus und werden daher seit langem als Farbstoffe sowie als funktionale Bausteine in elektrochemischen und elektronischen Materialien untersucht.[83] Ein bekanntes Beispiel ist das natürlich vorkommende Pyocyanin, das von *Pseudomonas aeruginosa* produziert wird und durch seine intensive Färbung sowie redoxaktive Eigenschaften charakterisiert ist. Darüber hinaus finden substituierte Phenazine Anwendung in elektrochemischen Systemen, etwa als organische Halbleiter oder in Batteriematerialien.[84]



Phenazin 5,10-Dihydrophenazin

Abbildung 12: Strukturformeln von Phenazin (links) und 5,10-Dihydrophenazin (rechts).

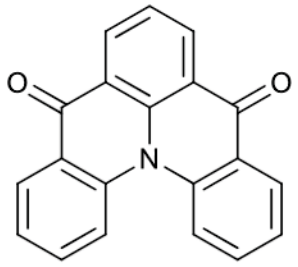
Von besonderem Interesse im Kontext moderner optoelektronischer Materialien sind Dihydrophenazine, die formal durch partielle Reduktion des Phenazingerüsts entstehen (Abbildung 12). Diese Verbindungen zeichnen sich durch eine nicht-planare, häufig schmetterlingsartige Geometrie aus, die zu einer partiellen räumlichen Trennung von Elektronendonor- und -akzeptor-Bereichen innerhalb des Moleküls führen kann. Dadurch ergeben sich günstige Voraussetzungen für die Ausbildung von angeregten Zuständen mit reduziertem Singulett-Triplett-Energieabstand.[85] Durch gezielte Substitution, beispielsweise mit elektronenziehenden oder -donierenden Gruppen, lassen sich die elektronischen Eigenschaften von Dihydrophenazinen gezielt

einstellen. Beispiele hierfür sind Carbazol- oder Triazin-substituierte Derivate, die in den letzten Jahren als effiziente organische Emitter untersucht wurden.[61, 86]

Darüber hinaus weisen Dihydrophenazine eine gute synthetische Zugänglichkeit auf, was ihre Anwendung in OLEDs und verwandten Technologien begünstigt. Die Möglichkeit, ihre Struktur gezielt zu variieren, macht sie zu einer vielseitigen Plattform für das Design funktionaler organischer Materialien mit maßgeschneiderten photophysikalischen Eigenschaften.

1.4.3 DiKTa

DiKTa (Chinolin[3,2,1-*de*]acridin-5,9-dion, früher bekannt als QAO) gehört zu den prominentesten Vertretern der MR-TADF-Materialklasse.[87-88] Die polyzyklische, starre Struktur führt zu einer lokalisierten elektronischen Anregung mit nur geringer Geometrieänderung zwischen Grund- und angeregtem Zustand (Abbildung 13). Im Vergleich zu klassischen DA-TADF-Emittern weisen DiKTa-basierte Systeme eine reduzierte Abhängigkeit von molekularen Konformationen auf, da Rotationsfreiheiten weitgehend unterdrückt sind. Dies wirkt sich positiv auf die Reproduzierbarkeit der Emissionscharakteristika und auf die spektrale Stabilität aus. Gleichzeitig begünstigt die starre Gerüststruktur eine erhöhte Stabilität gegenüber thermischer und photochemischer Degradation, was für Anwendungen mit hohen Betriebszeiten relevant ist.[88] Im Vergleich zu anderen MR-TADF-Emittern, die häufig auf borhaltigen π-Systemen beruhen, weist DiKTa eine charakteristische Grenzorbital-Verteilung auf und emittiert typischerweise im blauen bis grünlichen Spektralbereich. Durch Substitution und gezielte Modifikation des Grundgerüsts lässt sich die Emissionsfarbe weiter fein abstimmen.



Chinolin[3,2,1-*de*]acridin-5,9-dion
(DiKTa)

Abbildung 13: Strukturformel von Chinolin[3,2,1-*de*]acridin-5,9-dion (DiKTa).

Das in dieser Arbeit untersuchte Wirt-Gast-System verwendet DiKTa als Modellmolekül, um das MR-TADF-Konzept im Detail zu beleuchten. Durch die Einbettung von DiKTa in Metall-organische Gerüstverbindungen wird untersucht, wie die Umgebung und spezifische Wirt-Gast-Wechselwirkungen die vibronische Kopplung, die rISC-Prozesse und die Emissionsbandbreite beeinflussen. Auf dieser Grundlage lassen sich Designprinzipien ableiten, die für die Entwicklung zukünftiger hybrider Emittermaterialien auf Basis von MR-TADF-Systemen relevant sind.

2 Zielsetzung und Motivation

Metall-organische Gerüstverbindungen zählen aufgrund ihrer modularen Struktur, ihrer hohen Porosität und ihrer gezielt einstellbaren chemischen Eigenschaften zu den vielseitigsten Materialklassen der modernen Koordinationschemie. Durch die nahezu beliebige Kombination unterschiedlicher Metallknoten und organischer Linker lassen sich Gerüststrukturen mit definierten Porengrößen, Oberflächen und chemischen Funktionalitäten gezielt aufbauen. Gleichzeitig ermöglichen diese porösen Strukturen die Immobilisierung funktioneller Gastmoleküle und eröffnen damit die Möglichkeit, deren strukturelle und photophysikalische Eigenschaften gezielt zu beeinflussen. Insbesondere lumineszente Farbstoffe stellen aufgrund ihrer empfindlichen Reaktion auf ihre molekulare Umgebung geeignete Modellsysteme dar, um Wirt-Gast-Wechselwirkungen in Metall-organischen Gerüstverbindungen zu untersuchen.

Trotz der großen Zahl bekannter MOFs besteht weiterhin erheblicher Forschungsbedarf hinsichtlich der Zusammenhänge zwischen Gerüststruktur, Wirt-Gast-Wechselwirkungen und den daraus resultierenden Materialeigenschaften. Einerseits ist bislang nur unzureichend verstanden, wie sich die molekulare Struktur organischer Linker auf die Ausbildung koordinativer Netzwerke und deren Topologien auswirkt. Andererseits ist noch nicht vollständig geklärt, wie Gerüststruktur, Porengeometrie und die Wechselwirkungen zwischen Wirt und Gast die photophysikalischen Eigenschaften eingelagerter lumineszenter Farbstoffe beeinflussen. Dies gilt insbesondere für moderne multiresonante TADF-Emitter, deren schmalbandige Emission und hohe Farbreinheit sie zu vielversprechenden Kandidaten für zukünftige optoelektronische Anwendungen machen.

Vor diesem Hintergrund verfolgt die vorliegende Dissertation das Ziel, den Zusammenhang zwischen der Struktur von Metall-organischen Gerüstverbindungen, den photophysikalischen Eigenschaften lumineszenter Farbstoffe und den zugrunde liegenden Wirt-Gast-Wechselwirkungen systematisch zu untersuchen. Hierzu werden sowohl neue Koordinationsnetzwerke entwickelt und strukturell charakterisiert als auch unterschiedliche lumineszente Gastmoleküle gezielt in Metall-organische Gerüstverbindungen eingebracht. Dadurch sollen grundlegende Struktur-Eigenschafts-Beziehungen aufgeklärt und ein vertieftes Verständnis der Wechselwirkungen zwischen Gerüststruktur und Gastmolekülen geschaffen werden.

Zur Bearbeitung dieser Fragestellung gliedert sich die Dissertation in drei aufeinander aufbauende Teilprojekte:

Im ersten Teil der Arbeit werden neuartige dihydrophenazinbasierte Dicarboxylat- und Tetracarboxylat-Linker synthetisiert und als Bausteine für koordinative Netzwerke eingesetzt. Ziel ist es, den Einfluss der Linkerstruktur auf die Ausbildung neuer Koordinationspolymere, deren Sekundärbaueinheiten und Gerüsttopologien zu untersuchen. Die erhaltenen Strukturen werden mittels Einkristall- und Pulverröntgendiffraktometrie sowie weiterer analytischer Methoden umfassend charakterisiert, um grundlegende Struktur-Eigenschafts-Beziehungen aufzuklären.

Der zweite Teil der Dissertation beschäftigt sich mit der Einlagerung eines Flavinderivats in aluminiumbasierte Metall-organische Gerüstverbindungen. Im Mittelpunkt stehen die Untersuchung der Wirt-Gast-Wechselwirkungen sowie deren Einfluss auf die Lumineszenzeigenschaften des eingelagerten Farbstoffs. Darüber hinaus wird das Potenzial der erhaltenen Flavin@MOF-Komposite als fluoreszenzbasierte Sensoren für nitroaromatische Verbindungen untersucht.

Der Schwerpunkt des dritten Teils liegt auf der Einlagerung des multiresonanten TADF-Emitters DiKTa in MOF-5. Das Ziel bei diesem Projekt ist es, die strukturellen und photophysikalischen Eigenschaften des Emitters innerhalb einer definierten porösen Wirtsstruktur zu untersuchen und den Einfluss der räumlichen Isolation auf sein Lumineszenzverhalten zu bewerten. Hierzu werden verschiedene komplementäre Charakterisierungsmethoden eingesetzt, um sowohl die erfolgreiche Einlagerung als auch die Wechselwirkungen zwischen Wirt und Gast nachzuweisen. Ein besonderes Augenmerk liegt dabei auf der Unterdrückung aggregationsbedingter Effekte sowie auf dem Erhalt der charakteristischen MR-TADF-Photophysik im Festkörper.

Die Ergebnisse der drei Teilprojekte tragen gemeinsam zu einem vertieften Verständnis der Struktur, photophysikalischen Eigenschaften und der zugrundeliegenden Wirt-Gast-Wechselwirkungen lumineszenter Farbstoffe in Metall-organischen Gerüstverbindungen bei. Gleichzeitig liefern sie neue Erkenntnisse für das rationale Design MOF-basierter Hybridmaterialien und eröffnen Perspektiven für deren Einsatz in der chemischen Sensorik sowie in der organischen Optoelektronik.

3 Kumulativer Teil

In den folgenden Unterkapiteln werden die im Rahmen dieser Dissertation entstandenen und in Fachzeitschriften eingereichten oder bereits publizierten Arbeiten, bei denen die Verfasserin Erstautorin ist, vorgestellt. Jede Publikation wird durch eine kurze Zusammenfassung ergänzt, wobei zudem die jeweiligen Eigenanteile an der Arbeit dargelegt werden. Die einzelnen Veröffentlichungen sind jeweils als eigenständige Abschnitte dargestellt und in chronologischer Reihenfolge nach dem Veröffentlichungsdatum angeordnet.

Die in diesem Kapitel enthaltenen Abbildungen, Tabellen und Schemata entsprechen der Originaldarstellung der jeweiligen Publikationen und sind daher nicht an das Format des Haupttextes dieser Dissertation angepasst. Ebenso werden die Literaturverzeichnisse der einzelnen Veröffentlichungen unverändert übernommen und jeweils am Ende der entsprechenden Publikation aufgeführt. Dadurch kann es zu mehrfachen Zitierungen derselben Literaturquellen kommen.

Publikationen, an denen die Verfasserin als Co-Autorin beteiligt war, werden in einem separaten Kapitel 3.4 vorgestellt. Auch hier werden die Arbeiten jeweils kurz zusammengefasst und die eigenen Beiträge erläutert.

Kapitel 5 fasst die zum Zeitpunkt der Einreichung dieser Dissertation noch unveröffentlichten Forschungsergebnisse zusammen, die bislang nicht Bestandteil eines Manuskriptentwurfs sind. Die darin beschriebenen Arbeiten befinden sich derzeit noch in Bearbeitung.

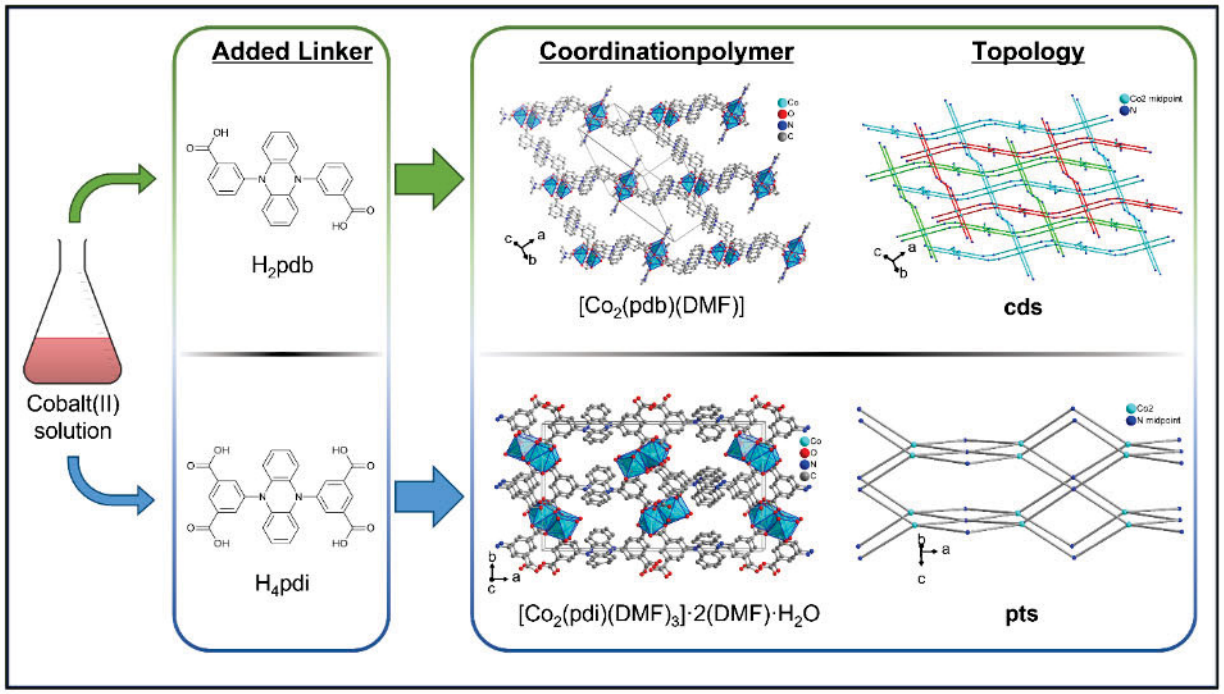
3.1 Cobalt Coordination Networks Based on the Linker (Phenazine-5,10-diyl)di- and Tetrabenzoate

Diese Arbeit wurde veröffentlicht in

Annette Vollrath, Xiang Liu, Nikolas Jansen, Philipp Seiffert, David Geller, Christoph Janiak, *Crystals* **2026**, *16*, 185. DOI: 10.3390/cryst16030185; Ref. [89]

Kurzzusammenfassung

Die Kobalt(II)-basierten Metall-organischen Gerüstverbindungen bzw. Koordinationspolymere [Co(pdb)(DMF)] und $[Co_2(pdi)(DMF)_3]\cdot 2DMF\cdot H_2O$ (H_2pdb = 3,3′-(Phenazin-5,10-diyl)dibenzoesäure; H_4pdi = 5,5′-(Phenazin-5,10-diyl)diisophthalsäure; DMF = *N,N*-Dimethylformamid) wurden durch solvothermale Synthese aus Kobalt(II)-nitrat und den entsprechenden organischen Linkern hergestellt. Systematische Untersuchungen der Synthesebedingungen zeigten einen deutlichen Einfluss des eingesetzten Metallions sowie des Gegenions auf die Gerüstbildung. Kristalline Koordinationspolymere konnten ausschließlich unter Verwendung von Kobalt(II)-nitrat erhalten werden, während andere Metallsalze sowie Kobalt(II)-chlorid und -sulfat keine kristallinen Produkte lieferten. Die Einkristallstrukturanalyse von [Co(pdb)(DMF)] ergab ein dreidimensionales Netzwerk, in dem dinukleare Kobalt-Einheiten als sekundäre Baueinheiten in einer Paddle-Wheel-Anordnung durch vier Carboxylatgruppen der organischen Linker miteinander verbunden sind. Das resultierende Gerüst besitzt eine cds- (oder $CdSO_4$-) Topologie, bei der die breiten Öffnungen durch zwei symmetrisch zueinander angeordnete Netze ausgefüllt werden, um eine dreifach interpenetrierte Struktur zu bilden. Im Fall von $[Co_2(pdi)(DMF)_3]\cdot 2DMF\cdot H_2O$ bilden zwei kristallographisch unterschiedliche Kobalt-Zentren das Gerüst, wobei ausschließlich eines der beiden Zentren mit allen vier Carboxylatgruppen des Tetracarboxylat-Linkers verknüpft ist und somit die Ausbildung des dreidimensionalen Netzwerks ermöglicht. Die Struktur kann einer pts- (oder Platin(II)-sulfid-) Topologie zugeordnet werden, wenn man das Co_2-Atom als tetraedrischen Knoten und den Linker als quadratisch-planaren Vierfachknoten betrachtet, wobei sich diese von klassischen pts-Gerüsten durch eine umgekehrte Anordnung der tetraedrischen und quadratisch-planaren Knoten unterscheidet.



Anteile an der Veröffentlichung

- Konzeption des Forschungsvorhabens gemeinsam mit Prof. Dr. C. Janiak.
- Entwicklung der Methodik und Durchführung der Versuche.
- Durchführung der Validierung, Datenaufbereitung sowie formalen Datenauswertung gemeinsam mit X. Li und N. Jansen.
- Durchführung der experimentellen Arbeiten gemeinsam mit X. Li, N. Jansen, P. Seiffert und D. Geller.
- Selbstständige Auswertung, graphische Darstellung und Interpretation der experimentellen Ergebnisse.
- Anfertigung des Manuskripts (Erstentwurf) sowie Erstellung der Visualisierungen gemeinsam mit Prof. Dr. C. Janiak.
- Überarbeitung des Manuskripts nach den Anmerkungen der Co-Autoren.
- Wissenschaftliche Betreuung, Bereitstellung der Ressourcen, Projektadministration und Einwerbung der Drittmittel durch Prof. Dr. C. Janiak.

crystals

MDPI

Article

Cobalt Coordination Networks Based on the Linker (Phenazine-5,10-diyl)di- and Tetrabenzoate

Annette Vollrath, Xiang Liu, Nikolas Jansen, Philipp Seiffert, David Geller and Christoph Janiak *

Institut für Anorganische Chemie und Strukturchemie, Heinrich-Heine-Universität, 40204 Düsseldorf, Germany; annette.vollrath@hhu.de (A.V.); xiang.liu@hhu.de (X.L.); nijan113@hhu.de (N.J.); philipp.seiffert@hhu.de (P.S.); david.geller@hhu.de (D.G.)
* Correspondence: janiak@uni-duesseldorf.de

Abstract

The crystal structures of the cobalt(II) metal–organic frameworks or coordination networks of [Co(pdb)(DMF)] and $[Co_2(pdi)(DMF)_3]\cdot 2(DMF)\cdot H_2O$ (H_2pdb = 3,3′-(phenazine-5,10-diyl)dibenzoic acid; H_4pdi = 5,5′-(phenazine-5,10-diyl)diisophthalic acid; DMF = *N*,*N*-dimethylformamide) were synthesized solvothermally from cobalt(II) nitrate and the free acid of the linker in DMF. Systematic solvothermal screening demonstrated strong metal- and counterion-dependent framework formation, as crystalline coordination polymers were obtained exclusively from cobalt(II) nitrate, whereas other metal salts and cobalt(II) chloride or sulfate produced no crystalline materials. In catena-[(*N*,*N*-dimethylformamide)-μ_4-3,3′-(phenazine-5,10-diyl)dibenzoate-cobalt(II)], [Co(pdb)(DMF)], the Co_2 units, acting as secondary building units, are coordinated by four carboxylate groups from four linkers in a paddle-wheel arrangement, giving a three-dimensional (3D) network with cds (or $CdSO_4$) topology, in which the wide openings are filled by two symmetry-related nets to form a threefold interpenetrated structure. In catena-[tris(*N*,*N*-dimethylformamide)-μ_8-5,5′-(phenazine-5,10-diyl)diisophthalate-dicobalt(II)] bis(*N*,*N*-dimethylformamide) hydrate, $[Co_2(pdi)(DMF)_3]\cdot 2(DMF)\cdot H_2O$, there are two different Co atoms, of which only Co_2 is connected to each of the four carboxylate groups of the tetracarboxylate linker and, thus, is responsible for 3D network formation. The network topology in $[Co_2(pdi)(DMF)_3]$ is pts (or platinum(II) sulfide) when taking the Co_2 atom as a tetrahedral node and the linker as a square-planar fourfold node; however, this arrangement is inverse to the common square-planar metal and tetrahedral linker nodes found in PtS and most pts topologies.

Keywords: cobalt coordination networks; dihydrophenazine; 3-fold interpenetrated cds topology; inverse pts topology; redox-active linker

Check for updates

Academic Editor: Peter Baran

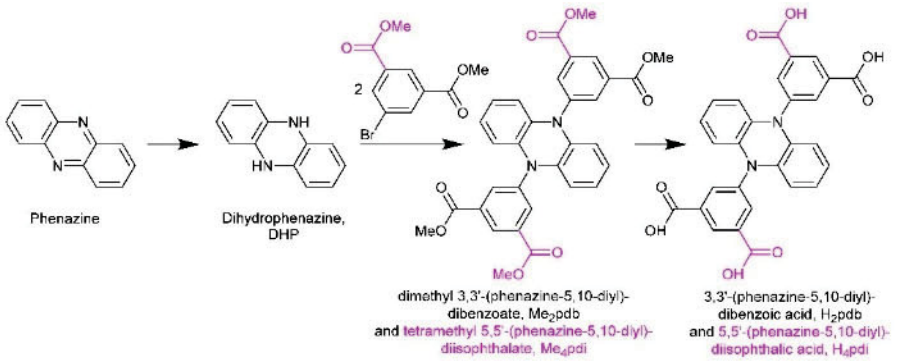
Received: 15 January 2026
Revised: 1 March 2026
Accepted: 2 March 2026
Published: 10 March 2026

Copyright: © 2026 by the authors. Licensee MDPI, Basel, Switzerland. This article is an open access article distributed under the terms and conditions of the Creative Commons Attribution (CC BY) license.

1. Introduction

Incorporating redox-active carboxylate linkers—such as those based on phenazine—into the construction of new coordination polymers (CPs) and metal–organic frameworks (MOFs) offers expanded opportunities to harness redox behavior [1–4]. Phenazine derivatives contain a dibenzo-fused pyrazine core and are well known for their intrinsic redox activity. They can be readily reduced to 5,10-dihydrophenazines, which, together with subsequent transformations, give access to a wide range of dihydrophenazine derivatives (Scheme 1) [5]. Dihydrophenazines (DHPs), particularly *N*,*N*′-substituted diaryl-phenazin-5,10-diyls, are electron-rich species that generate stable radical cations upon irradiation, heating, electrochemical oxidation, or treatment with suitable chemical oxidants [6]. Owing to their pronounced

redox activity and the stability of their radical cations [7,8], DHPs display distinctive optical, electronic, magnetic, and catalytic characteristics [9–11]. Several diaryl-substituted DHPs have been identified as effective photoredox catalysts for visible light-mediated atom transfer radical polymerization [12–17].



Scheme 1. Synthesis route to the free acids of the H_2pdb = 3,3′-(phenazine-5,10-diyl)dibenzoic acid (black skeletons) and H_4pdi = 5,5′-(phenazine-5,10-diyl)diisophthalic acid (black plus pink structure parts; the attached methylcarboxyl and carboxyl groups in pink are only present in the Me_4pdi and H_4pdi compounds). For details, see Section 2 and Section S2 in the Supplementary Materials.

Dihydrophenazine-based organic polymers [9,10,18], MOFs [10,19,20] and coordination cages [21] have been investigated for their electrochemical behavior [22–24] and have been explored as heterogeneous catalysts. While previous publications have reported on phenazine-based covalent organic frameworks (COFs) used for catalytic and optoelectronic applications [25–27], DHP-containing 2D and 3D covalent organic frameworks have demonstrated high efficiency as heterogeneous photocatalysts for the radical ring-opening polymerization of vinylcyclopropanes [18]. UiO-type MOF $[Zr_6(\mu_3\text{-}O)_4(\mu_3\text{-}OH)_4(pzdb)_6]$ (pzdb = 4,4′-(phenazine-5,10-diyl)dibenzoate)) [10] has been successfully utilized as a heterogeneous donor component to enhance catalytic electron donor–acceptor photoactivation. Similarly, the $[Zn_2(pzdb)_2(dabco)]\cdot 4DMF$ (dabco = 1,4-diazabicyclo[2.2.2]octane) framework has been applied as a heterogeneous catalyst for aza-Diels–Alder reactions [28].

Recently, UV/Vis/NIR spectroelectrochemistry revealed that the pzdb linker is the primary redox site in coordination polymers $[Zn(pzdb)(DEF)_2]$ and $[Co(Hpzdp)_2(DEF)_2]$ (DEF = *N*,*N*-diethylformamide) upon electrochemical oxidation or chemical oxidation with $SbCl_5$ based on the same color changes as in Me_2pzdb, together with EPR signals typical of ligand-based radical cations. However, the coordination polymers decomposed upon pzdb linker oxidation [29].

Here, we report the synthesis and characterization of two new coordination networks based on DHP-derived redox-active linkers H_2pdb and H_4pdi.

2. Materials and Methods

All chemicals were purchased from commercial suppliers and used without further purification (see Supplementary Material, Section S1 for details). Deionized water was employed in all procedures involving water using a Sartorius Arium Mini water purifier (Sartorius, Göttingen, Germany). Single-crystal X-ray diffraction data were collected on a Rigaku XtaLAB Synergy S instrument (Rigaku, Tokyo, Japan) equipped with a PhotonJet Cu Kα radiation source (λ = 1.54184 Å) and a hybrid pixel array detector. Suitable crystals were selected under a Leica M80 polarized-light microscope (Leica, Wetzlar, Germany) and mounted on a cryo-loop in oil. Data processing—including unit-cell refinement, data reduction, and absorption correction—was carried out with CrysAlisPro, version

https://doi.org/10.3390/cryst16030185

171.42.102a. Structures were solved and refined in Olex2, version 1.5, using SHELXT and SHELXL, respectively [30–32]. Molecular graphics were generated using Diamond 5 software [33].

Powder X-ray diffraction (PXRD) data were collected at room temperature on a Rigaku Mini-Flex600 diffractometer (Rigaku, Tokyo, Japan) (600 W, 40 kV, 15 mA) using Cu Kα radiation (λ = 1.54184 Å). The samples were dried for 12 h at 60 °C under vacuum. PXRD patterns were normalized to the intensity of the most intense peak. Simulated PXRD patterns were obtained from MERCURY 2020.3.0 using the single-crystal XRD data [34].

Fourier transform infrared (FT-IR) spectra were recorded between 500 and 4000 cm^{-1} using a Bruker TENSOR 37 spectrometer (Bruker, Billerica, MA, USA) in ATR mode (Platinum ATR-QL, Diamond). Nuclear magnetic resonance (NMR) spectra were measured on a Bruker Avance III 300 spectrometer (Bruker, Billerica, MA, USA) operating at 300 MHz for ^{1}H NMR and 150 MHz for ^{13}C NMR. Electron impact (EI) mass spectra were obtained using a Thermo Finnigan Trace DSQ spectrometer (Thermo Fisher Scientific, Waltham, MA, USA).

N_2 sorption measurements were carried out with a Belsorp Max II (Microtrac, MRB, Haan, Germany) volumetric gas sorption analyzer at 77 K. Samples were pre-dried for 12 h at 60 °C under vacuum, then activated at the sorption analyzer under turbomolecular pump vacuum ($5 \cdot 10^{-12}$ bar) for 3 h at 130 °C.

Thermogravimetric analysis (TGA) was carried out in air and under nitrogen on a Netzsch TG209 F3 Tarsus instrument (Netzsch, Selb, Germany) at a heating rate of 10 K min^{-1} up to 1000 °C. Gaseous products were analyzed with a GAM 200 mass spectrometer from InProcess Instruments (InProcess Instruments, Bremen, Germany). Melting points were measured in open capillaries using a Büchi Melting Point B-540 apparatus (Büchi Labortechnik AG, Flawil, Switzerland).

Elemental analyses were conducted on a PerkinElmer 2400 series II elemental analyzer (PerkinElmer, Waltham, MA, USA) (accuracy of 0.5%). The samples were dried at 180 °C under vacuum (10^{-3} bar).

Electrochemical experiments were performed using an Interfere 1010E potentiostat (Gamry Instruments, Warminster, PA, USA) coupled with an RRDE-3A system (ALS, Tokyo, Japan). Measurements were carried out in a three-electrode configuration, employing an Ag/AgCl reference electrode (stored in 3.5 mol L^{-1} KCl), a platinum counter electrode, and a glassy carbon working electrode with a diameter of 5 mm. The electrolyte consisted of nitrogen-purged acetonitrile containing 0.5 mol L^{-1} tetrabutylammonium hexafluorophosphate. The catalyst ink was prepared by dispersing 1 mg of the sample in a mixture of 0.25 mL of ethanol and 0.25 mL of water, followed by sonication for 30 min. Subsequently, 10 µL of the ink was drop-cast onto the working electrode and dried at 150 rpm, resulting in a catalyst loading of approximately 10 µg cm^{-2}. Cyclic voltammetry measurements were conducted over a potential range of −0.7 V to 1.5 V versus Ag/AgCl at a scan rate of 100 mV s^{-1}.

2.1. Synthesis of 5,10-Dihydrophenazine (Scheme S1)

Phenazine (4.00 g, 22.2 mmol) was dissolved in 50 mL of ethanol in a 500 mL round-bottom flask. Sodium dithionite (38.7 g, 222 mmol) was dissolved in 250 mL of deionized water. The two solutions were then combined in the flask, which was heated to 95 °C under stirring and reflux for 3 h. After the flask was cooled to room temperature. the reaction mixture was filtered, and the product was dried under vacuum for 40 min. Finally, the product was stored under a protective N_2 atmosphere. Yield: 3.69 g (91%). ^{1}H-NMR (300 MHz, DMSO-d_6): δ [ppm] = 7.29 (s, 2 H), 6.25 (dd, J = 6.7, 3.4 Hz, 4 H), 6.01 (dd, J = 6.7, 3.5 Hz, 4 H).

https://doi.org/10.3390/cryst16030185

2.2. Synthesis of Dimethyl-3,3′-(Phenazine-5,10-diyl)Dibenzoate (Me_2pdb) (Scheme S2)

A 100 mL three-neck flask was charged with 1.00 g of 5,10-dihydrophenazine (5.50 mmol), 2.60 g of 3-methyl 3-bromobenzoate (12.1 mmol), and 1.52 g of potassium carbonate (16.5 mmol). After sealing the flask, a solution of 0.062 g of palladium(II)-acetate (0.27 mmol) and 0.3 mL of tri-*tert*-butylphosphine dissolved in 60 mL of xylene was added. The reaction mixture was heated under stirring to reflux for 48 h. After cooling to room temperature, 100 mL of water was added to the reaction mixture, and it was extracted with 3 × 150 mL of dichlormethane. The combined organic phases were washed with 150 mL of brine solution (60 g NaCl in 300 mL water) and were dried over magnesium sulfate. The organic solution was concentrated using a rotary evaporator. After adding 5 mL of DCM and 40 mL of n-hexane, the product was recrystallized in the refrigerator. The precipitate was filtered off and dried under vacuum. Yield: 1.83 g (74%). ^{1}H-NMR (300 MHz, $CDCl_3$): δ [ppm] = 8.20–8.08 (m, 4 H), 7.71 (t, J = 9.0, 6.0 Hz, 2 H), 7.65–7.59 (m, 4 H), 6.28 (dd, J = 6.7, 3.4 Hz, 4 H), 5.58 (dd, J = 6.7, 3.4 Hz, 4 H), 3.94 (s, 6 H). %). ^{13}C{^{1}H}-NMR (600 MHz, $CDCl_3$): δ [ppm] = 166.16, 140.34, 136.31, 136.16, 133.73, 132.93, 131.51, 129.49, 121.13, 112.62, 52.36. [HR-ESI-MS] m/z = 450.16 (calculated for $^{12}C_{28}$ $^1H_{22}$ $^{14}N_2$ $^{16}O_4$ 450.16). IR (ATR): υ [cm^{-1}] = 3430, 3076, 3037, 3006, 2953, 2841, 2625, 2579, 1911, 1719, 1660, 1629, 1609, 1596, 1580, 1484, 1440, 1391, 1347, 1287, 1261, 1192, 1173, 1158, 1129, 1098, 1078, 1062, 991, 949, 928, 889, 838, 813, 794, 733, 693, 678, 643, 618, 558. Mp. = 255 °C.

2.3. Synthesis of 3,3′-(Phenazine-5,10-diyl)Dibenzoic Acid (H_2pdb) (Scheme S3)

A solution of 1.72 g (3.82 mmol) of dimethyl-3,3′-(phenazine-5,10-diyl)dibenzoate in 25 mL of 1,4-dioxane was prepared in a 100 mL flask. Then, 1.60 g of lithium hydroxide (38.2 mmol) and 15 mL of water were added to the reaction mixture, which was then heated to 100 °C for 24 h. After cooling to room temperature, the mixture was neutralized with concentrated hydrochloric acid (~1.9 mL). The precipitation was then filtered and dried under vacuum. Yield: 1.53 g (91%). ^{1}H-NMR (300 MHz, DMSO-d_6): δ [ppm] = 13.07 (s, 2 H), 8.08 (dt, 2 H), 7.92 (t, J = 9.0, 6.0 Hz, 2 H), 7.82 (t, J = 9.0, 6.0 Hz, 2 H), 7,73 (dt, 2 H), 6.30 (dd, J = 6.7, 3.4 Hz, 4 H), 5.52 (dd, J = 6.7, 3.4 Hz, 4 H). ^{13}C{^{1}H}-NMR (600 MHz, DMSO-d_6): δ [ppm] = 166.47, 139.94, 135.75, 134.75, 134.74, 132.00, 131.70, 129.25, 121.19, 112.49. [HR-ESI-MS] m/z = 422.13 (calculated for $^{12}C_{26}$ $^1H_{18}$ $^{14}N_2$ $^{16}O_4$ 422.13). IR (ATR): υ [cm^{-1}] = 3386, 3067, 2994, 2857, 2814, 2662, 2540, 1979, 1909, 1865, 1821, 1748, 1683, 1609, 1597, 1581, 1483, 1443, 1411, 1388, 1344, 1280, 1183, 1160, 1138, 1103, 1082, 1061, 1002, 990, 965, 928, 912, 838, 819, 757, 734, 693, 669, 643, 617, 568. Mp. > 350 °C.

2.4. Synthesis of Tetramethyl-5,5′-(Phenazine-5,10-diyl)Diisophthalate (Me_4pdi) (Scheme S4)

A 100 mL three-neck flask was charged with 1.00 g of 5,10-dihydrophenazine (5.50 mmol), 2.60 g of dimethyl-5-bromoisophthalate (12.1 mmol), and 1.52 g of potassium carbonate (16.5 mmol). After sealing the flask, a solution of 0.062 g of palladium(II)-acetate (0.27 mmol) and 0.3 mL of tri-*tert*-butylphosphine dissolved in 60 mL of xylene was added. The reaction mixture was heated under stirring to reflux for 48 h. After cooling to room temperature, 100 mL of water was added to the reaction mixture, and it was extracted with 3 × 150 mL of dichlormethane. The combined organic phases were washed with 150 mL of brine solution (60 g NaCl in 300 mL water) and were dried over magnesium sulfate. The organic solution was concentrated using a rotary evaporator. After adding 5 mL of DCM and 40 mL of *n*-hexane, the product was recrystallized in a refrigerator. The precipitate was filtered off and dried under vacuum. Yield: 2.12 g (68%). ^{1}H-NMR (300 MHz, $CDCl_3$): δ [ppm] = 8.80 (t, J = 3.0, 3.0 Hz, 2 H), 8.32 (d, 4 H), 6.32 (dd, J = 6.7, 3.4 Hz, 4 H), 5.59 (dd, J = 6.7, 3.4 Hz, 4 H), 3.98 (s, 12 H). ^{13}C{^{1}H}-NMR (600 MHz, $CDCl_3$): δ [ppm] = 165.47, 141.00, 137.72, 135.96, 134.35, 130.68, 121.66, 113.12, 52.79. [HR-ESI-MS] m/z = 566.17

(calculated for $^{12}C_{32}$ $^{1}H_{26}$ $^{14}N_2$ $^{16}O_8$ 566.17). IR (ATR): υ [cm^{-1}] = 3431, 3088, 3004, 2954, 2846, 1718, 1590, 1544, 1489, 1434, 1398, 1355, 1307, 1287, 1242, 1199, 1167, 1137, 1105, 1065, 998, 950, 938, 918, 898, 876, 834, 806, 784, 753, 741, 723, 686, 664, 618, 562. Mp. = 336 °C.

2.5. Synthesis of 5,5′-(Phenazine-5,10-diyl)Diisophthalic Acid (H_4pdi) (Scheme S5)

A solution of 1.00 g (1.77 mmol) of tetramethyl-5,5′-(phenazine-5,10-diyl)diisophthalate in 25 mL of 1,4-dioxane was prepared in a 100 mL flask. Then, 0.74 g of lithium hydroxide (17.7 mmol) and 15 mL of water were added to the reaction mixture, which was heated to 100 °C for 24 h. After cooling to room temperature, the mixture was neutralized with concentrated hydrochloric acid (~1.5 mL). The precipitation was then filtered and dried under vacuum. Yield: 0.71 g (79%). ^{1}H-NMR (300 MHz, D_2O): δ [ppm] = 8.33 (t, J = 3.0, 3.0 Hz, 2 H), 7.89 (d, 4 H), 6.30 (dd, J = 6.7, 3.4 Hz, 4 H), 5.67 (dd, J = 6.7, 3.4 Hz, 4 H). ^{13}C{^{1}H}-NMR (600 MHz, D_2O): δ [ppm] = 174.03, 140.06, 139.67, 136.08, 134.08, 128.94, 121.48, 113.00. IR (ATR): υ [cm^{-1}] = 3384, 3079, 3063, 2981, 2861, 2824, 2665, 2616, 2572, 2540, 1891, 1865, 1723, 1694, 1635, 1591, 1552, 1488, 1455, 1423, 1351, 1311, 1279, 1244, 1192, 1159, 1109, 1064, 1003, 957, 925, 847, 790, 756, 729, 693, 681, 661, 615, 602. Mp. > 350 °C.

2.6. Synthesis of Catena-[(N,N-Dimethylformamide)-μ$_4$-3,3′-(Phenazine-5,10-diyl)Dibenzoate-Cobalt(II)], [Co(pdb)(DMF)]

First, 15.0 mg of H_2pdb (0.034 mmol) and 20.0 mg of cobalt nitrate hexahydrate (0.068 mmol) were placed in a glass tube. Then, 2 mL of DMF was added to completely dissolve the solids. The tubes were sealed and placed in an oven at 100 °C for two days. Dark-red crystals were obtained as a final product. The crystals were washed with DMF and ethanol and dried under vacuum. Yield: 11 mg (56%). $C_{29}H_{23}CoN_3O_5$ ([Co(pdb)(DMF)]): calc. C C 63.04, H 4.20, N 7.61%; exp. C 62.14, H 4.23, N 7.76%.

MOFs and coordination networks cannot be purified by recrystallization as molecular compounds can. Importantly, varying degrees of missing linker or missing cluster defects lead to deviations from the ideal formula, which cannot be alleviated. A missing anionic linker cannot only be replaced by coordinated solvent but also needs hydroxide or anionic ligands from the metal salt precursor for charge compensation. Furthermore, a difficult-to-control loss of crystal or coordinating solvent molecules and possible hydration upon sample handling in air can also occur. Therefore, elemental analyses are often not reported for MOFs because of the known mismatch. Crystal-phase purity is usually established by matching the experimental and simulated PXRD.

2.7. Synthesis of Catena-[tris(N,N-Dimethylformamide)-μ$_8$-5,5′-(Phenazine-5,10-diyl)Diisophthalate-Dicobalt(II)] bis(N,N-Dimethylformamide) Hydrate [Co_2(pdi)$(DMF)_3$]·2(DMF)·H_2O

First, 17.9 mg of H_4pdi (0.035 mmol) and 20 mg of cobalt nitrate hexahydrate (0.070 mmol) were placed in a glass tube. Then, 2 mL of DMF was added to completely dissolve the solids. The tubes were sealed and placed in an oven at 100 °C for two days. Dark-red crystals were obtained as a final product. The crystals were washed with DMF and ethanol and dried under vacuum. Yield: 22 mg (62%). $C_{43}H_{51}Co_2N_7O_{14}$ ([Co_2(pdi)$(DMF)_3$]·2(DMF)·H_2O): calc. C C 51.24, H 5.10, N 9.73%; exp. C 48.56, H 3.58, N 6.73%. We note that for porous MOFs, the solvent content in the pores can change during sample handling, often leading to deviating elemental analyses (see also the comment on CHN analysis in Section 2.6).

https://doi.org/10.3390/cryst16030185

3. Results and Discussion

The syntheses of the linkers started with the reduction of phenazine with sodium dithionate to 5,10-dihydrophenazine (DHP, Scheme 1, Scheme S1) [1]. DHP is a light-green solid and was stored under a nitrogen atmosphere because of its easy re-oxidation in air. ^{1}H NMR spectroscopy (Figure S1) confirmed the product with high purity. In the next reaction step, dimethyl-3,3′-(phenazine-5,10-diyl)dibenzoate [3,3′-(phenazine-5,10-diyl)dibenzoate dimethyl ester] or tetramethyl-5,5′-(phenazine-5,10-diyl)diisophthalate was synthesized (Schemes S2 or S4) through Buchwald–Hartwig coupling [19,35,36]. The highest yields and purest products were obtained with palladium(II) acetate as the catalyst, tri-*tert*-butylphosphine as the ligand and potassium carbonate as the base. The products are yellow or red powders, and their constitution and high purity are confirmed by NMR spectroscopy (Figures S2–S5).

Finally, the methyl esters were hydrolyzed with LiOH in a 1,4-dioxane/H_2O mixture to give 3,3′-(phenazine-5,10-diyl)dibenzoic acid as a light-yellow solid (H_2pdb, Scheme S3) or 5,5′-(phenazine-5,10-diyl)diisophthalic acid as a dark-green solid (H_4pdi, Scheme S5). Again the ^{1}H-NMR spectra are consistent with the constitutions (Figures S6–S9). The bands in the infrared spectra of the esters and the free acids can be assigned (Figures S10 and S11).

Various futile synthesis attempts were performed with zirconium(IV) chloride, zirconium oxychloride octahydrate, aluminum chloride hexahydrate, copper(II) chloride monohydrate, nickel(II) sulfate hexahydrate and nickel(II) chloride hexahydrate, with H_2pdb and H_4pdi in *N*,*N*-dimethylformamide giving no or no crystalline products. This was evident from the fact that either no reflections were visible in the measured PXRD (amorphous solid) or the same reflections as the pure linker were visible. Needle-shaped crystals from zinc nitrate hexahydrate with H_2pdb in a molar ratio of 1:3 at 120 °C after two days were too small for single-crystal X-ray diffractometry. Good-quality crystals were obtained only in the reactions of cobalt(II) nitrate hexahydrate with H_2pdb and H_4pdi (both with a 2:1 molar ratio at 100 °C) after two days (Figures S12 and S13). The anion plays a certain role, as identical reactions of cobalt(II) sulfate heptahydrate and cobalt(II) chloride hexahydrate yielded no solid products.

The experimental powder X-ray diffraction patterns of the bulk crystallized cobalt compounds matched well with the simulated patterns derived from the crystal structures of [Co(pdb)(DMF)] and $[Co_2(pdi)(DMF)_3]\cdot 2(DMF)\cdot H_2O$, confirming their phase purity (Section S5, Figures S15 and S16).

3.1. Crystal Structures of [Co(pdb)(DMF)]

Figure 1 shows the extended asymmetric unit and cobalt coordination environment of [Co(pdb)(DMF)], and Table 1 lists the crystallographic data. The space group of this compound is I2/a. It belongs to the monoclinic crystal system, and the asymmetric unit consists of one cobalt(II) ion, two half pdb linkers and a DMF ligand. The pdb linker with N1 has a twofold rotation axis passing through the phenazine core perpendicular to the ring plane. The linker with N3 has an inversion center at the centroid of the phenazine ring. The cobalt(II) ion is square-pyramidally surrounded by five oxygen atoms and forms a Co_2 handle as the secondary building unit (SBU) with another symmetry-equivalent cobalt(II) ion. This Co_2 handle is surrounded by four carboxylate groups from four linkers in a paddle-wheel arrangement. Each pdb ligand acts as a tetradentate bridging ligand and connects two Co_2 handles, being thereby bound to four cobalt atoms. The axial directions of the paddle-wheel unit bind to the oxygen atoms of the monodentate DMF ligands.

https://doi.org/10.3390/cryst16030185

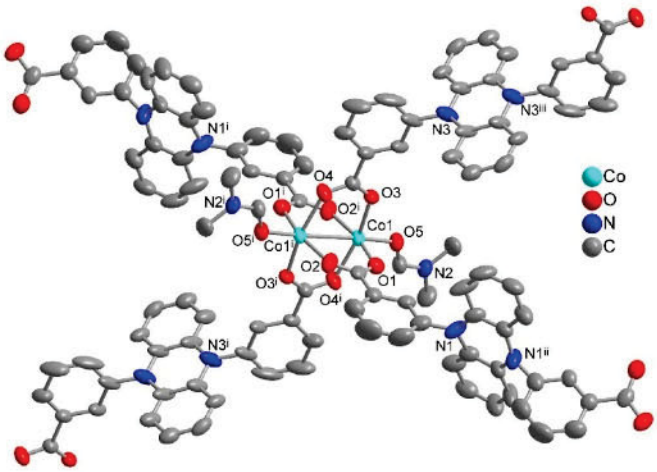


Figure 1. Expanded asymmetric unit for [Co(pdb)(DMF)]. Symmetry code: (i) −x + 1/2, −y + 3/2, −z + 3/2; (ii) −x + 3/2, y, −z + 1; (iii) −x, −y + 1, −z + 1 (50% thermal ellipsoids). Hydrogen atoms are not shown for clarity.

Table 1. Crystal data for [Co(pdb)(DMF)] and $[Co_2(pdi)(DMF)_3]\cdot 2(DMF)\cdot H_2O$.

	[Co(pdb)(DMF)]	**$[Co_2(pdi)(DMF)_3]\cdot 2(DMF)\cdot H_2O$**
empirical formula	$C_{29}H_{23}CoN_3O_5$	$C_{43}H_{51}Co_2N_7O_{14}$
mol wt (g mol^{-1})	552.43	1007.76
temperature (K)	150	150
crystal system	monoclinic	orthorhombic
space group	*I*2/a	*Pna*2_1
a (Å)	9.5099 (6)	26.9491 (5)
b (Å)	18.7609 (15)	15.5325 (3)
c (Å)	27.3129 (19)	11.4627 (2)
α (deg)	90	90
β (deg)	91.587 (6)	90
γ (deg)	90	90
volume, V ($Å^3$)	4871.1 (6)	4798.14 (15)
Z, Z′	8, 1	4, 1
D_{calc} (g/cm^3)	1.507	1.395
μ (mm^{-1})	5.922	6.02
F(000)	2280	2096
crystal size [mm^3]	0.09 × 0.05 × 0.04	0.1 × 0.07 × 0.05
wavelength (Å)	1.54184	1.54184
No. of unique reflections	4840	8579
No. of total reflections	27,266	64,849
No. of parameters	349	608

https://doi.org/10.3390/cryst16030185

Table 1. *Cont.*

	[Co(pdb)(DMF)]	$[Co_2(pdi)(DMF)_3]\cdot 2(DMF)\cdot H_2O$
R_{int}	0.1268	0.0715
$R[F^2 > 2\sigma(F^2)]$ [a]	0.0632	0.0445
$wR[F^2 > 2\sigma(F^2)]$ [a]	0.1270	0.1091
R, $wR(F^2)$ [all data] [a]	0.1248, 0.1523	0.0494, 0.1116
S [all data] [a]	1.073	1.041
$\Delta\rho_{max}$, $\Delta\rho_{min}$ ($e\cdot Å^{-3}$) [b]	0.678, −0.471	0.722, −0.365
CCDC No.	2522790	2522791

[a] $R = [\Sigma(||F_o| - |F_c||)/\Sigma|F_o|]$; $wR = [\Sigma[w(F_o^2 - F_c^2)^2]/\Sigma[w(F_o^2)^2]]^{1/2}$. Goodness-of-fit $S = [\Sigma[w(F_o^2 - F_c^2)^2]/(n - p)]^{1/2}$. [b] Largest difference peak and hole.

The selected bond lengths and bond angles can be found in Table 2. The bond lengths of the four cobalt–oxygen bonds in the equatorial plane range from 2.00 Å to 2.09 Å, and the bond length of the cobalt–oxygen(DMF) bond in the axial direction is approximately 2.03 Å. The cobalt–cobalt distance in the Co_2 handle is 2.81 Å. The O-Co-O bond angles between the cis-positioned O atoms of the pdb linkers in the paddle-wheel unit are all approximately 90°, while the trans-O-Co-O angles are significantly smaller (~164°) because the Co···Co separation (2.81 Å) is larger than the O···O separation (~2.23 Å) in a carboxyl group so that the Co atom is placed "above" the equatorial plane of the four oxygen atoms. Consequently, the O-Co-O5(DMF) bond angle is also significantly greater than 90°. There is no significant π–π interaction and only limited C-H···π and C–H···O interactions in the supramolecular packing of the adjacent networks in [Co(pdb)(DMF)] (see Section S9 for details).

Table 2. Selected bond lengths (Å) and angles (°) for [Co(pdb)(DMF)] [a].

Interaction	Bond Length [Å]	Interaction	Angle [°]
Co1—O1	2.006 (4)	O1—Co1—O5	98.90 (15)
Co1—O2 ^{i}	2.023 (4)	O1—Co1—O2 ^{i}	163.69 (16)
Co1—O3	2.023 (3)	O2 ^{i}—Co1—O4 ^{i}	89.53 (15)
Co1—O4 ^{i}	2.081 (3)	O2 ^{i}—Co1—O5	97.18 (15)
Co1—O5	2.027 (3)	O3—Co1—O4 ^{i}	163.52 (13)
Co1···Co1 ^{i}	2.8068 (14)	O3—Co1—O5	100.55 (13)
		O3—Co1—O2 ^{i}	89.66 (13)
O1—Co1—O3	90.06 (13)	O5—Co1—O4 ^{i}	95.88 (13)
O1—Co1—O4 ^{i}	86.15 (14)		

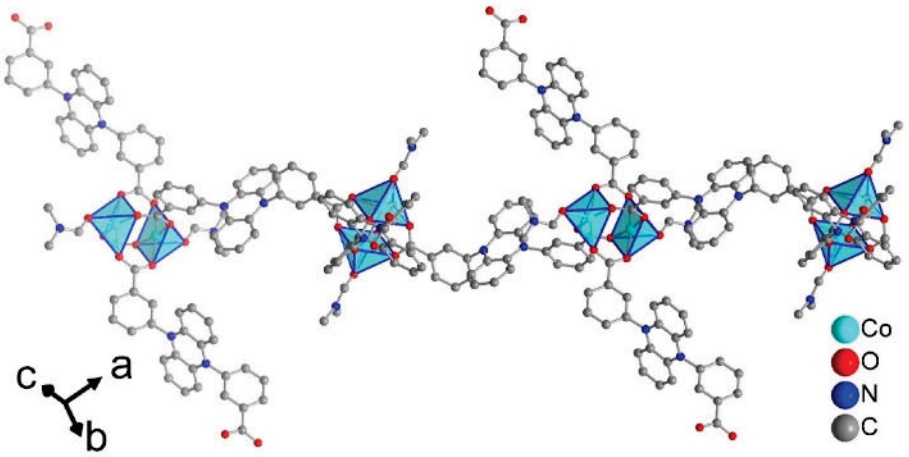
[a] Symmetry code: $i = -x + 1/2, -y + 3/2, -z + 3/2$.

The Co_2 handles or SBUs are then linked into a three-dimensional network with cds topology (Figure 2). In cds (or $CdSO_4$) topology [37–40], each SBU is connected to four neighboring nodes via the linkers. If one starts with the chain shown in Figure 2a, where alternatingly, each SBU connects to a parallel chain from top to bottom and front to back, then the 3D network in Figure 2b is obtained.

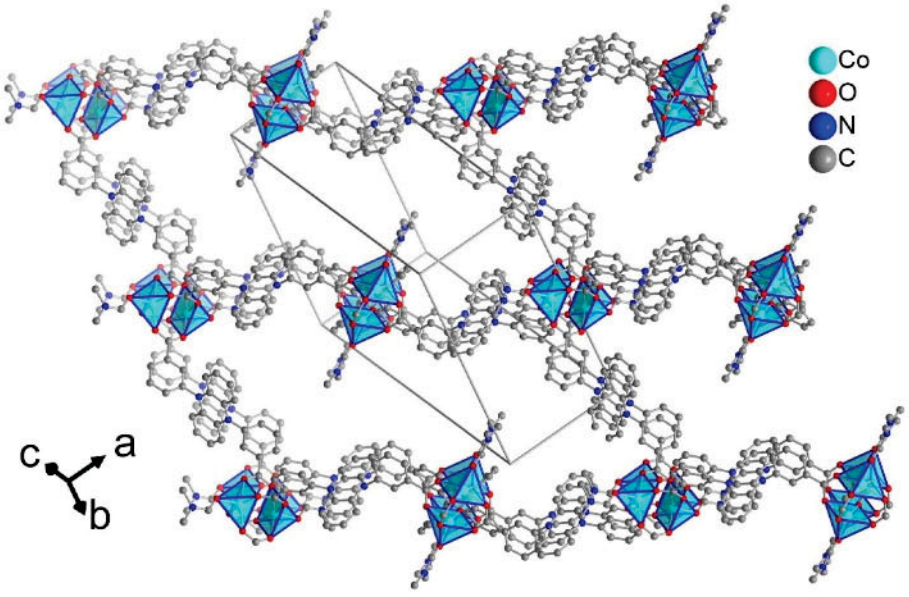
The single network has wide openings that are several Ångströms across (Figure S13), even taking into account the space-filling van der Waals surface (Figure 2c). These openings are filled with two symmetry-related nets through interpenetration, giving a threefold interpenetrated structure with cds topology (Figure 3). Consequently,

https://doi.org/10.3390/cryst16030185

no voids remain, and there is no porosity in the network. A threefold interpenetrated cds topology was described in 3D-[Co(pam)(bpa)(H_2O)$_2$]·DMF (H_2pam = pamoic acid, bpa = 1,2-di(4-pyridyl)ethylene, DMF = *N*,*N*-dimethylformamide) [41], and twofold interpenetrated cds net topologies were found in [Zn_2(BDC)(BPP)Cl_2] (BDC = benzene-1,4-dicarboxylate, BPP = 1,3-bis(4-pyridyl)propane) [42] and in [Cu(ceb)(bpmp)]·H_2O (ceb = 4-(carboxylatoethyl)benzoato, bpmp = 1,4-bis(pyridin-4-ylmethyl)piperazine) [43]. Further examples of interpenetrated networks with a cds topology are [Zn(Br-1,3-bdc)(NI-mbpy-34)] (Br-1,3-bdc = 5-bromobenzene-1,3-dicarboxylate, NI-mbpy-34 = *N*-(pyridin-3-ylmethyl)-4-(pyridin-4-yl)-1,8-naphthalimide) [44] and [M(μ-TBG)(μ-H_2O)(H_2O)$_2$]·2H_2O (M = Cu, Co and H_2TBG = terephthaloylbisglycine) [45]. A non-interpenetrated 3D network with cds topology was reported for [trans-Ni(H_2O)$_2$(μ-4,4′-bpy)$_2$](ClO_4)$_2$ (4,4′-bpy = 4,4′-bipyridine) [46].



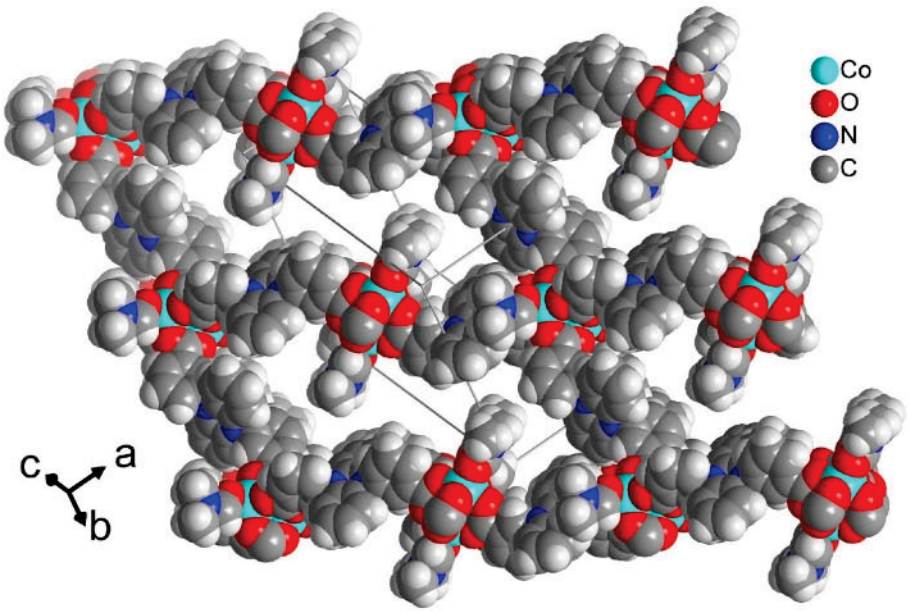
(**a**)



(**b**)

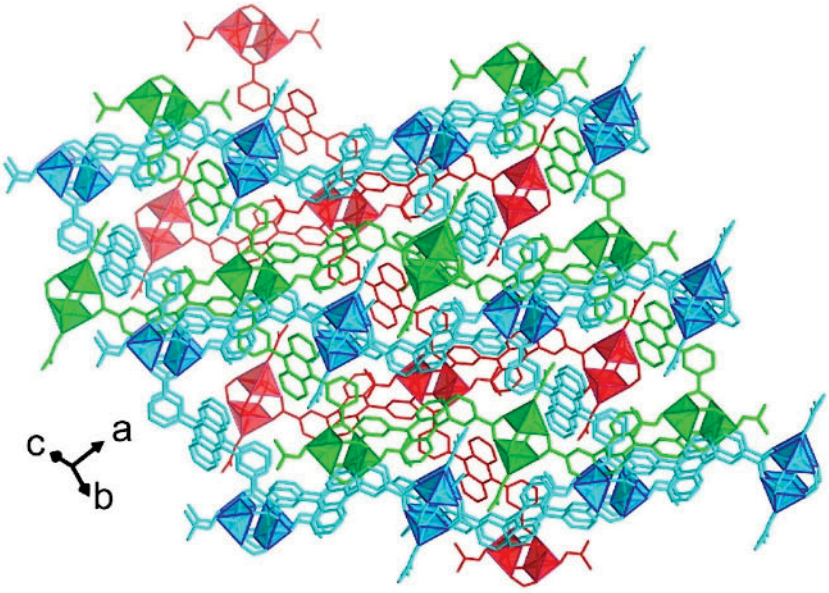
Figure 2. *Cont.*

https://doi.org/10.3390/cryst16030185



(**c**)

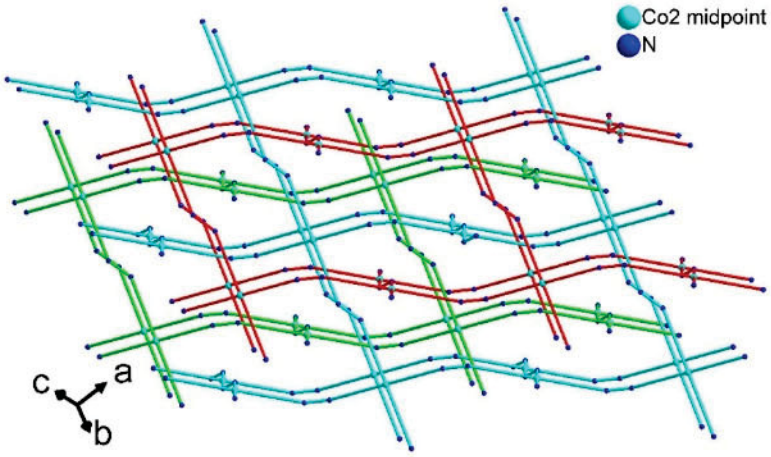
Figure 2. (**a**) Chain section of the 3D network in [Co(pdb)(DMF)], which is linked to parallel chains from top to bottom and front to back to give the full 3D network in (**b**) with cds topology. Hydrogen atoms are not shown for clarity, and the Co coordination is presented as polyhedra. (**c**) Space-filling view of the network with hydrogen atoms included.



(**a**)

Figure 3. *Cont.*

https://doi.org/10.3390/cryst16030185



(**b**)

Figure 3. (**a**) The threefold interpenetrated structure of [Co(pdb)(DMF)]. Each network is shown in a different color. (**b**) Schematic representation of the threefold interpenetrated cds net in [Co(pdb)(DMF)], taking the midpoint of the Co_2 handle as a fourfold node. The rods connect the Co_2 midpoints and the phenazine-ring nitrogen atoms.

The combined TGA-DTG curve of [Co(pdb)(DMF)] is shown in Figure S18, and the TG-MS (TGA coupled with mass spectrometry) measurement is shown in Figure S20. The sample was pre-dried for 14 h at 180 °C under vacuum, cooled down under vacuum and rapidly transferred to the TGA instrument. There is no detectable mass loss below approximately 300 °C. The first mass-loss event of about 13 wt% is evident in the DTG at 360 °C and assigned to the removal of the DMF ligand (theor. 13 wt%) The solvent removal transits into the network decomposition of [Co(pdb)] without a clear plateau, and the sample is completely decomposed at ~430 °C with a concomitant mass loss of 73 wt% (theor. 76 wt%), as corroborated by the pronounced DTG minimum at around 410 °C. The final residue remains unchanged at approximately 14–15 wt%, consistent with the formation of cobalt oxide (CoO; theor. 14 wt% for CoO, 15 wt% for Co_2O_3, and 11 wt% for Co).

3.2. Crystal Structure of $[Co_2(pdi)(DMF)_3]\cdot 2(DMF)\cdot H_2O$

Figure 4 depicts the extended asymmetric unit and cobalt coordination environment of $[Co_2(pdi)(DMF)_3]\cdot 2(DMF)\cdot H_2O$, and Table 1 gives the crystallographic data. The space group of this compound is $Pna2_1$ in the orthorhombic crystal system. The asymmetric unit contains two crystallographically different cobalt(II) ions, a full pdi linker, three coordinated DMF ligands, two non-coordinated DMF molecules and a water molecule of solvation. Both cobalt(II) ions are sixfold coordinated and surrounded by six oxygen atoms, and they, again, form a Co_2 handle as the secondary building unit. The Co1 ion is coordinated by the three DMF ligands and three carboxyl oxygen atoms of three different linkers in the facial configuration. Co2 is coordinated by four different pdi linkers, with two of them chelating and two monodentate. Each of the bridging linkers is connected to Co2, which can be seen as the primary metal node. Out of the four different carboxyl groups of the linker, two are monodentate bridging (O1-C-O2, O3-C-O4) between the two Co ions; one is bidentate bridging between Co1 and Co2 and, at the same time, chelating to Co2 (O5-C-O6 as κO:κO,κO′); and the last one is bidentate chelating to Co2 (O7-C-O8). From the perspective of the linker, each pdi ligand is bound to seven cobalt atoms, i.e., acts as a heptadentate-bridging ligand and connects four Co_2 handles. Three handles are connected

https://doi.org/10.3390/cryst16030185

to both cobalt atoms—one handle only through one Co atom. Selected bond lengths and angles are listed in Table 3.

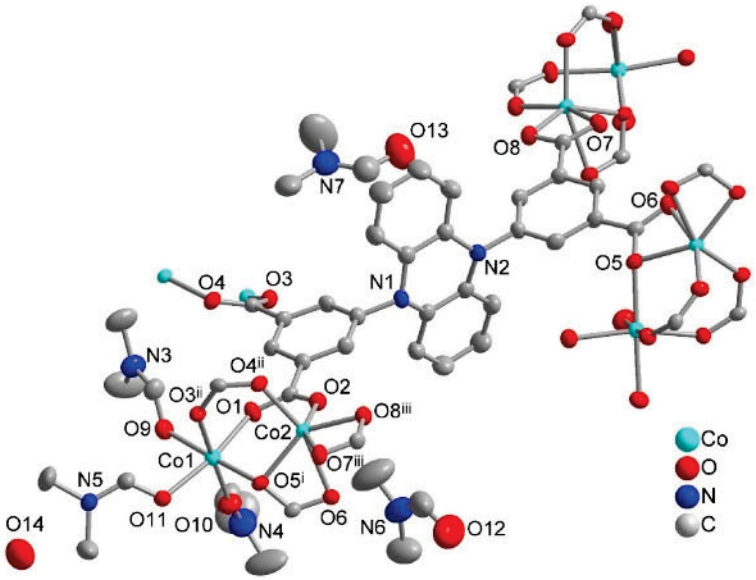


Figure 4. Expanded asymmetric unit for $[Co_2(pdi)(DMF)_3]\cdot 2(DMF)\cdot H_2O$. Symmetry code: (i) −x + 1/2, −y + 3/2, −z + 3/2; (ii) −x + 3/2, y, −z + 1; (iii) −x, −y + 1, −z + 1 (50% thermal ellipsoids). Hydrogen atoms are not shown for clarity.

Table 3. Selected bond lengths (Å) and angles (°) for $[Co_2(pdi)(DMF)_3]\cdot 2(DMF)\cdot H_2O$ [(a)].

Interaction	Bond Length [Å]	Interaction	Angles [°]
Co1—O1	2.072 (3)	O10—Co1—O5 [i]	91.01 (16)
Co1—O3 [ii]	2.040 (3)	O10—Co1—O11	91.32 (16)
Co1—O5 [i]	2.105 (3)	O10—Co1—O1	89.36 (16)
Co1—O9	2.128 (4)	O10—Co1—O9	91.85 (17)
Co1—O10	2.069 (4)	O11—Co1—O5 [i]	93.69 (14)
Co1—O11	2.097 (3)	O11—Co1—O9	86.46 (15)
Co2—O2	1.993 (3)		
Co2—O4 [ii]	2.037 (3)	O2—Co2—O5 [i]	106.59 (15)
Co2—O5 [i]	2.105 (3)	O2—Co2—O4 [ii]	94.93 (15)
Co2—O6 [i]	2.270 (4)	O2—Co2—O7 [iii]	153.89 (13)
Co2—O7 [iii]	2.265 (4)	O2—Co2—O8 [iii]	93.13 (14)
Co2—O8 [iii]	2.050 (3)	O2—Co2—O6 [i]	94.23 (15)
		O4 [ii]—Co2—O5 [i]	100.40 (13)
O1—Co1—O5 [i]	97.97 (13)	O4 [ii]—Co2—O7 [iii]	95.87 (14)
O1—Co1—O11	168.31 (14)	O4 [ii]—Co2—O8 [iii]	108.82 (15)

https://doi.org/10.3390/cryst16030185

Table 3. *Cont.*

Interaction	Bond Length [Å]	Interaction	Angles [°]
O1—Co1—O9	81.86 (14)	O4 ^{ii}—Co2—O6 ^{i}	160.17 (13)
O3 ^{ii}—Co1—O5 ^{i}	86.19 (14)	O5 ^{i}—Co2—O7 ^{iii}	94.72 (13)
O3 ^{ii}—Co1—O11	88.10 (15)	O5 ^{i}—Co2—O6 ^{i}	60.06 (12)
O3 ^{ii}—Co1—O1	91.80 (15)	O8 ^{iii}—Co2—O5 ^{i}	143.07 (13)
O3 ^{ii}—Co1—O9	90.95 (15)	O8 ^{iii}—Co2—O7 ^{iii}	60.87 (13)
O3 ^{ii}—Co1—O10	177.10 (16)	O8 ^{iii}—Co2—O6 ^{i}	88.18 (14)
Co1—Co2	3.368 (1)	Co2 ^{iv}—O5—Co1 ^{iv}	106.27 (14)

[a] Symmetry code: i = −x + 1/2, −y + 3/2, −z + 3/2; ii = −x + 3/2, y, −z + 1; iii = −x, −y + 1, −z + 1; iv = x + 1/2, −y + 3/2, z.

In $[Co_2(pdi)(DMF)_3]\cdot 2(DMF)\cdot H_2O$, crystal water and non-coordinated DMF solvent molecules are incorporated by hydrogen bonds in the crystal lattice. The hydrogen bonds of the crystal water molecule are shown in Figure 5. Hydrogen bond O14–H14A···O8^{ii} is between the water molecule and a cobalt-coordinating carboxyl oxygen atom of the pdi linker, and hydrogen bond O14–H14B···O13^{ii} is a bridge to a non-coordinated DMF molecule. These two hydrogen bonds are of medium strength, as the distance between the hydrogen atom and the accepting oxygen atom is between 1.9 and 2.0 Å in both cases. There is no π–π interaction—only C-H···π interactions originating from a coordinated DMF molecule in the packing of $[Co_2(pdi)(DMF)_3]\cdot 2(DMF)\cdot H_2O$. Also, the C–H···O interactions are largely between DMF molecules or from a coordinated DMF-CHO group to a cis-O atom of a carboxylate group. The water molecule accepts C-H bonds from DMF-CH_3 and a diisophthalate-CH (see Section S9 for details).

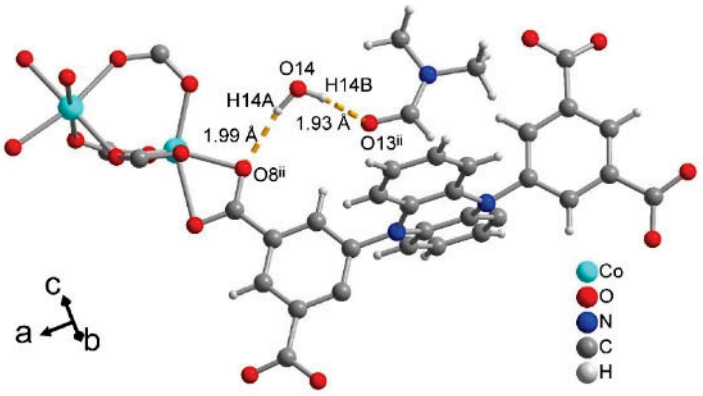


Figure 5. Hydrogen bonds (orange dotted lines) from the crystal water molecule in $[Co_2(pdi)(DMF)_3]\cdot 2(DMF)\cdot H_2O$.

The Co-pdi bridging action gives rise to a three-dimensional network (Figure 6). In this metal–ligand 3D network, there would be open channels (Figure 6a), which are, however, occupied by the coordinated DMF ligands, together with the DMF and H_2O solvent molecules of crystallization (Figure 6b). When the free solvent molecules are omitted in the network, only small voids remain (Figure 7).

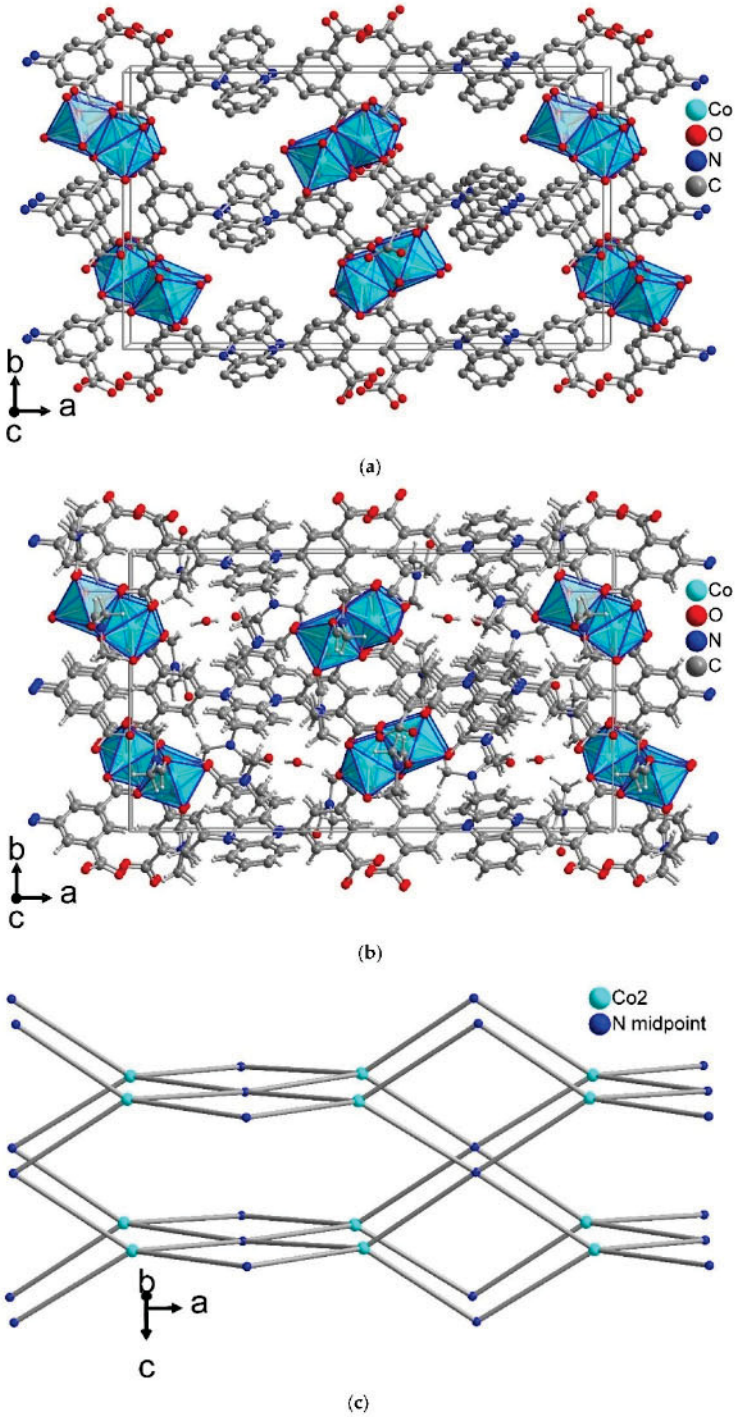


Figure 6. 3D network of $[Co_2(pdi)(DMF)_3]\cdot 2(DMF)\cdot H_2O$. (**a**) Hydrogen atoms, all DMF molecules and H_2O molecules are omitted for clarity. (**b**) Hydrogen atoms, all DMF molecules and H_2O molecules are shown within the unit cell. (**c**) Schematic representation of the pts net in $[Co_2(pdi)(DMF)_3]$, taking the Co2 atom and the linker as fourfold nodes. The rods connect the Co2 atom and the midpoint of the phenazine-ring nitrogen atoms.

https://doi.org/10.3390/cryst16030185

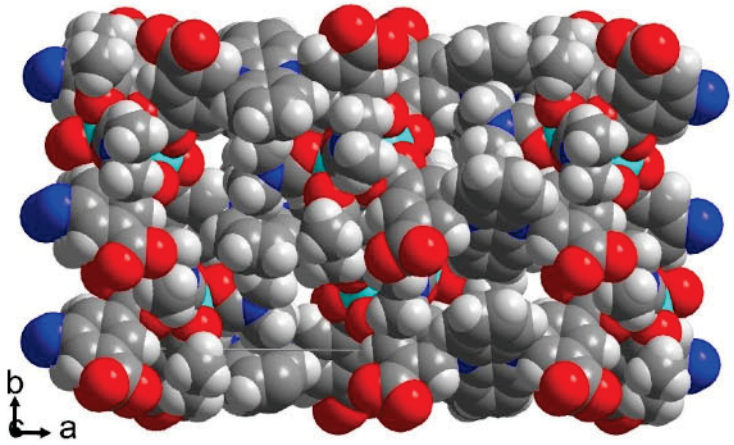


Figure 7. Space-filling view of the network $[Co_2(pdi)(DMF)_3]$ with the coordinated DMF ligands to illustrate remaining small voids when the DMF and H_2O solvent of crystallization were omitted (Co = cyan, O = red, N = blue, C = grey, H = white).

After activation, no N_2 gas uptake could be detected with a volumetric gas sorption analyzer; hence, there is no N_2 accessible porosity in the $[Co_2(pdi)(DMF)_3]$ network. In view of the tight framework packing, the removal of the free DMF was probably not fully achieved, the framework partially collapsed and the potential voids were too small. For sorption measurement, the samples were pre-dried for 12 h at 60 °C under vacuum, then activated at the sorption analyzer under turbomolecular pump vacuum ($5 \cdot 10^{-12}$ bar) for 3 h at 130 °C, as stated in Section 2. The PXRD of the activated $[Co_2(pdi)(DMF)_3]\cdot 2(DMF)\cdot H_2O$ sample shown in Figure S16 indicates that under these conditions, the sample turned amorphous, losing its defined pore structure.

The network topology in $[Co_2(pdi)(DMF)_3]$ is pts (or platinum(II) sulfide) [37,47–49] when taking the Co2 atom as a tetrahedral and the linker as a square–planar fourfold node (Figure 6c). Among the two Co atoms, only Co2 is connected to each of the four carboxyl groups of the linker and is responsible for 3D network formation. Compared to the PtS structure, which is composed of square–planar Pt(II) and tetrahedral sulfide atoms, the pts topology in $[Co_2(pdi)(DMF)_3]$ is reversed such that the metal node is tetrahedral and the linker square–planar.

For thermogravimetric analysis, the sample was pre-dried for 14 h at 180 °C under vacuum, cooled down under vacuum and rapidly transferred to the TGA instrument. The crystal solvent molecules water and DMF were removed under these conditions. The combined TGA–DTG curve (Figure S19) shows the first mass loss at ~300 °C due to the loss of the coordinated DMF (theor. 26 wt%). Without a pronounced plateau, the mass loss continues to ~390 °C with degradation of the organic linker (theor. 60 wt%). At 1000 °C, a residue of 21 wt% remains (theor. 18 wt% for CoO, 20 wt% for Co_2O_3, and 14 wt% for Co).

A comparison of the coordination polymer [Co(pdb)(DMF)] with the structurally related coordination polymers derived from isomeric dihydrophenazine-based dicarboxylate ligand H_2PZDB (Figure 8) [29] highlights the combined influence of metal coordination preferences and ligand geometry on framework assembly. Although the two ligands share the same dihydrophenazine core, the relative orientation of the carboxylate groups differs between the meta and para positions, resulting in different coordination modes and network topologies. In the zinc and cobalt(II) coordination polymers based on H_2PZDB [29], the axial or linear para-arrangement of the carboxylate functions favors extended but less densely interconnected networks, which predominantly adopt lower-dimensional

https://doi.org/10.3390/cryst16030185

architectures. In contrast, the pdb ligand employed in this work enforces a more angular coordination geometry through the meta-positions of the carboxylate groups, enabling tetradentate binding to dinuclear cobalt paddle-wheel units, and promotes the formation of a fully three-dimensional cds net with pronounced interpenetration.

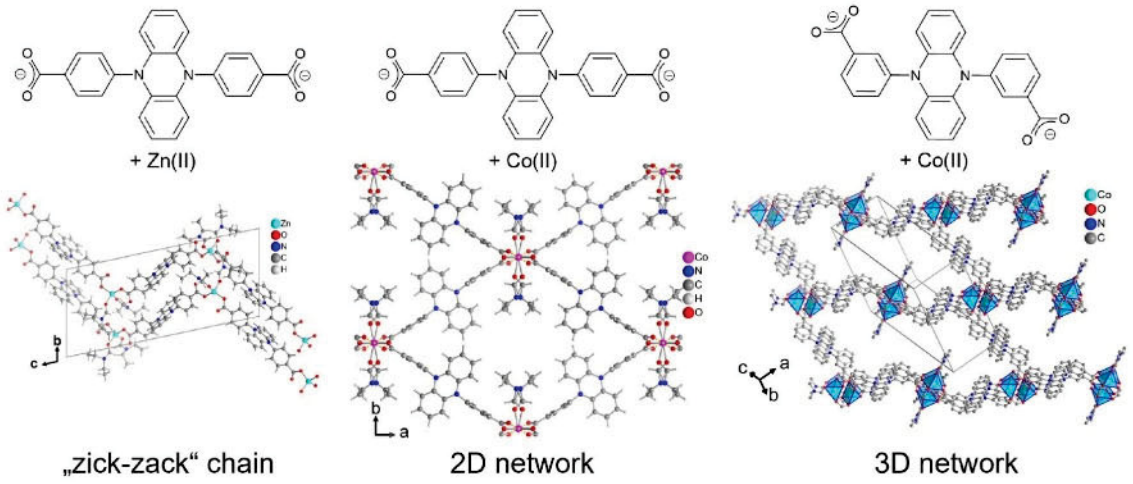


Figure 8. Simplified structural comparison of dihydrophenazine-based coordination polymers, highlighting the influence of ligand geometry and metal coordination on network topology. Coordination polymers based on isomeric dicarboxylate ligand H_2PZDB (**left** and **center**; adapted from Reference [29]) form less densely interconnected architectures, whereas the cobalt(II) coordination polymer [Co(pdb)(DMF)] reported in this work (**right**) adopts a three-dimensional, highly interpenetrated framework. The comparison illustrates how subtle changes in carboxylate connectivity, in combination with the coordination flexibility of cobalt(II), govern framework dimensionality and packing.

Cyclovoltammetric (CV) studies were performed to investigate the redox behavior of phenazine-containing cobalt coordination compounds. However, [Co(pdb)(DMF)] exhibits only limited electrochemical stability under the applied conditions, as evidenced by the progressive changes in the cyclovoltammograms upon repeated cycling. In particular, continuous decrease and distortion of the redox features are observed (Figure S27a), indicating irreversible processes and/or decomposition of the electroactive species. For $[Co_2(pdi)(DMF)_3]\cdot 2(DMF)\cdot H_2O$, no well-defined redox waves could be obtained within the accessible potential window (Figure S27b). The recorded currents are largely featureless and dominated by background processes, suggesting that the redox events of the compound are either electrochemically irreversible or masked by concurrent chemical reactions. Consequently, CV measurements were not further used for quantitative analysis of the redox properties but are provided here only to document the observed behavior.

4. Conclusions

Two cobalt(II) coordination networks based on dihydrophenazine-derived dicarboxylate and tetracarboxylate linkers H_2pdb and H_4pdi were synthesized solvothermally and structurally characterized. Crystalline products were obtained only with cobalt(II) nitrate, highlighting the sensitivity of framework formation to the metal ion and its counterion when using rigid, multitopic carboxylate linkers. Systematic solvothermal reactions with other metal salts (Zr(IV), Al(III), Cu(II), Ni(II), and Zn(II)) under comparable conditions resulted in no or non-crystalline products. Only cobalt(II) nitrate yielded single crystals

https://doi.org/10.3390/cryst16030185

suitable for X-ray diffraction; notably, analogous reactions with cobalt(II) sulfate or chloride were unsuccessful, indicating a pronounced counterion effect.

In [Co(pdb)(DMF)], dinuclear cobalt paddle-wheel units are linked by tetradentate pdb ligands into a three-dimensional cds net that exhibits threefold interpenetration and results in a densely packed framework. In contrast, $[Co_2(pdi)(DMF)_3]\cdot 2(DMF)\cdot H_2O$ contains two crystallographically distinct cobalt(II) centers, of which only one propagates the three-dimensional network, giving rise to an inverse pts topology with tetrahedral metal nodes and square–planar linker nodes.

These compounds demonstrate how the connectivity and geometry of dihydrophenazine-based carboxylate ligands govern the formation of secondary building units, network topology, and interpenetration in cobalt coordination polymers.

Supplementary Materials: The following supporting information can be downloaded at: https://www.mdpi.com/article/10.3390/cryst16030185/s1, Section S1: Chemicals used; Section S2: Reaction schemes for ligand syntheses; Section S3: NMR spectra; Section S4: IR spectra; Section S5: Overview of the conducted studies; Section S6: Crystal photographs and crystal structure images; Section S7: PXRD; Section S8: Thermogravimetric analyses; Section S9: Supramolecular analyses; Section S10: Electrochemical measurements. References [20,50–55] are cited in the Supplementary Materials.

Author Contributions: Conceptualization, A.V. and C.J.; methodology, A.V.; software, A.V.; validation, A.V., X.L. and N.J.; formal analysis, A.V., X.L., N.J., P.S. and D.G.; investigation, A.V., X.L., N.J., P.S. and D.G.; resources, C.J.; data curation, A.V., X.L. and N.J.; writing—original draft preparation, A.V. and C.J.; writing—review and editing, A.V. and C.J.; visualization, A.V. and C.J.; supervision, C.J.; project administration, C.J.; funding acquisition, C.J. All authors have read and agreed to the published version of the manuscript.

Funding: Funding was provided by the Deutsche Forschungsgemeinschaft (DFG) under grant 440366605 (for the Rigaku diffractometer). This work was supported by the Deutsche Forschungsgemeinschaft (DFG, German Research Foundation)—396890929/GRK 2482.

Data Availability Statement: The data presented in this study are available upon request from the corresponding author. The CCDC numbers 2522790–2522791 for compounds [Co(pdb)(DMF)] and $[Co_2(pdi)(DMF)_3]\cdot 2(DMF)\cdot H_2O$, respectively, contain the supplementary crystallographic data reported in this paper. These data can be obtained free of charge from the Cambridge Crystallographic Data Center via www.ccdc.cam.ac.uk/data_request/cif (accessed on 14 January 2026).

Acknowledgments: The authors would like to thank Birgit Tommes for providing the IR measurements. We also thank the Center for Molecular and Structural Analytics at Heinrich Heine University (CeMSA@HHU) for recording the mass spectrometric and NMR spectrometric data.

Conflicts of Interest: The authors declare no conflicts of interest.

References

1. Feng, S.; Wang, L.; Tian, L.; Liu, Y.; Hu, K.; Xu, H.; Wang, H.; Hua, J. Leveraging phenazine and dihydrophenazine redox dynamics in conjugated microporous polymers for high-efficiency overall photosynthesis of hydrogen peroxide. *Chem. Sci.* **2024**, *15*, 11972–11980. [CrossRef] [PubMed]
2. Ding, B.; Solomon, M.B.; Leong, C.F.; D'Alessandro, D.M. Redox-active ligands: Recent advances towards their incorporation into coordination polymers and metal-organic frameworks. *Coord. Chem. Rev.* **2021**, *439*, 213891. [CrossRef]
3. Liao, P.-Q.; Shen, J.-Q.; Zhang, J.-P. Metal–organic frameworks for electrocatalysis. *Coord. Chem. Rev.* **2018**, *373*, 22–48. [CrossRef]
4. D'Alessandro, D.M. Exploiting redox activity in metal–organic frameworks: Concepts, trends and perspectives. *Chem. Commun.* **2016**, *52*, 8957–8971. [CrossRef]
5. Lee, J.; Shizu, K.; Tanaka, H.; Nakanotani, H.; Yasuda, T.; Kaji, H.; Adachi, C. Controlled emission colors and singlet–triplet energy gaps of dihydrophenazine-based thermally activated delayed fluorescence emitters. *J. Mater. Chem. C* **2015**, *3*, 2175–2181. [CrossRef]

6. Dulov, D.A.; Bogdanov, A.V.; Dorofeev, S.G.; Magdesieva, T.V. *N,N*-Diaryldihydrophenazines as a Sustainable and Cost-Effective Alternative to Precious Metal Complexes in the PhotoredoxCatalyzed Alkylation of Aryl Alkyl Ketones. *Molecules* **2023**, *28*, 221. [CrossRef]
7. Corbin, D.A.; McCarthy, B.G.; van de Lindt, Z.; Miyake, G.M. Radical Cations of Phenoxazine and Dihydrophenazine Photoredox Catalysts and Their Role as Deactivators in Organocatalyzed Atom Transfer Radical Polymerization. *Macromolecules* **2021**, *54*, 4726–4738. [CrossRef]
8. Suzuki, S.; Takeda, T.; Kuratsu, M.; Kozaki, M.; Sato, K.; Shiomi, D.; Takui, T.; Okada, K. Pyrene-dihydrophenazine bis(radical cation) in a singlet ground state. *Org. Lett.* **2009**, *11*, 2816–2818. [CrossRef]
9. Unglaube, F.; Hünemörder, P.; Guo, X.; Chen, Z.; Wang, D.; Mejía, E. Phenazine Radical Cations as Efficient Homogeneous and Heterogeneous Catalysts for the Cross-Dehydrogenative Aza-Henry Reaction. *Helv. Chim. Acta* **2020**, *103*, e2000184. [CrossRef]
10. Lin, J.; Ouyang, J.; Liu, T.; Li, F.; Sung, H.H.-Y.M.; Williams, I.; Quan, Y. Metal-organic framework boosts heterogeneous electron donor–acceptor catalysis. *Nat. Commun.* **2023**, *14*, 7757. [CrossRef]
11. Hong, Q.-Y.; Huang, B.; Wu, M.-X.; Xu, L.; Zhao, X.-L.; Shi, X.; Yang, H.-B. Redox-Active Dihydrophenazine-Based Macrocycle: Synthesis, Conformation-Adaptive Behavior and Host-Guest Complexation with Tetracyanoquinodimethane. *Chin. J. Chem.* **2024**, *42*, 1895–1900. [CrossRef]
12. Theriot, J.C.; Lim, C.-H.; Yang, H.; Ryan, M.D.; Musgrave, C.B.; Miyake, G.M. Organocatalyzed atom transfer radical polymerization driven by visible light. *Science* **2016**, *352*, 1082–1086. [CrossRef] [PubMed]
13. Cheng, Y.; Li, Y.-X.; Liu, C.-H.; Zhu, Y.-Y.; Lin, W. Diaryl Dihydrophenazine-Based Porous Organic Polymers Enhance Synergistic Catalysis in Visible-Light-Driven Organic Transformations. *Angew. Chem. Int. Ed.* **2023**, *62*, e202310470. [CrossRef]
14. Corbin, D.A.; Puffer, K.O.; Chism, K.A.; Cole, J.P.; Theriot, J.C.; McCarthy, B.G.; Buss, B.L.; Lim, C.-H.; Lincoln, S.R.; Newell, B.S.; et al. Radical Addition to *N,N*-Diaryl Dihydrophenazine Photoredox Catalysts and Implications in Photoinduced Organocatalyzed Atom Transfer Radical Polymerization. *Macromolecules* **2021**, *54*, 4507–4516. [CrossRef] [PubMed]
15. Cole, J.P.; Federico, C.R.; Lim, C.-H.; Miyake, G.M. Photoinduced organocatalyzed atom transfer radical polymerization using low ppm catalyst loading. *Macromolecules* **2019**, *52*, 747–754. [CrossRef]
16. Su, X.; Jessop, P.G.; Cunningham, M.F. Versatility of organocatalyzed atom transfer radical polymerization and CO_2-switching for preparing both hydrophobic and hydrophilic polymers with the recycling of a photocatalyst. *Macromolecules* **2019**, *52*, 6725–6733. [CrossRef]
17. McCarthy, B.; Sartor, S.; Cole, J.; Damrauer, N.; Miyake, G.M. Solvent effects and side reactions in organocatalyzed atom transfer radical polymerization for enabling the controlled polymerization of acrylates catalyzed by diaryl dihydrophenazines. *Macromolecules* **2020**, *53*, 9208–9219. [CrossRef]
18. Wang, K.; Kang, X.; Yuan, C.; Han, X.; Liu, Y.; Cui, Y. Porous 2D and 3D Covalent Organic Frameworks with Dimensionality-Dependent Photocatalytic Activity in Promoting Radical Ring-Opening Polymerization. *Angew. Chem. Int. Ed.* **2021**, *60*, 19466–19476. [CrossRef]
19. Kochetygov, I.; Roth, J.; Espín, J.; Pache, S.; Justin, A.; Schertenleib, T.; Taheri, N.; Chernyshov, D.; Queen, W.L. A Simple, Transition Metal Catalyst-Free Method for the Design of Complex Organic Building Blocks Used to Construct Porous Metal-Organic-Frameworks. *Angew. Chem. Int. Ed.* **2023**, *62*, e202215595. [CrossRef]
20. Zhang, S.; Ma, X.-F.; Yang, Y.; Ren, H.; Li, W.; Liu, Y.; Xi, C.; Zheng, L.; Miao, Z. Phenazine-functionalized Zn-based metal organic framework for efficient visible light photocatalytic sulfides. *J. Solid State Chem.* **2025**, *351*, 125525. [CrossRef]
21. Jiang, W.L.; Huang, B.; Zhao, X.L.; Shi, X.; Yang, H.B. Strong halide anion binding within the cavity of a conformation-adaptive phenazine-based Pd_2L_4 cage. *Chem* **2023**, *9*, 2655–2668. [CrossRef]
22. Zhang, H.; Tanga, X.; Gu, C. Dihydrophenazine linked porous organic polymers for high capacitance and energy density pseudocapacitive electrodes and devices. *J. Mater. Chem. A* **2021**, *9*, 4984–4989. [CrossRef]
23. Vitaku, E.; Gannett, C.N.; Carpenter, K.L.; Shen, L.; Abruna, H.D.; Dichtel, W.R. Phenazine-Based Covalent Organic Framework Cathode Materials with High Energy and Power Densities. *J. Am. Chem. Soc.* **2020**, *142*, 16–20. [CrossRef] [PubMed]
24. Wu, M.-X.; Hong, Q.-Y.; Li, M.; Jiang, W.-L.; Huang, B.; Lu, S.; Wang, H.; Yang, H.-B.; Zhao, X.-L.; Shi, X. Self-assembly of conformation-adaptive dihydrophenazine-based coordination cages. *Chem. Commun.* **2024**, *60*, 1184–1187. [CrossRef]
25. Yu, J.; Cheng, L.; Zhang, X.; Shi, X.; Wang, H.-g. Integrating p-type phenazine into covalent triazine framework to achieve co-storage of cations and anions for quasi-solid-state dual-ion batteries. *Chem. Eng. J.* **2024**, *489*, 151320. [CrossRef]
26. Guo, J.; Xu, Y.; Jin, S.; Chen, L.; Kaji, T.; Honsho, Y.; Addicoat, M.A.; Kim, J.; Saeki, A.; Ihee, H.; et al. Conjugated organic framework with three-dimensionally ordered stable structure and delocalized π clouds. *Nat. Commun.* **2013**, *4*, 2736. [CrossRef]
27. Sun, H.; Ji, H.; Qiao, D.; Xu, Y.; Qu, X.; Qi, Y.; Feng, Z.; Zhang, X.; Zhang, F.; Wang, R.; et al. Vinylene-linked covalent organic frameworks based on phenanthroline for visible-light-driven bifunctional photocatalytic water splitting. *Chem. Eng. J.* **2025**, *507*, 160448. [CrossRef]
28. Jiang, W.-L.; Huang, B.; Wu, M.-X.; Zhu, Y.-K.; Zhao, X.-L.; Shi, X.; Yang, H.-B. Post-Synthetic Modification of Metal-Organic Frameworks Bearing Phenazine Radical Cations for aza-Diels-Alder Reactions. *Chem. Asian J.* **2021**, *16*, 3985–3992. [CrossRef]

https://doi.org/10.3390/cryst16030185

29. Püschel, D.; Nau, M.; Assahub, N.; Beglau, T.H.Y.; Hufnagel, N.; Jordan, D.; Heinen, T.; Strothmann, T.; Suta, M.; Winter, R.F.; et al. Zinc and Cobalt Coordination Polymers Based on the Redox-Active Linker 4,4′-(Phenazine-5,10-diyl)dibenzoate: Structures and Electrochemical Properties. *Eur. J. Inorg. Chem.* **2025**, *28*, e202500270. [CrossRef]
30. Dolomanov, O.V.; Bourhis, L.J.; Gildea, R.J.; Howard, J.A.K.; Puschmann, H. OLEX2: A complete structure solution, refinement and analysis program. *J. Appl. Crystallogr.* **2009**, *42*, 339–341. [CrossRef]
31. Sheldrick, G.M. SHELXT—Integrated space-group and crystal-structure determination. *Acta Crystallogr. A* **2015**, *71*, 3–8. [CrossRef] [PubMed]
32. Sheldrick, G.M. Crystal structure refinement with SHELXL. *Acta Crystallogr. C* **2015**, *71*, 3–8. [CrossRef] [PubMed]
33. Brandenburg, K. *Diamond*; Version 5.0.0; Crystal and Molecular Structure Visualization, Crystal Impact; K. Brandenburg & H. Putz Gbr: Bonn, Germany, 1997–2023.
34. Macrae, C.F.; Sovago, I.; Cottrell, S.J.; Galek, P.T.A.; McCabe, P.; Pidcock, E.; Platings, M.; Shields, G.P.; Stevens, J.S.; Towler, M.; et al. Mercury 4.0: From visualization to analysis, design and prediction. *J. Appl. Crystallogr.* **2020**, *53*, 226–235. [CrossRef] [PubMed]
35. Dai, G.; He, Y.; Niu, Z.; He, P.; Zhang, C.; Zhao, Y.; Zhang, X.; Zhou, H. A Dual-Ion Organic Symmetric Battery Constructed from Phenazine-Based Artificial Bipolar Molecules. *Angew. Chem. Int. Ed.* **2019**, *58*, 9902–9906. [CrossRef]
36. Koyama, D.; Dale, H.J.A.; Orr-Ewing, A.J. Ultrafast Observation of a Photoredox Reaction Mechanism: Photoinitiation in Organocatalyzed Atom-Transfer Radical Polymerization. *J. Am. Chem. Soc.* **2018**, *140*, 1285–1293. [CrossRef]
37. Delgado-Friedrichs, O.; O'Keeffe, M.; Yaghi, O.M. Three-periodic nets and tilings: Edge-transitive binodal structures. *Acta Crystallogr. A* **2006**, *62*, 350–355. [CrossRef]
38. Friedrichs, O.D.; O'Keeffe, M.; Yaghi, O.M. The $CdSO_4$, rutile, cooperite and quartz dual nets: Interpenetration and catenation. *Solid State Sci.* **2003**, *5*, 73–78. [CrossRef]
39. Friedrichs, O.D.; O'Keeffe, M. Three-periodic tilings and nets: Face-transitive tilings and edge-transitive nets revisited. *Acta Crystallogr. A* **2007**, *63*, 344–347. [CrossRef]
40. Moulton, B.; Abourahma, H.; Bradner, M.W.; Lu, J.; McManus, G.J.; Zaworotko, M.J. A new $6^5.8$ topology and a distorted $6^5.8$ $CdSO_4$ topology: Two new supramolecular isomers of $[M_2(bdc)_2(L)_2]_n$ coordination polymers. *Chem. Commun.* **2003**, 1342–1343. [CrossRef]
41. Gao, H.; Lou, X.H.; Li, Q.T.; Du, W.J.; Xu, C. Three-Fold Interpenetrated $CdSO_4$ Topology in a Co(II) Coordination Polymer Constructed From Pamoic Acid and N-Containing Auxiliary Ligand. *Synth. React. Inorg. Met.-Org. Nano-Met. Chem.* **2015**, *45*, 865–868. [CrossRef]
42. Zhang, J.; Chen, Y.-B.; Ji, Z.; Qin, Y.-Y.; Yao, Y.-G. A rare twofold interpenetrated cds topology in a Zn-organic polymer $[Zn_2(BDC)(BPP)Cl_2]_n$. *Inorg. Chem. Commun.* **2006**, *9*, 449–451. [CrossRef]
43. Gaskin, G.J.; LaDuca, R.L. Poly[[[μ-1,4-bis(pyridin-4-ylmethyl)piperazine][μ-4-(2-carboxylatoethyl)benzoato]copper(II)] monohydrate], a coordination polymer with twofold interpenetrated cds topology networks. *IUCrData* **2023**, *8*, x230855. [CrossRef] [PubMed]
44. Tsai, M.-J.; Liao, K.-S.; Wu, J.-Y. A Water-Stable 2-Fold Interpenetrating cds Net as a Bifunctional Fluorescence-Responsive Sensor for Selective Detection of Cr(III) and Cr(VI) Ions. *Nanomaterials* **2022**, *12*, 158. [CrossRef] [PubMed]
45. Kostakis, G.E.; Casella, L.; Hadjiliadis, N.; Monzani, E.; Kourkoumelis, N.; Plakatouras, J.C. Interpenetrated networks from a novel nanometer-sized pseudopeptidic ligand, bridging water, and transition metal ions with cds topology. *Chem. Commun.* **2005**, 3859–3861. [CrossRef]
46. Shi, Z.-C.; Wang, X.; Drozd, V.; Raptis, R.G. A Foldable Metal–Organic Framework with cds Topology Assembled via Four-Connected Square-Planar Single Ni^{2+}-Ion Nodes and Linear Bidentate Linkers. *Crystals* **2024**, *14*, 40. [CrossRef]
47. Zhang, J.; Xue, Y.-S.; Liang, L.-L.; Ren, S.-B.; Li, Y.-Z.; Du, H.-B.; You, X.-Z. Porous Coordination Polymers of Transition Metal Sulfides with PtS Topology Built on a Semirigid Tetrahedral Linker. *Inorg. Chem.* **2010**, *49*, 7685–7691. [CrossRef]
48. Yuan, A.-H.; Lu, R.-Q.; Zhou, H.; Chen, Y.-Y.; Li, Y.-Z. Three unique two-fold interpenetrated three-dimensional networks with PtS-type topology constructed from $[M(CN)_4]^{2-}$ (M = Ni, Pd, Pt) as "square-planar" building blocks. *CrystEngComm* **2010**, *12*, 1382–1384. [CrossRef]
49. Murphy, M.J.; D'Alessandro, D.M.; Kepert, C.J. A porous Mn(V) coordination framework with PtS topology: Assessment of the influence of a terminal nitride on CO_2 sorption. *Dalton Trans.* **2013**, *42*, 13308–13310. [CrossRef]
50. Mandić, V.; Kurajica, S.; Plodinec, M.; Panžić, I. Thermal Stability and Utilization of 1D-Nanostructured Co_3O_4 Rods Derived by Simple Solvothermal Processing. *Catalysts* **2022**, *12*, 1162. [CrossRef]
51. Spek, A.L. Structure Validation in Chemical Crystallography. *Acta Crystallogr. D* **2009**, *65*, 148–155. [CrossRef]
52. Janiak, C. A Critical Account on π–π Stacking in Metal Complexes with Aromatic Nitrogen-Containing Ligands. *J. Chem. Soc. Dalton Trans.* **2000**, 3885–3896. [CrossRef]

53. Yang, X.-J.; Drepper, F.; Wu, B.; Sun, W.-H.; Haehnel, W.; Janiak, C. From Model Compounds to Protein Binding: Syntheses, Characterizations and Fluorescence Studies of $[Ru^{II}(Bipy)(Terpy)L]^{2+}$ Complexes (Bipy = 2,2′-Bipyridine; Terpy = 2,2′:6′,2″-Terpyridine; L = Imidazole, Pyrazole and Derivatives, Cytochrome c). *Dalton Trans.* **2005**, 256–267. [CrossRef]
54. Takahashi, O.; Kohno, Y.; Iwasaki, S.; Saito, K.; Iwaoka, M.; Tomoda, S.; Umezawa, Y.; Tsuboyama, S.; Nishio, M. Hydrogen-Bond-Like Nature of the CH/π Interaction as Evidenced by Crystallographic Database Analyses and Ab Initio Molecular Orbital Calculations. *Bull. Chem. Soc. Jpn.* **2001**, *74*, 2421–2430. [CrossRef]
55. Nishio, M.; Umezawa, Y.; Honda, K.; Tsuboyama, S.; Suezawa, H. CH/π Hydrogen Bonds in Organic and Organometallic Chemistry. *CrystEngComm* **2009**, *11*, 1757–1788. [CrossRef]

Disclaimer/Publisher's Note: The statements, opinions and data contained in all publications are solely those of the individual author(s) and contributor(s) and not of MDPI and/or the editor(s). MDPI and/or the editor(s) disclaim responsibility for any injury to people or property resulting from any ideas, methods, instructions or products referred to in the content.

https://doi.org/10.3390/cryst16030185

Supplementary Material

Cobalt Coordination Networks Based on the Linker (Phenazine-5,10-diyl)di- and tetrabenzoate

Annette Vollrath, Xiang Liu, Nikolas Jansen, Philipp Seiffert, David Geller and Christoph Janiak *

Institut für Anorganische Chemie und Strukturchemie, Heinrich-Heine-Universität 40204 Düsseldorf, Germany

* *Correspondence: janiak@uni-duesseldorf.de*

Emails: annette.vollrath@hhu.de, xiang.liu@hhu.de, nijan113@hhu.de, philipp.seiffert@uni-duesseldorf.de, david.geller@hhu.de, janiak@uni-duesseldorf.de

Content

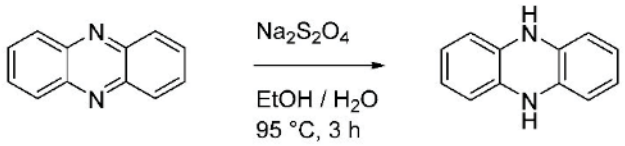
Section S1 Chemicals used 2
Section S2 Reaction schemes for ligand syntheses (Scheme S1-S5) 3
Section S3 NMR spectra 5
Section S4 IR spectra 14
Section S5 Overview of the conducted studies 16
Section S6 Crystal photographs and crystal structure images 20
Section S7 PXRD 22
Section S8 Thermogravimetric analyses 24
Section S9 Supramolecular analyses 27
Section S10 Electrochemical measurements 34

Section S1 Chemicals used

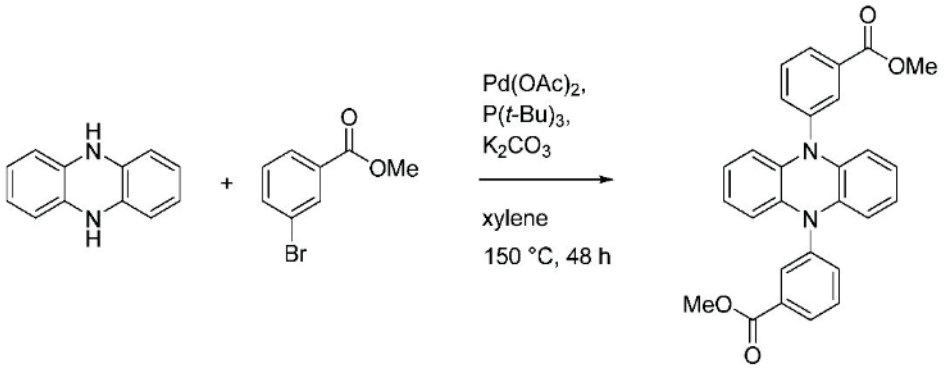
Table S1. List of chemicals used.

Chemical	Purity [%]	Supplier
Cobalt(II) nitrate hexahydrate	≥ 98	Carl Roth
Dimethyl-5-Iodoisophthalate	98.45	BLDpharm
Hydrochloric acid	37	VWR Chemicals
Lithium hydroxide monohydrate	p.a.	AppliChem
Magnesium sulfate	99.0	VWR Chemicals
Methyl-3-bromobenzoate	97	BLDpharm
Palladium(II) acetate	99.9	BLDpharm
Phenazine	99.87	BLDpharm
Potassium carbonate	99.5	Grüssing
Sodium dithionite	85	Acros Organics
Tri-*tert*-butyl-phosphine	98	Merck
1,4-Dioxane	≥ 99.8	Fisher Chemical
Chloroform	≥ 99	Fisher Chemical
Dichlormethane (DCM)	99.8	Fisher Chemical
Ethanol	≥ 99.8	Honeywell
n-Hexane	≥ 95	Sigma Aldrich
N,*N*-Dimethylformamide (DMF)	≥ 99.5	Fisher Chemical
Xylene (isomer mixture)	98.7	VWR Chemicals

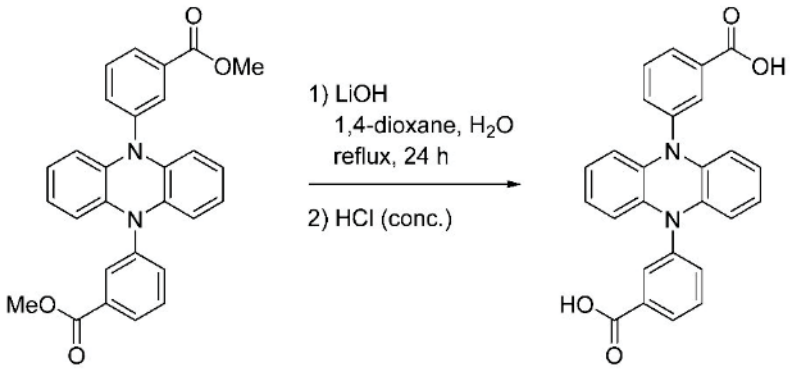
Section S2 Reaction schemes for ligand syntheses (Scheme S1-S5)



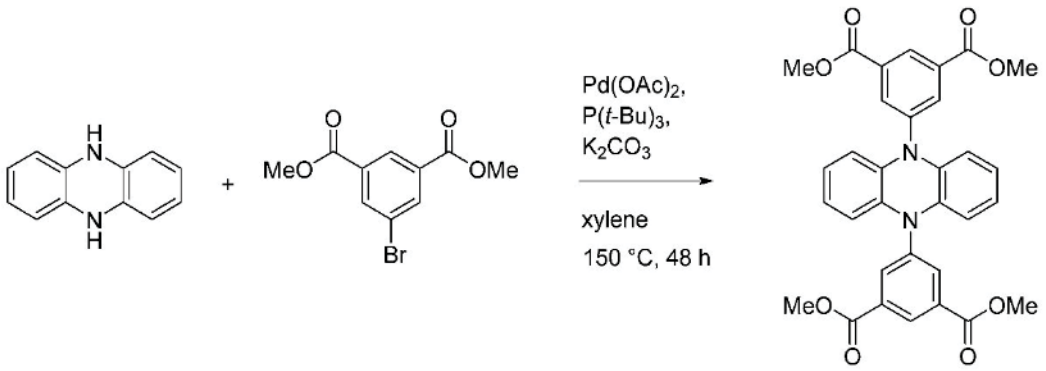
Scheme S1. Synthesis of 5,10-dihydrophenazine.



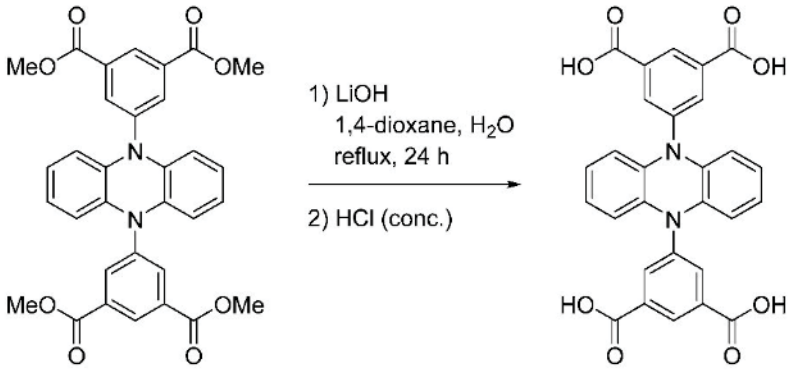
Scheme S2. Synthesis of dimethyl-3,3'-(phenazine-5,10-diyl)dibenzoate.



Scheme S3. Synthesis of 3,3'-(phenazine-5,10-diyl)dibenzoic acid (H_2pdb).



Scheme S4. Synthesis of tetramethyl-5,5'-(phenazine-5,10-diyl)diisophthalate.



Scheme S5. Synthesis of 5,5'-(phenazine-5,10-diyl)diisophthalic acid (H_4pdi).

Section S3 NMR spectra

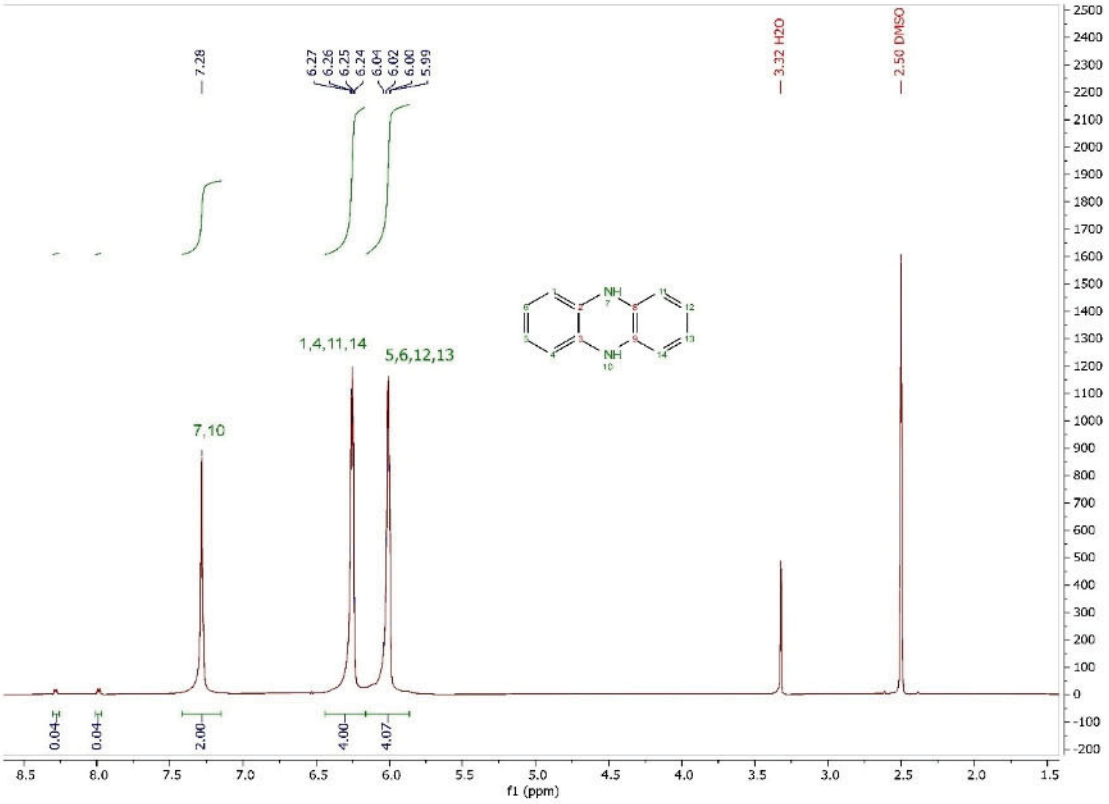


Figure S1. ^{1}H-NMR-spectrum of 5,10-dihydrophenazin (300 MHz, DMSO-d_6).
The two doublets at 6.01 ppm and 6.26 ppm can be attributed to the two benzene rings in 5,10-dihydrophenazine, while the singlet at 7.29 ppm can be assigned to the NH protons. At 8.00 ppm and 8.30 ppm, there are two further signals that can be assigned to the remaining or re-oxidized phenazine starting material. The percentage content of phenazine in the sample can be calculated from the ratios of the signals of the reactant to the product as 1%.

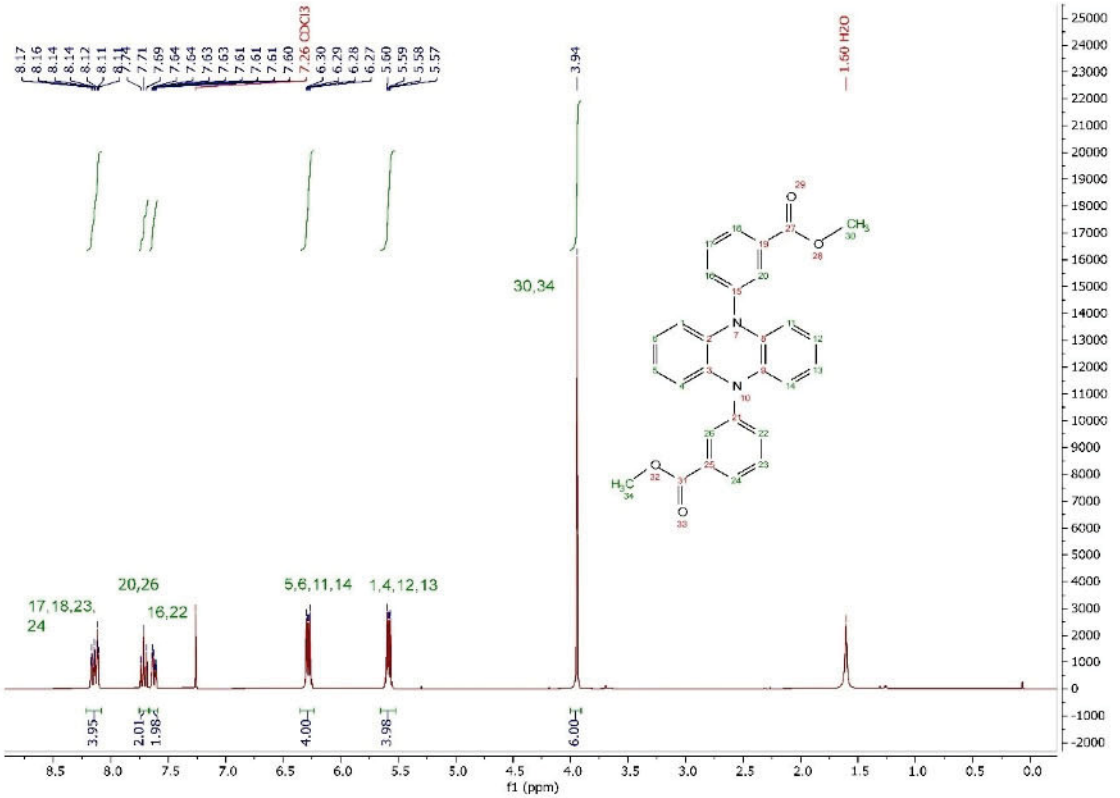


Figure S2. ^{1}H-NMR-spectrum of dimethyl-3,3'-(phenazine-5,10-diyl)dibenzoate (H_2pdb) (300 MHz, $CDCl_3$). In the ^{1}H NMR spectrum, the singlet at 3.94 ppm can be assigned to the two methyl groups in dimethyl-3,3'-(phenazine-5,10-diyl)dibenzoate, while the doublet at 5.58 ppm and 6.28 ppm can be assigned to the protons in the 5,10-dihydrophenazine core. The multiplet from 7.59 ppm to 7.65 ppm can be assigned to the protons at positions 20 and 25 of the benzenoate ring and the triplet at 7.71 ppm belongs to the protons at positions 21 and 26. The multiplet from 8.08 ppm to 8.20 ppm can be assigned to the other four protons on the benzoate ring. In addition, a small water signal at 1.60 ppm is observed, which may originate from the water in the sample and the water contained in the solvent.

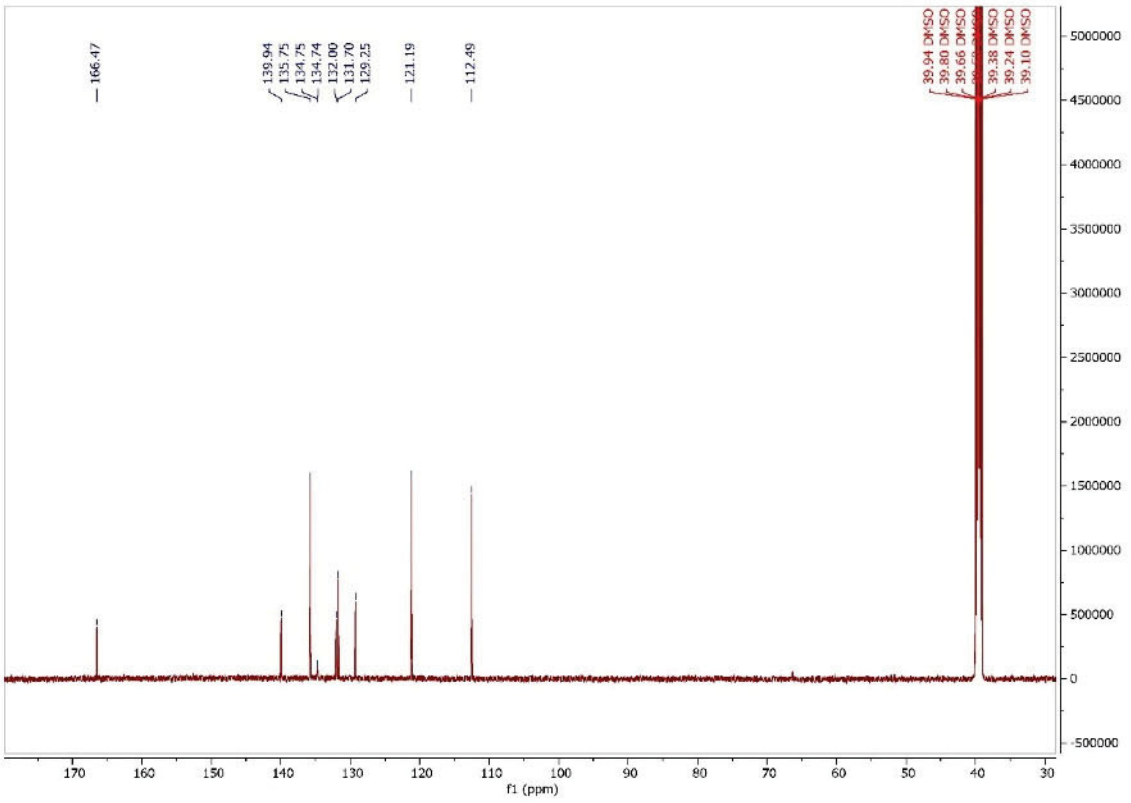
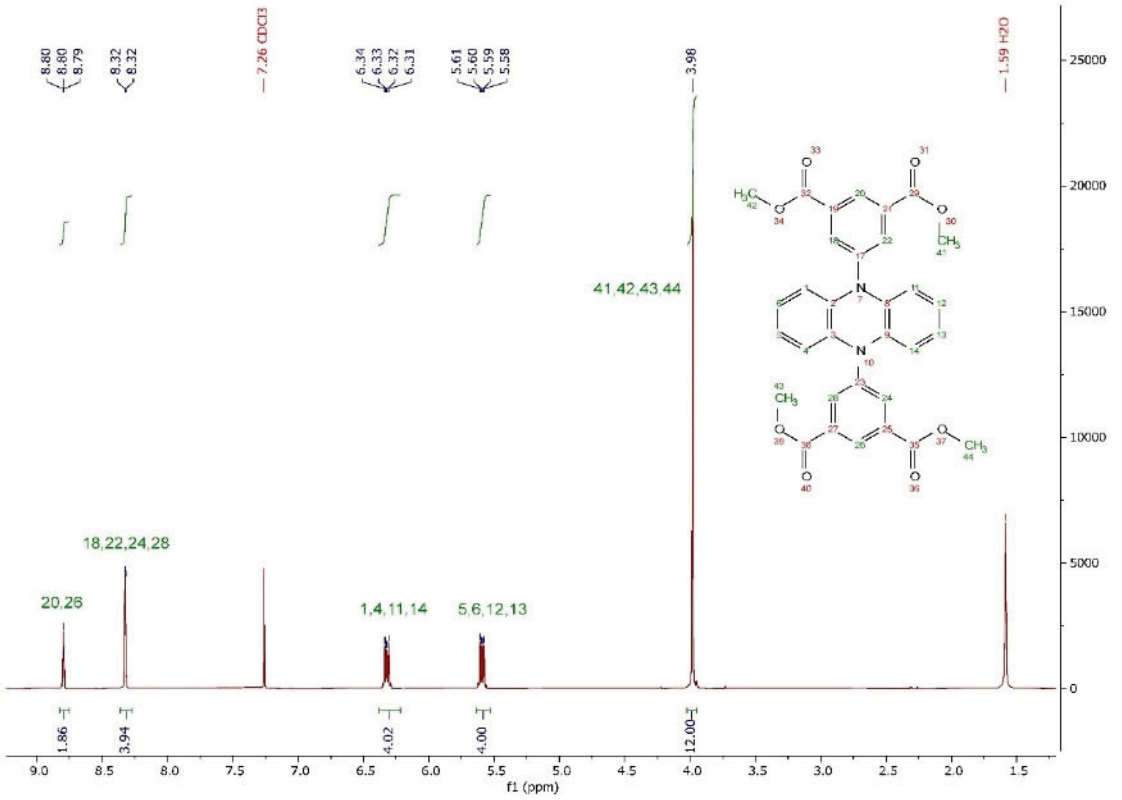


Figure S3. $^{13}C\{1H\}$-NMR-spectrum of dimethyl-3,3'-(phenazine-5,10-diyl)dibenzoate (600 MHz, $CDCl_3$).



71

Figure S4. ^{1}H-NMR-spectrum von tetramethyl-5,5'-(phenazine-5,10-diyl)diisophthalate (300MHz, $CDCl_3$). All five chemically different signals were observed in the ^{1}H NMR spectrum. The singlet located at 3.98 ppm can be assigned to the four methyl groups, while the two doublets of doublets at 5.59 and 6.32 ppm can be assigned to the protons of the 5,10-dihydrophenazine core of this molecule. The two signals between 8.0 ppm and 9.0 ppm belong to the three protons of the isophthalate benzene rings.

72 73 74 75 76

77

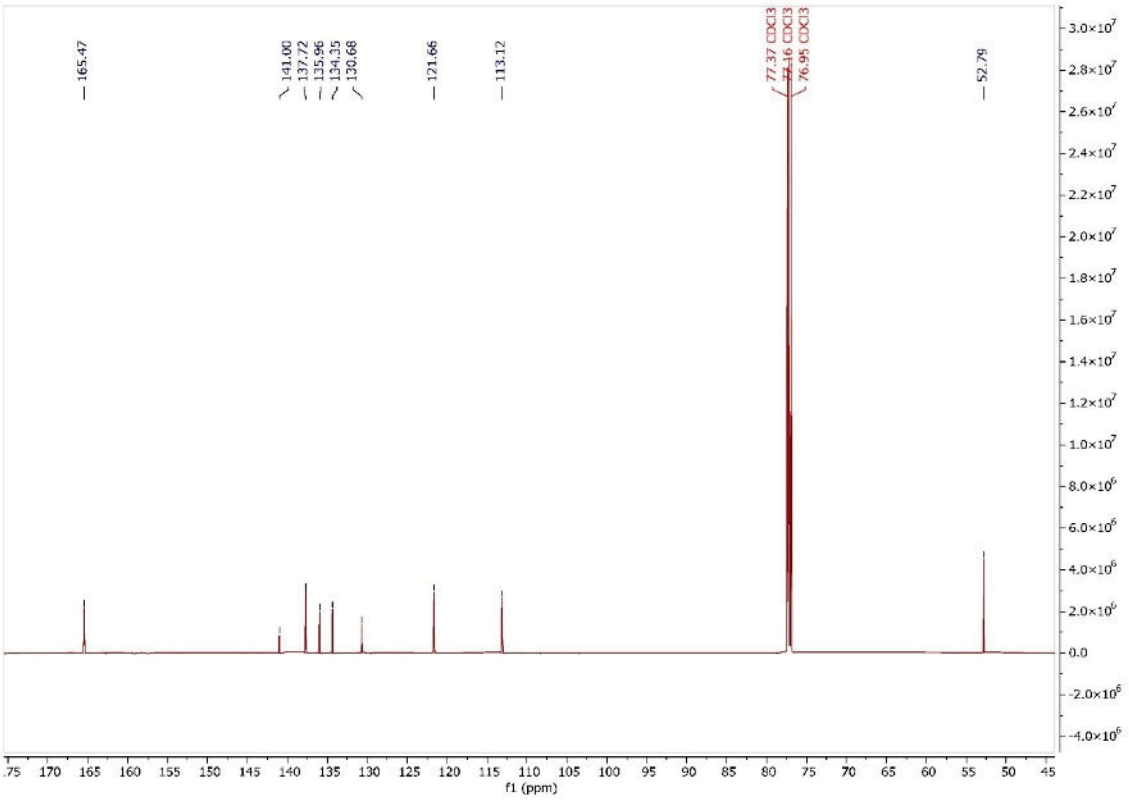


Figure S5. $^{13}C\{1H\}$-NMR-spectrum von tetramethyl-5,5'-(phenazine-5,10-diyl)diisophthalate (600MHz, $CDCl_3$).

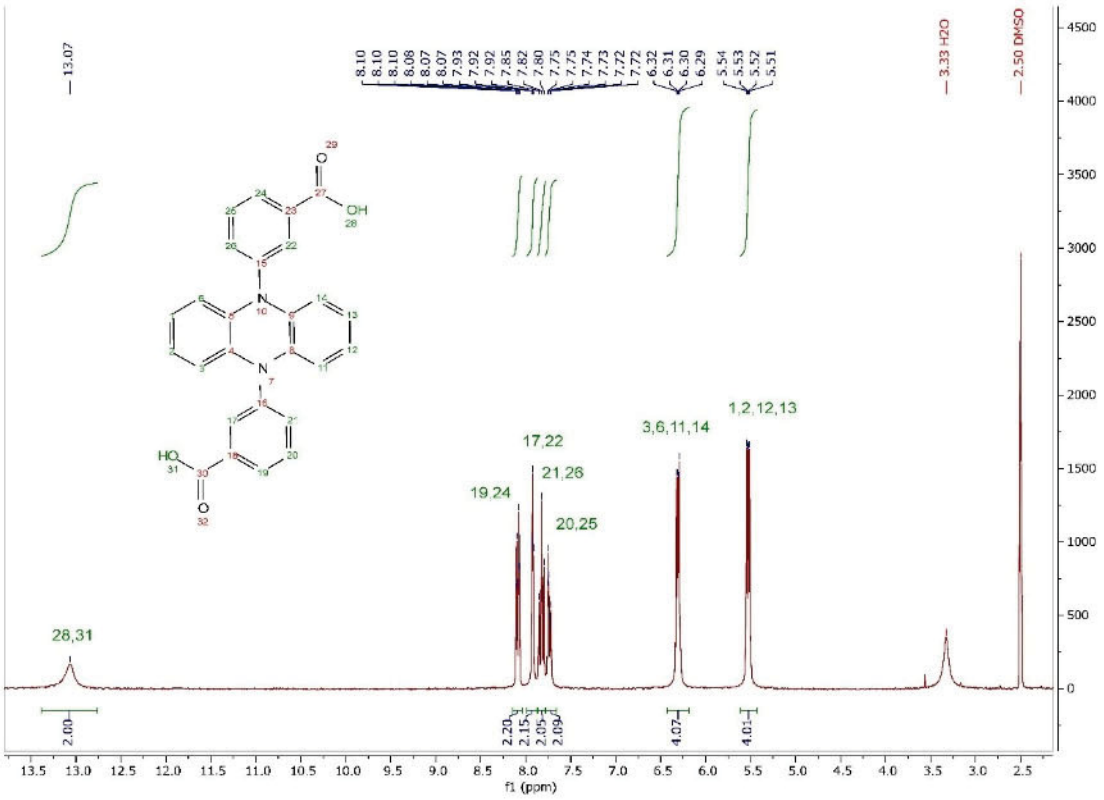


Figure S6. ^{1}H-NMR-spectrum of 3,3'-(phenazine-5,10-diyl)dibenzoic acid (H_2pdb) (300 MHz, DMSO-d_6). The two doublets at 5.52 ppm and 6.30 ppm can be assigned to the protons on the two anellated benzene rings of the 5,10-dihydrophenazine core. The four signals between 7.60 ppm and 8.20 ppm can be assigned to the protons on the two benzoate rings. The integrals in the spectrum correspond exactly to the expected number of hydrogen atoms.

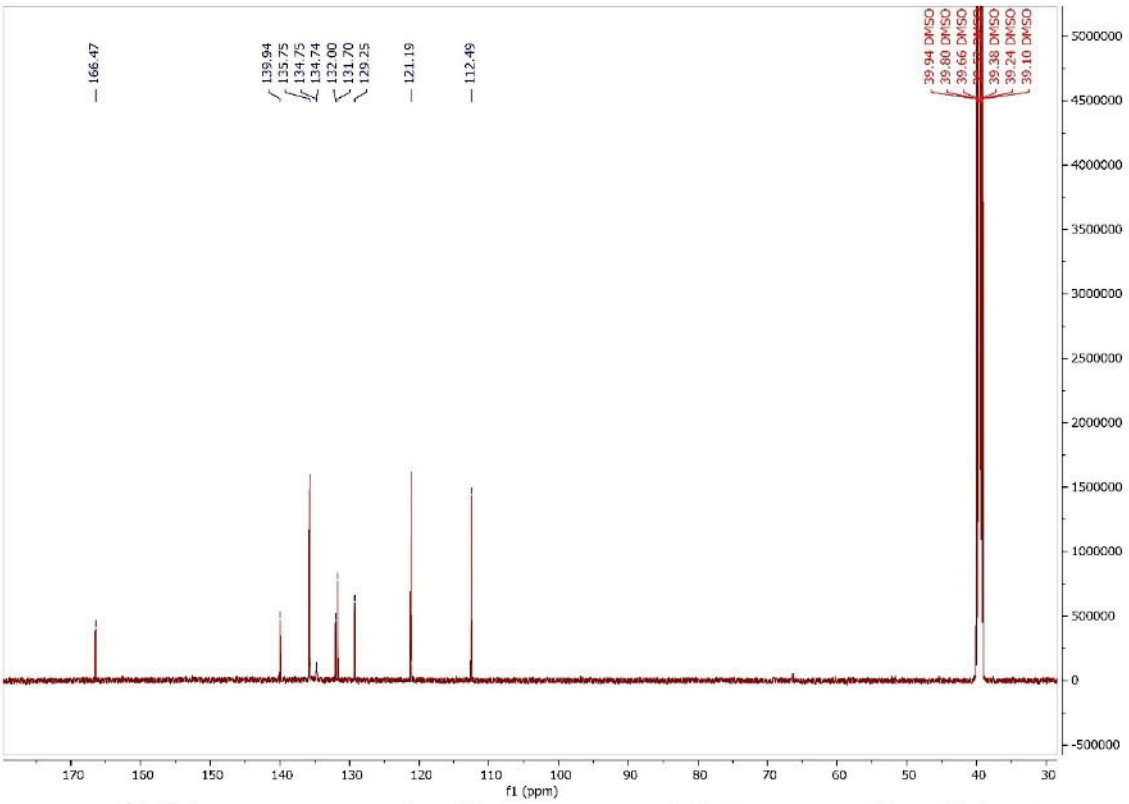


Figure S7. $^{13}C\{^{1}H\}$-NMR-spectrum of 3,3'-(phenazine-5,10-diyl)dibenzoic acid (H_2pdb) (600 MHz, DMSO-d_6).

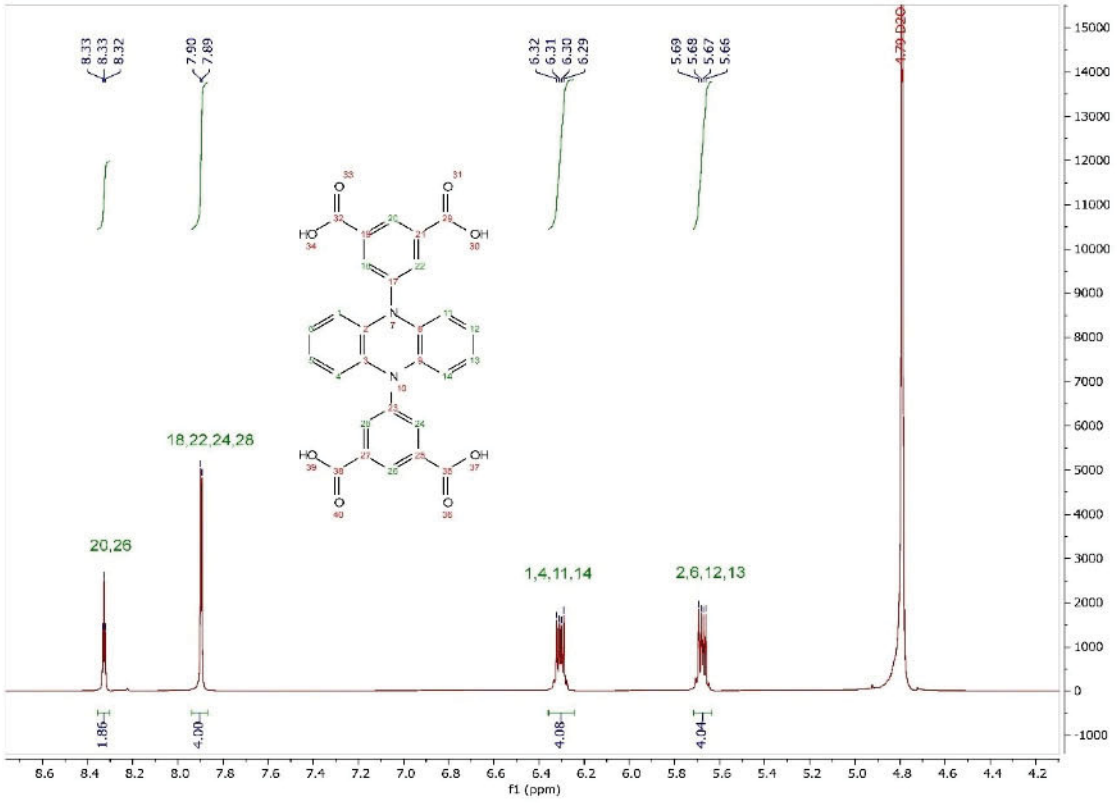


Figure S8. ^{1}H-NMR-Spectrum of 5,5'-(phenazine-5,10-diyl)diisophthalic acid (H_4pdi) (300 MHz, D_2O). The two doublets at 5.81 ppm and 6.44 ppm can be assigned to the 5.10-dihydrophenazine core, the two signals between 8.0 ppm and 8.5 ppm to the protons on the two isophthalate rings. The integrals correspond to the number of protons in the molecule.

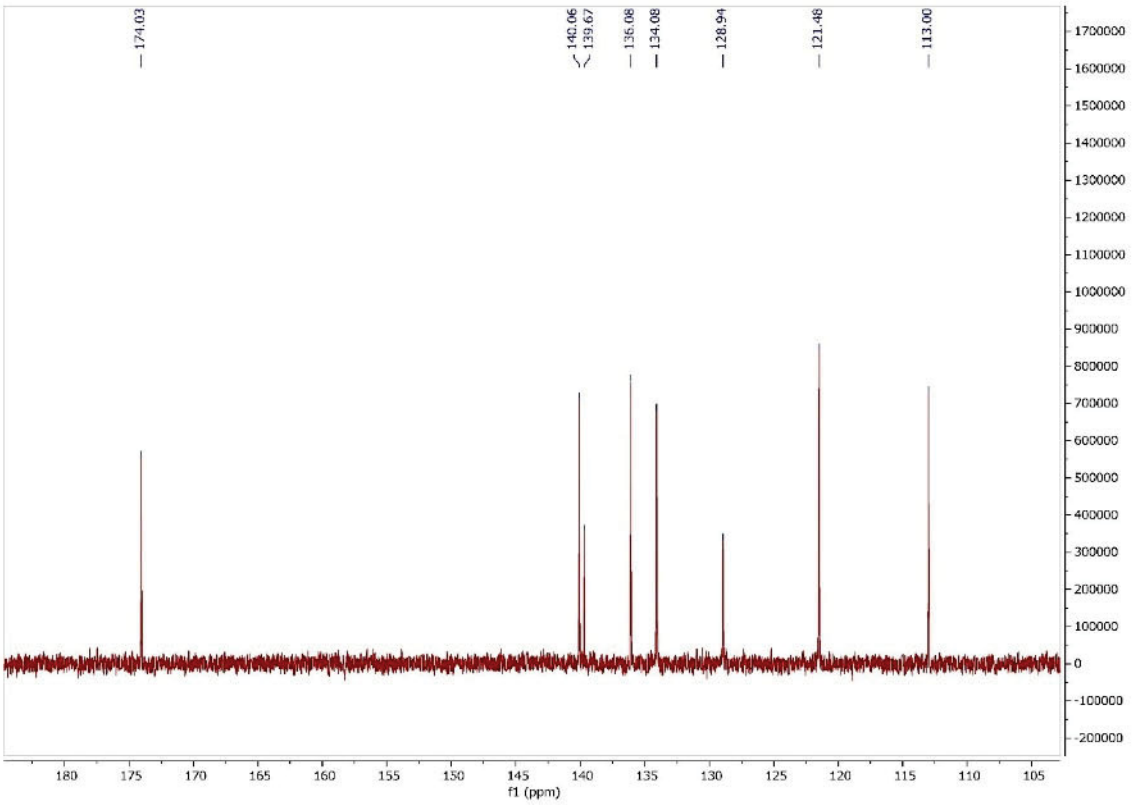


Figure S9. $^{13}C\{^{1}H\}$-NMR-Spectrum of 5,5'-(phenazine-5,10-diyl)diisophthalic acid (H_4pdi) (600 MHz, D_2O).

Section S4 IR spectra

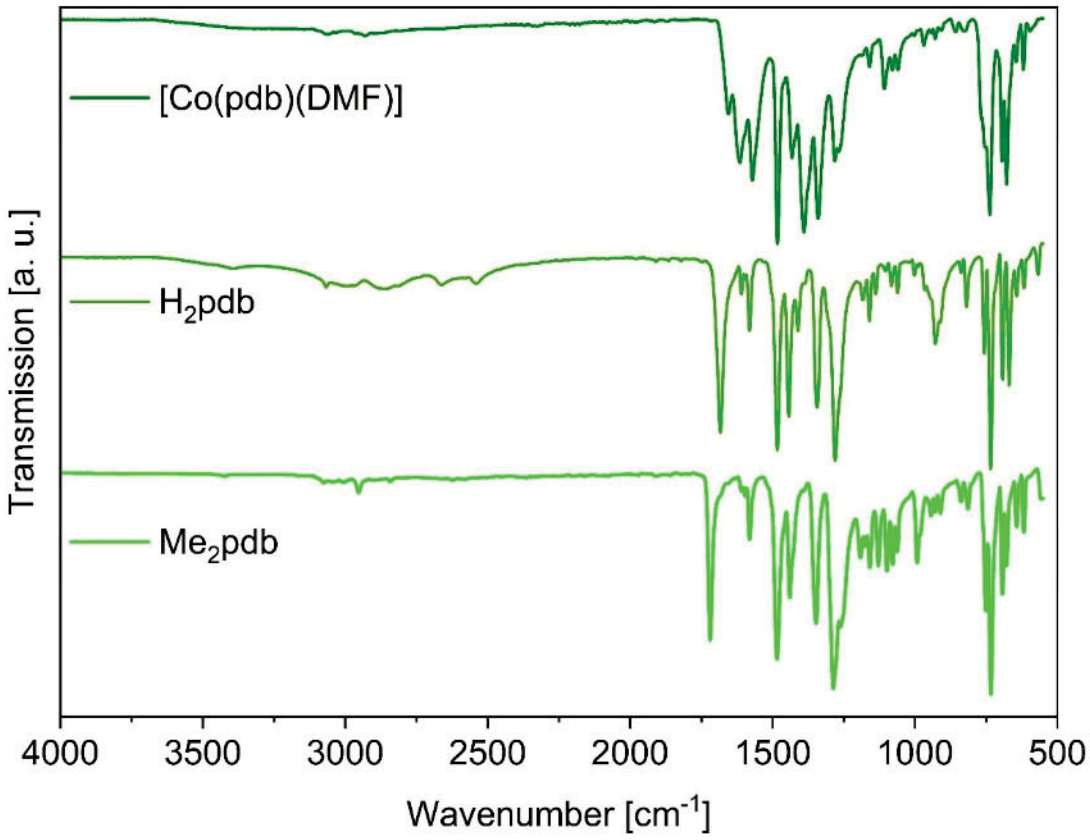


Figure S10. IR spectra of [Co(pdb)(DMF)] (dark green), of 3,3'-(phenazine-5,10-diyl)dibenzoic acid (H_2pdb, olive green) and dimethyl-3,3'-(phenazine-5,10-diyl)dibenzoate (Me_2pdb, light green).

In the spectrum of the coordination polymer, no absorption band corresponding to the O–H stretching vibration is observed in the range between 2400 and 3200 cm^{-1}, which is clearly present in the spectrum of the dibenzoic acid linker H_2pdb and absent in the spectrum of the corresponding methyl ester Me_2pdb. This indicates deprotonation of the carboxylic acid groups upon coordination to the cobalt centers. The C=O stretching vibration of the carboxylic acid group is observed in the H_2pdb linker spectrum at 1682 cm^{-1}, while the ester C=O stretching vibration in Me_2pdb appears at a slightly higher wavenumber. In the spectrum of the coordination polymer, this band is replaced by two bands at 1655 and 1615 cm^{-1}, which can be assigned to the asymmetric and symmetric stretching vibrations of the coordinated carboxylate groups, confirming their bridging coordination mode. Additionally, an absorption band at 1483 cm^{-1} is observed in the spectra of the coordination polymer as well as in both linker compounds and can be attributed to the C=C stretching vibration of the aromatic benzene rings. The band at approximately 1280 cm^{-1}, present in all spectra, can be assigned to C–O stretching vibrations of the carboxylate or ester groups, potentially with contributions from C–N stretching modes. A strong absorption band at 1390 cm^{-1} appears in the spectrum of the coordination polymer and can be attributed to the C–N stretching vibration of coordinated DMF molecules, supporting the presence of DMF in the coordination environment of the cobalt centers.

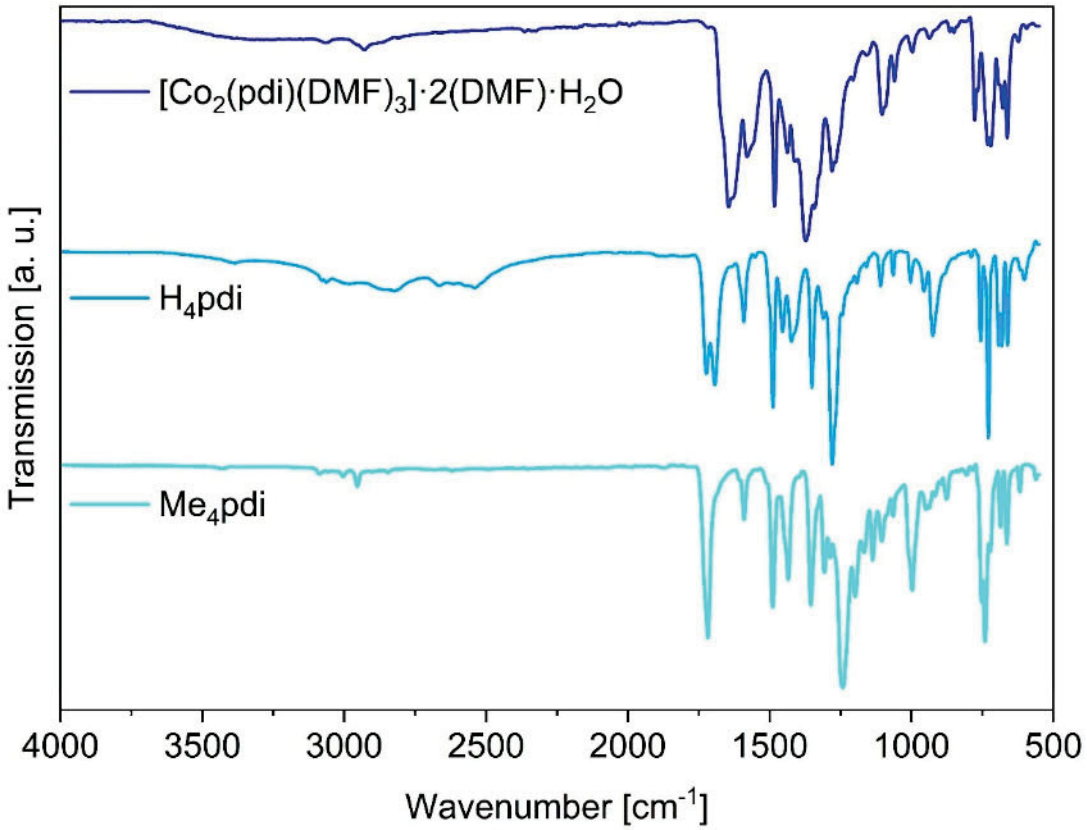


Figure S11. IR spectra of $[Co_2(pdi)(DMF)_3]\cdot 2(DMF)\cdot H_2O$ (dark blue), 5,5'-(phenazine-5,10-diyl)diisophthalic acid (H_4pdi, light blue) and tetramethyl-5,5'-(phenazine-5,10-diyl)diisophthalate (Me_4pdi, cyan).

In the spectrum of the free acid linker H_4pdi, a broad absorption band in the range between 2400 and 3300 cm^{-1} is observed, which can be assigned to the O–H stretching vibration of the carboxylic acid groups. This band is absent in the spectra of both the coordination compound and the Me_4pdi, indicating deprotonation of the carboxylic acid groups upon coordination to the cobalt centers. In the spectrum of H_4pdi, a strong band at approximately 1690 cm^{-1} is attributed to the C=O stretching vibration of the carboxylic acid groups. Upon coordination, this band is replaced by multiple bands in the range between 1650 and 1550 cm^{-1} in the spectrum of the coordination compound. These bands can be assigned to the asymmetric and symmetric stretching vibrations of coordinated carboxylate groups, consistent with their involvement in metal coordination. An absorption band around 1480 cm^{-1} is present in the spectra of the coordination compound as well as in both linker derivatives and can be attributed to the C=C stretching vibrations of the aromatic rings of the pdi linker. Additional bands observed in the region between 1300 and 1400 cm^{-1} can be assigned to C–O stretching vibrations of the carboxylate or ester groups, potentially overlapping with contributions from C–N stretching modes. Furthermore, a strong absorption band in the coordination compound around 1390 cm^{-1} can be attributed to the C–N stretching vibration of coordinated DMF molecules, confirming the presence of DMF in the coordination environment. The broad absorption observed above 3300 cm^{-1} can be assigned to O–H stretching vibrations of lattice water molecules.

Section S5 Overview of the conducted studies

Table S2. Overview of the metal salts, linkers, any additives or modulators, temperatures, metal-to-linker ratio, and results used.

Metal salt $Co(NO_3)_2 \cdot 6\ H_2O$ (giving [Co(pdb)(DMF)])								
Sample	**Metal salt [mg]**	**H_2pdb [mg]**	**DABCO [mg]**	**Acid (20 µL)**	**Temperature [°C]**	**Molar M:L ratio**	**Results**	**Yields [%]**
1	20	15			100	2:1	Dark red crystals	69
2	20	15	3.9		100	2:1	Dark red crystals	40
3	16	12			100	2:1	Dark red crystals	38
4	16	11.9			100	2:1	Dark red crystals	38
5	14.7	11			100	2:1	Dark red crystals	37
6	15.3	11.5			100	2:1	Dark red crystals	42
7	14.7	11	2.9		100	2:1	Dark red crystals	36
8	15.3	11.5		HCl	100	2:1	PXRD H_2pdb linker	-
9	15.7	11.6		TFA	100	2:1	Dark red crystals	34
10	16.1	12.1		HAc	100	2:1	Dark red crystals	42
11	18.8	14			100	2:1	Dark red crystals	49
12	15.7	11.8			100	2.1	Dark red crystals	46
13	18.8	14.1			100	2:1	Dark red crystals	48
Metal salt $CoSO4 \cdot 7\ H_2O$								
Sample	**Metal salt [mg]**	**H_2pdb [mg]**	**DABCO [mg]**	**Acid (20 µL)**	**Temperature [°C]**	**Molar M:L ratio**	**Results**	**Yields [%]**
1	3.2	10		TFA	120	1:3	PXRD H_2pdb linker	-
Metal salt $CoCl_2 \cdot 6\ H_2O$								
Sample	**Metal salt [mg]**	**H_2pdb [mg]**	**DABCO [mg]**	**Acid (20 µL)**	**Temperature [°C]**	**Molar M:L ratio**	**Results**	**Yields [%]**
1	2.7	15	1.3	HAc	100	1:3	PXRD H_2pdb linker	-
2	2.7	15		HAc	120	1:3	PXRD H_2pdb linker	-
3	2.7	15	1.3	HCl	100	1:3	PXRD H_2pdb linker	-
4	2.7	15	1.3	TFA	120	1:3	PXRD H_2pdb linker	-
5	2.7	15	1.3		120	1:3	PXRD H_2pdb linker	-
Metal salt $Co(NO_3)_2 \cdot 6\ H_2O$ (giving $[Co(pdi)(DMF)_3] \cdot 2(DMF) \cdot H_2O$)								
Sample	**Metal salt [mg]**	**H_4pdi [mg]**	**DABCO [mg]**	**Acid (20 µL)**	**Temperature [°C]**	**Molar M:L ratio**	**Results**	**Yields [%]**
1	20	15			100	2:1	Dark red crystals	62
2	20	15	3.9		100	2:1	Dark red crystals	49
3	16	12			100	2:1	Dark red crystals	39
4	16	11.9			100	2:1	Dark red crystals	31
5	14.7	11			100	2:1	Dark red crystals	34
6	15.3	11.5			100	2:1	Dark red crystals	31
7	14.7	11	2.9		100	2:1	Dark red crystals	29
8	15.3	11.5		HCl	100	2:1	PXRD H_4pdi linker	-
9	15.7	11.6		TFA	100	2:1	Dark red crystals	34
10	16.1	12.1		HAc	100	2:1	Dark red crystals	40
11	18.8	14			100	2:1	Dark red crystals	59
12	15.7	11.8			100	2.1	Dark red crystals	47

13	18.8	14.1			100	2:1	Dark red crystals	67
14	17.5	15			120	2:1	Dark red crystals	72
15	17.5	15	3.3		120	2:1	Dark red crystals	59
16	21	18			120	2:1	Dark red crystals	57
17	20.3	17.5			120	2:1	Dark red crystals	58
Metal salt: $Zn(NO_3)_2{\cdot}6\,H_2O$								
Sample	**Metal salt [mg]**	**H_2pdb [mg]**	**DABCO [mg]**	**Acid (20 µL)**	**Temperature [°C]**	**Molar M:L ratio**	**Results**	**Yields [%]**
1	17	25			100	1:1	PXRD H_2pdb linker	-
2	34	25			100	2:1	PXRD H_2pdb linker	-
3	51	25			100	3:1	PXRD H_2pdb linker	-
4	13	50			100	1:2	PXRD H_2pdb linker	-
5	13	75			100	1:3	PXRD H_2pdb linker	-
6	6.8	20			120	1:2	PXRD H_2pdb linker	-
7	6.8	20		HCl	120	1:2	PXRD H_2pdb linker	-
8	6.8	20		HAc	120	1:2	PXRD H_2pdb linker	-
9	3.4	10		TFA	120	1:2	PXRD H_2pdb linker	-
10	6.8	30			120	1:3	PXRD H_2pdb linker	-
11	6.8	30		HCl	120	1:3	PXRD H_2pdb linker	-
12	6.8	30		HAc	120	1:3	PXRD H_2pdb linker	-
13	6.8	30		TFA	120	1:3	PXRD H_2pdb linker	-
14	3.4	15	1.3		120	1:3	PXRD H_2pdb linker	-
15	3.4	15	1.3	HCl	120	1:3	PXRD H_2pdb linker	-
16	3.4	15	1.3	HAc	80	1:3	Yellow crystals[1]	36
17	4.2	15.2	1.6	HAc	80	1:3	Yellow crystals[1]	34
18	7.4	30.5	3.0	HAc	80	1:3	Yellow crystals[1]	38
19	3.4	15	1.3	TFA	120	1:3	PXRD H_2pdb linker	-
Metal salt: $Zn(NO_3)_2{\cdot}6\,H_2O$								
Sample	**Metal salt [mg]**	**H_4pdi [mg]**	**DABCO [mg]**	**Acid (20 µL)**	**Temperature [°C]**	**M:L ratio**	**Results**	**Yields [%]**
1	17.5	15			120	2:1	Dark yellow crystals	45
2	17.5	15	3.3		120	2:1	Dark yellow crystals	40
3	21	18			120	2:1	Dark yellow crystals	38
4	20.3	17.5			120	2:1	Dark yellow crystals	37
Metal salt: $ZrCl_4$								
Sample	**Metal salt [mg]**	**H_2pdb [mg]**	**DABCO [mg]**	**Acid (20 µL)**	**Temperature [°C]**	**Molar M:L ratio**	**Results**	**Yields [%]**
1	13.3	25			100	1:1	PXRD H_2pdb linker	-
2	26.6	25			100	2:1	Amorphous solid	60
3	39.9	25			100	3:1	Amorphous solid	68
4	13.3	50			100	1:2	Amorphous solid	50
5	13.3	75			100	1:3	Amorphous solid	55
6	5.3	20			120	1:2	Amorphous solid	54
7	5.3	20		HCl	120	1:2	Amorphous solid	49
8	5.3	20		HAc	120	1:2	PXRD H_2pdb linker	-
9	2.7	10		TFA	120	1:2	Amorphous solid	61

10	5.3	30			120	1:3	Amorphous solid	49
11	5.3	30		HCl	120	1:3	Amorphous solid	45
12	5.3	30		HAc	120	1:3	Amorphous solid	46
13	5.3	30		TFA	120	1:3	Amorphous solid	39
Metal salt: $ZrOCl_2 \cdot 8\ H_2O$								
Sample	**Metal salt [mg]**	**H_2pdb [mg]**	**DABCO [mg]**	**Acid (20 µL)**	**Temperature [°C]**	**Molar M:L ratio**	**Results**	**Yields [%]**
1	18	25			100	1:1	Amorphous solid	58
2	36	25			100	2:1	Amorphous solid	49
3	54	25			100	3:1	Amorphous solid	61
4	18	50			100	1:2	Amorphous solid	55
5	18	75			100	1:3	Amorphous solid	51
6	7.4	20			120	1:2	Amorphous solid	54
7	7.4	20		HCl	120	1:2	Amorphous solid	49
8	7.4	20		HAc	120	1:2	Amorphous solid	42
9	3.7	10		TFA	120	1:2	Amorphous solid	42
10	7.4	30			120	1:3	Amorphous solid	47
11	7.4	30		HCl	120	1:3	Amorphous solid	51
12	7.4	30		HAc	120	1:3	Amorphous solid	50
13	7.4	30		TFA	120	1:3	Amorphous solid	48
Metal salt: $AlCl_3 \cdot 6\ H_2O$								
Sample	**Metal salt [mg]**	**H_2pdb [mg]**	**DABCO [mg]**	**Acid (20 µL)**	**Temperature [°C]**	**Molar M:L ratio**	**Results**	**Yields [%]**
1	5.5	20			120	1:2	Amorphous solid	60
2	5.5	20		HCl	120	1:2	Amorphous solid	57
3	5.5	20		HAc	120	1:2	Amorphous solid	59
4	2.6	10		TFA	120	1:2	Amorphous solid	49
5	5.5	30			120	1:3	Amorphous solid	48
6	5.5	30		HCl	120	1:3	Amorphous solid	48
7	5.5	30		HAc	120	1:3	Amorphous solid	46
8	5.5	30		TFA	120	1:3	Amorphous solid	48
Metal salt: $NiSO_4 \cdot 6\ H_2O$								
Sample	**Metal salt [mg]**	**H_2pdb [mg]**	**DABCO [mg]**	**Acid (20 µL)**	**Temperature [°C]**	**Molar M:L ratio**	**Results**	**Yields [%]**
1	3	15		TFA	120	1:3	PXRD H_2pdb linker	-
Metal salt: $Ni(NO_3)_2$								
Sample	**Metal salt [mg]**	**H_2pdb [mg]**	**DABCO [mg]**	**Acid (20 µL)**	**Temperature [°C]**	**Molar M:L ratio**	**Results**	**Yields [%]**
1	16.6	25			100	1:1	PXRD H_2pdb linker	-
2	33.2	25			100	2:1	PXRD H_2pdb linker	-
3	49.8	25			100	3:1	PXRD H_2pdb linker	-
4	16.6	50			100	1:2	PXRD H_2pdb linker	-
5	16.6	75			100	1:3	PXRD H_2pdb linker	-
6	6.7	20			120	1:2	PXRD H_2pdb linker	-
7	6.7	20		HCl	120	1:2	PXRD H_2pdb linker	-
8	6.7	20		HAc	120	1:2	PXRD H_2pdb linker	-
9	1.6	10		TFA	120	1:4	Light yellow solid	40
Metal salt: $NiCl_2 \cdot 6\ H_2O$								

Sample	Metal salt [mg]	H_2pdb [mg]	DABCO [mg]	Acid (20 µL)	Temperature [°C]	Molar M:L ratio	Results	Yields [%]
1	5.4	20		TFA	120	1:2	PXRD H_2pdb linker	-
2	5.4	30		HCl	120	1:3	PXRD H_2pdb linker	-
3	5.4	30		HAc	120	1:3	PXRD H_2pdb linker	-
4	5.4	30		TFA	120	1:3	PXRD H_2pdb linker	-
5	5.4	30			120	1:3	PXRD H_2pdb linker	-
Metal salt: $CuCl_2 \cdot H_2O$								
Sample	**Metal salt [mg]**	**H_2pdb [mg]**	**DABCO [mg]**	**Acid (20 µL)**	**Temperature [°C]**	**Molar M:L ratio**	**Results**	**Yields [%]**
1	3	20			120	1:2	PXRD H_2pdb linker	-
2	3	20		HCl	120	1:2	PXRD H_2pdb linker	-
3	3	20		HAc	120	1:2	PXRD H_2pdb linker	-
4	1.5	10		TFA	120	1:2	PXRD H_2pdb linker	-
5	3.1	30			120	1:3	PXRD H_2pdb linker	-
6	3.1	30		HCl	120	1:3	PXRD H_2pdb linker	-
7	3.1	30		HAc	120	1:3	PXRD H_2pdb linker	-
8	3.1	30		TFA	120	1:3	PXRD H_2pdb linker	-

Results with "PXRD H_2pdb linker" or with "PXRD H_4pdi linker" mean that the measured PXRD shows the same reflections as the pure linker and no reflections were measured for "amorphous solid." The PXRD pattern which shows only reflections of the free linker indicates that no crystalline coordination polymer was formed under these conditions and that the linker recrystallized from the reaction mixture. The absence of reflections of the metal salt is attributed to the fact that the metal precursor remained dissolved as solvated species in the mother liquor (and/or in an amorphous form), which is not detectable by PXRD. Powder diffraction therefore only reflects the crystalline solid phase present after the reaction, namely the unreacted linker.

3 mL of DMF (*N*,*N*-dimethylformamide) was used in each reaction. Used acids: HCl = hydrochloric acid (c = 12 mol/L); HAc = acetic acid (neat); TFA = trifluoroacetic acid (neat).

When DABCO was used in the syntheses, a molar ratio of 1 relative to the linker was used.

Some approaches were repeated for reproduction purposes.

In some experiments, different acids were tested as modulators. Acidic modulators have been reported in the literature for the synthesis of such coordination polymers (especially MOFs), as they influence nucleation and crystallization kinetics and, through competitive coordination to the metal centers, can control framework formation and defect generation. The variation referred to the identity of the acid in order to examine how differences in coordination strength and steric properties affect framework assembly.

Section S6 Crystal photographs and crystal structure images

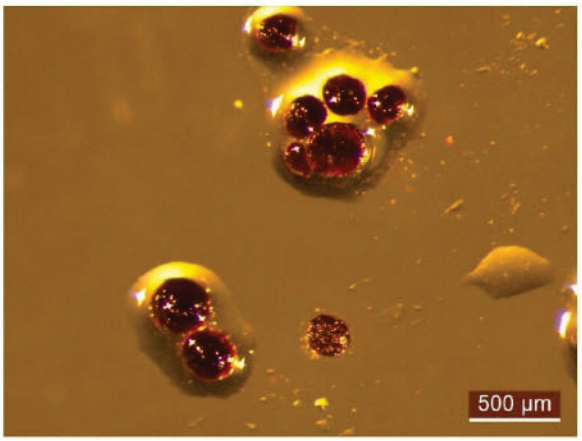


Figure S12. Light microscope photograph of [Co(pdb)(DMF)].

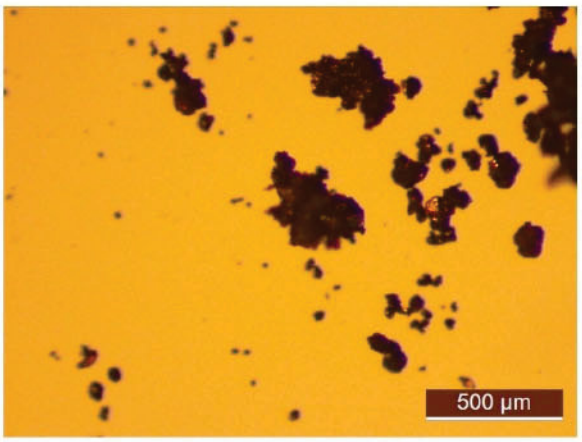


Figure S13. Light microscope photograph of $[Co_2(pdi)(DMF)_3]\cdot 2(DMF)\cdot H_2O$.

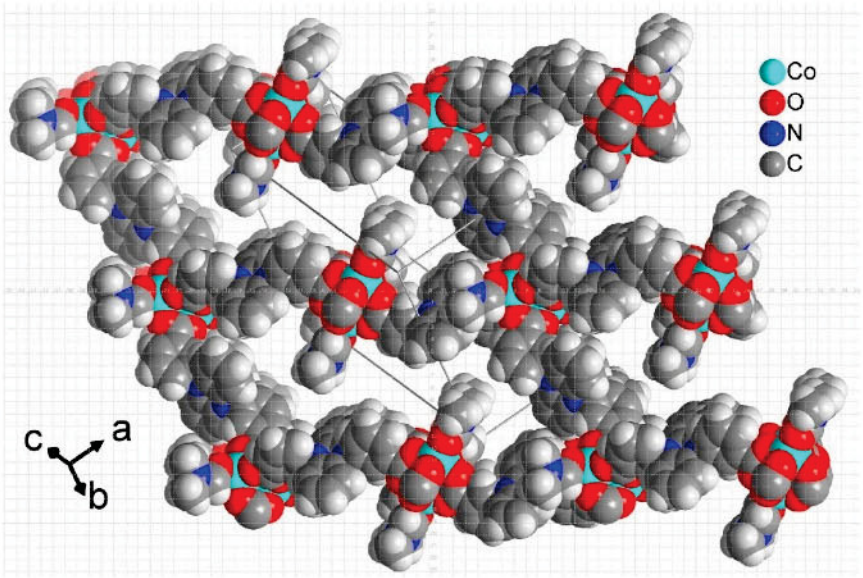


Figure S14. Space-filling view of the [Co(pdb)(DMF)] network with hydrogen atoms included. The edges of the square in the underyling grid are 1 Å.

Section S7 PXRD

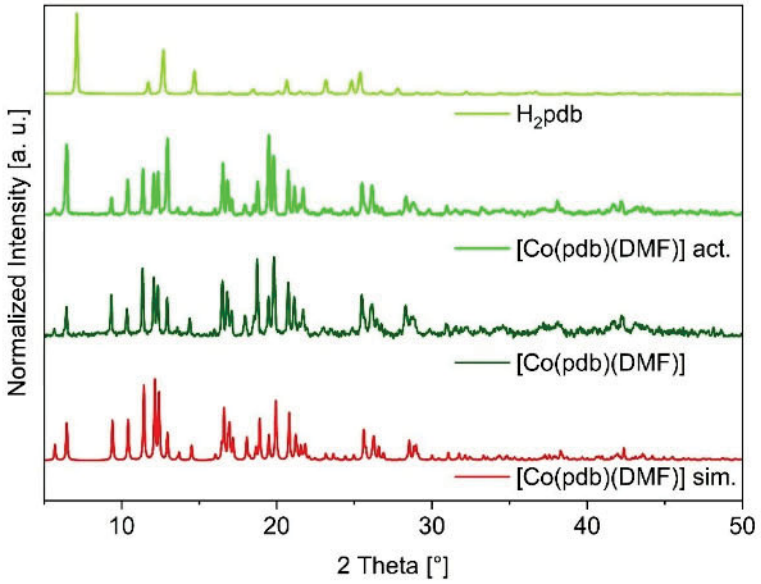


Figure S15. Powder X-ray diffraction pattern of dimethyl-3,3'-(phenazine-5,10-diyl)dibenzoate (H_2pdb) (yellow-green), simulated (sim.) (red) and experimental powder X-ray diffraction patterns of [Co(pdb)(DMF)] before (olive green) and after activation (light green). Activation was done on the pre-dried sample (12 h at 60 °C under vacuum) for 3 h at 130 °C under turbomolecular pump vacuum ($5 \cdot 10^{-12}$ bar).

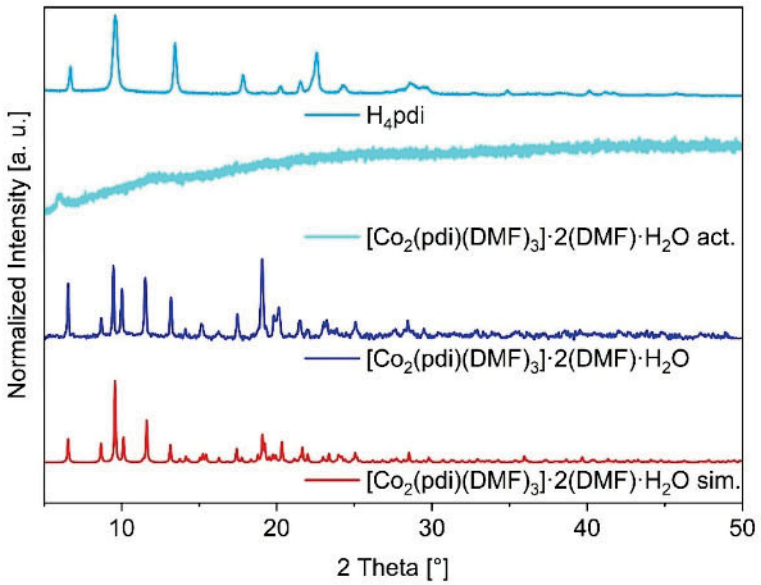
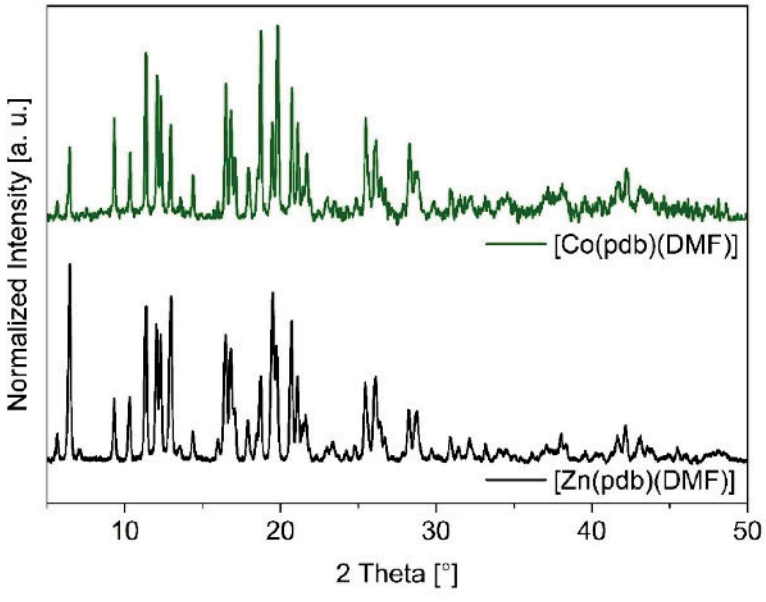
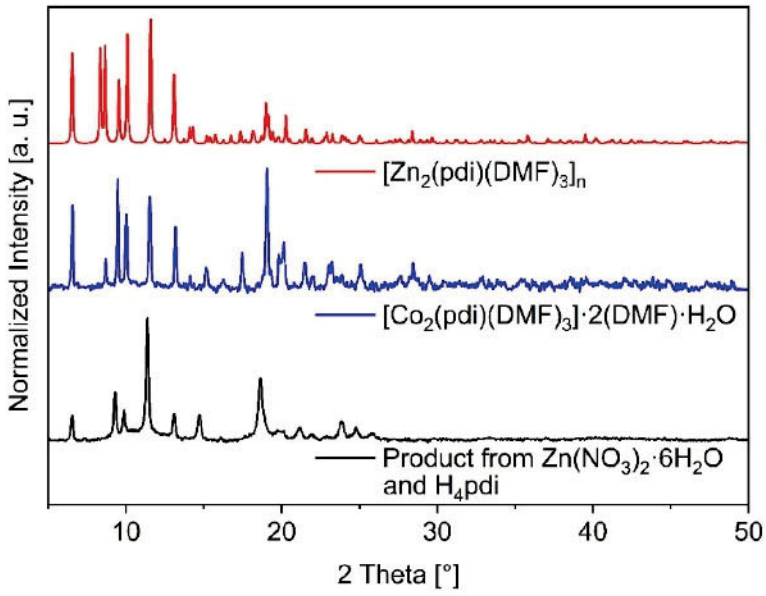


Figure S16. Powder X-ray diffraction pattern of 5,5'-(phenazine-5,10-diyl)diisophthalic acid (H_4pdi) (light blue), simulated (sim.) (red) and experimental powder X-ray diffraction patterns of [Co_2(pdi)(DMF)$_3$]·2(DMF)·H_2O before (dark blue) and after acitvation (cyan). Activation was done on the pre-dried sample (12 h at 60 °C under vacuum) for 3 h at 130 °C under turbomolecular pump vacuum ($5 \cdot 10^{-12}$ bar). Also, milder activation conditions (16 h at 60 °C under vacuum) yielded an amorphous product with a featureless PXRD pattern.



a)



b)

Figure S17. (a) Powder X-ray diffraction patterns of [Co(pdb)(DMF)] (olive green) and the isostructural zinc complex from the reaction of $Zn(NO_3)_2 \cdot 6\ H_2O$ and H_2pdb (black); (b) Powder X-ray diffraction patterns of $[Co_2(pdi)(DMF)_3] \cdot 2(DMF) \cdot H_2O$ (blue), the isostructural zinc complex from the reaction of $Zn(NO_3)_2 \cdot 6\ H_2O$ and H_4pdi (black) and isostructural $[Zn_2(pdi)(DMF)_3]_n$ (red) from the literature (where the linker is denoted as PDPA) [1]. The crystal solvent in the publication of the 298 K structure of $[Zn_2(pdi)(DMF)_3]_n$ had been omitted and was not refined.

The experimental PXRD of [Co(pdb)(DMF)] and the resulting zinc complex showed a matching pattern with reflections at the same 2θ angles and of similar intensity (Figure S17a) which verified that the structures are isostructural with each other.

Section S8 Thermogravimetric analyses

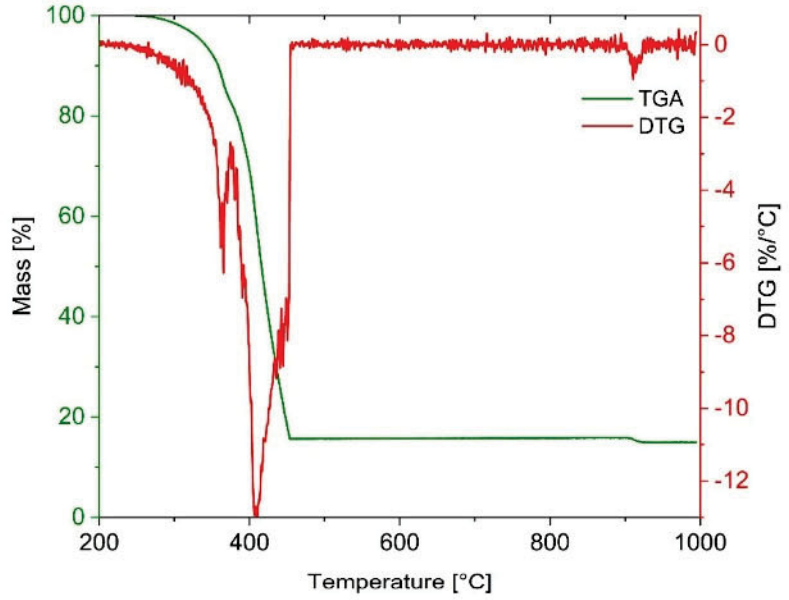


Figure S18. TGA and DTG of [Co(pdb)(DMF)] under synthetic air after drying for 14 h at 180 °C and handling under vacuum (10^{-3} bar), heating rate 10 K min^{-1}. The minor mass decrease observed at temperatures above ~900 °C can be attributed to the thermal transformation of cobalt(II,III) oxide, Co_2O_3 to cobalt(II) oxide, CoO, which is known to occur at elevated temperatures and would correspond to only a small mass change [2].

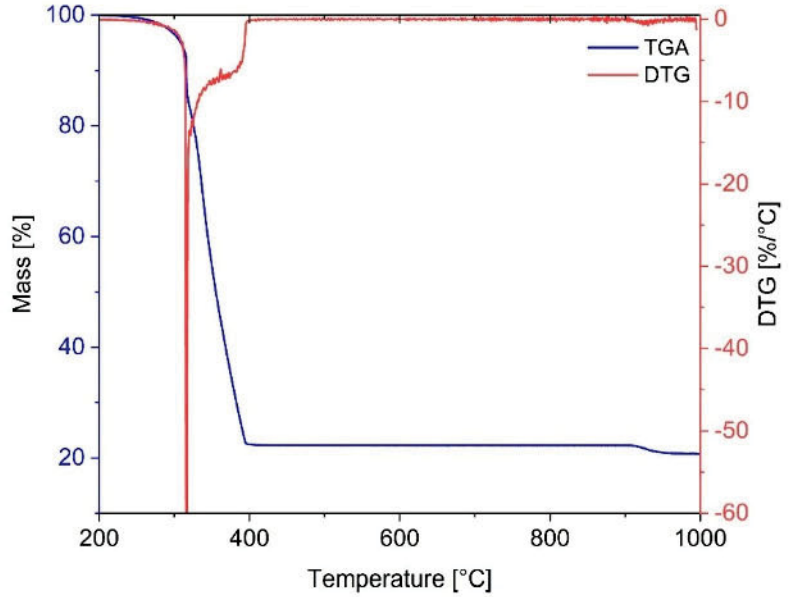


Figure S19. TGA and DTG of $[Co_2(pdi)(DMF)_3]\cdot 2(DMF)\cdot H_2O$ under synthetic air after drying for 14 h at 180 °C under vacuum (10^{-3} bar), heating rate 10 K min^{-1}. The minor mass decrease observed at temperatures above ~900 °C can be attributed to the thermal transformation of cobalt(II,III) oxide, Co_2O_3 to cobalt(II) oxide, CoO, which is known to occur at elevated temperatures and would correspond to only a small mass change [2].

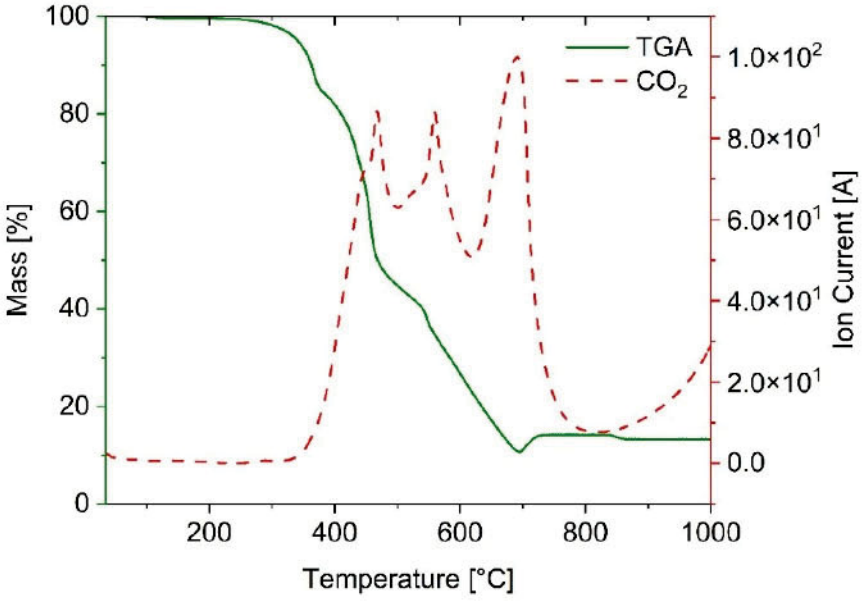


Figure S20. TGA coupled with mass spectrometry, TG-MS of [Co(pdb)(DMF)] (carried out under nitrogen, heating rate 10 K min^{-1}). The sample was dried for 14 h at 180 °C under vacuum (10^{-3} bar).

The coupled TGA–MS measurement of [Co(pdb)(DMF)] under nitrogen reveals a framework decomposition dominated by decarboxylation and subsequent carbonization. Below 200 °C, only a negligible mass loss is observed and no CO_2 evolution is detected, indicating the absence of significant solvent release or linker degradation. The onset of decomposition occurs at approximately 300-350 °C, followed by a first sharp and then more gradual mass-loss between ca. 420 and 690 °C, which coincides with CO_2 evolution from decarboxylation and is assigned to the decomposition of the organic linker. Above ~750-800 °C, gas evolution ceases and a stable cobalt-oxide residue remains with 14-15 wt%, consistent with the formation of cobalt oxide CoO (theor. 14 wt% for CoO, 15 wt% for Co_2O_3, 11 wt% for Co). Although the measurement was carried out under nitrogen, cobalt oxide species can form due to oxygen originating from the carboxylate groups (internal oxygen source) during thermal decomposition. On the other hand, the dip in mass% at 700 °C is probably due to the initial formation of cobalt metal under the nitrogen atmosphere which then forms cobalt oxide by reacting with oxygen impurities in the nitrogen purge gas giving the mass% gain with increasing temperature.

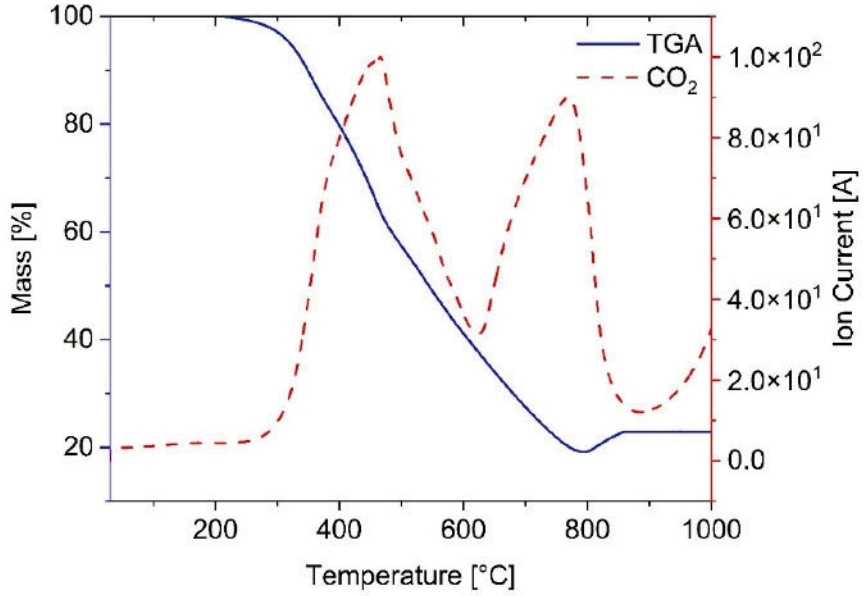


Figure S21. TGA coupled with mass spectrometry, TG-MS of $[Co_2(pdi)(DMF)_3]\cdot 2(DMF)\cdot H_2O$ (carried out under nitrogen, heating rate 10 K min^{-1}). The sample was dried for 14 h at 180 °C under vacuum (10^{-3} bar).

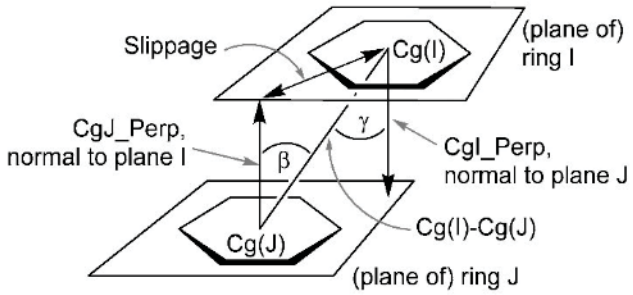
The coupled TGA-MS analysis of $[Co_2(pdi)(DMF)_3]$ starts with the first mass loss at ~300 °C due to the loss of the coordinated DMF (theor. 26 wt%) and continues without a plateau to ~790 °C with degradation of the organic linker (theor. 60 wt%). A concomitant CO_2 evolution from decarboxylation underscores the decomposition of the organic linker. At 1000 °C, a residue of 21 wt% remains (theor. 18 wt%, 20 wt% for Co_2O_3, 14 wt% for Co) which may also include a carbonaceous matrix still present under the nitrogen atmosphere. The dip in mass% at just below 800 °C is probably due to the initial formation of cobalt metal under the nitrogen atmosphere which then forms cobalt oxide by reacting with oxygen impurities in the nitrogen purge gas giving the mass% gain with increasing temperature.

Section S9 Supramolecular analyses

The supramolecular analyses for possible π–π, C–H-π and C–H···O interactions was carried out with the program PLATON [3]

a) Analysis for compound [Co(pdb)(DMF)]

The PLATON-listing "Analysis of Short Ring-Interactions" for possible π-stacking interactions yielded a single long π-stacking contact for [Co(pdb)(DMF)].
For comparison, "strong" π-stacking interactions have rather short centroid-centroid contacts (<3.8 Å), near parallel ring planes (alpha < 10° to ~0° or even exactly 0° by symmetry), small slip angles (β, γ <25°) and vertical displacements (slippage <1.5 Å) which translate into a sizable overlap of the aryl-plane areas (Scheme S6, Table S3, Figure S22) [4,5].



Scheme S6. Graphical presentation of the parameters used for the description of π-π stacking.

Table S3. Packing analysis for possible π-stacking interactions in [Co(pdb)(DMF)].

==========

Analysis of short ring-interactions with Cg-Cg distances < 4.0 Ang., Alpha < 20.000 Deg. and Beta < 60.0 Deg.

==========

- Cg(I) = Plane number I (= ring number in () above)
- Alpha = Dihedral Angle between Planes I and J (Deg)
- Beta = Angle Cg(I)-->Cg(J) or Cg(I)-->Me vector and normal to plane I (Deg)
- Gamma = Angle Cg(I)-->Cg(J) vector and normal to plane J (Deg)
- Cg-Cg = Distance between ring Centroids (Ang.)
- CgI_Perp = Perpendicular distance of Cg(I) on ring J (Ang.)
- CgJ_Perp = Perpendicular distance of Cg(J) on ring I (Ang.)
- Slippage = Distance between Cg(I) and Perpendicular Projection of Cg(J) on Ring I (Ang).

Cg(I)	Cg(J)	[ARU(J)]	Cg-Cg	Alpha	Beta	Gamma	CgI_Perp	CgJ_Perp	Slippage
Cg5	Cg5	[2456.01]	3.966(3)	16.5(2)	17.5	17.5	3.782(2)	3.782(2)	1.195

[2456] = iv = -1/2-X, Y, 1-Z

Cg5 = centroid of ring C14-C15-C16-C17-C18-C19

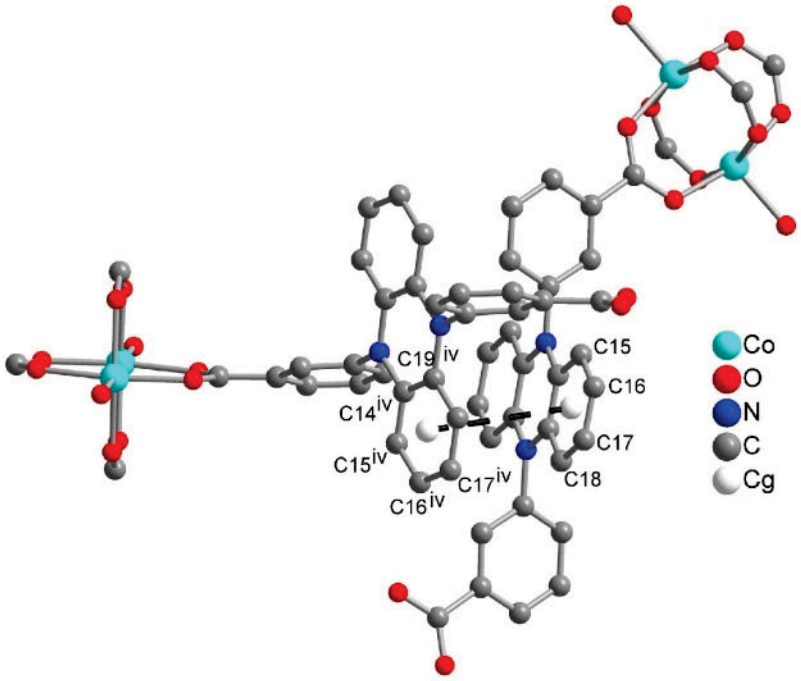
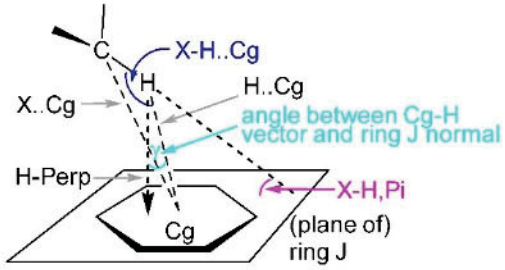


Figure S22. π-π interactions in the packing of [Co(pdb)(DMF)] in the crystal, indicated as a dashed black line with the centroid-centroid contact of 3.966 Å. Further details of this π-π interaction, are listed in the above Table S3 (Cg = ring centroid). Symmetry transformation iv = -1/2-X, Y, 1-Z.

Limited C-H···π contacts were found for [Co(pdb)(DMF)].

Significant intermolecular C-H···π contacts start below around 2.7 Å for the (C-)H···ring centroid distances with H-perp also starting at below 2.6-2.7 Å and C-H··Cg > 145° (Scheme S7, Table S4, Figure S23 [6,7].



Scheme S7. Graphical presentation of the parameters used for the description of CH-π interactions.

Table S4. Analysis of *inter*molecular C–H...Cg(pi-ring) interactions (H..Cg < 3.0 Ang. - Gamma < 30.0 Deg) in [Co(pdb)(DMF)].

- Cg(J) = Center of gravity of ring J (Plane number above)

- H-Perp = Perpendicular distance of H to ring plane J

- Gamma = Angle between Cg-H vector and ring J normal

- X-H..Cg = X-H-Cg angle (degrees)

- X..Cg = Distance of X to Cg (Angstrom)

- X-H, Pi = Angle of the X-H bond with the Pi-plane (i.e.' Perpendicular = 90 degrees, Parallel = 0 degrees)

C--H(I)	Cg(J)	[ARU(J)]	H..Cg	H-Perp	Gamma	X-H..Cg	X..Cg	X-H,Pi
C9 -H9	Cg3	[4475.01]	2.72	2.53	22	150	3.571(8)	78
C21 -H21	Cg5	[4465.01]	2.83	2.69	18	137	3.565(9)	4

[4475] = v = -1/2+X, 2-Y, Z

[4465] = vi = -1/2+X, 1-Y, Z

Cg3 = centroid of ring C1-C2-C3-C4-C5-C6

Cg5 = centroid of ring C14-C15-C16-C17-C18-C19

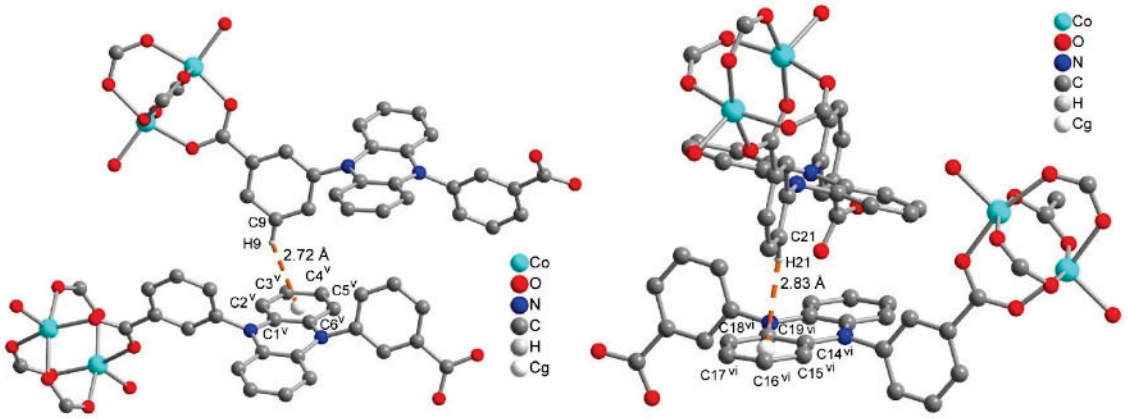


Figure S23. C-H···π interactions in the packing of [Co(pdb)(DMF)] in the crystal, indicated as dashed orange lines with the H-centroid distance. Further details of these C-H···π interactions are listed in the above Table S4 (Cg = ring centroid). Symmetry transformations v = -1/2+X, 2-Y, Z, vi = -1/2+X, 1-Y, Z.

Table S5. Packing analysis for possible C–H···O interactions in [Co(pdb)(DMF)].

==========

Analysis of Potential Hydrogen Bonds and Schemes with d(D...A) < R(D)+R(A)+0.50, d(H...A) < R(H)+R(A)-0.12 Ang., D-H...A > 100.0 Deg

==========

Note: - ARU codes in [] are with reference to the Coordinates printed above (Possibly transformed, when MOVE /= 1.555)

==========

Donor --- H....Acceptor	[ARU]	D - H	H...A	D...A	D - H...A
C3 --H3 O4	[1655.01]	0.95	2.57	3.377(6)	143
C27 --H27 O4	[7566.01]	0.95	2.50	3.122(6)	123

C28	--H28A	O3	[4565.01]	0.98	2.57	3.257(6)	127

[7566.] = [7_566] = i = 1/2-x, 3/2-y, 3/2-z

[4565.] = [6_665] = vii = 1/2+x, 1-y, z

[1655.] = [1_655] = viii = 1+x, y, z

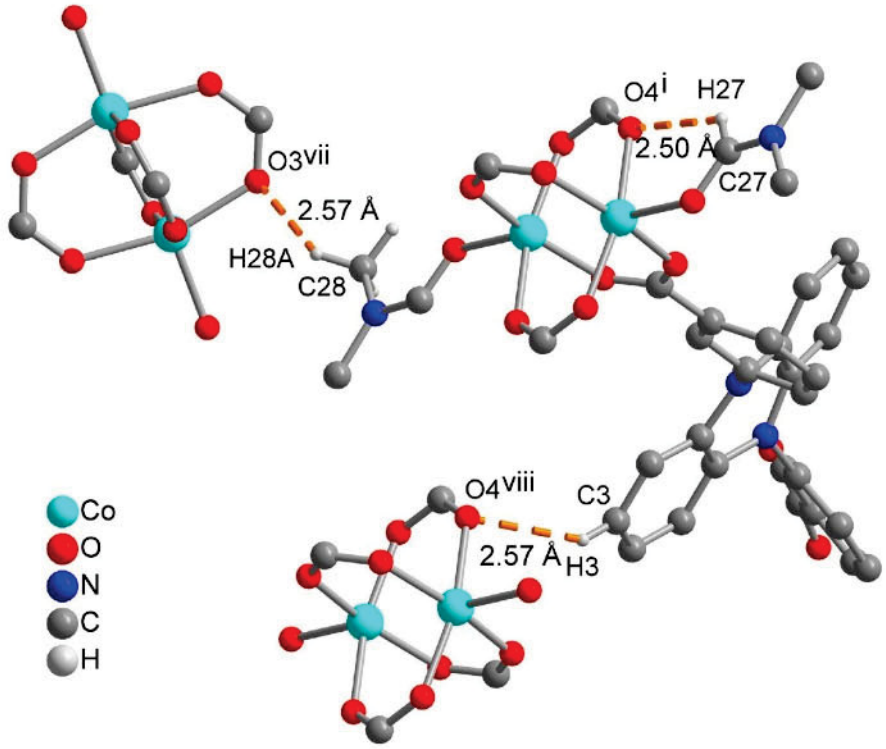


Figure S24. C-H···O contacts in the packing of [Co(pdb)(DMF)] in the crystal, indicated as dashed orange lines with the H···O distances. Further details of these C-H···O interactions, including the symmetry transformations are listed in the above Table S5.

b) Analysis for compound $[Co_2(pdi)(DMF)_3]\cdot 2(DMF)\cdot H_2O$

See also the general comments on the distances and angles of π–π and C–H-π interactions given in the analysis for compound [Co(pdb)(DMF)]

The PLATON-listing "Analysis of Short Ring-Interactions" for possible π-stacking interactions yielded no π-stacking contact with a centroid-centroid distance of less than 4.0 Å for $[Co_2(pdi)(DMF)_3]\cdot 2(DMF)\cdot H_2O$. The shortest centroid-centroid distance was 4.78 Å.

Also, limited C-H···π contacts were found for $[Co_2(pdi)(DMF)_3]\cdot 2(DMF)\cdot H_2O$.

Table S6. Analysis of *inter*molecular C–H...Cg(pi-ring) interactions (H..Cg < 3.0 Ang. - Gamma < 30.0 Deg) in $[Co_2(pdi)(DMF)_3]\cdot 2(DMF)\cdot H_2O$.

- Cg(J) = Center of gravity of ring J (Plane number above)
- H-Perp = Perpendicular distance of H to ring plane J
- Gamma = Angle between Cg-H vector and ring J normal
- X-H..Cg = X-H-Cg angle (degrees)
- X..Cg = Distance of X to Cg (Angstrom)
- X-H, Pi = Angle of the X-H bond with the Pi-plane (i.e.' Perpendicular = 90 degrees, Parallel = 0 degrees)

C–H(I)	Cg(J)	[ARU(J)]	H..Cg	H-Perp	Gamma	X-H..Cg	X..Cg	X-H,Pi
C36 -H36A	Cg11	[2664.01]	2.82	2.79	8.4	144	3.658(10)	51
C37 -H37A	Cg11	[4465.01]	2.96	2.80	19	130	3.668(10)	33
C41 -H41	Cg12	[1555.01]	2.88	2.85	7.7	149	3.726(10)	64

[2664] = ii = 1-X, 1-Y, -1/2+Z

[4465] = i = -1/2+X, 3/2-Y, Z

[1555] = X, Y, Z

Cg11 = centroid of ring C1-C2-C3-C4-C5-C6

Cg12 = centroid of ring C7-C8-C9-C10-C11-C12

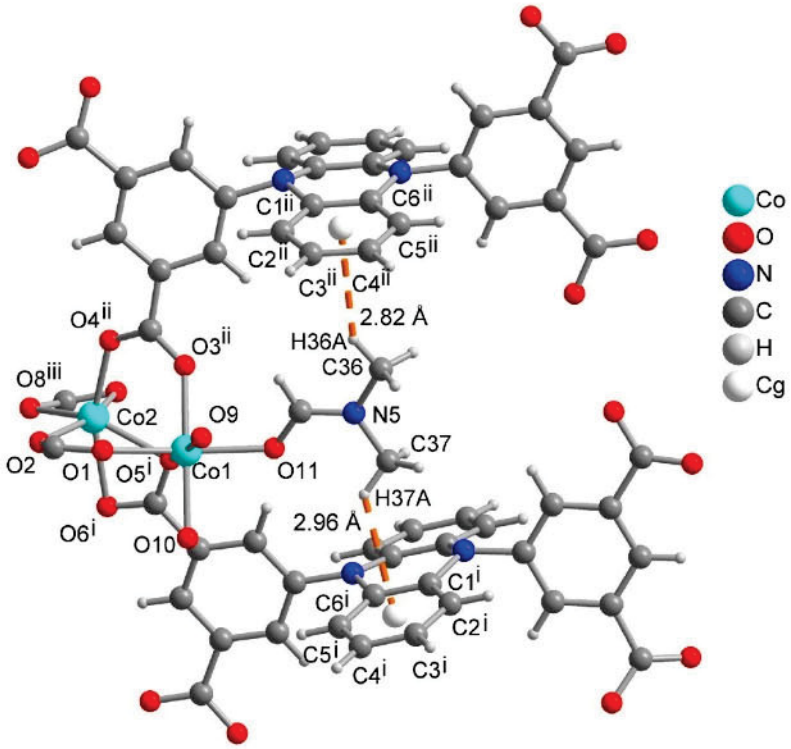


Figure S25. C-H···π interactions in the packing of $[Co_2(pdi)(DMF)_3]\cdot 2(DMF)\cdot H_2O$ in the crystal, indicated as dashed orange lines with the H-centroid distances. Further details of these C-H···π interactions are listed in the above Table S6 (Cg = ring centroid). Symmetry transformations i = $x-1/2$, $-y+3/2$, z; ii = $-x+1$, $-y+1$, $z-1/2$; iii = $-x+3/2$, $y+1/2$, $z-1/2$.

Table S7. Packing analysis for possible C–H···O interactions in $[Co_2(pdi)(DMF)_3]\cdot 2(DMF)\cdot H_2O$

Analysis of Potential Hydrogen Bonds and Schemes with d(D...A) < R(D)+R(A)+0.50, d(H...A) < R(H)+R(A)-0.12 Ang., D-H...A > 100.0 Deg

Note: - ARU codes in [] are with reference to the Coordinates printed above (Possibly transformed, when MOVE /= 1.555)

Donor --- H....Acceptor [ARU]	D - H	H...A	D...A	D - H...A
C14--H14 O14 [4565.04]	0.95	2.60	3.547(9)	175
C22--H22 O11 [4565.01]	0.95	2.42	3.300(6)	154
C29--H29 O3 [2664.01]	0.95	2.43	3.047(7)	122
C32--H32 O9 [ ]	0.95	2.55	3.130(9)	120
C33--H33B O12 [2675.02]	0.98	2.35	3.261(15)	154
C35--H35 O3 [2664.01]	0.95	2.49	3.028(6)	116
C36--H36B O14 [1555.04]	0.98	2.34	3.177(11)	143
C43--H43B O12 [1545.02]	0.98	2.53	3.483(14)	163

Note: the intramolecular C-H···O contacts within the DMF molecules, that is, from the CH_3 group to the aldehyde with acute C-H···O angles of less than 110° are not listed.

[2664.] = ii = 1-x, 1-y, -1/2+z

[4565.] = iv = 1/2+x, 3/2-y, z

[2675.] = v = 1-x, 2-y, 1/2+z

[1545.] = vi = x, -1+y, z

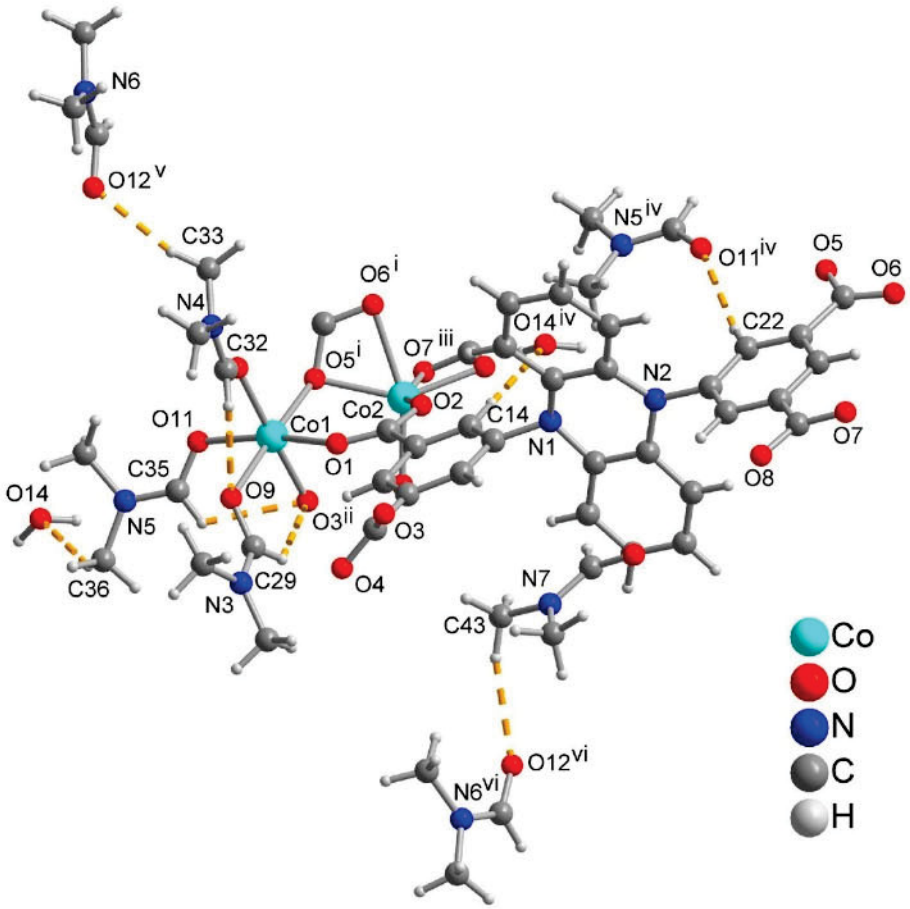
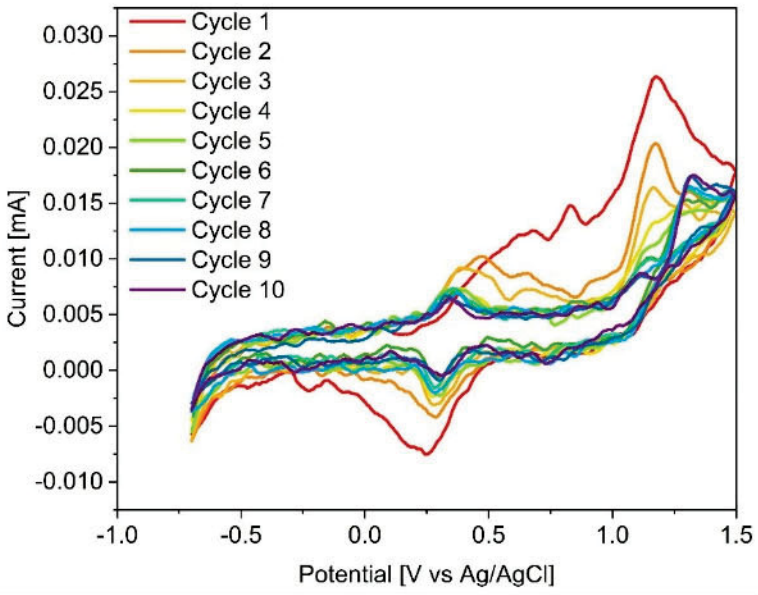
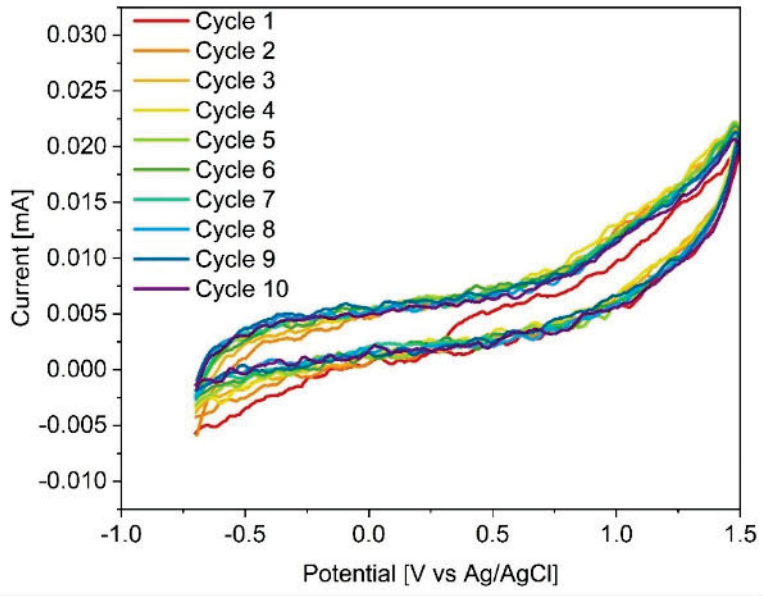


Figure S26. C-H···O contacts in the packing of $[Co_2(pdi)(DMF)_3]\cdot 2(DMF)\cdot H_2O$ in the crystal, indicated as dashed orange lines. Further details of these C-H···O interactions are listed in the above Table S7. Symmetry transformations i = *x*−1/2, -*y*+3/2, *z*; ii = −*x*+1, −*y*+1, *z*−1/2; iii = −*x*+3/2, *y*+1/2, *z*−1/2, iv = 1/2+x, 3/2-y, z; v = 1-x, 2-y, 1/2+z; vi = x, -1+y, z.

Section S10 Electrochemical measurements



a)



(b)

Figure S27. Cyclic voltammograms recorded over ten consecutive cycles for (a) [Co(pdb)(DMF)] and (b) $[Co_2(pdi)(DMF)_3]\cdot 2(DMF)\cdot H_2O$. In both cases, significant changes of the voltammetric response upon cycling or the absence of well-defined redox features are observed, indicating limited electrochemical stability and predominantly irreversible redox behavior.

1 Zhang, S.; Ma, X.-F.; Yang, Y.; Ren, H.; Li, W.; Liu, Y.; Xi, C.; Zheng, L.; Miao, Z. Phenazine-functionalized Zn-based metal organic framework for efficient visible light photocatalytic sulfides. *J. Solid State Chem.* **2025**, *351*, 125525. https://doi.org/10.1016/j.jssc.2025.125525.

2 Mandić, V.; Kurajica, S.; Plodinec, M.; Panžić, I. Thermal Stability and Utilization of 1D-Nanostructured Co_3O_4 Rods Derived by Simple Solvothermal Processing. *Catalysts* **2022**, *12* (10), 1162. https://doi.org/10.3390/catal12101162.

3 Spek, A. L. Structure Validation in Chemical Crystallography. *Acta Crystallogr. D* **2009**, *65*, 148–155. https://doi.org/10.1107/S090744490804362X.

4 Janiak, C. A Critical Account on π–π Stacking in Metal Complexes with Aromatic Nitrogen-Containing Ligands. J. Chem. *Soc., Dalton Trans.* **2000**, 3885–3896. https://doi.org/10.1039/b003010o.

5 Yang, X.-J.; Drepper, F.; Wu, B.; Sun, W.-H.; Haehnel, W.; Janiak, C. From Model Compounds to Protein Binding: Syntheses, Characterizations and Fluorescence Studies of $[Ru^{II}(Bipy)(Terpy)L]^{2+}$ Complexes (Bipy = 2,2′-Bipyridine; Terpy = 2,2′:6′,2″-Terpyridine; L = Imidazole, Pyrazole and Derivatives, Cytochrome c). *Dalton Trans.* **2005**, 256–267. https://doi.org/10.1039/B414999H.

6 Takahashi, O.; Kohno, Y.; Iwasaki, S.; Saito, K.; Iwaoka, M.; Tomoda, S.; Umezawa, Y.; Tsuboyama, S.; Nishio, M. Hydrogen-Bond-Like Nature of the CH/π Interaction as Evidenced by Crystallographic Database Analyses and Ab Initio Molecular Orbital Calculations, *Bull. Chem. Soc. Jpn.* **2001**, *74*, 2421–2430. https://doi.org/10.1246/bcsj.74.2421

7 Nishio, M.; Umezawa, Y.; Honda, K.; Tsuboyama, S.; Suezawa, H. CH/π Hydrogen Bonds in Organic and Organometallic Chemistry. *CrystEngComm* **2009**, *11*, 1757-1788. https://doi.org/10.1039/b902318f.

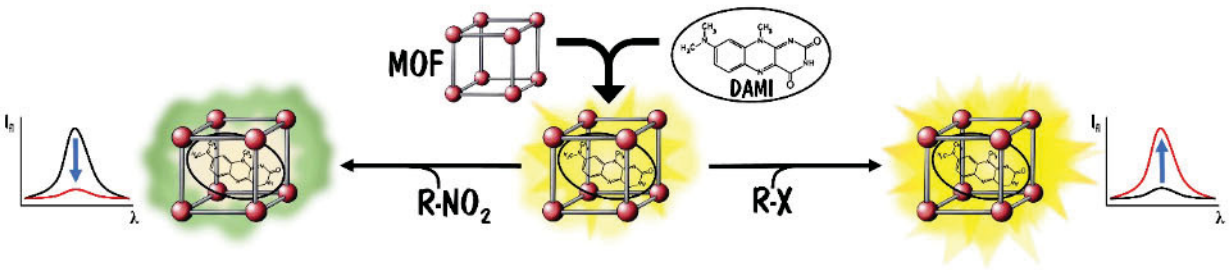
3.2 Investigations on the Luminescence Behavior of a Flavin Derivative Incorporated into Al-based Metal-Organic Frameworks for the Sensing of Aromatic Nitro Compounds

Diese Arbeit wurde veröffentlicht in

Annette Vollrath, Vasily Gvilava, Philipp Seiffert, Constantin Czekelius, Christoph Janiak, *Z. Anorg. Allg. Chem.* **2026**, e70183. DOI: 10.1002/zaac.70183; Ref. [90]

Kurzzusammenfassung

Die post-synthetische Einlagerung des Flavin-Derivats 8-(Dimethylamino)-10-methylisoalloxazin (DAMI) in die aluminiumbasierten Metall-organischen Gerüstverbindungen (MOFs) DUT-4, DUT-5 und MIL-53 wurde untersucht. Während DAMI im reinen Feststoff keine Fluoreszenz zeigt, tritt diese sowohl in Lösung als auch nach der Einlagerung in MOFs in Form einer „Festkörperlösung“ deutlich auf. Die erhaltenen DAMI@MOF-Komposite reagierten mit einer ausgeprägten Änderung ihrer Fluoreszenz auf die Adsorption verschiedener Gastmoleküle. Verbindungen mit Methylgruppen oder Chloratomen führten zu einer Verstärkung der Fluoreszenzintensität, wohingegen Nitroverbindungen (Nitrobenzol, 4-Nitrotoluol und 4-Nitrophenol) eine effektive Fluoreszenzlöschung bewirkten. Dieses Verhalten wurde auf die energetische Anpassung der Molekülorbitale von Farbstoff und Gastmolekül zurückgeführt, wodurch ein photoinduzierter Elektronentransfer (PET) ermöglicht wird. Elektronenakzeptierende Nitroverbindungen fördern dabei den Elektronentransfer vom angeregten DAMI auf das Gastmolekül und verursachen eine Fluoreszenzlöschung, während elektronendonierende Gastmoleküle Elektronen auf DAMI übertragen und dadurch die Fluoreszenz verstärken. Unter den untersuchten Verbindungen zeigte Nitrobenzol den stärksten Effekt und löschte bis zu 99 % der Fluoreszenz von DAMI@MOF unter einer mit Nitrobenzol gesättigten Atmosphäre bei 25 °C. Dies entsprach einer Dampfphasenkonzentration von etwa 14 µg/L, die aus einer 0,1 mg/mL Nitrobenzol-Lösung erzeugt wurde.



Anteile an der Veröffentlichung

- Konzeption des Forschungsvorhabens gemeinsam mit Prof. Dr. C. Janiak.
- Entwicklung der Methodik.
- Durchführung der experimentellen Untersuchungen gemeinsam mit Dr. V. Gvilava, P. Seiffert und Prof. Dr. C. Czekelius.
- Durchführung der Validierung, Datenaufbereitung sowie formalen Auswertung der experimentellen Ergebnisse.
- Selbstständige Auswertung, graphische Darstellung und Interpretation der experimentellen Ergebnisse.
- Anfertigung des Manuskripts (Erstentwurf) gemeinsam mit Prof. Dr. C. Janiak und Prof. Dr. C. Czekelius.
- Überarbeitung des Manuskripts gemeinsam mit Dr. V. Gvilava, Prof. Dr. C. Janiak und Prof. Dr. C. Czekelius.
- Wissenschaftliche Betreuung durch Prof. Dr. C. Janiak.
- Bereitstellung der Ressourcen, Projektadministration und Einwerbung der Drittmittel durch Prof. Dr. C. Janiak.

Zeitschrift für anorganische und allgemeine Chemie

Journal of Inorganic and General Chemistry
ZAAC
Zeitschrift für anorganische und allgemeine Chemie

RESEARCH ARTICLE OPEN ACCESS

Investigations on the Luminescence Behavior of a Flavin Derivative Incorporated Into Al-Based Metal–Organic Frameworks for the Sensing of Aromatic Nitro Compounds

Annette Vollrath[1] | Vasily Gvilava[1] | Philipp Seiffert[1] | Constantin Czekelius[2] | Christoph Janiak[1]

[1]Institut für Anorganische Chemie und Strukturchemie, Heinrich-Heine-Universität Düsseldorf, Düsseldorf, Germany | [2]Institut für Organische Chemie und Makromolekulare Chemie, Heinrich-Heine-Universität Düsseldorf, Düsseldorf, Germany

Correspondence: Christoph Janiak (janiak@uni-duesseldorf.de)

Received: 28 January 2026 | **Revised:** 16 June 2026 | **Accepted:** 23 June 2026

Keywords: electron transfer | flavin | metal-organic framework | MOF | nitroarene sensing | quenching

ABSTRACT

The incorporation of the flavin derivative 8-(dimethylamino)-10-methylisoalloxazine (DAMI) into the Al-based metal-organic frameworks (MOFs) DUT-4, DUT-5, and MIL-53 by a postsynthetic method was investigated. DAMI shows no fluorescence in the neat solid state, only in solution and when incorporated into a MOF as "solid solution." The fluorescence of the DAMI@MOF composites responded sensitively to the adsorption of guest molecules. Compounds containing methyl groups or chlorine enhanced the fluorescence intensity, whereas nitro compounds (nitrobenzene, 4-nitrotoluene, 4-nitrophenol) quenched the fluorescence. This behavior is attributed to the energy alignment between dye and guest orbitals, which enables photoinduced electron transfer (PET) from excited DAMI to electron-withdrawing nitro compounds, resulting in fluorescence quenching, whereas excited electron-donating guests yield PET to DAMI and lead to fluorescence enhancement. Among the tested compounds, nitrobenzene quenched 99% of the fluorescence of solid DAMI@MOF under a saturated-air atmosphere at 25°C, corresponding to a vapor phase concentration of approximately 14 µg/L generated from a 0.1 mg/mL nitrobenzene solution.

1 | Introduction

The detection of aromatic nitro compounds, which are used inter alia in explosives, is an important issue for homeland security, human health, and the environment in general. Therefore, there is an interest in developing instrumental alternatives to detector dogs for rapid, sensitive, and selective on-the-fly explosive detection [1].

Metal-organic frameworks (MOFs) are highly porous crystalline materials consisting of inorganic metal ions or clusters, coordinated to organic bridging linkers [2–4]. The chemical tunability and the high porosity of MOFs make them particularly suitable for the development of new sensors [5, 6]. A large number of MOFs have been reported as luminescent sensors for pollutants [7, 8] (including metal ions [9, 10] or volatile organic compounds (VOCs) [11]), for biomolecules [12], or for nitro compounds [13–19]. In most cases, the quenching of fluorescence by the analytes is used for sensing. Thereby, the MOF sensors often contain luminescent linkers in combination with diamagnetic d^{10} zinc(II) or cadmium(II) metal ions, or they contain luminescent lanthanoid metals. Luminescent MOFs of this type for the selective detection of nitroarene explosives were pioneered by Li et al., with

Dedicated to Prof. Dr. Claus Feldmann on the occasion of his 60th birthday.

This is an open access article under the terms of the Creative Commons Attribution License, which permits use, distribution and reproduction in any medium, provided the original work is properly cited.

© 2026 The Author(s). *Zeitschrift für anorganische und allgemeine Chemie* published by Wiley-VCH GmbH.

the microporous crystalline MOFs $[Zn_2(bpdc)_2(bpee)]\cdot 2$ DMF and $[Zn_2(oba)_2(bpy)]\cdot$DMA (bpdc = 4,4′-biphenyldicarboxylate, bpee = 1,2-bipyridylethene, oba = 4,4′-oxybis(benzoate), and bpy = 4, 4′-bipyridine) [13, 20]. The fluorescence originating from the used linker in the MOF is quenched by the aromatic nitro compound 2,4-dinitrotoluene or the plastic explosive taggant 2,3-dimethyl-2,3-dinitrobutane. Another example from Fan et al. is the functionalized MOF NU-1000-NH_2, where the fluorescence originating from the MOF linker is quenched and was used to detect different aromatic nitro compounds due to the interaction of the electron donor ($-NH_2$) and electron acceptor ($-NO_2$) groups [21].

The fluorescence quenching through nitroarenes proceeds via a photoinduced electron transfer (donor–acceptor) mechanism. Electron-deficient aromatic nitro compounds engage in π–π interactions with the MOF linker and serve as electron acceptors for photoexcited electrons originating from the electron-rich linker [22–26].

Flavins are organic compounds with a core of a heterocyclic isoalloxazine ring (Figure 1) [27]. Naturally occurring flavins are riboflavin, also called vitamin B_2 and roseoflavin [28, 29]. Due to its conjugated nature, the parent isoalloxazine moiety in flavins can act as a chromophore. It absorbs light in the blue region of the visible spectrum at about 450 nm, resulting in its yellow visible color [30]. Various studies have investigated the photophysical and photochemical properties of flavins, including possible applications, for example, as blue-light photosensors [31]. The photophysical properties of flavins can be significantly modulated by substituents on the isoalloxazine ring, as different functional groups influence absorption and emission characteristics by altering electronic structure and excited-state dynamics [32]. In the present study, the amino group of derivative 8-(dimethylamino)-10-methylisoalloxazine (DAMI) is expected to influence the electron density around the isoalloxazine system and thus its excited-state behavior, consistent with observations that substituent identity at *N*-10 and other positions strongly affects the optical properties of flavin analogs [33, 34]. Among the various flavin derivatives, DAMI is of particular interest because the strongly electron-donating dimethylamino substituent modifies the electronic structure of the isoalloxazine chromophore and enhances its sensitivity toward changes in the local environment. As a result, DAMI is expected to exhibit pronounced fluorescence responses upon interaction with guest molecules capable of influencing excited-state electron-transfer processes. Furthermore, the strong fluorescence of DAMI in solution and its susceptibility to aggregation-caused quenching (ACQ) in the solid state make it an attractive model system for investigating fluorescence restoration through confinement in MOF pores.

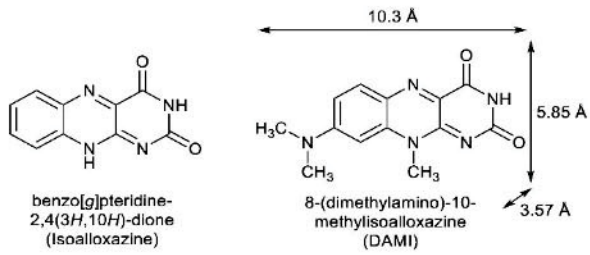


FIGURE 1 | Structure of the heterocyclic isoalloxazine parent compound (left) and the DAMI derivative with molecular dimensions which include the van der Waals surface (right).

It is long known that flavines can form intermolecular conjugates with organic compounds, which also includes their self-aggregation, which can lead to fluorescence quenching. Hence, for device fabrication, it must be taken into account that the neat flavines exhibit the phenomenon of aggregation-caused quenching in their solid state [35, 36]. A liquid solution, where fluorescence is observed from the separated dye molecules in the absence of ACQ, is usually not amenable for a detection device, but ACQ can also be prevented through the confinement of isolated dye molecules in the pores of a MOF. At the same time, the luminescent dyes [37–41] are somewhat protected from dynamic quenching with oxygen [42]. Thereby, dye@MOF presents a "solid-solution" with the dye in a handleable solid form for device fabrication. Recently, fluorinated flavin derivatives were incorporated into MOFs, leading to an increase in solid-state fluorescence of the dyes with higher lifetime and quantum yields [43]. dye@MOF compounds have been reported as sensors for VOCs or different ions [44–46]. Others were used for the detection of various nitroarenes such as 2,4,6-trinitrophenol, 4-nitrophenol, or 1,3-dinitrobenzene [46, 47].

Here, we report DAMI@Al-MOF composites, which can be easily synthesized by solvothermal methods and with inexpensive chemicals, acting as selective sensors toward aromatic nitro compounds.

2 | Results and Discussion

In this study, we investigated the incorporation of DAMI into three aluminum MOFs, namely DUT-4, DUT-5 [48], and MIL-53 [49]. They were selected as host frameworks to systematically study the influence of pore size, rigidity, and flexibility on the photophysical behavior of an encapsulated flavin dye. All three materials are aluminum-based, ensuring optically silent metal centers and high structural stability, while offering distinct pore architectures ranging from rigid small and large pores (DUT-4, DUT-5) to the flexible breathing behavior of MIL-53. This combination enables a comparative investigation of confinement and host-guest interactions on fluorescence and analyte-induced quenching. Due to the poor solubility of DAMI in the solvents used in the syntheses, a postsynthetic incorporation method was chosen. DAMI was incorporated into the MOFs by postsynthetic diffusion over a period of 3 days at a concentration of 0.6 mmol/L DAMI in chloroform (CH_3Cl) with activated Al-MOF (outgassed at 140°C under vacuum for 5 hr at a pressure of $<10^{-3}$ bar), that is liquid impregnation of the solid MOF with a DAMI solution (without evaporation) (Figure 2). With this method, the guest molecule should be of a similar size to the pore window of the MOF (see Figure S2 in SI for the MOF pore dimensions).

The crystal phase purity of the neat MOFs and its preservation upon DAMI incorporation were assessed by powder X-ray diffraction, with the diffractograms shown in Figure S3. The obtained reflexes of the neat MOFs and the DAMI@MOF

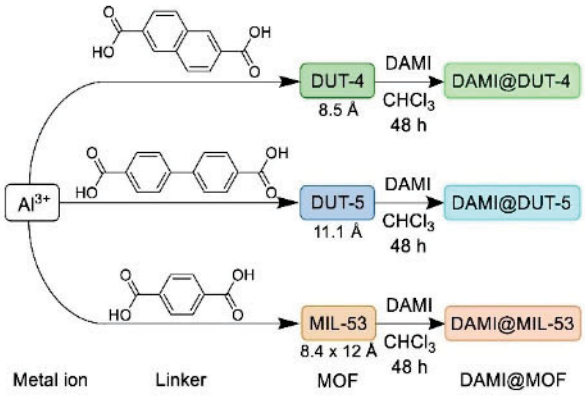


FIGURE 2 | Schematic illustration of the building blocks of the used Al-based MOFs and the formation of the composites by liquid impregnation of the solid MOF with a DAMI solution in chloroform. The pore sizes are listed under each MOF (cf. Figure S2).

composites are in good agreement with the simulated powder patterns. The composites show no missing or additional reflections in the diffraction pattern; hence, the dye loading has no influence on the crystalline structure of the MOFs. The powder X-ray diffraction (PXRD) pattern of DAMI@MIL-53 is dominated by the large-pore form of the framework. However, considering the low dye loading, the presence of a minor fraction of locally constrained dye environments cannot be excluded, as such species may remain below the detection limit of PXRD. If there are no extended ordered narrow-pore domains, that is, not enough repeating unit cells to form constructive interference, then only diffuse scattering rather than distinct diffraction peaks will be obtained. In contrast, fluorescence spectroscopy is highly sensitive to the local environment of the dye molecules and can therefore detect distinct emissive species that are not readily distinguishable by diffraction methods. Consequently, the observed dual emission may originate from DAMI molecules experiencing different confinement environments, potentially including both large-pore-like and narrow-pore-like regions.

The loading of DAMI@MOF was quantified by UV/Vis spectroscopy from the difference in the solution absorption before and after the diffusion into the MOF (see details in SI, Table S1, Sections S7 and S8.1). To ensure that no dye was adsorbed on the outer surface of the MOFs, the washing solutions were examined using UV/Vis spectroscopy after washing the composites. The porosity of the neat MOFs and the composites was assessed through analysis of the nitrogen sorption isotherms by the derived Brunauer-Emmett-Teller (BET) surface areas and micropore volumes, which are given comparatively in Figure S4 and Table 1.

Although the UV/Vis determination indicates relatively low dye loading, a substantial reduction in the pore volume was observed upon dye incorporation. These discrepancies suggest that even small amounts of dye can significantly affect the internal porosity, probably due to preferential adsorption at pore apertures, which leads to partial pore blockage [52].

All three neat MOFs show a type I nitrogen adsorption–desorption isotherm, as in the literature (Figure S4) [51, 53, 54]. The increase in nitrogen uptake at high partial pressure ($pp_0^{-1} > 0.9$) for DUT-4 and DUT-5 is attributed to the condensation in the interparticular macropores. The BET surface areas obtained here for DUT-5 are in the same range as in the original literature, while for DUT-4 and MIL-53, higher values were achieved for both the surface areas and the micropore volumes (Table 1).

After the incorporation of DAMI, the composites have lower BET surface areas and smaller micropore volumes, which is an indication of a successful incorporation of the dye into the MOFs, at least in the outer layers [52].

From the thermogravimetric analysis, the neat MOFs and the composites are stable to over 400°C for DUT-4 and DUT-5 and to over 500°C for MIL-53 after the solvent molecules in the pores were removed up to 150°C (Figure S5). Above these temperatures, the MOFs and the composites undergo thermal degradation of the linker molecules.

The Fourier-transform infrared (FT-IR) spectra of the neat MOFs and their composites in Figure S6 look almost identical, as expected from the low amount (≤0.20 wt%) of incorporated dye.

The environment of the flavin derivative plays an important role in its photophysical properties. As neat solid, DAMI is a deep red powder which does not show luminescence under UV light irradiation ($\lambda_{exc} = 365$ nm) (Figure 3a). When the solid is dissolved in chloroform, the solution has a yellow color and exhibits luminescence after UV excitation, with a maximum of the emission band at 522 nm. Yet, this emission is only observed with the solvents chloroform and dichloromethane. In the solvents water, methanol, ethanol, dimethyl sulfoxide, 2-propanol, and acetone, no fluorescence is detected (Figure 3b, Figure S8 in SI). The enhanced fluorescence intensity of the isoalloxazine dye in chloroform and dichloromethane is due to the effective solvation of the dye molecules in these solvents. Good solvation prevents the close intermolecular contacts that typically lead to aggregation-caused quenching [55]. In solvents in which solubility is poor, dye molecules tend to form aggregates or dimers via π–π stacking or hydrogen bonding. These aggregates facilitate nonradiative decay pathways by providing alternative relaxation routes for the excited states, thereby reducing the fluorescence quantum

TABLE 1 | BET surface areas and micropore volumes of the neat MOFs compared to the literature values and the composites.

	S_{BET} [m^2g^{-1}]		Micropore volume [cm^3g^{-1}]		DAMI loading [wt%]
Sample	**neat MOF (Lit.)**	**DAMI@MOF**	**neat MOF (Lit.)**	**DAMI@MOF**	**DAMI@MOF**
DUT-4	1555 (1308) [50]	994	0.85 (0.68)	0.22	0.15
DUT-5	1614 (1613) [51]	712	0.70 (0.61)	0.45	0.20
MIL-53	1529 (1140) [49]	762	0.60 (0.48)	0.32	0.10

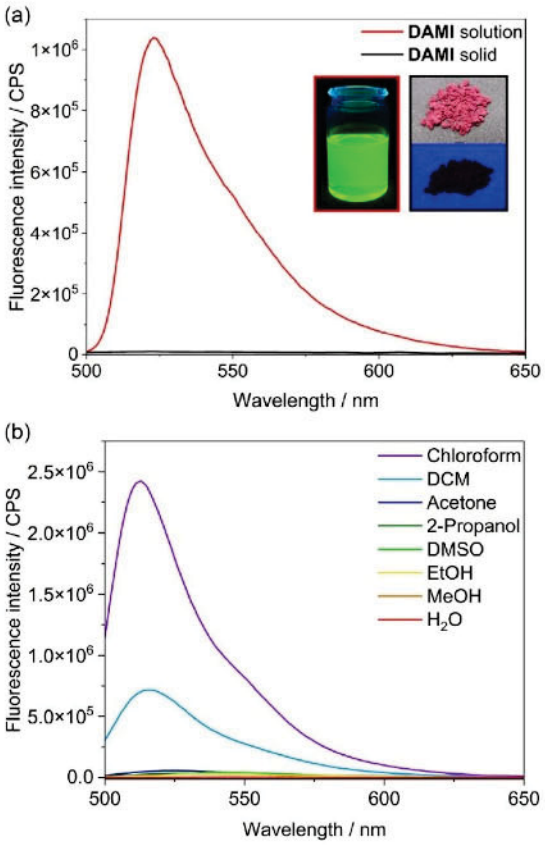


FIGURE 3 | (a) Fluorescence spectra of DAMI as a solid (black curve) and dissolved in chloroform (red curve) (c = 174 mg/L; λ_{exc} = 365 nm). Insert: DAMI in chloroform solution under UV irradiation (λ_{exc} = 365 nm) and DAMI as a solid (top: under daylight, bottom: under UV irradiation); (b) Fluorescence spectra of DAMI in different solvents.

yield. Furthermore, the moderate polarity and relatively low protic nature of chloroform and dichloromethane minimize solvent-induced fluorescence quenching mechanisms, such as excited-state proton transfer or charge–transfer complexes, thereby preserving the dye's emissive properties.

The absence of fluorescence in the solid state is primarily due to aggregation-caused quenching. In this phase, the dye molecules are forced into close proximity, promoting strong π–π stacking interactions between their aromatic cores. These close intermolecular contacts facilitate noncovalent interactions, such as exciton coupling as well as energy or charge transfer, between adjacent molecules. Consequently, the excited states of the dye molecules are rapidly deactivated through nonradiative decay pathways, rather than emitting photons [56]. Additionally, the formation of excimers or exciplexes in aggregates can introduce new nonemissive relaxation channels. Consequently, the photoluminescence quantum yield in the aggregated solid state is significantly lower than that of isolated molecules in solution, where such interactions are minimized [35].

However, under certain conditions, such as higher concentrations, DAMI molecules tend to aggregate and form J-aggregates. These aggregates are characterized by a head-to-tail arrangement of the molecules, leading to new low-energy excited states and red-shifted fluorescence emission [57]. This is reflected in the appearance of a shoulder or secondary emission band on the low-energy (red) side of the main fluorescence peak at around 550 nm, as observed in the emission spectra of DAMI in chloroform (Figure 3a).

Upon addition of liquid benzene, toluene, chlorobenzene, nitrobenzene, mesitylene, and *p*-xylene to a chloroform solution of DAMI, only nitrobenzene quenched the luminescence of the dye (Figure S8a in SI). Subsequently, it was tested whether other nitro compounds could also quench the DAMI luminescence. A chloroform solution of DAMI (c = 0.1 mg/mL) was mixed with 0.5 mL of the nitro compounds 4-nitrotoluene (4-NT), 4-nitrophenol (4-NP), 2,6-dinitrotoluene (2,6-DNT), nitromethane (NM), and nitrobenzene (NB). All samples showed a reduced fluorescence (Figure 4 and Figure S7 in SI).

The incorporation of DAMI into the MOFs DUT-4, DUT-5, and MIL-53 results in solid composites which fluoresce under UV light irradiation, whereas the solid dye and the neat MOFs did not show luminescence between 500 and 650 nm (Figure 3a, Figures 5, 6). The incorporation of the dye as isolated molecules into the channels of the MOFs prevents their aggregation and, hence, the ACQ effect.

The MOF structure and the dye loading indicate that it is unlikely for more than one DAMI molecule to occupy a single pore. Steric hindrance between two large DAMI molecules prevents strong π-π stacking interactions inside the same pore, so aggregation-related quenching due to multiple DAMI molecules per pore can be excluded. Smaller guest molecules, such as nitrobenzene, however, can coadsorb alongside a single DAMI molecule without steric conflict, and their presence does not induce aggregation-related quenching. Thus, the observed fluorescence changes can be attributed to interactions between DAMI and the adsorbed guest molecules rather than confinement-induced

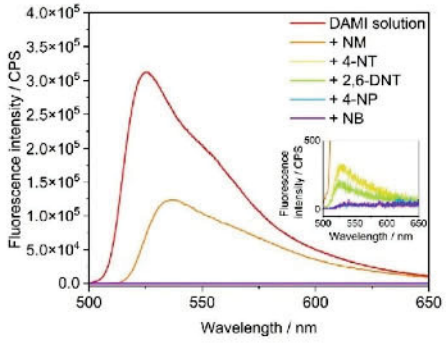


FIGURE 4 | Fluorescence spectra of DAMI in chloroform and added analytes. A solution of DAMI in chloroform (1 mg/mL, 10.0 mL) was prepared. Quenching experiments were performed for qualitative comparison by addition of 0.5 mL of neat liquid analyte or 0.5 mg of solid analyte dissolved in 0.5 mL chloroform (c = 1 mg/mL) directly to the dye solution, resulting in a total volume of 10.5 mL. NM = nitromethane, 4-NT = 4-nitrotoluene, 2,6-DNT = 2,6-dinitrotoluene, 4-NP = 4-nitrophenol, NB = nitrobenzene.

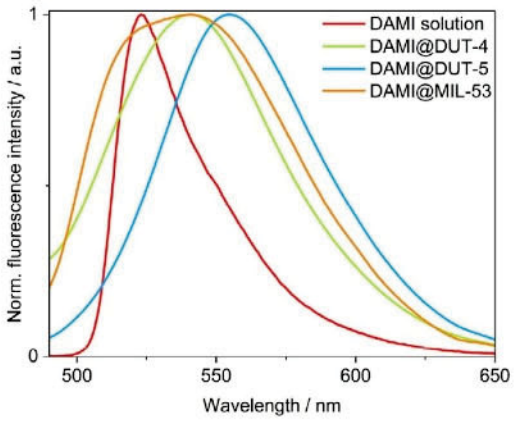


FIGURE 5 | Fluorescence spectra of DAMI dissolved in chloroform (red, ($c = 0.1$ mg/mL, 10.0 mL)) and the solid composites DAMI@DUT-4 (green), DAMI@DUT-5 (blue), and DAMI@MIL-53 (orange) ($\lambda_{exc} =$ 365 nm).

aggregation within the pore. However, dye-pore wall interactions may still play a role, as the dye molecules can experience weak host-guest interactions with the MOF framework, potentially affecting their orientation and local environment without causing aggregation. Instead, if present, potential quenching effects could arise from interactions between molecules located in neighboring pores, from the external surface of the crystals, or from these dye-framework interactions. This underlines the concept of solid-solution, as the embedded dye retains photophysical properties like the dissolved dye. Importantly, this does not preclude efficient interactions with externally introduced quenching analytes, such as nitroarene vapors, which can still diffuse into the pores and interact directly with the isolated dye molecules, either with or without contributions from pore-wall interactions, to facilitate electron transfer processes leading to fluorescence quenching.

For the DAMI@DUT-4 samples, the maximum emission wavelength is at 541 nm, and for the DAMI@DUT-5 samples, it is at 555 nm. The fluorescence of the DAMI@DUT-5 composites is red-shifted with respect to the fluorescence of DAMI in chloroform solution with $\lambda_{max} = 522$ nm (Figure 5). The bathochromic shift reaches the position of the shoulder at ~550 nm in the chloroform spectrum of DAMI and is caused by the host–guest interaction of DAMI and the linker in the MOFs with DAMI-to-ligand charge transfer [58]. The DAMI@MIL-53 sample shows an even broader emission peak with a maximum at 541 nm and a shoulder at 520 nm. This shoulder appears at the same wavelength as the emission maximum of the dye in chloroform (Figure 5). Therefore, the high-energy shoulder in the composite may be due to the isolated dye molecule. The MOF MIL-53 exhibits a special property called the "breathing effect" (Figure S2c in SI), where the pore size adapts to the presence and absence of guest molecules.

The composites can contain a combination of emitters, including flavin monomers and aggregates. The bathochromic shift observed in the spectra, along with the appearance of shoulders, suggests host-guest interactions but also the presence of

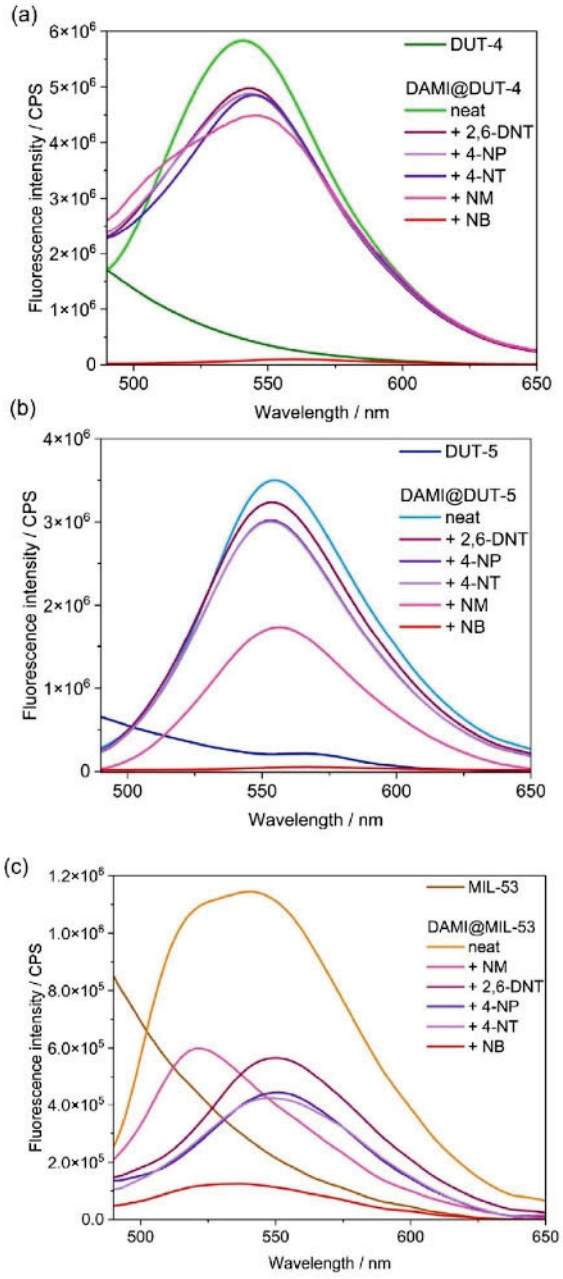


FIGURE 6 | Fluorescence spectra of (a) DUT-4, (b) DUT-5, and (c) MIL-53 of the neat MOF, the solid composites, and the composites under the saturated-air vapor atmosphere of nitro compounds at 25°C after 1 h of exposure (Figure S1b) ($\lambda_{exc} = 365$ nm). NM = nitromethane, 4-NT = 4-nitrotoluene, 2,6-DNT = 2,6-dinitrotoluene, 4-NP = 4-nitrophenol, NB = nitrobenzene.

fluorescent J-aggregates as additional contributors to the emission. Flavin confinement in general within MOF composites can produce J-aggregates with varying stoichiometries. Crucially, the emission behavior of these chromophore aggregates is heavily influenced by the strength of excitonic coupling and charge transfer interactions, both of which are determined by

their orientation, stoichiometry, and chemical composition. As a result, a diverse range of fluorescent species is expected for flavin@MOFs [43].

The composites were investigated for possible gas-sensing properties of nitro compounds. When the composites were exposed to nitroarene vapors (2,6-dinitrotoluene, 4-nitrophenol, 4-nitrotoluene, nitromethane, and nitrobenzene) at their saturation vapor pressure at 25°C for 1 hr, the fluorescence intensity of the composites was reduced (Figure 6). The markedly different quenching efficiencies of various nitro compounds can be attributed to a combination of factors such as accessibility to the MOF pores due to molecular structure and volatility and the possibility for π–π interactions. 2,6-Dinitrotoluene possesses two nitro groups; however, steric hindrance from the ortho substituents reduces molecular planarity and hampers effective π–π overlap with the dye. Furthermore, its significantly lower vapor pressure ($\sim 5.67 \times 10^{-4}$ mmHg at 25°C) leads to a reduced gas-phase concentration, limiting its uptake into the MOF under identical conditions and thereby decreasing the observed quenching efficiency. 4-Nitrophenol can form hydrogen bonds with the amide group of DAMI. Such interactions may distort the molecular geometry and interfere with optimal alignment between the analyte and the dye. In addition, its low vapor pressure ($\sim 5.00 \times 10^{-4}$ mmHg at 25°C) restricts its availability in the gas phase, resulting in fewer effective interactions with the dye@MOF system. Although 4-nitrotoluene is structurally similar to nitrobenzene, the presence of a methyl substituent affects its molecular geometry and intermolecular interactions. Its moderate vapor pressure (~0.02 mmHg at 25°C) enables some uptake into the MOF pores; however, quenching remains less efficient, likely due to suboptimal packing and weaker intermolecular interactions. Nitromethane, despite its high vapor pressure (~35.8 mmHg at 25°C) and facile diffusion into the MOF pores, lacks an aromatic π-system and therefore cannot participate in π–π stacking interactions. As a result, its interaction with the dye is limited to weak, nonspecific van der Waals forces, leading to minimal quenching. In contrast, nitrobenzene exhibits the most efficient quenching behavior due to its planar structure, favorable molecular size, and ability to engage in π–π stacking with the dye. Its comparatively high vapor pressure (~0.24 mmHg at 25°C) further facilitates rapid vapor-phase diffusion into the MOF pores, ensuring efficient contact with the photoactive chromophores.

Overall, the trend in quenching efficiency, nitrobenzene > 2,6-dinitrotoluene > 4-nitrophenol > 4-nitrotoluene > nitromethane, reflects a delicate interplay between electronic driving force for photoinduced electron transfer, molecular accessibility to the dye within the MOF pores, the strength of specific host-guest interactions such as π–π stacking, and the compound's volatility, which governs the rate of molecular uptake under vapor-phase sensing conditions.

In DAMI@DUT-4, the fluorescence spectrum is dominated by a single emission band, indicating a largely homogeneous dye environment within the rigid framework (Figure 6a). Although DUT-4 features slightly smaller pores compared to DUT-5, the dye molecules appear to be relatively mobile and well accessible, resulting in predominantly dynamic quenching governed by efficient analyte diffusion. The dynamic quenching behavior can be confirmed by measuring the lifetimes, which were shorter for the treated composites than for the untreated composites when using nitrobenzene as an example (Table S3 in SI). Nitrobenzene exhibits the strongest quenching effect, while nitromethane and the bulkier aromatic nitro compounds show moderate to weaker quenching efficiencies.

Despite its larger pore size, DAMI@DUT-5 displays a markedly different quenching behavior (Figure 6b). The flavin molecules are likely more strongly immobilized by host–guest interactions or coordination to the framework, leading to reduced effective accessibility for larger aromatic nitro compounds. Therefore, quenching by 2,6-dinitrotoluene, 4-nitrophenol, and 4-nitrotoluene is less efficient than in DUT-4. In contrast, the small and highly mobile nitromethane can efficiently reach and dynamically quench the flavin molecules in DUT-5, resulting in a pronounced reduction of the emission intensity.

In the case of DAMI@MIL-53, Figure 6c reveals that different emissive states of the dye are selectively quenched by different nitro compounds. This behavior can be rationalized by the flexible nature of the framework, which gives rise to two distinct emissive dye populations associated with large- and narrow-pore forms. This dual-emission behavior leads to selective quenching of individual emission bands depending on analyte size and electronic properties. The higher energy emission band at ~520 nm is attributed to comparatively isolated DAMI molecules located in the large-pore form of MIL-53, where host-guest interactions are weak. This emission is efficiently quenched by all investigated aromatic nitro compounds, with nitrobenzene showing the strongest effect. In contrast, the lower-energy emission band centered at ~550 nm is assigned to DAMI species experiencing stronger interactions with the MOF framework, presumably located in the narrow-pore form of MIL-53. Quenching of this emission is generally less efficient, indicating reduced accessibility of the analytes to these constrained environments. Among the investigated compounds, nitrobenzene and, to a lesser extent, the small nitromethane exhibit the highest quenching efficiency for this band. The nonaromatic nitromethane preferentially quenches only the DAMI species located in the large pores and is unable to penetrate or induce opening of the narrow pores containing the constrained DAMI molecules. Consequently, the emission originating from the narrow-pore DAMI remains largely unaffected, while the large-pore fluorescence is selectively quenched. Adsorption of aromatic nitro compounds, on the other hand, appears to induce a transformation of MIL-53 toward the large-pore form, leading to partial quenching of both emissive states. Due to its favorable size, planarity, and electronic properties, nitrobenzene is able to almost completely quench the DAMI fluorescence.

Figure 7 shows a comparison of the quenching percentage of the nitro compounds on the composites, which was calculated by using the proportion of the initial fluorescence and the quenched fluorescence (see section S8.2 in SI for further information). It can be clearly seen that nitrobenzene is the most effective attenuator of fluorescence in all three composites.

The quenching of the nitro compounds can be explained by a photoinduced electron transfer donor–acceptor mechanism (Figure 8). The observation of the quenching for nitroarene

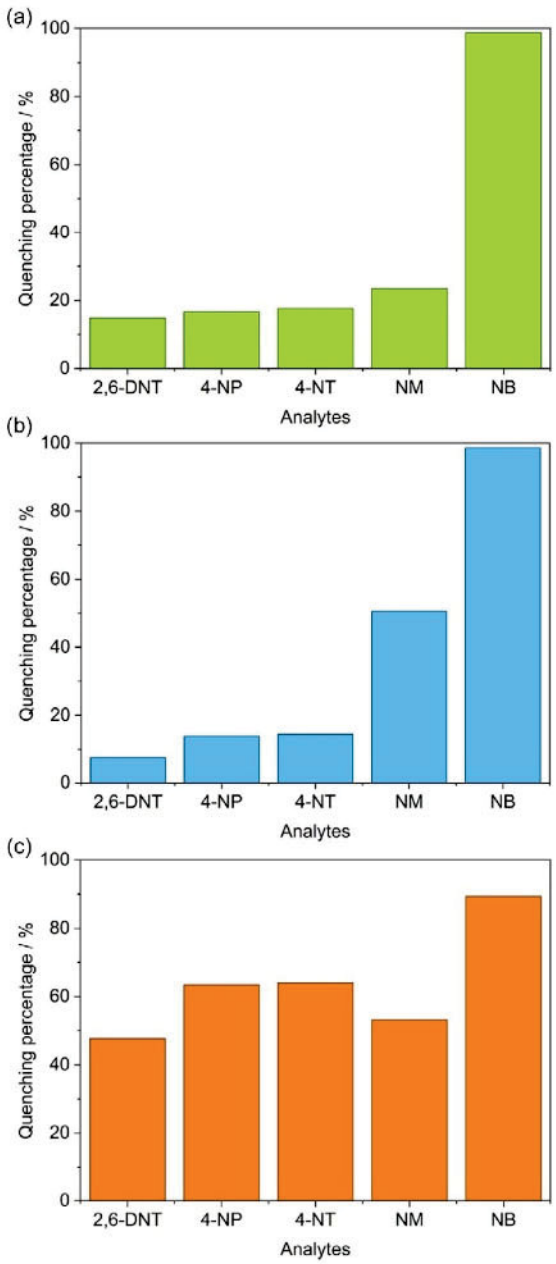


FIGURE 7 | Percentage of fluorescence quenching by the saturated-air vapor atmosphere of different nitro compound analytes at 25°C after 1 h of exposure; (a) DAMI@DUT-4, (b) DAMI@DUT-5, (c) DAMI@MIL-53. NM = nitromethane, 4-NT = 4-nitrotoluene, 2,6-DNT = 2,6-dinitrotoluene, 4-N*P* = 4-nitrophenol, NB = nitrobenzene.

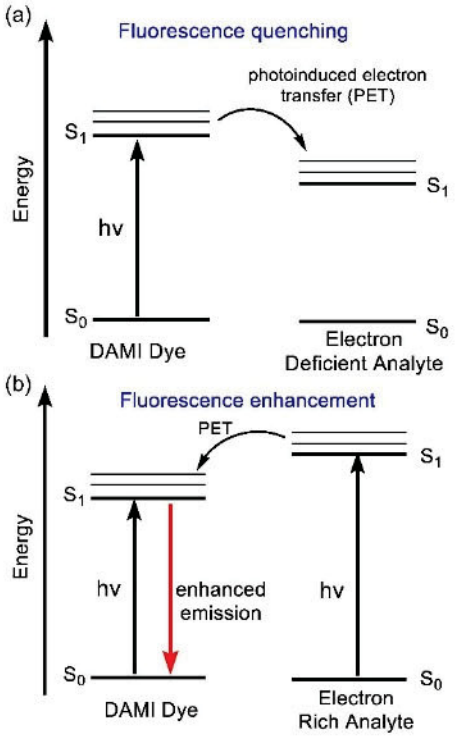


FIGURE 8 | Qualitative Jabłoński-type energy diagrams illustrating (a) fluorescence quenching and (b) fluorescence enhancement of a dye based on photoinduced electron transfer (PET). In case (a), PET from the excited singlet state (S_1) of the dye to an electron-deficient analyte provides a nonradiative deactivation pathway, resulting in fluorescence quenching. In case (b), PET from the excited singlet state (S_1) of the analyte to DAMI leads to its enhanced fluorescence emission.

analytes is driven by the relative energetics of the excited fluorophore and the analyte. Upon photoexcitation, the flavin derivative becomes a much stronger reducing agent than in the ground state. The electron-rich excited state can donate an electron to the low-lying LUMO of the nitro compound acceptor, whose electron-deficient character stabilizes the transferred electron. In a simple orbital-energy picture, efficient quenching occurs when the LUMO of the excited state of the analyte lies significantly below the singly-occupied MO (the former LUMO) of the excited flavin derivative (Figure 8a, Figure 9, and Table S2 in SI).

There is literature data on the theoretical calculations and highest occupied molecular orbitals (HOMO)-lowest unoccupied molecular orbitals (LUMO) energies of substituted arenes [62], but these studies used different sets of parameters and methods for the arenes that we compare here. Here, we calculate all of them using the same method to ensure a consistent and comparable overview, also for comparison to the energies of DAMI. It should be noted that the density functional theory (DFT) calculations were performed for the isolated arene and DAMI molecules and therefore do not account for confinement effects, host-guest interactions, or other electronic influences arising from incorporation within the MOF pores. Previous computational studies have shown that adsorption and confinement within porous materials can alter the electronic structure of guest molecules through framework-guest interactions and changes in the local electrostatic environment [63, 64]. Consequently, changes in frontier orbital energies upon adsorption cannot be excluded. However, capturing these effects would require elaborate calculations on DAMI@MOF, arene@MOF, and arene+DAMI@MOF models using sufficiently large replicated unit cells and explicit host-guest interactions, which was beyond the scope of the present study. Therefore, the calculated HOMO and LUMO energies are not intended to

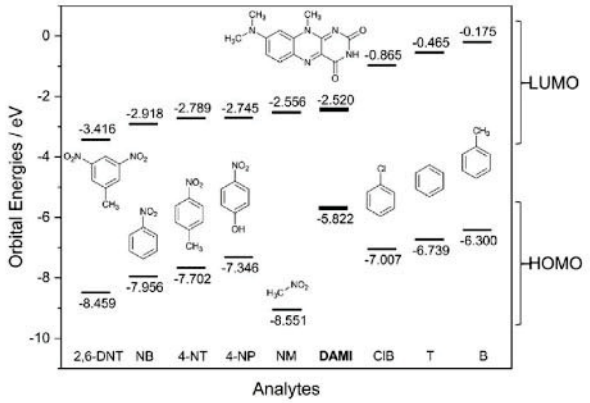


FIGURE 9 | Overview of the calculated HOMO and LUMO energies in eV of DAMI and the analytes. See section 8.3 in SI for the theoretical methods. 2,6-DNT = 2,6-dinitrotoluene, NB = nitrobenzene. 4-NT = 4-nitrotoluene, 4-N*P* = 4-nitrophenol, NM = nitromethane, ClB = chlorobenzene, T = toluene, B = benzene. The ground state geometries were optimized by DFT calculations using the Gaussian09 [59] with the implemented B3LYP functional [60, 61] and Pople's 6-31G (d, p) basic set.

represent the electronic structure of DAMI@MOF quantitatively or directly. Nevertheless, the dye-loaded MOFs can be regarded as solid-solution-like systems in which the dye molecules remain largely isolated and are expected to retain key features of their intrinsic electronic structure. Within these limitations, the calculated frontier orbital energies provide a qualitative framework for comparing the relative donor and acceptor properties of the investigated analytes and for rationalizing the experimentally observed trends in fluorescence enhancement and quenching.

Nitrobenzene contains only a strongly electron-withdrawing nitro group, resulting in a comparatively low-lying LUMO. In contrast, in 4-nitrotoluene and 4-nitrophenol, the electron-withdrawing effect of the nitro group is partially counteracted by the electron-donating methyl and hydroxy substituents, respectively, leading to a higher LUMO energy compared to nitrobenzene. Nitromethane exhibits a LUMO level that is energetically less favorable for efficient photoinduced electron transfer from excited DAMI, which explains its comparatively weak quenching efficiency. Although 2,6-dinitrotoluene possesses the lowest LUMO energy among the investigated analytes due to the presence of two nitro groups, its quenching efficiency is limited by steric effects and its very low vapor pressure. Together with 4-nitrophenol, its vapor pressure is approximately five orders of magnitude lower than that of nitrobenzene, resulting in a reduced effective analyte concentration in the MOF pores. These combined electronic and physicochemical properties of the nitro compounds give rise to the observed differences in quenching efficiency.

The pronounced quenching effect of nitrobenzene can thus be attributed to the favorable alignment of its low-lying LUMO with the excited state of DAMI as well as its relatively high vapor pressure (Table S2 in SI).

If photoinduced electron transfer from the excited DAMI molecule to the LUMO of the analyte is responsible for fluorescence quenching, analytes with LUMO levels located above that of excited DAMI are expected to induce a fluorescence-enhancing effect. In this case, electron transfer from the excited analyte to the lower-lying LUMO of DAMI becomes energetically favorable (Figure 8b, Figure 9), leading to an increase in DAMI fluorescence intensity (Table S2 in SI). This enhancement effect is demonstrated in Figure 10 for the aromatic compounds lacking a nitro group, benzene, toluene, and chlorobenzene. Their higher-lying LUMO levels arise from the absence of strongly electron-withdrawing substituents and, in combination with their sufficiently high vapor pressures, result in efficient adsorption and electron transfer to DAMI (Table S2 in SI).

Toluene shows the strongest fluorescence enhancement among the investigated aromatic analytes. This behavior can be attributed primarily to the electron-donating +I effect of the methyl substituent, which increases the electron density of the aromatic π-system and raises the HOMO energy level of toluene. As a result, photoexcitation of toluene is facilitated, leading to a higher population of its excited state (LUMO). This enhances the efficiency of photoinduced electron transfer from the excited toluene molecule to the LUMO of DAMI, thereby increasing the fluorescence intensity. In addition, the relatively high vapor pressure of toluene promotes efficient adsorption within the MOF composite, further contributing to the observed fluorescence enhancement. Benzene, which lacks electron-donating substituents, exhibits a lower HOMO energy and reduced electron density compared to toluene. Consequently, excitation and subsequent electron transfer to the fluorophore are less efficient, resulting in a moderate fluorescence enhancement. Nevertheless, benzene's relatively high vapor pressure supports effective adsorption in the MOF composite. Chlorobenzene shows the weakest fluorescence enhancement among the studied analytes. This can be attributed to the strong electron-withdrawing inductive effect of the chlorine substituent, which decreases the electron density of the aromatic ring and lowers the HOMO energy level, thereby reducing the efficiency of photoexcitation and electron donation. Although chlorine can donate electron density via resonance through its lone pairs, this contribution is minor and limited by the poor overlap between chlorine's 3p orbitals and the carbon's 2p orbitals of the benzene ring. As a result, the population of the excited state and subsequent electron transfer to

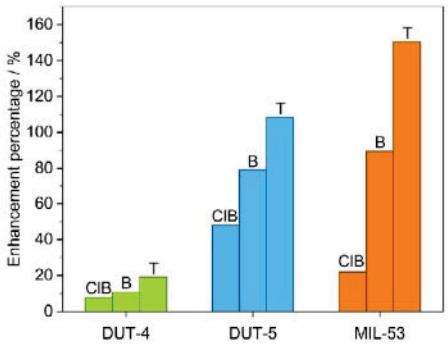


FIGURE 10 | Percentage of fluorescence enhancements of DAMI@MOF by the saturated-air vapor atmosphere of three nonnitro compounds at 25°C after 1 h of exposure (ClB = chlorobenzene, B = benzene, T = toluene).

DAMI are significantly reduced. Furthermore, the comparatively low fluorescence enhancement observed for chlorobenzene may be related, in part, to its lower vapor pressure relative to benzene and toluene. Nevertheless, adsorption in the MOF is expected to depend on multiple parameters, including vapor pressure, molecular dimensions, diffusion, and analyte-framework interactions. Together, these electronic and physical factors account for the comparatively weak fluorescence enhancement observed for chlorobenzene.

For all three investigated host materials (DAMI@DUT-4, DAMI@DUT-5, and DAMI@MIL-53), the aromatic-loaded composites exhibit excitation profiles that differ markedly from those of the corresponding parent DAMI@MOF materials (Figure S12). In particular, a pronounced excitation contribution is observed in the UV region between approximately 250 and 350 nm after adsorption of the aromatic analytes. The similar spectral features observed for benzene-, toluene-, and chlorobenzene-loaded samples suggest that the fluorescence enhancement is associated with the presence of aromatic guest molecules within the MOF pores.

However, the excitation spectra could only be recorded above 250 nm due to instrumental limitations and detector sensitivity. Consequently, the deep-UV region containing the most intense electronic transitions of benzene, toluene, and chlorobenzene could not be accessed experimentally. Therefore, the observed spectral changes cannot be interpreted as direct proof that excitation occurs exclusively on the aromatic guest molecules. Instead, the data indicate that adsorption of aromatic analytes modifies the excitation pathway of the DAMI@MOF composites. The fluorescence enhancement is therefore attributed to a combination of guest-induced effects, including possible guest-assisted excitation processes, altered dye-framework interactions, and changes in the local environment of the embedded DAMI molecules.

It should be noted that the fluorescence responses obtained under saturated-vapor conditions are influenced by the vapor pressures of the analytes and therefore should not be interpreted solely as intrinsic quenching or enhancement efficiencies. Consequently, the values shown in Figures 7 and 10 represent apparent fluorescence responses under saturated-air vapor conditions. To assess the influence of vapor pressure, the quenching and enhancement data were additionally evaluated using a vapor-pressure-normalized relative response index (Table S4 and S5), employing nitrobenzene as the reference analyte for the quenching experiments and toluene as the reference for the fluorescence-enhancement experiments. This normalization provides a qualitative comparison of the fluorescence response relative to the gas-phase availability of each analyte. The resulting values demonstrate that the observed fluorescence behavior cannot be explained by vapor pressure alone. Although gas-phase availability clearly contributes to the apparent response, significant differences remain after normalization, indicating that analyte-specific factors such as adsorption affinity, pore accessibility, host-guest interactions, and electron-transfer efficiency also influence the fluorescence response. Therefore, the observed enhancement and quenching behavior arise from a combination of vapor-phase availability and specific interactions between the analytes and the DAMI@MOF composites. Figure 11 was not subjected to this normalization because it depicts time-dependent quenching experiments using only nitrobenzene, for which the vapor pressure remains constant throughout the series.

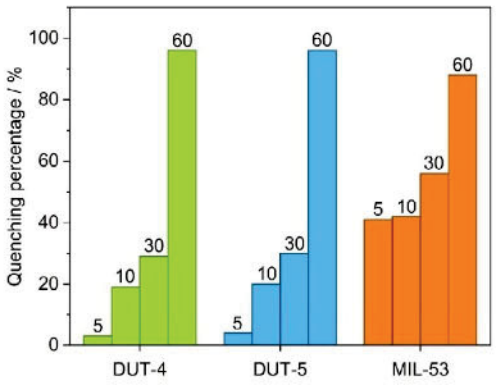


FIGURE 11 | Quenching percentage of the composites treated in saturated nitrobenzene (NB-) atmosphere after 5, 10, 30, and 60 min.

It was also investigated whether the quenching effect of the composites after exposure to an atmosphere containing aromatic nitro compounds is reversible or not. It was observed that fluorescence intensities were not attenuated even after several months. The samples were exposed to air during this time, but this had no significant effect on the quenching. The luminescence of the composites can be restored only from the nitro compound-adsorbed sample, for example, for NB@DAMI@MOF by heating at 130°C under vacuum for 2 h (Figure S9 and S10 in SI). Only through this elaborate procedure the fluorescence in the composites can be restored. The effect could be used, for example, as a sensor in a nonreversible "history" indicator tag for exposure to nitro compounds, proving the previous handling or presence of aromatic nitro compounds, akin to temperature or tilt history indicator tags. Such history indicator tags cannot easily be set back to the original state once a certain temperature has been exceeded or a package has been tilted over a certain angle [65].

In addition, the time-dependent quenching behavior was investigated for NB. The samples were exposed to the nitrobenzene atmosphere, and the spectra were recorded after different times (Figure S11 in SI). An overview of the quenching percentage is shown in Figure 11.

3 | Conclusions

In summary, we reported the postsynthetic incorporation of 8-(dimethylamino)-10-isoalloxazine (DAMI) into the different Al-based metal-organic frameworks DUT-4, DUT-5, and MIL-53 as DAMI@MOF. While neat solid DAMI does not fluoresce, the incorporated dye shows similar luminescence properties as DAMI dissolved in $CHCl_3$, which underlines the concept of "solid solutions" for the DAMI@MOF composites. Under the saturated-air vapor atmosphere of volatile nitro compounds, a quenching effect was observed for the

DAMI@MOF samples. To the contrary, compounds without a nitro group, such as chlorobenzene, toluene, and benzene, yielded a fluorescence enhancement, which was highest for toluene. Quenching and enhancement are rationalized by the relative energies of the DAMI LUMO and guest analyte LUMO orbitals, which result in photoinduced electron transfer (PET) with quenching from excited DAMI to the electron-deficient nitro compounds and PET with enhancement from excited electron-rich aromatic molecules to DAMI. The MOF comparison demonstrates that fluorescence quenching in rigid frameworks such as DUT-4 and DUT-5 is primarily governed by analyte accessibility and diffusion, whereas in flexible MIL-53, the quenching process is strongly influenced by the presence of multiple emissive dye states and analyte-induced structural transformations of the host framework. The presented dye@MOF composites combine structural precision with high sensitivity toward nitro compounds, especially nitrobenzene. Despite moderate response kinetics, the system offers key advantages in terms of stability, controllability, and selectivity. Its modular architecture further opens up diverse opportunities for optimization and application, both in fundamental research and in the development of robust "history" tag sensing platforms.

4 | Experimental Section

4.1 | Chemicals

All chemicals were commercially obtained (from Alfa Aesar, Acros Organics, BLDpharm, Sigma Aldrich, or TCI America) and used as received without further purification.

4.2 | Powder X-Ray Diffraction (PXRD)

PXRD patterns were measured at ambient temperature using a Rigaku MiniFlex diffractometer (600 W, 40 kV, 15 mA) with Cu Kα radiation ($\lambda = 1.54182$ Å) between $5° < 2\Theta < 50°$. The diffractograms were obtained on a flat "low background sample holder." The analysis of the diffractograms was performed with the software Match 3.11.

4.3 | Nitrogen Sorption Measurements

BET surface areas and pore volumes were obtained from the nitrogen adsorption–desorption measurements using a Belsorp Max II from Microtrac MRB at 77 K. Prior to the isothermal sorption experiments, the samples were outgassed at 140°C under vacuum for 5 h at a pressure of $<10^{-3}$ bar.

4.4 | Thermogravimetric Analysis (TGA)

Thermogravimetric analysis (TGA) was carried out using a Netzsch TG 209 in the range between 30 and 1000°C with a 10°C min^{-1} heating rate under a nitrogen atmosphere.

4.5 | Fourier Transform Infrared Spectroscopy (FT-IR)

FT-IR spectra were measured on a Bruker Tensor 37 with KBr pellets at room temperature.

4.6 | Quantum Chemical Calculations

Quantum chemical calculations were used to evaluate the HOMO and LUMO energy levels of the compounds. The ground state geometries were optimized by DFT calculations using Gaussian09 [59] with the implemented B3LYP functional [61, 65] and Pople's 6-31G (d, p) basic set [66].

4.7 | Fluorescence Spectroscopy

Fluorescence spectra were measured at ambient temperature using a FluoroMax-4 spectrofluorometer from Horiba Scientific. Unless otherwise stated, the spectra have been measured at an excitation wavelength of 365 nm and an integration time of 0.5 s. For better presentation, the recorded spectra were smoothed and the scatter peaks removed. All spectra and diagrams were plotted with OriginPro 2021b.

4.8 | Synthesis of 8-Dimethylamino-10-Methylbenzo[g]pteridine-2,4-(3*H*,10*H*)-Dione (8-Dimethylamino-10-Methylisoalloxazine, DAMI)

The synthesis of the dye (DAMI) followed a procedure described by King et al. [67]. The characterization is described in the publication of Hasford and Rizzo [68], and verification of the successful synthesis and purity was carried out in a manner analogous to their publication.

4.9 | Synthesis of DUT-4

The synthesis of DUT-4 followed a procedure described by Senkovska et al. [48]. In a Pyrex glass tube, 527 mg (1.4 mmol) of aluminum nitrate nonahydrate and 261 mg (1.2 mmol) of 2,6-naphthalenedicarboxylic acid were dissolved in 30 mL of DMF. The solution was heated to 120°C for 24 h. Then, the product was washed two times with 30 mL of DMF and two times with 30 mL of ethanol. After the last centrifugation, the MOF was dried for 16 h at 80°C under vacuum. Yield: 0.422 g. The successful synthesis was verified by a matching experimental and simulated powder X-ray diffractogram (Figure S3a) and by a nitrogen sorption study with BET surface area determination, giving 1555 m^2/g as in the literature [50].

4.10 | Synthesis of DUT-5

The synthesis of DUT-5 followed a procedure described by Senkovska et al. [48]. In a reaction vessel, 361 mg (1.5 mmol) of biphenyl-4,4′-dicarboxylic acid was dissolved in 60 mL of

DMF and heated to 110°C. In small portions, the amount of 762 mg (2.0 mmol) of aluminum nitrate nonahydrate was added to the solution over 5 h. After that, heating was continued overnight. The product was washed two times with 20 mL of DMF and two times with 20 mL of ethanol. Then, the MOF was dispersed in 100 mL of ethanol and heated to reflux for 24 hr. After centrifugation, the MOF was dried for 16 hr at 60°C under vacuum. Yield: 0.252 g. The successful synthesis was verified by a matching experimental and simulated powder X-ray diffractogram (Figure S3a) and by a nitrogen sorption study with BET surface area determination, giving 1614 m^2/g as in the literature [50].

4.11 | Synthesis of MIL-53

The synthesis of MIL-53 followed a procedure described by Loiseau et al. [49]. In an autoclave, 5.25 g (14 mmol) of aluminum nitrate nonahydrate and 1.17 g (7 mmol) of terephthalic acid were dissolved in 20 mL of distilled water. The solution was stirred for 1 h at room temperature and was heated afterward to 200°C for 72 h. The product was washed two times with 10 mL of water. Then, the solvent was replaced by 50 mL of DMF in which the MOF was stirred for 3 h at 180°C. The product was washed two times with DMF (2 × 10 mL) and one time with methanol (15 mL). The sample was dried at 60°C under vacuum for 2 h to obtain MIL-53(Al) (as synthesized). To obtain MIL-53 (Al)lt (narrow pore form), the sample was stirred in 50 mL of methanol for 24 h at room temperature, and after centrifugation, dried at 60°C for 2 h under vacuum. After activation at 150°C under vacuum overnight for a complete removal of solvent molecules, MIL-53(Al)ht (large pore form) was obtained. Yield: 0.654 g. The successful synthesis was verified by a matching experimental and simulated powder X-ray diffractogram (Figure S3a) and by a nitrogen sorption study with BET surface area determination, giving 1529 m^2/g as in the literature [49].

4.12 | Incorporation of DAMI in MOFs

Prior to incorporation, MOFs were activated at 120°C for 24 h under vacuum and then stored at 60°C under vacuum to protect the samples from moisture. The incorporations were performed in Pyrex tubes, which were tightly sealed after sample preparation. 200 mg of each MOF was weighed into the tubes, and 10 mL of the saturated dye solution (in chloroform, $c = 174$ mg/L) was added. The suspensions were stirred at room temperature for 36 h. The samples were then centrifuged, and the supernatant solutions were removed using a syringe for an immediate measurement of the residual DAMI concentration by UV/Vis spectroscopy to determine the DAMI uptake from the difference. The composites were washed after the embedding so that DAMI, which adhered to the outside of the MOF, was removed.

4.13 | Quenching Experiments

All quenching experiments were carried out at 25°C. Prior to quenching studies, 200 mg of each solid neat nitro compound (4-nitrotoluene, 4-nitrophenol, and 2,4-dinitrotoluene) was placed in a glass vessel (20 mL). It was tightly sealed for several days to ensure an equilibrated vapor pressure of each analyte. Similar procedures were followed for the liquid analytes (nitrobenzene, nitromethane, chlorobenzene, benzene, toluene). 1 mL of each neat analyte was placed in a glass vessel (20 mL) and sealed tightly for several days. For the quenching experiments, the activated composites were placed in smaller glass vessels, which were placed in the glass vessels with the saturated-air vapor atmosphere (Figure S1). After the specified exposure time (5, 10, or 30 min, typically 1 h), the treated composites were removed, and the solid-state DAM@MOF emission spectra were measured with the fluorescence spectrophotometer.

Acknowledgments

A. V. thanks M. P. Rademacher from the research group of Prof. Peter Gilch for the support with the fluorescence measurements. This work was supported by the Deutsche Forschungsgemeinschaft (DFG, German Research Foundation)—396890929/GRK 2482.

Open Access funding enabled and organized by Projekt DEAL.

Funding

This study was supported by Deutsche Forschungsgemeinschaft (396890929/GRK 2482).

Conflict of Interest

The authors declare no conflicts of interest.

Data Availability Statement

The data that support the findings of this study are available in the supplementary material of this article.

References

1. K. G. Furton, L. J. Myers, "The Scientific Foundation and Efficacy of the use of Canines as Chemical Detectors for Explosives," *Talanta* 54 (2001): 487–500, https://doi.org/10.1016/S0039-9140(00)00546-4.

2. O. M. Yaghi, M. O.-Keeffe, N. W. Ockwig, H. K. Chae, M. Eddaoudi, and J. Kim, "Reticular Synthesis and the Design of New Materials," *Nature* 423 (2003): 705–714, https://doi.org/10.1038/nature01650.

3. Q. Wang and D. Astruc, "State of the Art and Prospects in Metal–Organic Framework (MOF)-Based and MOF-Derived Nanocatalysis," *Chemical Reviews* 120 (2020): 1438–1511, https://doi.org/10.1021/acs.chemrev.9b00223.

4. S. Dang, Q.-L. Zhu, and Q. Xu, "Nanomaterials Derived from Metal–organic Frameworks," *Nature Reviews Materials* 3 (2018): 1–14, https://doi.org/10.1038/natrevmats.2017.75.

5. E. A. Dolgopolova, A. M. Rice, C. R. Martin, and N. B. Shustova, "Photochemistry and Photophysics of MOFs: Steps towards MOF-Based Sensing Enhancements," *Chemical Society Reviews* 47 (2018): 4710–4728, https://doi.org/10.1039/C7CS00861A.

6. L. E. Kreno, K. Leong, O. K. Farha, M. Allendorf, R. P. Van Duyne, and J. T. Hupp, "Metal–Organic Framework Materials as Chemical Sensors," *Chemical Reviews* 112, no. 2 (2012): 1105–1125, https://doi.org/10.1021/cr200324t.

7. A. Karmakar, E. Velasco, and J. Li, "Metal-Organic Frameworks as Effective Sensors and Scavengers for Toxic Environmental Pollutants," *National Science Review* 9 (2022): nwac091, https://doi.org/10.1093/nsr/nwac091.

8. S. Tajik, H. Beitollahi, F. G. Nejad, et al., "Performance of Metal–organic Frameworks in the Electrochemical Sensing of Environmental Pollutants," *Journal of Materials Chemistry A* 9 (2021): 8195–8220, https://doi.org/10.1039/D0TA08344E.

9. S. A. A. Razavi and A. Morsali, "Metal Ion Detection Using Luminescent-MOFs: Principles, Strategies and Roadmap," *Coordination Chemistry Reviews* 415 (2020): 213299, https://doi.org/10.1016/j.ccr.2020.213299.

10. F.-M. Wang, L. Zhou, E. Velasco, et al., "Tuning Chromophore-Based LMOF Dimensionality to Enhance Detection Sensitivity for Fe^{3+} Ions," *ACS Omega* 6, no. 25 (2021): 16498–16506, https://doi.org/10.1021/acsomega.1c01148.

11. Y. Shen, A. Tissot, and C. Serre, "Recent Progress on MOF-Based Optical Sensors for VOC Sensing," *Chemical Science* 13 (2022): 13978–14007, https://doi.org/10.1039/D2SC04314A.

12. M. Daniel, G. Mathew, M. Anpo, and B. Neppolian, "MOF Based Electrochemical Sensors for the Detection of Physiologically Relevant Biomolecules: An Overview," *Coordination Chemistry Reviews* 468 (2022): 214627, https://doi.org/10.1016/j.ccr.2022.214627.

13. S. Pramanik, C. Zheng, X. Zhang, T. J. Emge, and J. Li, "New Microporous Metal–Organic Framework Demonstrating Unique Selectivity for Detection of High Explosives and Aromatic Compounds," *Journal of the American Chemical Society* 133 (2011): 4153–4155, https://doi.org/10.1021/ja106851d.

14. S. Pramanik, Z. Hu, C. Zheng Xiao Zhang, S. Kelly, and J. Li, "A Systematic Study of Fluorescence-Based Detection of Nitroexplosives and Other Aromatics in the Vapor Phase by Microporous Metal–Organic Frameworks," *Chemistry – A European Journal* 19 (2013): 15964–15971, https://doi.org/10.1002/chem.201301194.

15. S. Hu, S. Pramanik, K. Tan, et al., "Selective, Sensitive, and Reversible Detection of Vapor-Phase High Explosives via Two-Dimensional Mapping: A New Strategy for MOF-Based Sensors," *Crystal Growth & Design* 13 (2013): 4204–4207.

16. A. Sharma, D. Kim, J.-H. Park, et al., "Mechanistic Insight into the Sensing of Nitroaromatic Compounds by Metal-Organic Frameworks," *Communications Chemistry* 2 (2019): 239, https://doi.org/10.1038/s42004-019-0135-2.

17. Y.-T. Yan, J. Liu, G.-P. Yang, et al., "Highly Selective Luminescence Sensing for the Detection of Nitrobenzene and Fe^{3+} by New Cd(Ii)-Based MOFs," *CrystEngComm* 20 (2018): 477–486, https://doi.org/10.1039/C7CE01920C.

18. D. Ma, B. Li, X. Zhou, et al., "A Dual Functional MOF as a Luminescent Sensor for Quantitatively Detecting the Concentration of Nitrobenzene and Temperature," *Chemical Communications* 49 (2013): 8964–8966, https://doi.org/10.1039/C3CC44546A.

19. S. Jensen, K. Tan, W. Lustig, et al., "Quenching of Photoluminescence in a Zn-MOF Sensor by Nitroaromatic Molecules," *Journal of Materials Chemistry C* 7 (2019): 2625–2632, https://doi.org/10.1039/C8TC06281A.

20. A. Lan, K. Li, H. Wu, et al., "A Luminescent Microporous Metal–Organic Framework for the Fast and Reversible Detection of High Explosives," *Angewandte Chemie International Edition* 48 (2009): 2334–2338, https://doi.org/10.1002/anie.200804853.

21. H. Li, Q. Chen, Z. Zhang, Z. Wang, Z. Gong, and M. Fan, "Functionalized Fluorescent Zr-MOF Based on Photoinduced Electron Transfer for Highly Sensitive Detection of Nitroaromatic Explosives," *Dyes and Pigment* 210 (2023): 111035, https://doi.org/10.1016/j.dyepig.2022.111035.

22. W.-J. Li, J. Lü, S.-Y. Gao, Q.-H. Li, and R. Cao, "Electrochemical Preparation of Metal–organic Framework Films for Fast Detection of Nitro Explosives," *Journal of Materials Chemistry A* 2 (2014): 19473–19478, https://doi.org/10.1039/C4TA04203D.

23. S. J. Toal and W. C. Trogler, "Polymer Sensors for Nitroaromatic Explosives Detection," *Journal of Materials Chemistry* 16 (2006): 2871–2883, https://doi.org/10.1039/B517953J.

24. B. Gole, A. K. Bar, and P. S. Mukherjee, "Fluorescent Metal–organic Framework for Selective Sensing of Nitroaromatic Explosives," *Chemical Communications* 47 (2011): 12137–12139, https://doi.org/10.1039/C1CC15594F.

25. M. S. Meaney and V. L. McGuffin, "Luminescence-Based Methods for Sensing and Detection of Explosives," *Analytical and Bioanalytical Chemistry* 391 (2008): 57–2576, https://doi.org/10.1007/s00216-008-2194-6.

26. A. Penzkofer, A. K. Bansal, S.-H. Song, and B. Dick, "Fluorescence Quenching of Flavins by Reductive Agents," *Chemical Physics* 336 (2007): 14–21, https://doi.org/10.1016/j.chemphys.2007.05.009.

27. B. König, S. Kümmel, E. Svobodová, and R. Cibulka, "Flavin Photocatalysis," *Physical Sciences Reviews* 3, no. 8 (2018): 1–17, https://doi.org/10.1515/psr-2017-0168.

28. M. Mack and S. Grill, "Riboflavin Analogs and Inhibitors of Riboflavin Biosynthesis," *Applied Microbiology and Biotechnology* 71 (2006): 265–275, https://doi.org/10.1007/s00253-006-0421-7.

29. P. Zirak, A. Penzkofer, T. Mathes, and P. Hegemann, "Photo-Dynamics of Roseoflavin and Riboflavin in Aqueous and Organic Solvents," *Chemical Physics* 358 (2009): 111–122, https://doi.org/10.1016/j.chemphys.2008.12.026.

30. D. Green, P. Roy, C. R. Hall, et al., "Excited State Resonance Raman of Flavin Mononucleotide: Comparison of Theory and Experiment," *The Journal of Physical Chemistry A* 125 (2021): 6171–6179, https://doi.org/10.1021/acs.jpca.1c04063.

31. A. Losi, "Flavin-based Blue-light Photosensors: A Photobiophysics Update," *Photochemistry and Photobiology* 83 (2007): 1283–1300, https://doi.org/10.1111/j.1751-1097.2007.00196.x.

32. A. Reiffers, C. Torres Ziegenbein, A. Engelhardt, R. Kühnemuth, P. Gilch, and C. Czekelius, "Impact of Mono-Fluorination on the Photophysics of the Flavin Chromophore," *Photochemistry and Photobiology* 94 (2018): 667–676, https://doi.org/10.1111/php.12921.

33. D.-M. Răsădean, T. Machida, K. Sada, C. R. Pudney, and G. D. Pantoş, "Flavin Mimetics: Synthesis and Photophysical Properties," *Tetrahedron* 82 (2021): 131925, https://doi.org/10.1016/j.tet.2021.131925.

34. M. Kowalczyk, E. Sikorska, I. V. Khmelinskii, J. Komasa, M. Insińska-Rak, and M. Sikorski, "Spectroscopy and Photophysics of Flavin-Related Compounds: Isoalloxazines," *Journal of Molecular Structure* 756 (2005): 47–54, https://doi.org/10.1016/j.theochem.2005.09.005.

35. Y. Huang, J. Xing, Q. Gong, et al., "Reducing Aggregation Caused Quenching Effect through Co-Assembly of PAH Chromophores and Molecular Barriers," *Nature Communications* 10 (2019): 169, https://doi.org/10.1038/s41467-018-08092-y.

36. C. Wang and Z. Li, "Molecular Conformation and Packing: Their Critical Roles in the Emission Performance of Mechanochromic Fluorescence Materials," *Materials Chemistry Frontiers* 1 (2017): 2174–2194, https://doi.org/10.1039/C7QM00201G.

37. P. Horcajada, C. Serre, M. Vallet-Regi, M. Sebban, F. Taulelle, and G. Férey, "Metal–Organic Frameworks as Efficient Materials for Drug Delivery," *Angewandte Chemie International Edition* 118 (2006): 61201–66124, https://doi.org/10.1002/anie.200601878.

38. P. D. Patil and G. D. Yadav, "Rapid In Situ Encapsulation of Laccase into Metal-Organic Framework Support (ZIF-8) under Biocompatible Conditions," *ChemistrySelect* 3 (2018): 4669–4675, https://doi.org/10.1002/slct.201702852.

39. M.-J. Dong, M. Zhao, S. Ou C. Zou, and C.-D. Wu, "A Luminescent Dye@MOF Platform: Emission Fingerprint Relationships of Volatile Organic Molecules," *Angewandte Chemie International Edition* 126 (2014): 1575–1605, https://doi.org/10.1002/ange.201307331.

40. M. Gutiérrez, Y. Zhang, and J.-C. Tan, "Confinement of Luminescent Guests in Metal–Organic Frameworks: Understanding Pathways from Synthesis and Multimodal Characterization to Potential Applications of LG@MOF Systems," *Chemical Reviews* 122 (2022): 10438–10483, https://doi.org/10.1021/acs.chemrev.1c00980.

41. U. Ryu, H. S. Lee, K. S. Park, and K. M. Choi, "The Rules and Roles of Metal–organic Framework in Combination with Molecular Dyes," *Polyhedron* 154 (2018): 275–294, https://doi.org/10.1016/j.poly.2018.07.043.

42. T.-O. Knedel, S. Buss, I. Maisuls, et al., "Encapsulation of Phosphorescent Pt(II) Complexes in Zn-Based Metal–Organic Frameworks toward Oxygen-Sensing Porous Materials," *Inorganic Chemistry* 59 (2020): 7252–7264, https://doi.org/10.1021/acs.inorgchem.0c00678.

43. D. Püschel, S. Hédé, I. Maisuls, et al., "Enhanced Solid-State Fluorescence of Flavin Derivatives by Incorporation in the Metal-Organic Frameworks MIL-53(Al) and MOF-5," *Molecules* 28 (2023): 2877, https://doi.org/10.3390/molecules28062877.

44. J.-P. Zheng, S. Ou, M. Zhao, and C.-D. Wu, "A Highly Sensitive Luminescent Dye@MOF Composite for Probing Different Volatile Organic Compounds," *ChemPlusChem* 81 (2016): 758–763, https://doi.org/10.1002/cplu.201600057.

45. Y. Li, Z. Wei, Y. Zhang, et al., "Dual-Emitting EY@Zr-MOF Composite as Self-Calibrating Luminescent Sensor for Selective Detection of Inorganic Ions and Nitroaromatics," *ACS Sustainable Chemistry & Engineering* 7, no. 6 (2019): 6196–6203, https://doi.org/10.1021/acssuschemeng.8b06500.

46. H.-R. Fu, Y. Zhao, T. Xie, M.-L. Han, L.-F. Ma, and S.-Q. Zang, "Stable Dye-Encapsulated Indium–organic Framework as Dual-Emitting Sensor for the Detection of Hg^{2+}/$Cr_2O_7^{2-}$ and a Wide Range of Nitro-Compounds," *Journal of Materials Chemistry C* 6 (2018): 6440–6448, https://doi.org/10.1039/C8TC01571F.

47. D.-M. Chen, N.-N. Zhang, C.-S. Liu, and M. Du, "Dual-Emitting Dye@MOF Composite as a Self-Calibrating Sensor for 2,4,6-Trinitrophenol," *ACS Applied Materials & Interfaces* 9, no. 29 (2017): 24671–24677, https://doi.org/10.1021/acsami.7b07901.

48. I. Senkovska, F. Hoffmann, M. Fröba, J. Getzschmann, W. Böhlmann, and S. Kaskel, "New Highly Porous Aluminium Based Metal-Organic Frameworks: Al(OH)(ndc) (ndc=2,6-Naphthalene Dicarboxylate) and Al(OH)(bpdc) (bpdc=4,4′-Biphenyl Dicarboxylate)," *Microporous and Mesoporous Materials* 122 (2009): 93–98, https://doi.org/10.1016/j.micromeso.2009.02.020.

49. T. Loiseau, C. Serre, C. Huguenard, et al., "A Rationale for the Large Breathing of the Porous Aluminum Terephthalate (MIL-53) Upon Hydration," *Chemistry – A European Journal* 10 (2004): 1373–1382, https://doi.org/10.1002/chem.200305413.

50. S. Halis, N. Reimer, A. Klinkebiel, U. Lüning, and N. Stock, "Four New Al-Based Microporous Metal-Organic Framework Compounds with MIL-53-Type Structure Containing Functionalized Extended Linker Molecules," *Microporous and Mesoporous Materials* 216 (2015): 13–19, https://doi.org/10.1016/j.micromeso.2015.01.030.

51. G. Zi, Z. Yan, Y. Wang, et al., "Catalytic Hydrothermal Conversion of Carboxymethyl Cellulose to Value-Added Chemicals over Metal–organic Framework MIL-53(Al)," *Carbohydrate Polymers* 115 (2015): 146–151, https://doi.org/10.1016/j.carbpol.2014.08.065.

52. M. Ma, A. Gross, D. Zacher, et al., "Use of Confocal Fluorescence Microscopy to Compare Different Methods of Modifying Metal–organic Framework (MOF) Crystals with Dyes," *CrystEngComm* 13 (2011): 2828–2832, https://doi.org/10.1039/C0CE00416B.

53. C. Jansen, N. Assahub, A. Spieß, et al., "The Complexity of Comparative Adsorption of C6 Hydrocarbons (Benzene, Cyclohexane, n-Hexane) at Metal–Organic Frameworks," *Nanomaterials* 12 (2022): 3614, https://doi.org/10.3390/nano12203614.

54. S. Nießing and C. Janiak, "Studies on Catalytic Activity of MIL-53(Al) and Structure Analogue DUT-5(Al) Using Bdc- and Bpdc-Ligands Functionalized with l-Proline in a Solid-Solution Mixed-Linker Approach," *Molecular Catalysis* 467 (2019): 70–77, https://doi.org/10.1016/j.mcat.2019.01.029.

55. H. Fan, L. Nurtay, N. E. Safronov, P. A. Slepukhin, N. P. Belskaya, and E. Benassi, "Aggregation-Caused Quenching or Aggregation-Induced (Enhanced) Emission? the Decisive Role of Aggregation in Solvents and Their Mixtures," *Journal of Molecular Liquids* 433 (2025): 127901, https://doi.org/10.1016/j.molliq.2025.127901.

56. H. Xu and P. Cheng, "Metal–organic Frameworks with Aggregation-induced Emission," *Aggregate* 5 (2024): e518, https://doi.org/10.1002/agt2.518.

57. A. Eisfeld and J. S. Briggs, "The J- and H-Bands of Organic Dye Aggregates," *Chemical Physics* 324 (2006): 376–384, https://doi.org/10.1016/j.chemphys.2005.11.015.

58. K. Müller-Buschbaum, F. Beuerle, and C. Feldmann, "MOF Based Luminescence Tuning and Chemical/Physical Sensing," *Microporous and Mesoporous Materials* 216 (2015): 171–199, https://doi.org/10.1016/j.micromeso.2015.03.036.

59. M. J. Frisch, G. W. Trucks, H. B. Schlegel, et al., *Gaussian 09, Revision A.02*. (Gaussian Inc., 2016).

60. A. D. Becke, "Density-Functional Exchange-Energy Approximation with Correct Asymptotic Behavior," *Physical Review. A, Atomic, Molecular, and Optical Physics* 38 (1988): 3098–3100, https://doi.org/10.1103/PhysRevA.38.3098.

61. C. Lee, W. Yang, and R. G. Parr, "Development of the Colle-Salvetti Correlation-Energy Formula into a Functional of the Electron Density," *Physical Review. B* 37 (1988): 785–789, https://doi.org/10.1103/PhysRevB.37.785.

62. J. Wang, J. Wu, L. Lu, et al., "Two Chemically Stable Cd(II) Polymers as Fluorescent Sensor and Photocatalyst for Aromatic Dyes," *Polymers* 10 (2018): 274, https://doi.org/10.3390/polym10030274.

63. N. Jodaeeasl, S. Wang, A. Hu, and G. H. Peslherbe, "Comprehensive DFT Investigation of Small-Molecule Adsorption on the Paradigm M-MOF-74 Family of Metal–organic Frameworks," *Physical Chemistry Chemical Physics* 27 (2025): 3068–3082, https://doi.org/10.1039/D4CP02873B.

64. D. Adhikari, R. Karki, K. Adhikarki, and N. Pantha, "Mg-MOF-74: A Novel Material for Adsorption and Detection of Toxic Gases," *AIP Advances* 15 (2025): 025314, https://doi.org/10.1063/5.0249796.

65. C. Waldhans, A. Albrecht, R. Ibald, D. Wollenweber, S.-J. Sy, and J. Kreyenschmidt, "Temperature Control and Data Exchange in Food Supply Chains: Current Situation and the Applicability of a Digitalized System of Time–Temperature-Indicators to Optimize Temperature Monitoring in Different Cold Chains," *Journal of Packaging Technology and Research* 8 (2024): 79–93, https://doi.org/10.1007/s41783-024-00165-2.

66. P. C. Hariharan and J. A. Pople, "The Influence of Polarization Functions on Molecular Orbital Hydrogenation Energies," *Theoretica Chimica Acta* 28 (1973): 213–222, https://doi.org/10.1007/BF00533485.

67. F. E. King, R. M. Acheson, and A. B. Yorke-Long, "389. The Synthesis of 7-Amino-Alloxazines and -Isoalloxazines," *Journal of the Chemical Society* 151 (1948): 1926–1931, https://doi.org/10.1039/JR9480001926.

68. J. J. Hasford and C. J. Rizzo, "Linear Free Energy Substituent Effect on Flavin Redox Chemistry," *Journal of the American Chemical Society* 120 (1998): 2251–2255, https://doi.org/10.1021/ja972992n.

Supporting Information

Additional supporting information can be found online in the Supporting Information section.

Supporting Information

Investigations on the Luminescence Behavior of a Flavin Derivative Incorporated into Al-based Metal-Organic Frameworks for the Sensing of Aromatic Nitro Compounds

Annette Vollrath[a], Vasily Gvilava[a], Philipp Seiffert[a], Constantin Czekelius[b] and Christoph Janiak[a]*

[a] Institut für Anorganische Chemie und Strukturchemie, Heinrich-Heine-Universität Düsseldorf, D-40225 Düsseldorf, Germany

[b] Institut für Organische Chemie und Makromolekulare Chemie, Heinrich-Heine-Universität Düsseldorf, D-40225 Düsseldorf, Germany

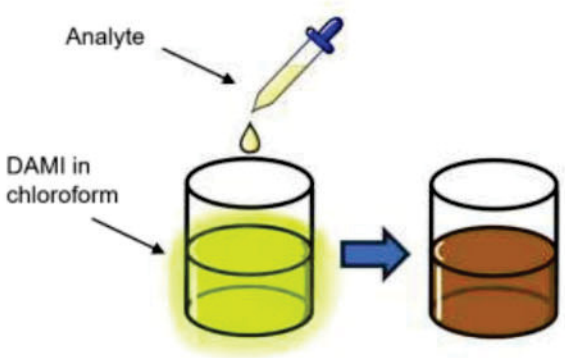
Emails:

annette.vollrath@hhu.de; vasily.gvilava@gmail.com; philipp.seiffert@hhu.de; constantin.czekelius@hhu.de

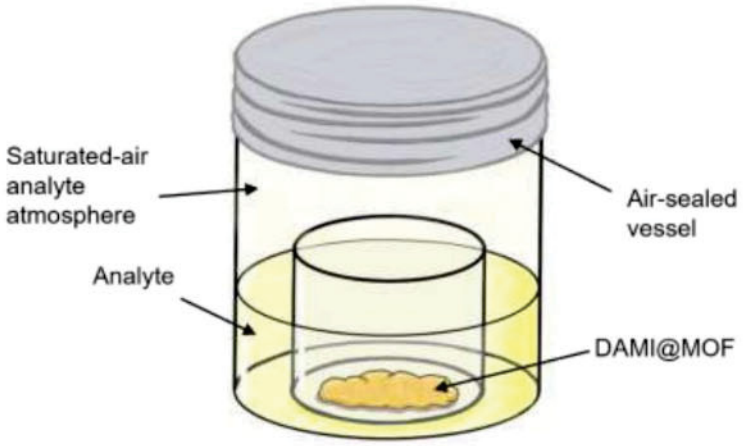
Table of contents

S1. Experimental Setup for Sensing Experiments 2
S2. Al-based MOFs 3
S3. PXRD 4
S4. Nitrogen sorption analysis 5
S5. TGA 6
S6. FT-IR spectra 7
S7. UV/Vis spectroscopy 8
S8. Calculations 9
S9. Fluorescence behavior 10
S10. References 15

S1. Experimental Setup for Sensing Experiments



a)



b)

Figure S1. Schematic illustration of the quenching experiment setup a) with DAMI dissolved in chloroform and b) with the solid composites under the saturated-air vapor atmosphere of the arene or nitroarene analytes (25 °C, defined exposure time).

S2. Al-based MOFs

Using 2,6-naphthalenedicarboxylate (ndc^{2-}) as a linker, DUT-4 (DUT = Dresden University of Technology) can be synthesized.[1] The three-dimensional framework has rectangular tunnel with a cross-section of 8.5 x 8.5 Å (Figure S2a). It is the porous analog of the previously known non-porous MIL-69.[2]

With biphenyl-4,4'-dicarboxylate ($bpdc^{2-}$), DUT-5 is obtained.[1] The framework structure is the same as in DUT-4, but the pores are larger with a cross-section of 11.1 x 11.1 Å (Figure S2b).

The first reports on Al-based MOFs were published by Férey and co-workers.[3] They introduced MIL-53 (MIL = Matériaux de l´Institut Lavoisier, Materials of Institute Lavoisier) [Al(OH)(bdc)], which consists of trivalent aluminium as the inorganic building block and benzene-1,4-dicarboxylate (bdc^{2-}) as the linker (Figure S2c). It forms one-dimensional rhombic channels with a cross-section of 8.4 x 12 Å for the large-pore form. This MOF exhibits a special property known as the "breathing effect".[4,5,6] The pore size changes between a narrow pore form, when water or small gas molecules are incorporated, and a large-pore form which is obtained upon activation.

The DAMI dye in this project has a dimension of 5.85 x 10.3 Å and fits into the pores or tunnels of the Al-MOFs used here.

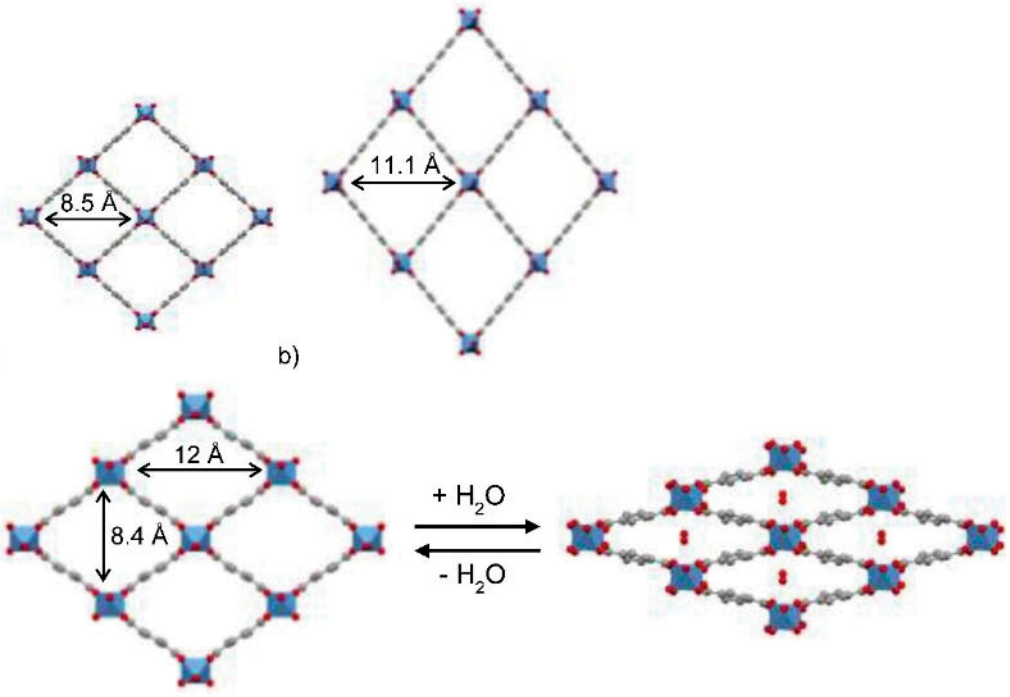
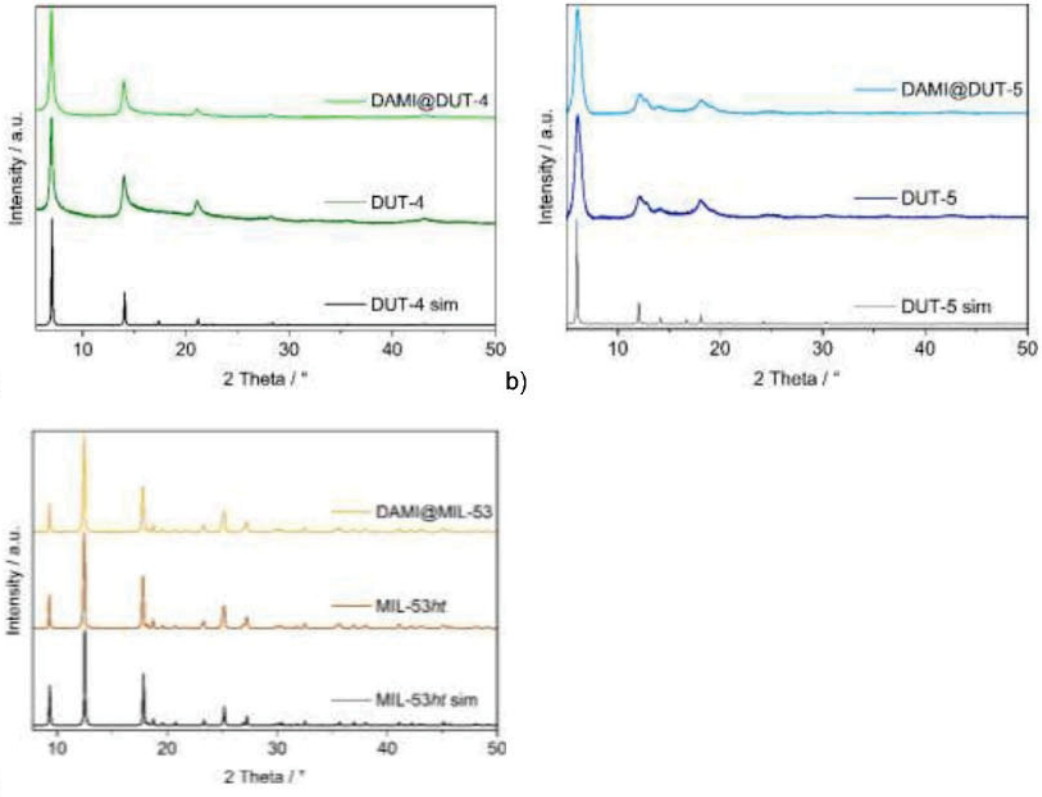


Figure S2. Structure of a) DUT-4, b) DUT-5 and c) MIL-53 (left: large pore form, right: narrow pore form). The structures were created from the CCDC cif-files 691978 (DUT-4),[1] 691979 (DUT-5),[1] 220475 (MIL-53-lp),[3] and 220477 (MIL-53-np).[3]

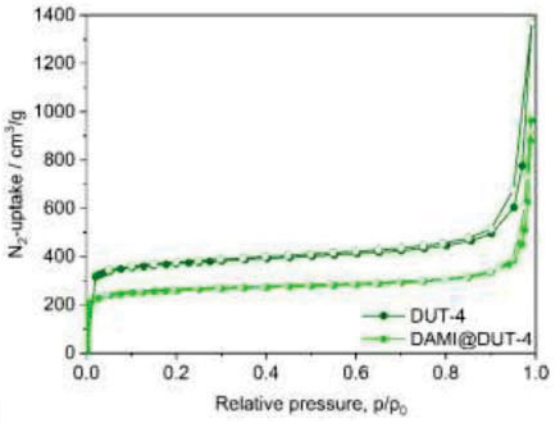
61 **S3. PXRD**



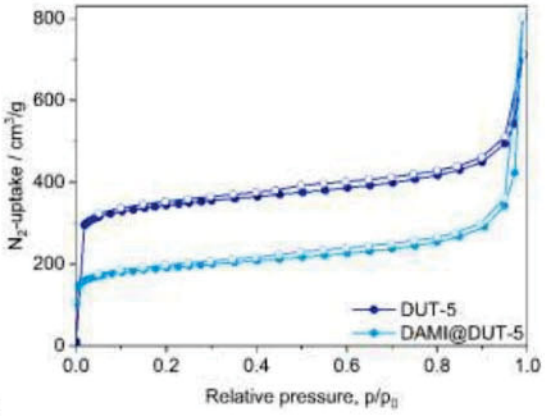
64 **Figure S3.** PXRD patterns of the neat MOFs and the composites compared with the simulated patterns
65 for a) DUT-4 (CSD-Refcode: 691978)[1], b) DUT-5 (CSD-Refcode: 691979)[1], c) MIL-53*ht* (large-pore
66 form) (CSD-Refcode: 220475)[3].

67

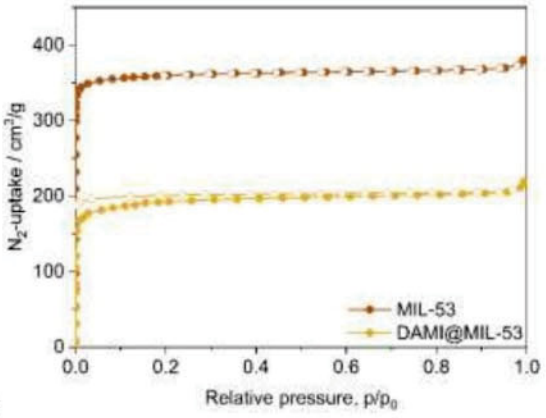
S4. Nitrogen sorption analysis



a)



b)



c)

Figure S4. Nitrogen-sorption isotherms at 77 K of the neat MOFs compared with the isotherms of the composites for a) DUT-4, b) DUT-5, c) MIL-53. The filled symbols represent the adsorption branch, the empty symbols represent the desorption branch.

S5. TGA

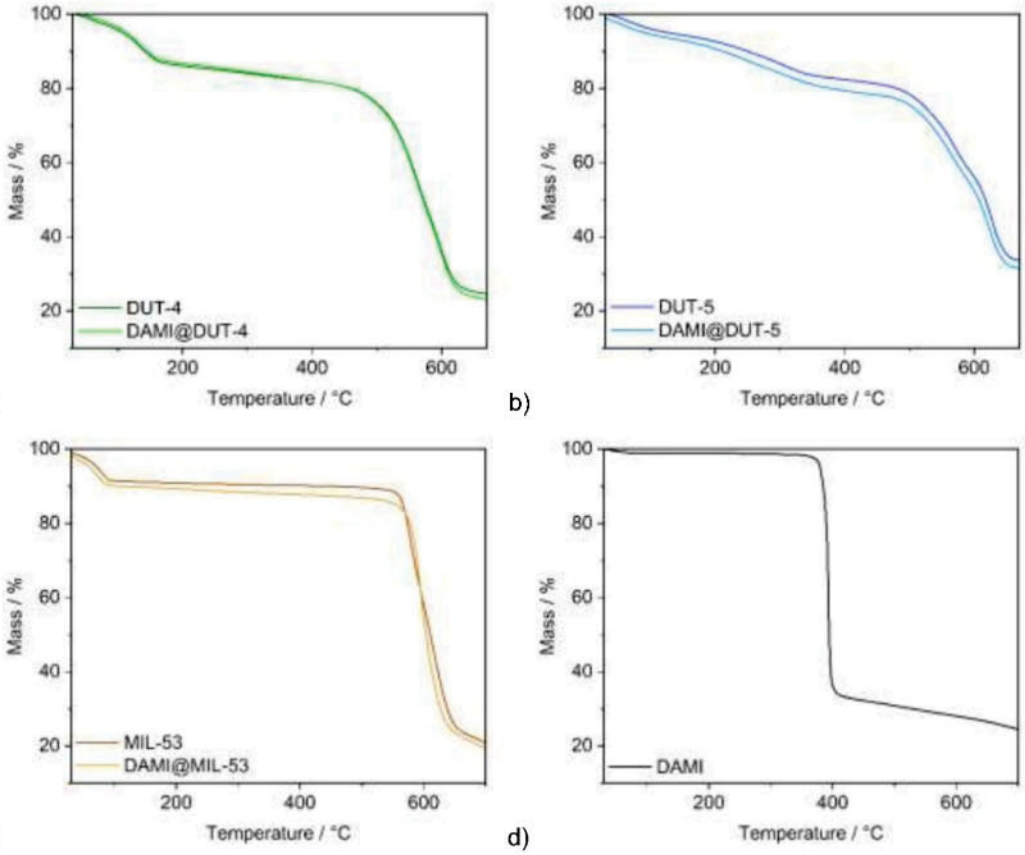


Figure S5. TGA curves of the neat MOFs compared with the TGA curves of the composites for a) DUT-4, b) DUT-5, c) MIL-53 and d) DAMI under nitrogen atmosphere with a heating rate of 10 K/min.

S6. FT-IR spectra

In the region between 1400 cm^{-1} and 1700 cm^{-1} the absorption bands for the carboxylate group of the linkers appear. The bands in the area between 1508 cm^{-1} and 1630 cm^{-1} are attributed to the -COO asymmetric stretch and the bands between 1409 cm^{-1} and 1444 cm^{-1} to the -COO symmetric stretch. In the IR spectra of MIL-53 and the respective composite, the narrow absorption band at 3612 cm^{-1} is assigned to the μ-OH group bridging the aluminum atoms. In DUT-4 and DUT-5, narrow bands in the 3650–3700 cm^{-1} region are attributed to terminal or weakly hydrogen-bonded OH groups, likely associated with hydroxyl moieties at the metal clusters.

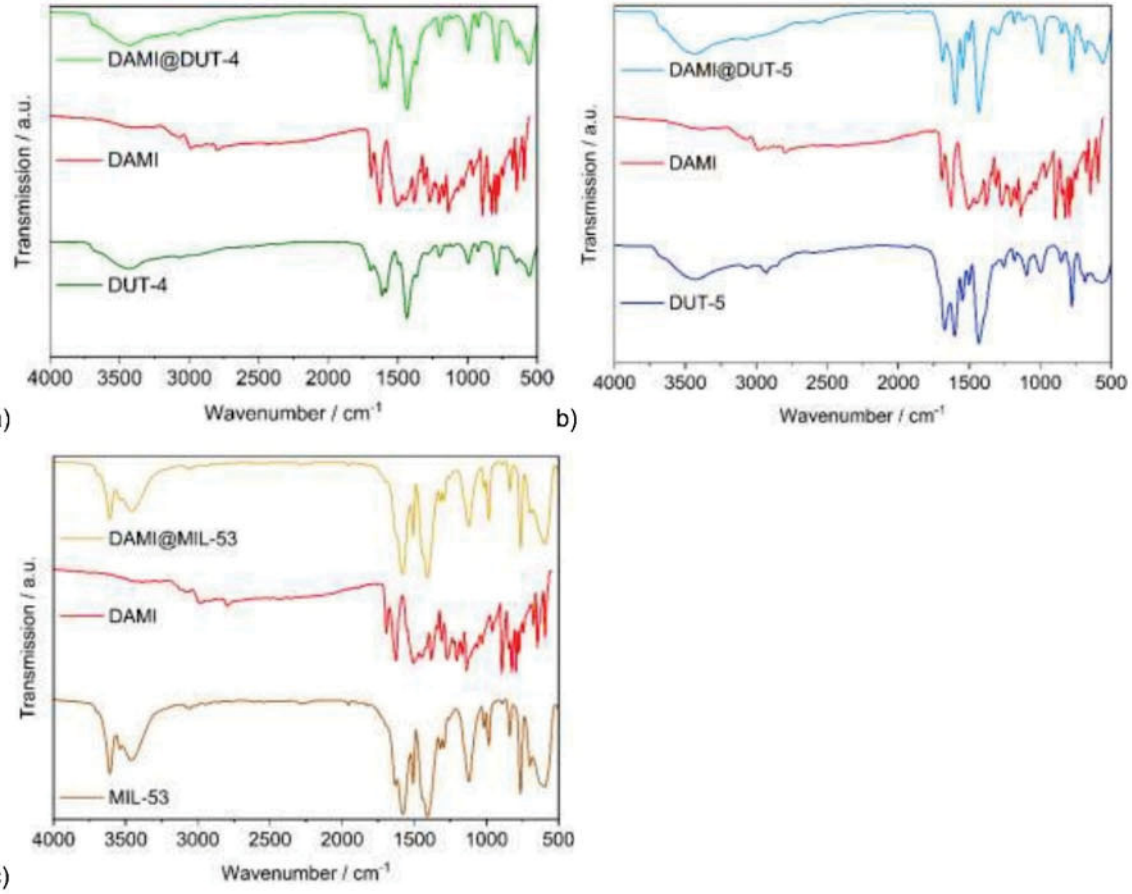


Figure S6. IR-spectra of the neat MOFs, compared with the IR spectra of DAMI and of the composites for a) DUT-4, b) DUT-5, c) MIL-53.

S7. UV/Vis spectroscopy

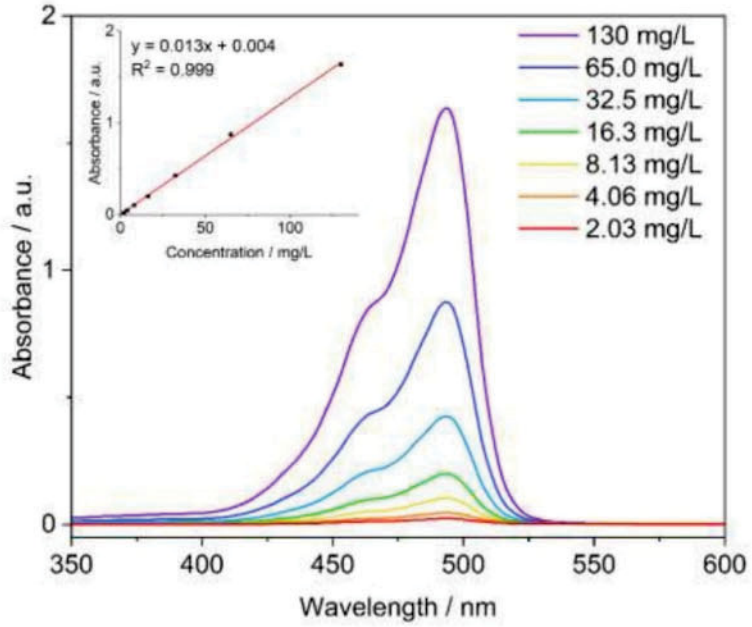


Figure S7. UV/Vis measurements and calibration curve for the determination of the DAMI concentration of the saturated dye solution.

Table S1. Determination of the DAMI loading in the DAMI@MOF composites using the UV/Vis spectroscopy by comparing the intensities of the dye solution before and after the incorporation.

Sample	Intensity at λ_{em} = 493 nm	Dye concentration of the supernatant after incorporation [mg/L]	Concentration of the saturated solution [mgL]	Loading [wt%]
DAMI@DUT-4	1.873	143.8	174.2	0.15
DAMI@DUT-5	1.745	133.9	174.2	0.20
DAMI@MIL-53	2.030	155.8	174.2	0.10

S8. Calculations

8.1 Dye loading

$$dye\ loading\ (wt\%) = \frac{mass\ of\ incorporated\ DAMI}{mass\ of\ DAMI@MOF} \times 100\% \quad (1)$$

The spectroscopic analysis showed that composites could be produced with a dye loading of 0.15 wt% in DUT-4, 0.20 wt% in DUT-5 and 0.10 wt% in MIL-53 corresponding to a filling of the pore volume of 74%, 36% and 47%, respectively. For the molar ratio mol(DAMI) per formula unit of the MOF by using the following formula

$$dye\ loading\ (mol\%) = \frac{mol\ of\ incorporated\ DAMI}{mol\ (DAMI) + mol(MOF)} \times 100\% \quad (2)$$

giving results of 0.38 mmol% in DUT-4, 0.31 mmol% in DUT-5 and 0.35 mmol% in MIL-53.

8.2 Quenching/enhancement efficiency

$$quenching\ (\%) = \frac{I_0 - I}{I_0} \times 100\% \quad (3)$$

$$enhancement\ (\%) = \frac{I - I_0}{I_0} \times 100\% \quad (4)$$

I_0 = fluorescence intensity before exposure to the analyte

I = fluorescence intensity after exposure to the analyte

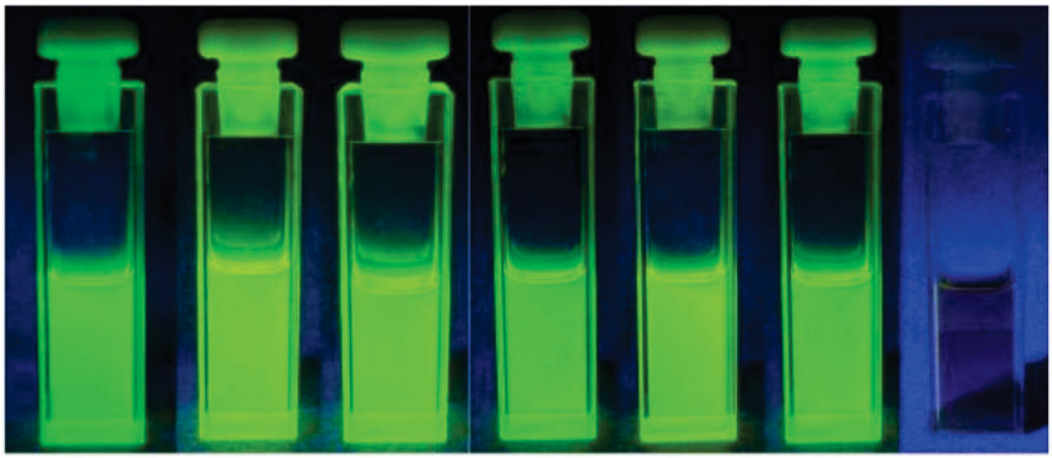
8.3 Theoretical calculations

Table S2. Vapor pressures and calculated HOMO and LUMO energies in eV of DAMI and the analytes obtained from density functional theory (DFT, basis set B3LYP/6-31G (d,p)).

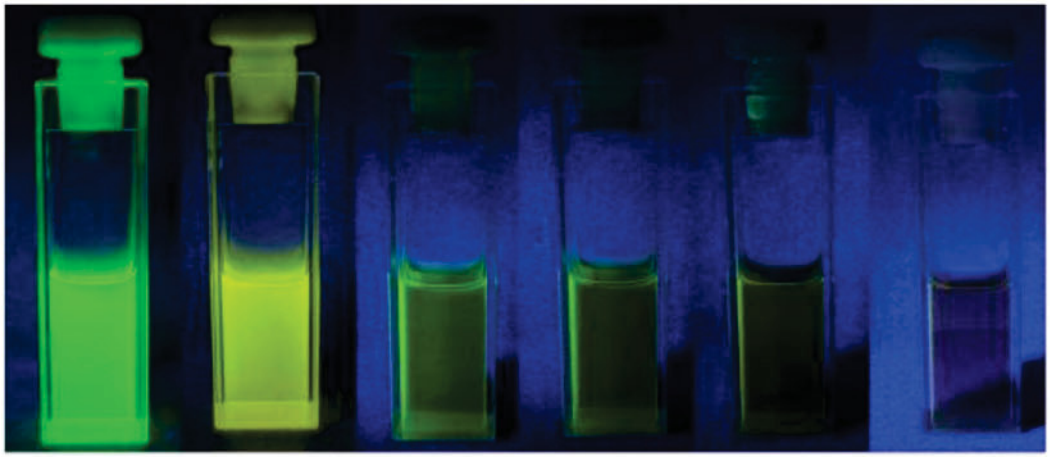
Analyte	Vapor pressure [mmHg] at 25 °C [a]	E_{HOMO} [eV]	E_{LUMO} [eV]	$\Delta E_{HOMO-LUMO}$ [eV]
DAMI	-	-5.822	-2.520	3.302
Nitrobenzene (NB)	0.24	-7.956	-2.918	5.038
4-Nitrotoluene (4-NT)	0.02	-7.702	-2.789	4.913
4-Nitrophenol (4-NP)	$5.00 \cdot 10^{-4}$	-7.346	-2.745	4.601
2,6-Dinitrotoluene (2,6-DNT)	$5.67 \cdot 10^{-4}$	-8.459	-3.416	5.043
Nitromethane (NM)	35.8	-8.551	-2.556	6.095
Benzene (B)	95.2	-6.739	-0.465	6.274
Toluene (T)	28.4	-6.300	-0.175	6.125
Chlorobenzene (ClB)	11.8	-7.007	-0.865	6.142

[a] Data of the vapor pressures for the nitro-containing compounds are found in literature 7 and for the non-nitro-containing compounds in 8.

S9. Fluorescence behavior



a)



b)

Figure S8. Quenching test by adding different solvents to dissolved DAMI in 1 mL chloroform (c = 0.1 mg/mL, $3.69 \cdot 10^{-4}$ mol/L).
(a) added solvent (0.5 mL each): (B = benzene, T = toluene, ClB = chlorobenzene, M = mesitylene, *p*-X = *para*-xylene, NB = nitrobenzene.
(b) added solvent (0.5 mL each): NM = nitromethane, 4-NT = 4-nitrotoluene, 2,6-DNT = 2,6-dinitrotoluene, 4-NP = 4-nitrophenol, NB = nitrobenzene.

Table S3. Photophysical data for DAMI in solution, and for the DAMI@MOF composites before and after treatment with NB.

Sample	$\lambda_{F,max}$ [nm] [a]	τ_1 (x_1), τ_2 (x_2), τ_3 ($x3$) [ns] [b]	τ_x [ns] [c]
DAMI in $CHCl_3$ [0.1 mg/mL]	522	5.9 (1.00)	5.9
DAMI@DUT-4	541	10.5 (0.91), 24.1 (0.09)	11.7
NB@DAMI@DUT-4	543	11.5 (0.35), 4.2 (0.65)	6.7
DAMI@DUT-5	555	0.9 (0.56), 4.2 (0.35), 8.6 (0.08)	2.7
NB@DAMI@DUT-5	556	0.9 (0.78), 4.0 (0.19), 9.2 (0.03)	1.6
DAMI@MIL-53	541	2.8 (0.03), 0.5 (0.97), 6.7 (0.004)	0.6
NB@DAMI@MIL-53	530	1.9 (0.02), 0.3 (0.98), 5.4 (0.004)	0.3

[a] Wavelength of the fluorescence maximum; λ_{exc} = 365 nm. [b] Fluorescence lifetime (λ_{exc} = 375 nm): τ_i (x_i) species i lifetime (fraction). [c] τ_x species-weighted average lifetime.

Table S4. Vapor pressures and vapor-pressure-normalized fluorescence responses of DAMI@MOFs at 25 °C.

Analyte	Vapor pressure [mmHg, 25 °C] [a]	DUT-4		DUT-5		MIL-53	
		Quenching [%]	Relative response index [b]	Quenching [%]	Relative response index [b]	Quenching [%]	Relative response index [b]
2,6-DNT	$5.67 \cdot 10^{-4}$	14.8	72.0	7.60	37.0	63.4	341
4-NP	$5.00 \cdot 10^{-4}$	16.6	71.2	13.9	59.7	53.1	252
4-NT	0.02	17.6	2.14	14.4	1.75	64.0	8.60
NM	35.8	23.4	0.0016	50.5	0.0034	47.7	0.0036
NB	0.24	98.7	1.00	98.6	1.00	89.3	1.00

[a] Data of the vapor pressures for the nitro-containing compounds are found in literature 7.
[b] Relative response index calculated as $(Q/p_{vap})/(Q_{NB}/p_{vap,NB})$, where Q is the fluorescence quenching percentage and p_{vap} is the vapor pressure at 25 °C.

Table S5. Vapor-pressure-normalized fluorescence enhancement responses.

Analyte	Vapor pressure [mmHg, 25 °C] [a]	DUT-4		DUT-5		MIL-53	
		Enhancement [%]	Relative response index [b]	Enhancement [%]	Relative response index [b]	Enhancement [%]	Relative response index [b]
CIB	11.8	7.83	0.99	48.0	1.08	22.0	0.35
B	95.2	10.8	0.17	79.1	0.22	89.4	0.18
T	28.4	19.0	1.00	108	1.00	151	1.00

[a] Data of the vapor pressures for the non-nitro-containing compounds are found in literature 8.
[b] Relative response index calculated as $(E/p_{vap})/(E_T/p_{vap,T})$, where E is the fluorescence enhancement percentage and p_{vap} is the vapor pressure at 25 °C.

The normalized values provide a qualitative comparison of the fluorescence response relative to the vapor-phase availability of the analytes. They should not be interpreted as intrinsic quenching or

enhancement constants, as adsorption affinity, molecular size, diffusion, and analyte–framework interactions also contribute to the overall response.

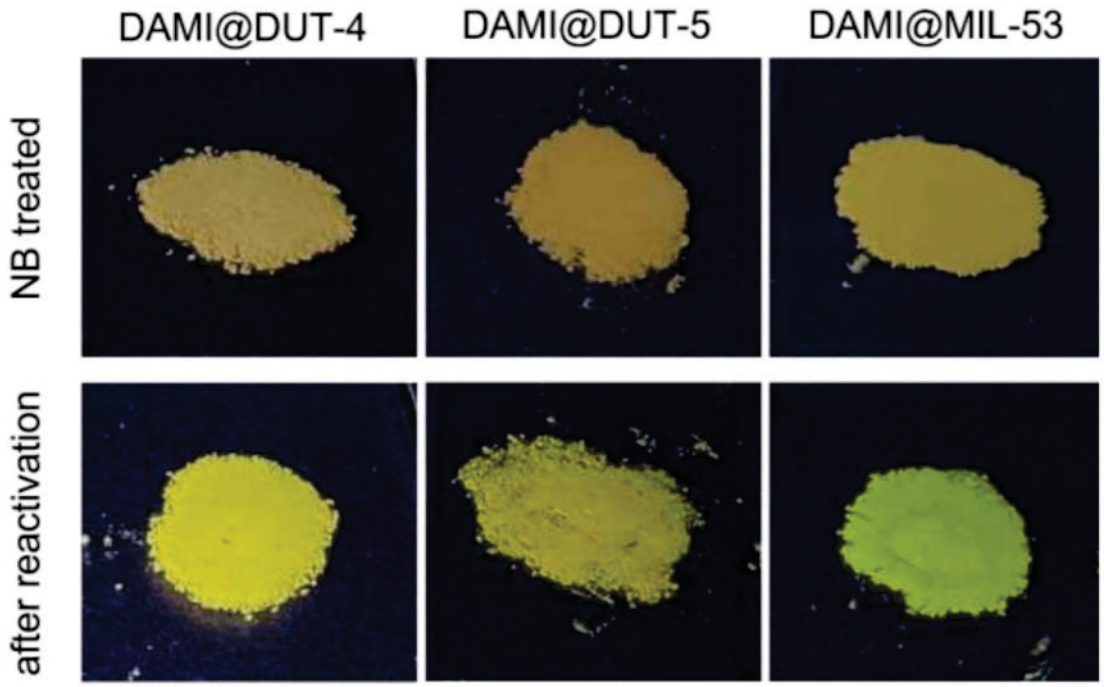


Figure S9. Pictures of treated composites under a nitrobenzene atmosphere taken under a UV-lamp before (top) and after new activation (bottom) under vacuum at 130 °C for 2 h.

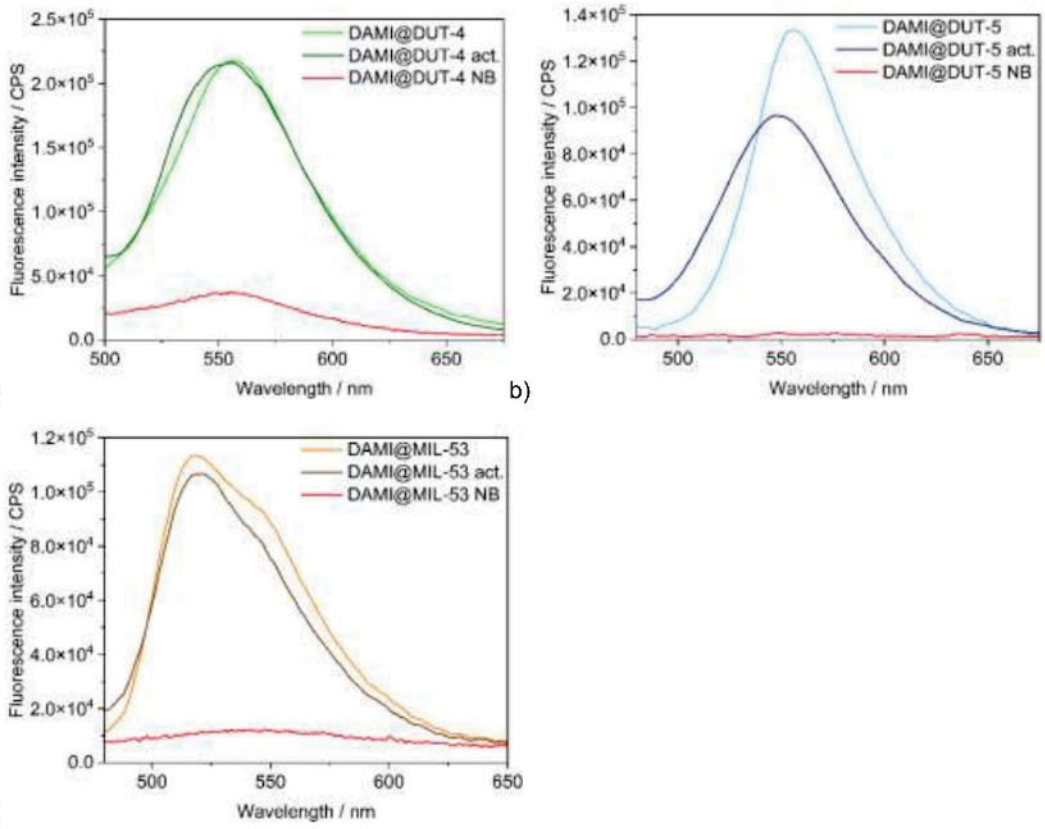


Figure S10. Fluorescence spectra of composites, treated in nitrobenzene atmosphere, before and after new activation under vacuum at 130 °C for 2 h.

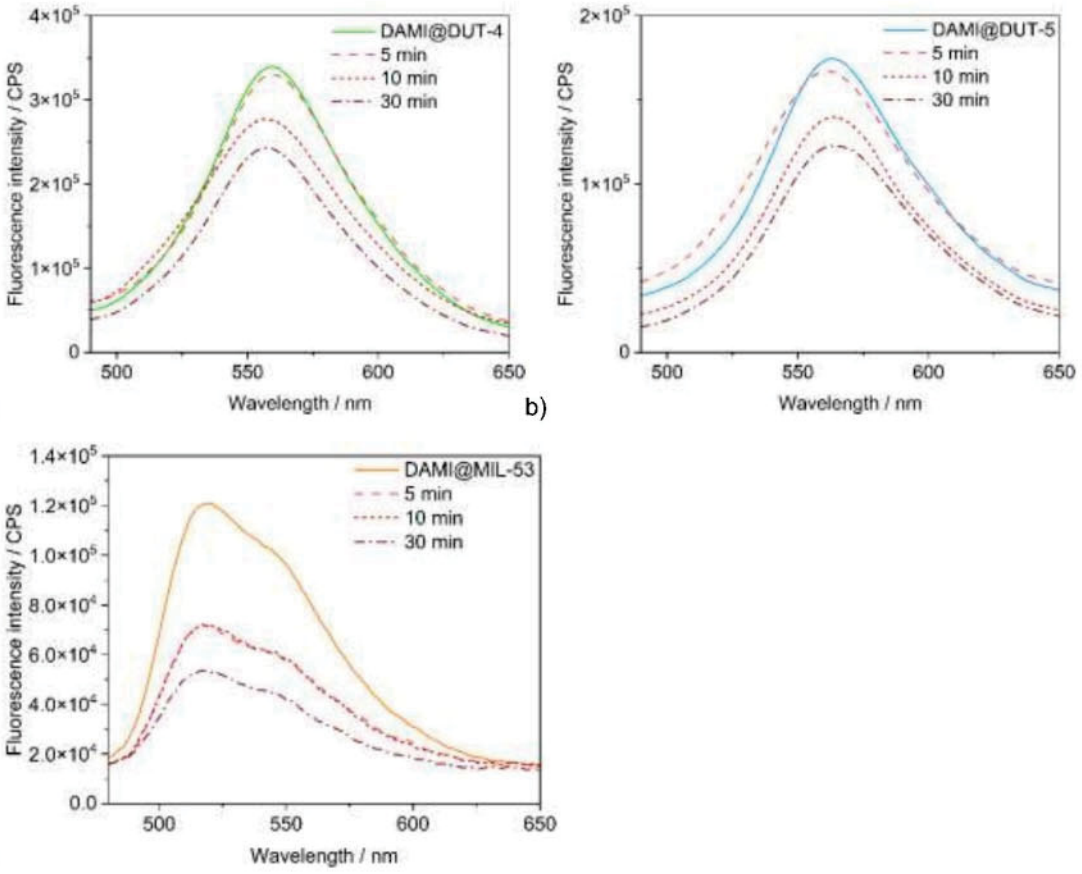
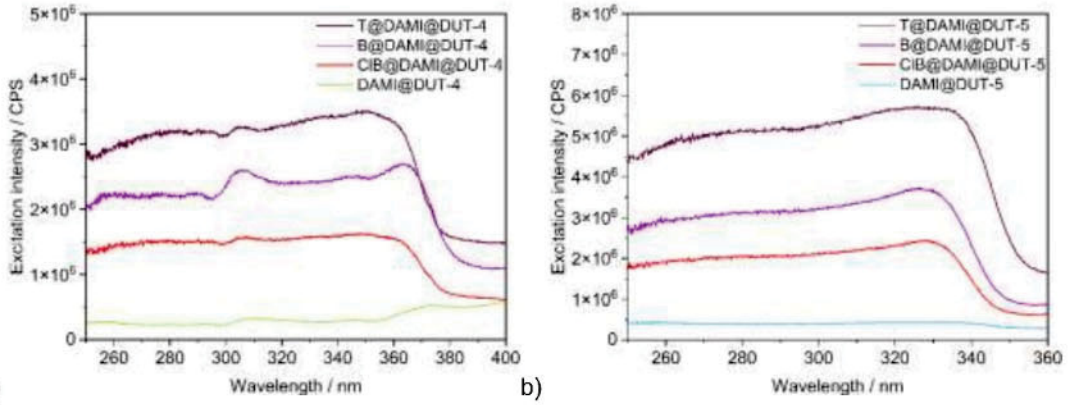
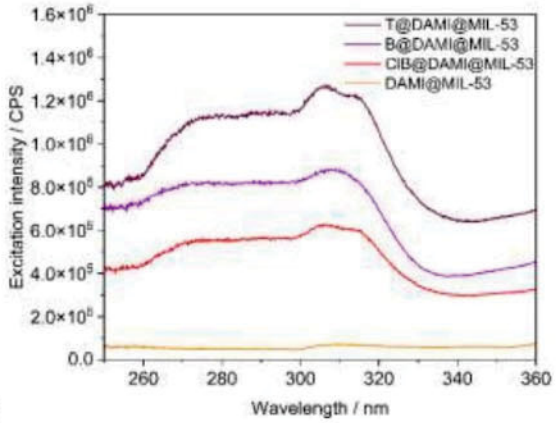


Figure S11. Time-dependent fluorescence quenching of the composites in nitrobenzene atmosphere.



174 a) b)



175 c)

176 **Figure S12.** Excitation spectra of the DAMI@MOF composites before and after exposure to toluene (T),
177 benzene (B), and chlorobenzene (ClB) vapors. λ_{em} = 541 nm for DUT-4 and MIL-53, λ_{em} = 555 nm for
178 DUT-5.

179

180

181 **S10. References**

[1] I. Senkovska, F. Hoffmann, M. Fröba, J. Getzschmann, W. Böhlmann, S. Kaskel, *Microporous Mesoporous Mater.* **2009**, *122*, 93-98.
[2] T. Loiseau, C. Mellot-Draznieks, H. Muguerra, G. Férey, M. Jaouas, F. Taulelle, *C. R. Chimie* **2005**, *8*, 765-772.
[3] G. Férey, M. Latroche, C. Serre, F. Millange, T. Loiseau, A. Percheron Guégan, *Chem. Commun.* **2003**, 2976-2977.
[4] T. Loiseau, C. Serre, C. Huguenard, G. Fink, F. Taulelle, M. Henry, T. Bataille, G. Férey, *Chem. Eur. J.* **2004**, *10*, 1373-1382.
[5] C. Serre, S. Bourrelly, A. Vimont, N. A. Ramsahye, G. Maurin, P. L. Llewellyn, M. Daturi, Y. Filinchuk, O. Leynaud, P. Barnes, G. Férey, *Adv. Mater.* **2007**, *19*, 2246-2251.
[6] G. Férey, C. Serre, *Chem. Soc. Rev.* **2009**, *38*, 1380-1399.
[7] https://haz-map.com, accessed 27.05.2026.
[8] T. E. Daubert, R. Danner (1989). Physical and Thermodynamic Properties of Pure Chemicals: Data Compilation. Washington, D.C.: Taylor and Francis, p. 361.

3.3 From Aggregation to Isolation: Preserving MR-TADF Emission of DiKTa in MOF-5

Diese Arbeit wurde eingereicht in

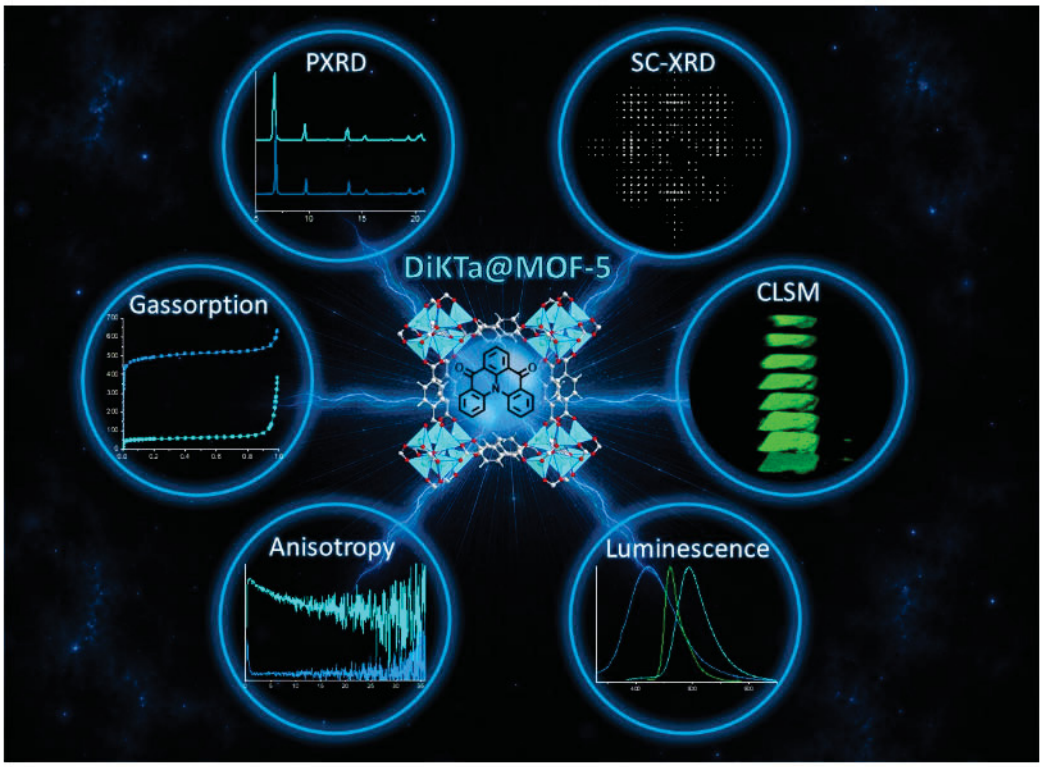
Annette Vollrath,‡ Marcus N. A. Fetzer,‡ Jennifer Kremper,‡ Benedikt Bendel, Ralf Kühnemuth, Markus Suta, Jan Meisner, Oliver Weingart, Christoph Janiak

Adv. Opt. Mater. **2026**

‡ Diese Autoren haben zu gleichen Teilen an dieser Publikation beigetragen.

Kurzzusammenfassung

In dieser Arbeit berichten wir über die erstmalige Einbindung des multiresonanten TADF-Emitters DiKTa (Chinolino-[3,2,1-*de*]acridin-5,9-dion) in ein mikroporöses metallorganisches Gerüst (MOF). DiKTa zählt zu den vielversprechenden Schmalbandemittern für organische Leuchtdioden (OLEDs), dessen photophysikalische Eigenschaften im Festkörper jedoch maßgeblich durch Aggregation, Molekülpackung und Orientierung beeinflusst werden. Durch die Einlagerung in die definierten Poren von MOF-5 konnten die Farbstoffmoleküle räumlich voneinander isoliert, orientiert und stabilisiert werden und bietet eine Plattform, um dessen Photophysik über herkömmliche Festkörper- oder Lösungssysteme hinaus zu untersuchen und zu optimieren. Aufgrund der passenden Porengröße wurde MOF-5 als Wirtsmaterial ausgewählt. Die DiKTa@MOF-5-Komposite wurden in Form von Einkristallen mit unterschiedlichen Farbstoffbeladungen durch eine solvothermale *in situ*-Synthese hergestellt. Umfangreiche strukturelle und photophysikalische Untersuchungen bestätigten eine intensive Lumineszenz sowie eine deutliche Abhängigkeit der optischen Eigenschaften von der Beladung. Im Vergleich zu DiKTa in Lösung zeigten die Komposite nur eine geringfügige Verbreiterung der Emissionsbanden, während die zeitaufgelösten Messungen vergleichbare Zerfallszeiten ergaben. Fluoreszenzanisotropiemessungen lieferten Hinweise auf eine bevorzugte Orientierung der DiKTa-Moleküle innerhalb der MOF-Poren. Ergänzende BET- und PXRD-Analysen zeigten den Einfluss der Farbstoffbeladung auf die Porosität und die strukturelle Integrität des Gerüsts. Darüber hinaus ermöglichten QM/MM-Berechnungen ein detailliertes Verständnis des multiresonanten TADF-Verhaltens von DiKTa innerhalb der dynamischen Umgebung.



Anteile an der Veröffentlichung

- Konzeption des Forschungsvorhabens gemeinsam mit Dr. M. N. A. Fetzer und Prof. Dr. C. Janiak.
- Entwicklung der Methodik gemeinsam mit Dr. M. N. A. Fetzer.
- Durchführung der experimentellen Untersuchungen gemeinsam mit Dr. M. N. A. Fetzer, B. Bendel und Dr. R. Kühnemuth.
- Durchführung der Validierung, Datenaufbereitung sowie formalen Auswertung der experimentellen Ergebnisse gemeinsam mit Dr. M. N. A. Fetzer und J. Kremper.
- Selbstständige graphische Darstellung und Visualisierung der experimentellen Ergebnisse gemeinsam mit Dr. M. N. A. Fetzer.
- Anfertigung des Manuskripts (Erstentwurf) gemeinsam mit Dr. M. N. A. Fetzer und J. Kremper.
- Wissenschaftliche Betreuung, Auswertung der Ergebnisse sowie Überarbeitung des Manuskripts durch Prof. Dr. M. Suta, Prof. Dr. J. Meisner, Dr. O. Weingart und Prof. Dr. C. Janiak.
- Bereitstellung der Ressourcen durch Prof. Dr. C. Janiak.
- Projektadministration und Einwerbung der Drittmittel durch Prof. Dr. M. Suta, Prof. Dr. J. Meisner, Dr. O. Weingart und Prof. Dr. C. Janiak.

From Aggregation to Isolation: Preserving MR-TADF Emission of DiKTa in MOF-5

Annette Vollrath,‡[a] Marcus N. A. Fetzer,‡[a] Jennifer Kremper,‡[b,c] Benedikt Bendel,[d] Ralf Kühnemuth,[e] Markus Suta,[d] Jan Meisner,*[b] Oliver Weingart,*[c,f] and Christoph Janiak*[a]

[a]Inorganic and Structural Chemistry, Heinrich Heine University Düsseldorf, Universitätsstraße 1, D-40225 Düsseldorf, Germany

[b]Institute for Physical Chemistry, Theory and Simulation of Complex Systems, Heinrich Heine University Düsseldorf, Universitätsstr. 1, 40225 Düsseldorf, Germany

[c]Institute for Theoretical and Computational Chemistry, Photodynamics, Heinrich Heine University Düsseldorf, Universitätsstr. 1, 40225 Düsseldorf, Germany

[d]Inorganic Photoactive Materials, Heinrich Heine University Düsseldorf, Universitätsstraße 1, D-40225 Düsseldorf, Germany

[e]Institute for Molecular Physical Chemistry, Heinrich Heine University Düsseldorf, Universitätsstraße 1, D-40225 Düsseldorf, Germany

[f]Center for Information and Media Technology, Heinrich Heine University Düsseldorf, Universitätsstraße 1, 40225 Düsseldorf, Germany.

‡ These authors contributed equally to this work.

* Corresponding authors

Keywords:

DiKTa; metal-organic framework; solid-solution; thermally activated delayed fluorescence (TADF); multi-resonance; QM/MM calculations

Abstract:

We report the first incorporation of the multi-resonant thermally activated delayed fluorescence (TADF) emitter DiKTa (quinolino-[3,2,1-*de*]acridine-5,9-dione) into a microporous metal-organic framework (MOF). DiKTa is a narrowband emitter with high relevance for organic light-emitting diodes (OLEDs), but its solid-state performance is strongly influenced by aggregation, molecular packing, and orientation. Encapsulating DiKTa in MOF-5 provides a defined porous environment that spatially isolates, orients

and stabilizes the emitter, controls its local arrangement, and offers a platform to study and tune its photophysics beyond conventional solid-state or solution systems. Based on the molecular dimensions of DiKTa, MOF-5 is selected as a host due to its suitable pore size. DiKTa@MOF-5 composites with different emitter loadings are synthesized as single crystals via solvothermal in situ synthesis. Structural and photophysical analyses reveal bright emission, loading-dependent properties, and slightly broadened full width at half maximum values compared to DiKTa in solution. Time-resolved measurements show decay times comparable to solution-phase DiKTa. Fluorescence anisotropy reveals the preferred orientation of DiKTa inside the MOF pores, while BET and PXRD analyses clarify how loading affects porosity and framework integrity. QM/MM calculations further describe the multi-resonant TADF behavior in a dynamic environment.

1. Introduction

Over the last few decades, the interest in new organic chromophores has increased significantly, due to their potential application in OLEDs in electronic devices such as smartphones, TVs or other types of displays.[1-3] These new compounds provide a simple, efficient and cost-effective alternative to the commonly used noble metal-based phosphorescent emitters.[4-6] One of the major problems is the low internal quantum efficiency of only 25% from the excited singlet state upon injection of charge carriers compared to 75% from the excited triplet states according to spin statistics. To overcome this problem, the concept of thermally activated delayed fluorescence (TADF) emitters, known since the beginning of the 20th century, is of great interest.[7-11] It relies on a thermally accessible energy gap ΔE_{ST} between these S_1 and T_1 excited states to favor fast reverse intersystem crossing at ambient temperature, where a significant part of the triplet excitons can be converted to the emitting singlet state which formally allows harvesting 100% of the electrically generated excitons. As a result, TADF materials have the potential to achieve internal quantum efficiencies approaching 100%.[12-13] The energy gap is largely determined by the overlap between the highest occupied molecular orbital (HOMO) and the lowest unoccupied molecular orbital (LUMO).[14-17] The vast majority of TADF emitters are based on a twisted and separated donor-acceptor architecture on a molecular scale, where the HOMO is located on the donor and the LUMO on the acceptor. This type of structure exploits a structurally imposed limited overlap of HOMO and LUMO but has the disadvantage of

rotational degrees of freedom, which leads to a broadening of the emission band with full widths at half maximum (FWHMs) in the range of 80-200 nm on a wavelength scale (≥ 3809 cm^{-1}). For display applications, in which high color purity and a wide color gamut are demanded, these FWHMs are still too large.[18-20] A common solution to this issue is an enhancement of structural rigidity, which was realized by Hatakeyama *et al.*[21] with the class of multi-resonant TADF (MR-TADF) emitters. A common representative of this class of emitters is DABNA-1 with a strongly extended π-conjugated, covalently fused backbone and orthogonal positioning of electron-donating (e.g., N, O, P, S) and -deficient functionalities (e.g., B, C=O) to retain beneficially small ΔE_{ST} values by means of a small HOMO-LUMO overlap.[22-24] With this strategy, smaller FWHMs of less than 30 nm (1130 cm^{-1} in case of DABNA-1) to be achieved.[25-29] However, these conditions are typically observed only in solutions, where intermolecular interactions such as aggregation effects can be minimized by adjustment of concentration or solvent polarity. In the solid state, many organic emitters show significantly different photophysical behavior due to enhanced π–π stacking, aggregation-induced phenomena, or excitonic coupling.[30-32] These usually undesirable effects limit the use of MR-TADF emitters as neat solids in most optoelectronic applications, for which they are typically diluted into polymer films as alternative host matrices.

An alternative chemical approach to limit aggregation in the solid state could be the usage of porous materials such as metal-organic frameworks (MOFs). In those compounds, metals or metal clusters, also known as SBUs, are combined with organic linker molecules [33-35] to form crystalline three-dimensional coordination networks with high porosity and surface areas of several thousand square meters per gram.[36] Variation of the metal salts or linkers help design MOFs for the desired application in terms of pore size porosity and surface area,[37-40] stability,[41-42] or morphology.[43-44] This high level of adaptability motivated the usage of MOFs in a wide variety of areas, such as the encapsulation of guest molecules like enzymes,[45-47] pharmaceuticals or nanoparticles,[48-51] heterogeneous catalysis,[52-54] gas adsorption and separation,[55-57] thermal energy conversion,[58-60] water decontamination,[61-63] and sensor technology.[64-67] In the field of dye encapsulation, substantial research efforts have focused on exploiting host–guest architectures for photonic and sensing applications.[68-69] Notably, Sun *et al.* reported efficient and tunable white-light emission from a Guest@MOF system based on an encapsulated iridium complex,

demonstrating the potential of these materials for solid-state lighting.[70] Moreover, the realization of electrically driven MOF-based light-emitting devices has extended the scope of such systems beyond fundamental photophysical studies toward functional optoelectronic applications.[71] At the same time, dye-encapsulated MOFs have attracted considerable attention as luminescent sensing platforms for metal ions and other analytes, owing to their highly tunable host–guest interactions and optical responses.[72]

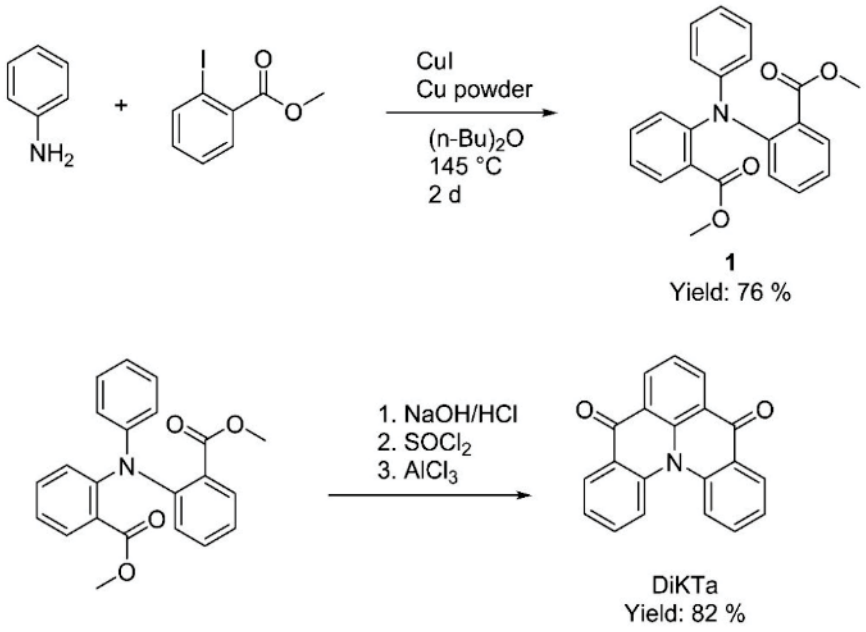
Our work focused on the incorporation of the MR-TADF emitter DiKTa and the resulting photophysical properties of the obtained composites. DiKTa belongs to a class of ketone-based MR-TADF emitters that have attracted significant attention in the field of next-generation OLED technologies due to their narrow-band sky-blue emission, high color purity, and efficient triplet absorption.[24] DiKTa and its derivatives have demonstrated excellent performance in OLED devices, particularly in the blue-to-green spectral range, making them attractive candidates for advanced optoelectronic applications.[73-75] The incorporation of functional organic emitters into MOFs has recently emerged as a promising strategy for controlling photophysical processes through spatial confinement and tailored guest-host interactions. In particular, the successful integration of highly luminescent organic dyes into MOF architectures has demonstrated the potential to control energy transfer and excited-state dynamics in confined environments.[76] However, while such approaches have already been investigated for conventional fluorescent and phosphorescent emitters, to the best of our knowledge, the incorporation of MR-TADF emitters into MOFs remains largely unexplored. Given the exceptional color purity and narrow-band emission of MR-TADF materials, extending guest-host engineering concepts to this class of emitters could open up new avenues for advanced photonic and optoelectronic materials. Therefore, in this study, we investigate the behavior of the MR-TADF emitter DiKTa in MOF-5 as a solid solution, aiming to understand its structural integrity, emission properties, and potential advantages conferred by the MOF matrix. The photophysical results obtained for the composites were compared with the results in solution and as a solid. To complement these experimental efforts, we provide a comprehensive theoretical description of the photophysical properties of the emitter. While previous computational studies on MR-TADF systems often relied on vacuum,[24, 73, 77-79] PCM models,[79-80] or focused on the crystal environment,[79-80] we present the first QM/MM simulations of DiKTa in solution, in order to mimic the solid-solution behavior of dyes in MOFs, using

TD-DFT[81-82] and the high-level DFT/MRCI[83-85] method. This approach allows us to accurately capture specific solute–solvent interactions and dynamic solvation effects.

2. Results and Discussion

2.1 Synthesis and photophysical properties of DiKTa

For our investigations, DiKTa was synthesized following the work of Hall *et al.*[75] and J. E. Field *et al.*[86] (see Scheme 1). In a Jordan-Ullmann coupling, aniline was reacted with methyl 2-iodobenzoate using copper iodide and powdered copper as catalysts. The product obtained could be re-functionalized to the corresponding acyl chloride and then converted to a closed DiKTa in a Friedel-Crafts acylation reaction using $AlCl_3$ as a Lewis acid catalyst. The products were obtained with high yields of 76 % and 82 %. The overall yield was 62 %. These values are in good agreement with literature reports.[75, 86]



Scheme 1. Synthesis of DiKTa.

The successful synthesis was confirmed by NMR and mass spectroscopy (see Section S3, SI). The pure solid DiKTa is a yellow crystalline powder which shows strong yellow luminescence under UV light at ambient temperature (Figure 1a). The excitation spectrum of the pure solid shows a broad excitation band with a maximum at 380 nm. The emission has its maximum at 541 nm with a FWHM of 98 nm (3199 cm^{-1}) (Figure 1b).

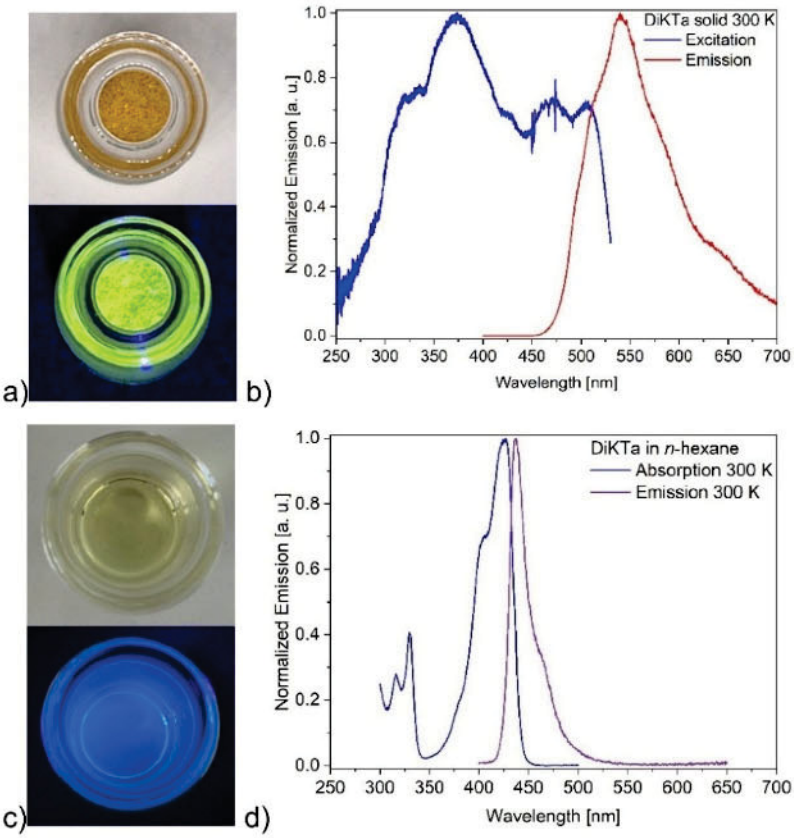


Figure 1. a) Solid DiKTa under daylight (top) and UV-light (λ_{exc} = 365 nm). b) Excitation (λ_{em} = 540 nm) and emission (λ_{exc} = 360 nm) spectra of solid DiKTa. c) DiKTa in *n*-hexane under daylight (top) and UV-light (λ_{exc} = 365 nm). d) Absorption and emission (λ_{exc} = 360 nm) spectra of DiKTa in *n*-hexane.

This value is larger than the otherwise highlighted FWHMs of classic MR-TADF emitters in solution.[75] Dependent on the concentration, a solution of DiKTa in *n*-hexane shows a yellowish color (Figure 1a). Under UV light it shows an emission in the blue-turquoise region (Figure 1c). Steady-state measurements in *n*-hexane show a narrow band emission at 436 nm and an overlapping absorption with a maximum at 426 nm (Figure 1d). The resulting Stokes shift is 10 nm (538.4 cm^{-1}). In addition to the literature-known bathochromic shift of the emission maxima with increasing polarity of the solvent used for DiKTa and DiKTa-based compounds (Figure 2a), also concentration-dependent bathochromic shifts in solution could be observed that indicate aggregation effects (Figure 2b and Figure S7).[75] With increasing solvent polarity, the FWHMs are within a small range (21 nm or 1082.9 cm^{-1} in *n*-hexane and 38 nm or 1631.4 cm^{-1} in DMF).

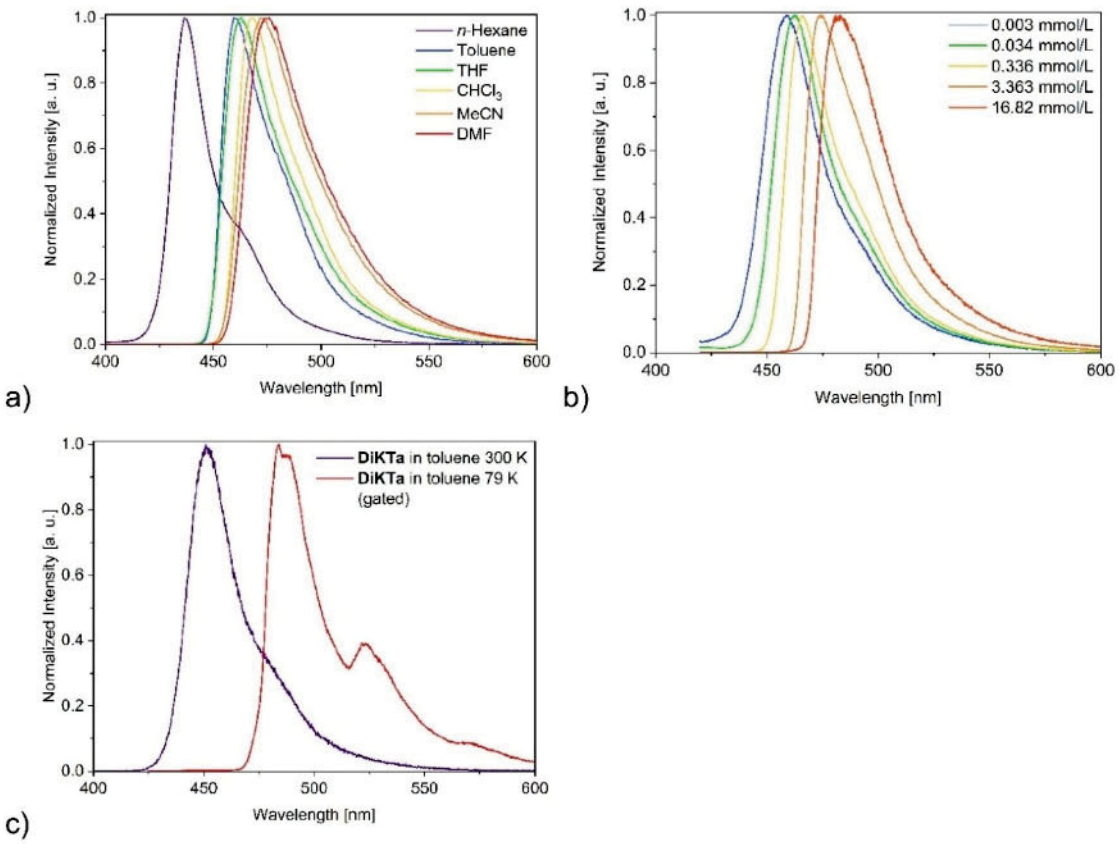


Figure 2. Emission spectra of DiKTa with a) solvatochromic shift with different solvents (λ_{exc} = 360 nm). b) Concentration-dependent shift in chloroform (λ_{ex} = 360 nm). c) DiKTa in toluene at 300 K (λ_{exc} = 335 nm, see [75]) and 79 K with a delay of 10 ms and a window of 10 ms (λ_{exc} = 420 nm, for comparison with lifetime measurements).

In contrast, the emission FWHM remains almost constant in a range of 30 to 34 nm (1347.9 cm^{-1} to 1423.6 cm^{-1}) with increasing concentration (Figure 2b and Figure S7). Steady-state measurements at 79 K revealed a pronounced red-shift of the emission maximum to 484 nm (Figure 2c and Figure S8a). At this low temperature, rISC is effectively suppressed, resulting in dominant phosphorescence from the excited triplet state. This allowed the determination of ΔE_{ST}, which was calculated to 0.19 eV (see Figure S8b, SI). Time-resolved luminescence studies on DiKTa as a polymer film at room temperature revealed both a prompt fluorescence component of 5.7 ns and a delayed fluorescence component of 16 µs. Upon cooling to 79 K, a significant elongation of the decay time was observed that has to be interpreted as phosphorescence from a decoupled triplet state. The measured decay components in a polymer film (2 wt% in PMMA) at 79 K were 8.1 ns for the prompt fluorescence and 115 ms for the phosphorescence. These results are in good agreement with literature

reports (see SI, Figures S9 and S10 for lifetime plots).[75] In powdered form, the time-resolved luminescence of DiKTa is pronouncedly different compared to that in a polymer film. A decay time of 799 ns is recorded at room temperature for solid DiKTa that elongates to 882 µs at 79 K (Figure S11 and Table S1). These results indicate that DiKTa exhibits MR-TADF emitter properties exclusively in solution or in a polymer film, but not in the solid state.

2.2 Quantum chemical calculations

To investigate the electronic structure and photophysical properties of DiKTa, we performed a series of quantum-chemical calculations. The ground-state (S_0) geometry was optimized with density functional theory (DFT) using the ωB97X-D functional[87]. The range-separation parameter ω was optimally tuned via Koopmans' theorem (see SI, Figure S33), yielding ω = 0.17 $bohr^{-1}$. Unless stated otherwise, the def2-SVP basis set[88-89] was used for geometry optimizations and frequency calculations. All stationary points were validated as minima by vibrational analyses. To investigate the fluorescence behavior, optimizations were performed for the S_1- and T_1 states using time-dependent DFT (TD-DFT)[81-82]; higher states were assessed at the vertical excitation level due to nearby conical intersections. DFT and TD-DFT Calculations were carried out with Gaussian 16[90]. For more accurate excitation energies and oscillator strengths, DFT/MRCI[83-85] computations employing the R2018 Hamiltonian[85] were conducted based on single-point BH-LYP/def2-TZVP calculations performed in TURBOMOLE 7.2.[91] All single and double excitations within an active space of 8 electrons in 8 orbitals were considered. The configuration space was truncated at 0.8 E_h and refined at 1.0 E_h, yielding 10 singlet and 9 triplet roots relevant for optical transitions. Absorption and emission spectra were simulated from vertical transitions with Gaussian broadening (FWHM 0.3 eV for absorption and emission). Difference densities and geometries in different environments were visualized with VMD[92].

To capture specific solute–solvent interactions, QM/MM simulations were performed for DiKTa in cyclohexane (CX), acetonitrile (MeCN), and water (H_2O). In these simulations, DiKTa was treated quantum-mechanically at the ωB97X-D/def2-SVP level and molecular-mechanically using GAFF2[93] parameters. The solvent was only described by molecular mechanics. For the MM description, GAFF2[93] parameters

were used for CX, ff14SB[94] for MeCN, and TIP3P[95] for H_2O. Point charges for CX and MeCN were derived via a two-step procedure: first, the electrostatic potential was calculated at the HF/6-31G* level (Gaussian 16[90]), then restrained electrostatic potential (RESP[96]) charges were obtained with the antechamber[97] package by re-fitting the ESP according to the Merz–Singh–Kollman scheme.[98]
The positions of the solvent molecules were sampled. From the work of Shedge *et al.*[99] the initial solvent configuration of CX was obtained. Custom boxes were generated for MeCN and H_2O.[100] The solvent arrangement around DiKTa (20 Å radius) was relaxed using steepest descent and conjugate gradient minimization, followed by 200 ps molecular dynamics (MD) in Amber16[101] under periodic boundary conditions. Long-range electrostatics interactions beyond 8 Å were treated with the particle mesh Ewald summatcion method.[102] The temperature was regulated using a Langevin thermostat and the pressure (1 bar) was maintained using a Berendsen barostat.[103] For propagation of MD simulations the Verlet algorithm[102] was used. From each trajectory, ten snapshots were extracted every 20 ps and optimized with COBRAMM 2.0[104] using electrostatic embedding. Each system comprised DiKTa and the 1000 nearest solvent molecules. The chromophore and all molecules within 4 Å were allowed to freely move; outer layers were kept fixed during the optimization. Finally, DFT/MRCI[83-85] single-point calculations were carried out on the optimized QM/MM structures, including MM point charges of the solvent molecules

In the QM/MM calculations all optimized structures showed a helical arrangement among the lower part of the conjugated π-system (Figure S28) due to sterical interactions between hydrogen atoms. Depending on the DiKTa to solvent interaction the resulting torsion of the conjugated π-system (Figure S29) increased. The smallest torsion angle is found for cyclohexane, while the largest occurs for water. In the ground state, torsion angles ranging from 44.7° to 48.0° were observed. The excited state geometries exhibited torsion angles ranging from 47.1° – 50.4° for the S_1 and 45.8° – 49.8° the T_1 state (Figure S29). With increasing solvent polarity, both the adiabatic singlet state S_1 and the triplet state T_1 are energetically stabilized with respect to the ground state. Both states were mainly characterized by HOMO→LUMO excitations with dominant ππ* character, and the relative contribution of ππ* configurations in S_1 and T_1 increased with solvent polarity. The second excited singlet state S_2 exhibited nπ* character in all environments. In the QM/MM calculations, the energy of the S_2

state increased with solvent polarity, while the vacuum computations slightly deviate from this trend. In vacuum and CX, a similar behavior was found for the T_2 state, which is a mixture of ππ* and nπ* configurations. With increasing solvent polarity, the mixed T_2 state is shifted to higher energy, forming T_3 in acetonitrile and T_4 in water, while in these solvents a ππ* state corresponds to the T_2 state. An analysis of the electron density difference between electronic ground state S_0 and the lowest excited states revealed: For the S_1 and T_1 states, the electron density difference was delocalized over the entire aromatic system and displays alternating electron-rich and electron-poor regions (Figure 3).

The difference densities of the S_2 state are characterized by electron depletion at the heteroatom-centered lone pair orbitals and accumulation within the adjacent π* systems. Additionally, increased short-range charge transfer (SRCT) is observable with higher solvent polarity. The T_2 state shows a simultaneous density depletion in one of the lone-pair regions and redistribution across the π-conjugated framework. In more polar solvents, such as MeCN and H_2O, the difference density of T_2 is dominated by a pronounced delocalization of density over the aromatic core and diminished contribution from the lone pair. In these environments, the spatial distribution of the density closely resembles that observed for S_1 and T_1.

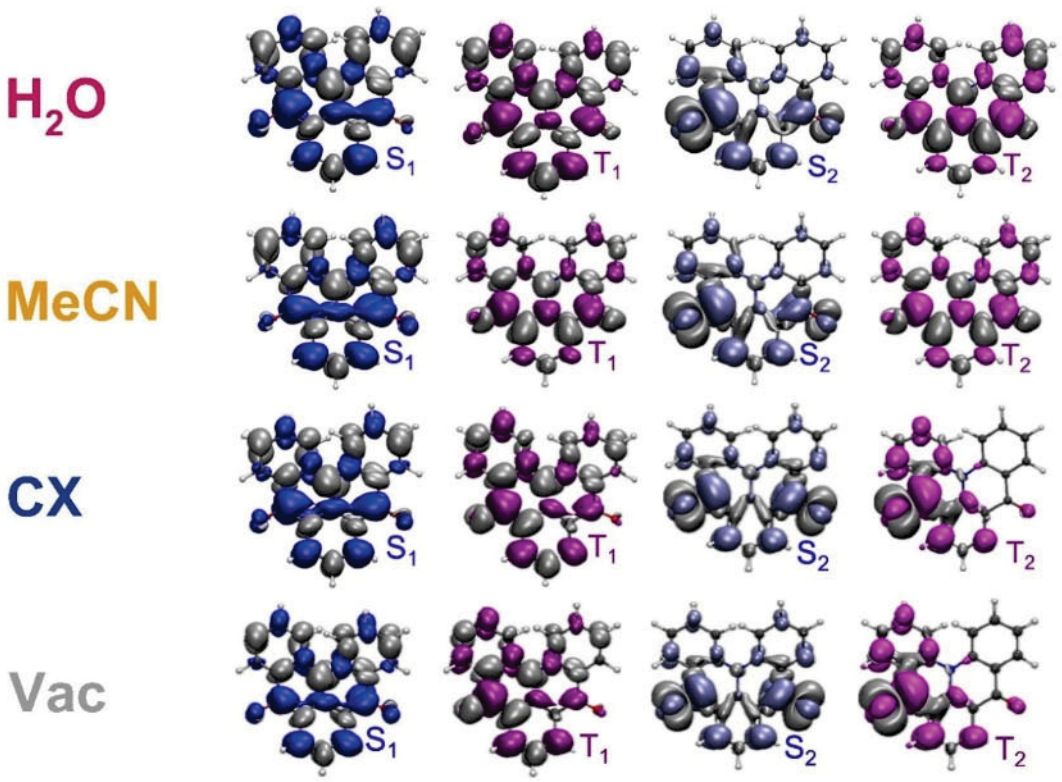


Figure 3. Electron density difference plots of DiKTa in vacuum (Vac) and cyclohexane (CX), acetonitrile (MeCN), and water (H_2O) upon excitation $S_0 \rightarrow S_1$ (gray → blue) and $S_0 \rightarrow S_2$ (gray → ice blue) calculated at the relaxed S_1 geometry, as well as $S_0 \rightarrow T_1$ (gray → purple) and $S_0 \rightarrow T_2$ (gray → magenta) calculated at the relaxed T_1 geometry. Gray regions indicate a decrease in electron density upon excitation (isovalue −0.001 e/bohr³), while the colored regions represent an increase in electron density (isovalue +0.001 *e*/bohr³) The solvation molecules of the QM/MM computations are not shown for clarity.

The calculated averaged absorption spectra exhibited marginal differences across all studied environments (Table 1, Figure 4). Vacuum, CX and MeCN showed three well-separated absorption bands. In water, the absorption spectrum had two bands, with the higher-energy band having two shoulders. In all cases, the lowest-energy absorption band appeared between 392 nm and 427 nm, dependent on the polarity of the solvent, which are attributed to $S_{1,2} \leftarrow S_0$ transitions. The next absorption band located between 309 nm and 321 nm shows a comparably low oscillator strength in all environments and is assigned to $S_{3-5} \leftarrow S_0$ transitions, which are dominantly nπ* and ππ* transitions. The highest energetic absorption bands between 262 nm and 271 nm correspond to $S_{6-9} \leftarrow S_0$ transitions of ππ* nature and are characterized by the largest oscillator strengths (0.28-0.34). Emission bands range from 422 nm in vacuum to 457 nm in H_2O. The oscillator strength of the emission decreases with increasing solvent polarity, because of a stronger charge-transfer character of the HOMO-LUMO excitation. A bathochromic shift was observed for both absorption and emission

spectra with increasing environment polarity. In addition to the averaged spectra discussed above, the analysis of individual snapshot contributions provides deeper insight into dynamic solvation effects (Figure 4). In all solvents, the absorption and emission spectra display multiple bands with varying intensity and energy. As the solvent polarity increases, both the absorption and emission spectra broaden, indicative of enhanced solute–solvent interactions. The broadest spectral distribution was observed in water, which can be attributed to hydrogen bonding and pronounced electronic reorganization.

Table 1. Simulated absorption and emission properties of DiKTa in vacuum (Vac) and different solvents (CX, MeCN, H_2O) using explicit QM/MM solvation. Shown are the positions of the visible absorption bands (λ_{abs}), their respective oscillator strengths (*f*), the emission maxima (λ_{em}), the corresponding emission oscillator strengths, the radiative rate constants of fluorescence $k_{rad}(f)$ and the adiabatic energy gap between S_1 and T_1 state. For the solvents the averaged values from all snapshots were used.

	λ_{abs} /nm	*f*	λ_{em} /nm	*f*	k_{rad}(f) /s^{-1}	ΔE_{ST} (adiabatic) /eV
Vac	262, 309, 392	0.34, 0.06, 0.25	422	0.27	$9.41 \cdot 10^7$	0.34
CX	271, 318, 408	0.29, 0.06, 0.25	435	0.22	$7.86 \cdot 10^7$	0.27
MeCN	271, 321, 419	0.35, 0.06, 0.25	448	0.21	$7.33 \cdot 10^7$	0.32
H_2O	274, 291, 321, 427	0.28, 0.19 0.06, 0.24	457	0.16	$6.99 \cdot 10^7$	0.32

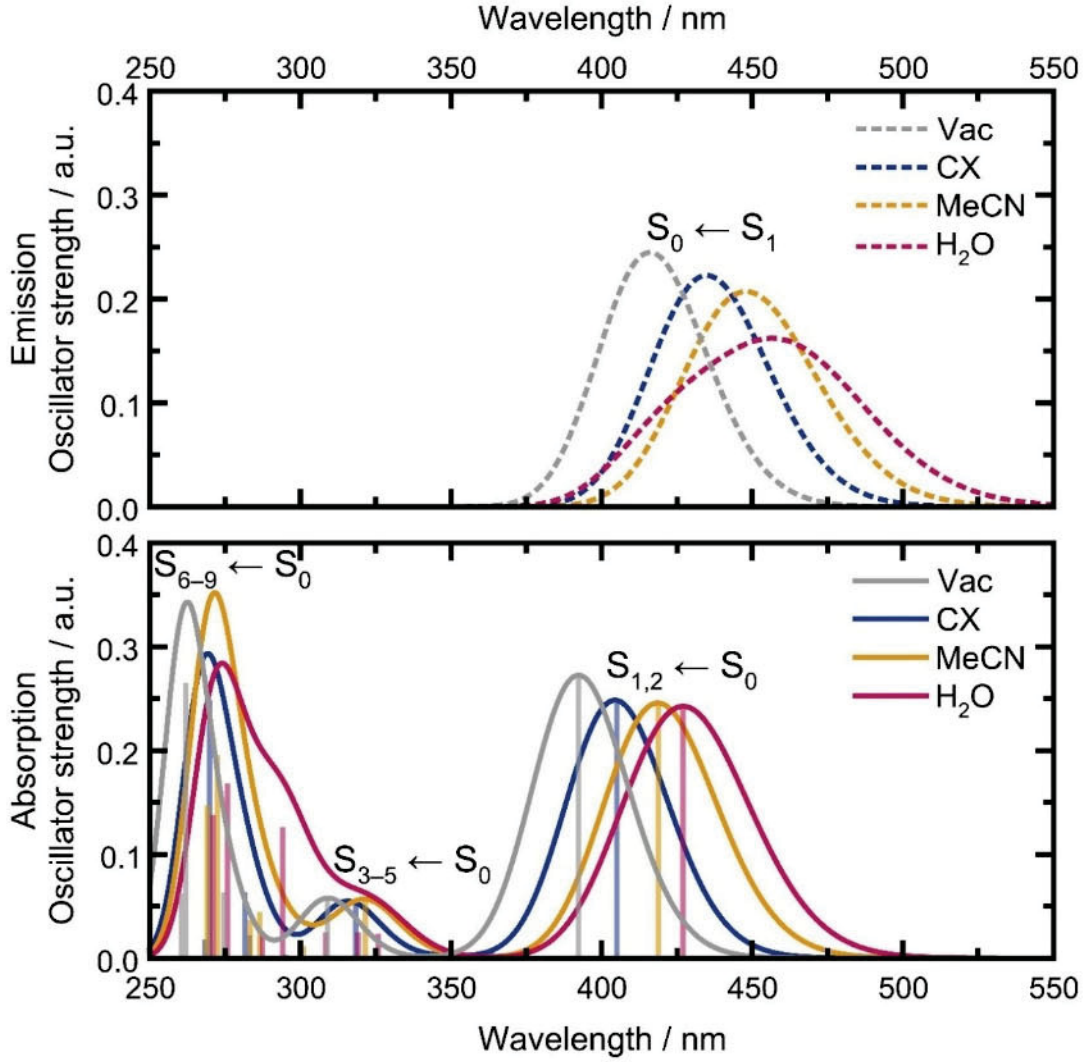


Figure 4. Calculated average absorption (solid lines) and emission (dotted lines) spectra of DiKTa in vacuum (Vac, grey), cyclohexane (CX, blue), acetonitrile (MeCN, orange) and water (H_2O, magenta) obtained from QM/MM calculations. The vertical bars (sticks) represent the individual vertical electronic transitions and their oscillator strengths, color-coded by environment as above.

The optimized geometries of DiKTa and their difference densities in vacuum are in excellent agreement with the previously postulated structures in literature.[24, 73, 77-79] Beyond a purely static description, the QM/MM simulations performed here reveal a significant impact of explicit solvation on the molecular geometries. The degree of deformation of the conjugated π-system depended on the solvent and the intensity of the intermolecular interactions between DiKTa and the solvent molecules. The structural dynamics is directly reflected in the optical properties. Within the sampling, both the absorption and emission spectra displays a pronounced dependence on the

intermolecular interactions with the solvent molecules, manifesting in significantly varying energies and intensities of the individual bands. With increasing solvent polarity, the spectra undergo further broadening, which can be attributed to enhanced solute–solvent interactions and pronounced electronic reorganization. This is reflected in the increasing charge transfer character of the HOMO→LUMO excitation, which is more stabilized energetically. Another reason for the change in the absorption spectra is the energetic destabilization of the $n\pi^*$ states. Furthermore, our results underscored the suitability of DiKTa as an MR-TADF emitter, as the calculations confirm high oscillator strengths combined with small ΔE_{ST} values. The agreement of the averaged simulated spectra and the radiative rate constants with the experimental solution data of this work and related literature[73, 75, 77] validates the reliability of the QM/MM approach for this system. By employing this explicit treatment of the environment and sampling position of surrounding molecules, the model captures the dynamic solvation effects and intermolecular coupling that are inaccessible with simplified continuum models, thereby providing a more accurate description of the photophysics in diverse chemical environments.

2.3 Encapsulation of DiKTa

The encapsulation of the DiKTa molecules into the MOF-5 matrix was carried out as *in situ* approaches with different DiKTa concentrations in the reaction mixture (c = 0.06 mmol L^{-1} – 0.5 mmol L^{-1}). The comparison between pore size (12 Å) and DiKTa size (10-11 Å) should make an incorporation into defined pores without defects feasible.[105] In addition to the encapsulation of DiKTa, we also synthesized neat MOF-5 according to the literature (Section S5 in the SI). [106] All compounds were washed with dichloromethane (DCM) to remove non-incorporated dye and starting compound residues. In this way, we were able to grow cubic single crystals with an edge length of up to 1.5 mm. With increasing concentration of DiKTa used in the reaction mixture, an increasingly intense yellow color of the composites could be observed, starting from colorless crystals for neat MOF-5. Figure 5 depicts the color change in the MOF-5 single crystals under both daylight and UV light. All composites emit in the wavelength range from blue to turquoise under UV light (λ_{exc} = 365 nm), while neat powdered DiKTa exhibits strong yellow fluorescence (*cf.* Figure 1a).

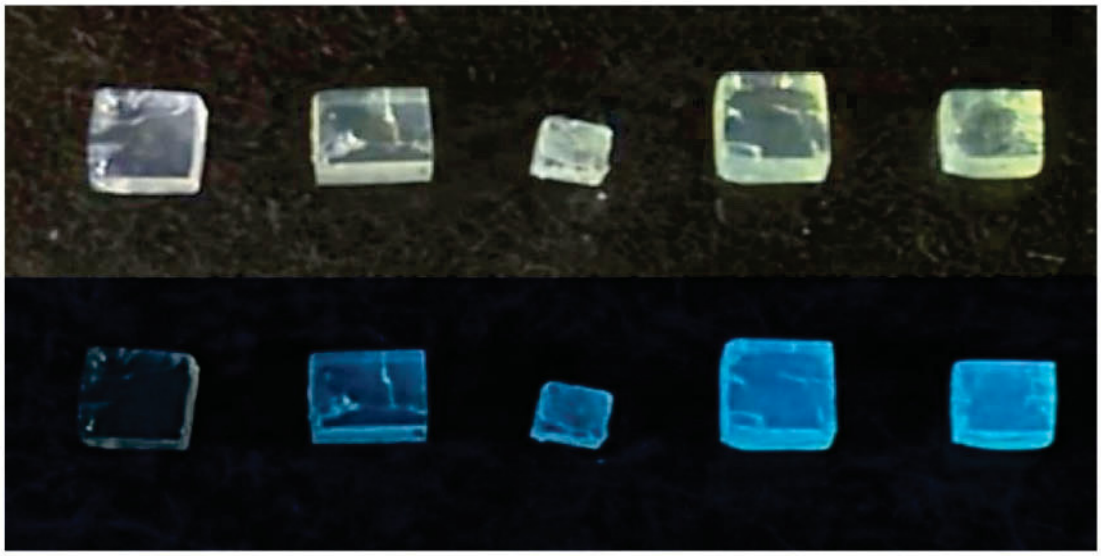


Figure 5. Single crystals of (from left to right) neat MOF-5, **DiKTa**@MOF-$5_{0.03}$, **DiKTa**@MOF-$5_{0.05}$, **DiKTa**@MOF-$5_{0.09}$, and **DiKTa**@MOF-$5_{0.13}$. Both under daylight (top) and UV-light (λ_{exc} = 365 nm).

All composites retain the MOF-5 structure based on powder X-ray diffraction (PXRD) measurements (Figure 6a and Figure S12).

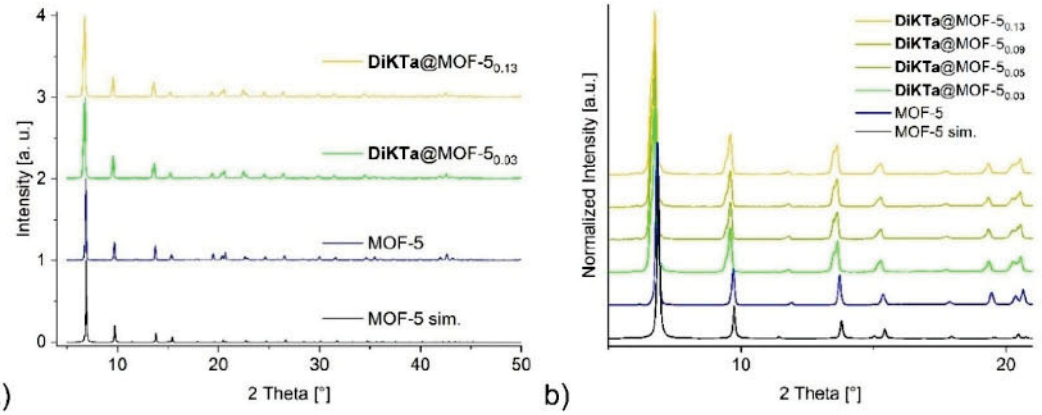


Figure 6. Powder X-ray diffraction patterns of MOF-5 and the lowest and highest loaded **DiKTa**@MOF-5 composite (Cu K_α radiation with λ = 1.541 Å, 40 kV, 15 mA, 600 W) in the range of a) 2θ = 5° – 50° and b) 2θ = 5° – 20°. The simulated diffraction pattern of MOF-5 (CCDC No. 819641) is depicted in black color.

No Bragg reflections of any starting compound were identified. Therefore, we assume that the neat MOF-5 and all the composites were formed as crystal phase pure material. The exact DiKTa loading of the synthesized composites was determined by digestion-based UV-Vis spectroscopy. Depending on the initial concentration, loadings of 0.03 wt% up to 0.13 wt% were determined, denoting the composites as **DiKTa**@MOF-$5_{0.03}$ to **DiKTa**@MOF-$5_{0.13}$, respectively (see Section S6 in the SI for

more details). Based on these results, we calculated the molar ratio of DiKTa molecules to MOF-5 pores, which falls within the range of 0.0008 and 0.0034 DiKTa molecules per pore for **DiKTa**@MOF-$5_{0.03}$ to **DiKTa**@MOF-$5_{0.13}$, respectively (see Section S7 in the SI for a more detailed description).

A more detailed analysis of the PXRD data, shown in Figure 6b, shows a consistent and concentration-dependent shift and broadening of the Bragg reflections to lower 2θ values with increasing DiKTa loading. This systematic change in the diffraction pattern serves as an indication of the successful encapsulation of DiKTa molecules within the porous structure of the MOF-5 framework. The observed shifts indicate small but measurable changes in the lattice parameters, which can be explained by a lattice expansion of the MOF due to the incorporated DiKTa molecules. This structural change caused by the incorporation of guest molecules into the MOF framework shares an analogy to the gate-opening mechanism in ZIF-8 or the breathing behavior characteristic of MIL-53. In all cases, the respective framework reacts to the presence of guest species by subtle or pronounced adjustments in pore size or geometry.[107-108] The concomitant broadening of reflections may be attributed to increasing structural disorder or microstrain within the MOF lattice as more DiKTa molecules are incorporated. This disorder likely arises from the expectedly random occupation of the pores by the DiKTa dye molecules. These observations further support the conclusion that DiKTa encapsulation involves true structural integration into the host matrix rather than mere surface adsorption. Overall, powder X-ray diffraction support the incorporation of guest molecules into the MOF-5 matrix.

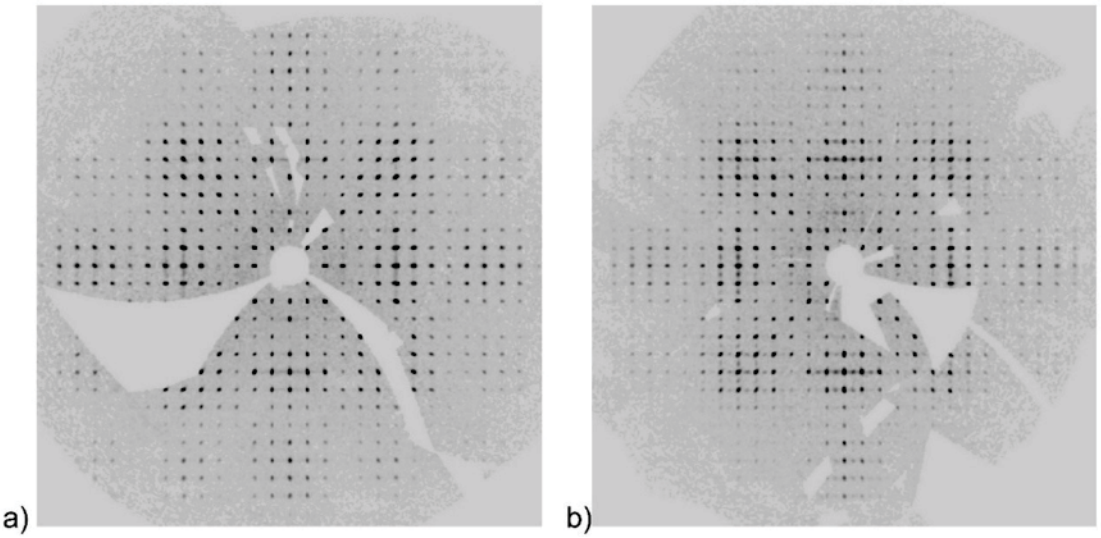


Figure 7. Reciprocal space section of the *h0l* plane of the unloaded MOF-5 (a) and DiKTa@MOF-$5_{0.13}$ (b), obtained from single-crystal X-ray diffraction data.

In addition, single-crystal structural analyses were performed on pure MOF-5 and the loaded DiKTa@MOF-$5_{0.13}$ (Figure 7). A comparison of the reciprocal space diagrams of the unloaded and loaded MOFs reveals distinct differences in the diffraction patterns and, consequently, in the crystal structure. The unloaded MOF exhibits only sharp and regularly spaced main peaks, indicating a high degree of crystalline order and the periodic structure of the framework. The arrangement of the peaks also suggests a high degree of symmetry.

In addition to the main peaks, further peaks can be observed between the positions of the basic structure's peaks in the loaded MOF. The presence of these additional peaks suggests the formation of a superstructure and indicates that the guest molecules embedded within the pores are not randomly distributed, but rather form a partially ordered arrangement. Similar changes to the crystal structure resulting from guest-host interactions involving guest molecules, such as solvents, have already been described for MOF-5-based systems, as demonstrated, for example, in the publication by Pallach *et al.*[109]

In addition, diffuse, stripe-like intensities appear between the Bragg reflections. Such diffuse scattering signals are often associated with disordered guest molecules or solvent residues in the pores of MOFs.[110-111]

The presence of additional reflections and diffuse scattering indicates that the loading process gives rise to both ordered and disordered structural components within the pore system. Together with the results from other characterization methods, the single-

crystal data thus provide further evidence of the successful incorporation of the dye into the pores of the MOF.

Despite this low pore loading, we were able to detect significant effects of the differently loaded composites, which are compiled in Figure 8. Upon increasing loading with DiKTa, the determined surface areas and pore volumes for the N_2 adsorption isotherms decrease drastically (Table 2). While pure MOF-5 single-crystals show a specific BET surface area of 1973 $m^2 g^{-1}$, only 213 $m^2 g^{-1}$ could be determined for the highest probed loading of 0.13 wt%.

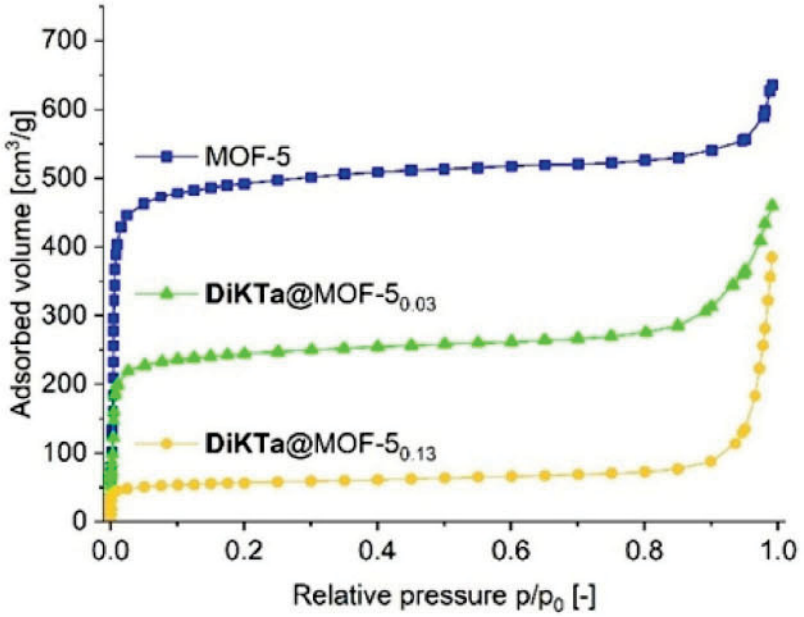


Figure 8. Nitrogen adsorptions isotherms at 77 K of neat MOF-5 (1973 $m^2 g^{-1}$)(blue) and the lowest (965 $m^2 g^{-1}$)(green) and highest (213 $m^2 g^{-1}$)(yellow) loaded **DiKTa**@MOF-5 composite.

Table 2. Results of nitrogen sorption measurements for MOF-5 and DiKTa@MOF-5 composites.

Compound	**DiKTa Loading [wt%][a]**	S_{BET} **[$m^2 g^{-1}$]**	$V_{pore\ (total)}$ **[$cm^3 g^{-1}$][b]**
MOF-5 literature	-	240 to 4400 [36]	
MOF-5 as-synthesized	-	1973	0.98
DiKTa@MOF-$5_{0.03}$	0.03	965	0.71
DiKTa@MOF-$5_{0.05}$	0.05	540	0.62
DiKTa@MOF-$5_{0.09}$	0.09	499	0.58

DiKTa@MOF-$5_{0.13}$	0.13	213	0.57

[a] Calculated by UV-Vis digestion analysis. [b] Total pore volume at p/p_0 = 0.9.

The observed low nitrogen uptake additionally indicates successful incorporation of DiKTa molecules into the MOF-5 structure. The reduced nitrogen adsorption can be attributed to the pore loading by the DiKTa molecules, which restrict the access of N_2 molecules to the surface. This gives us further indication of the successful encapsulation of the dye in the MOF-5 structure (for all nitrogen sorption measurements, see Figure S13).

2.4 Photophysical properties of **DiKTa**@MOF-5 composites

All synthesized composites show cyan luminescence upon UV excitation (Figure 5) that is characteristic of DiKTa at elevated concentrations or when dissolved in highly polar solvents (*cf.* Figure 2a and b). The recorded emission maxima are in the range of 487 to 494 nm with FHWMs of 61 ± 1 nm (2509.7 cm^{-1} to 2514.3 cm^{-1}) at ambient temperature (Figure 9a). The observed appearance of the emission spectra suggests that the polarity of the MOF matrix is higher than that of DMF (λ_{em} = 475 nm).

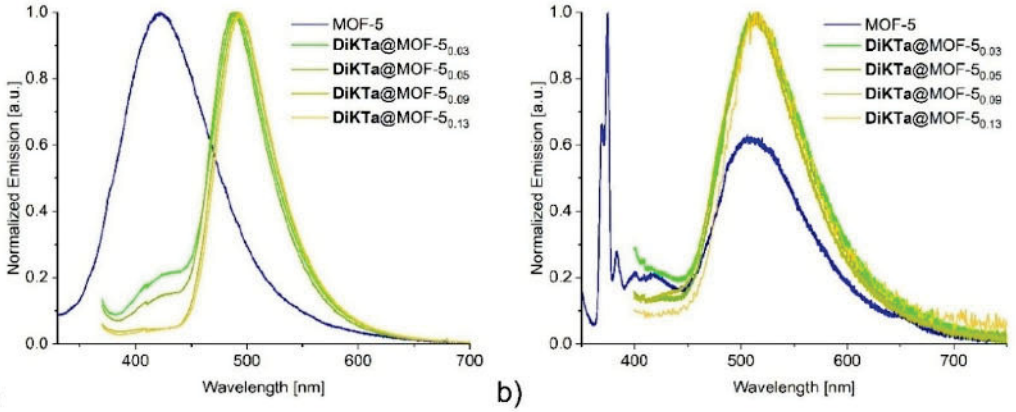


Figure 9. a) Emission spectra of MOF-5 (λ_{exc} = 290 nm) and the **DiKTa**@MOF-5 composites at 298 K (λ_{exc} = 345 nm). b) Emission spectra of MOF-5 (λ_{exc} = 325 nm) and the **DiKTa**@MOF-5 composites at 79 K (λ_{exc} = 345 nm).

Notably, a small systematic bathochromic shift of the emission maximum is observed with increasing DiKTa concentration in the composite. This concentration-dependent spectral shift consistent with the behavior of DiKTa in solution suggests intermolecular interactions between the incorporated DiKTa molecules. Furthermore, with increasing

DiKTa loading (Figure 9a), the intensity of the intrinsic emission of MOF-5 at around 420 nm decreases relative to that of the incorporated DiKTa dye.

Compared to the emission maxima of the composites recorded at room temperature (Figure 9a), a pronounced red shift of the emission maximum is recorded at 79 K (Figure 9b) with all composites exhibiting maxima at 515 nm and FWHMs of 93 ± 5 nm (3190.8 cm^{-1} to 3614.5 cm^{-1}), regardless of the dye percentage. This temperature-dependent shift is indicative of phosphorescence originating from the excited triplet state due to the suppression of thermally activated reverse intersystem crossing at low temperatures. These results suggest that the photophysical behavior of DiKTa within the composites is very similar to that of the dye in solution, supporting the conclusion that the dye molecules are distributed within the MOF matrix. The resulting materials can be described by the concept of solid solution for dyes@MOFs.

We estimated the probability *p* for the incorporation of a given number of DiKTa molecules per pore in MOF-5, assuming a random distribution of dyes (Section S7 in the SI). Based on the average occupation numbers estimated in the Supporting Information (Section S7), our calculations indicate that the probability $p(n > 1)$, of more than one DiKTa molecule per pore is consistently close to zero across all studied loading levels. This suggests that an occupancy of a pore with more than one dye molecule is highly unlikely. As a consequence, it can be inferred that DiKTa molecules are predominantly distributed as isolated guests within the MOF-5 matrix rather than forming clusters, which may favor uniform guest-host interactions and minimize excitonic coupling or self-quenching effects.

To gain a more comprehensive understanding of the integration and spatial distribution of DiKTa molecules within the MOF-5 framework, confocal laser scanning microscopy (CLSM) was performed on the synthesized single-crystal composites. The fluorescence microscope images shown in Figure 10 clearly show that the characteristic emission signal of the DiKTa dye, here in green, is present throughout the crystal structure (for all composites, see Figure S16 and S17, SI).

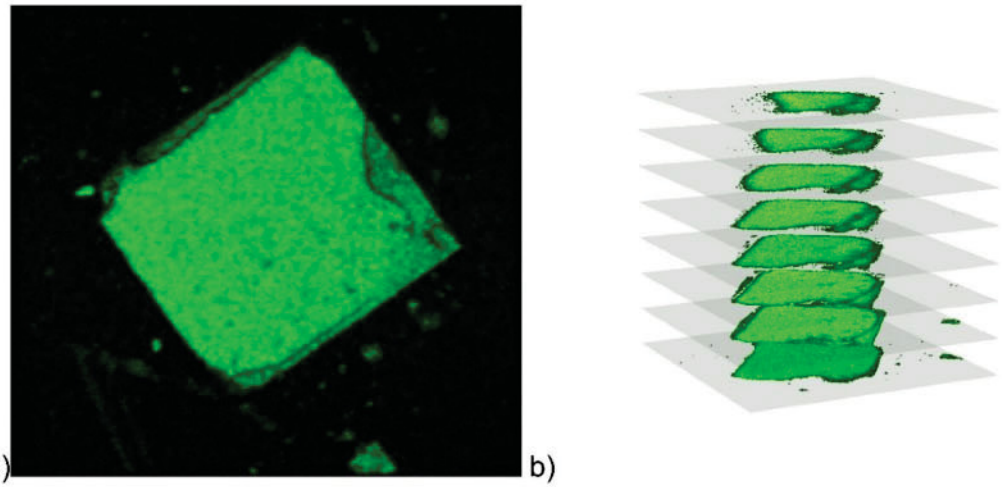


Figure 10. Confocal images of **DiKTa**@MOF-5. a) Measured single crystal viewed from above. b) Stack of sectional planes of **DiKTa**@MOF-5 (pulsed excitation at λ_{exc} = 440 nm, repetition rate 26.7 MHz, λ_{em} = 460-500 nm). Each sectional plane represents a measurement thickness of 8.7 µm.

The uniform green coloration of the individual layers, which is visible both in the inner and outer regions of the crystals, strongly indicates a homogeneous distribution of the dye within the MOF matrix. This observation is particularly interesting because an uneven distribution or distribution limited to the surface would typically lead to irregular or peripheral fluorescence. This phenomenon is often observed in post-synthetic dye loading processes.[67] In such cases, the dye molecules are often quickly immobilized on the outer surface or in the pores near the surface of the framework, resulting in inhomogeneous loading and incomplete penetration of the MOF material. This can have a significant impact on their photophysical properties. However, the continuously observed emission confirms that the DiKTa molecules were successfully embedded throughout the entire crystal volume during the formation of the MOF-5 structure. This homogeneous distribution indicates that the DiKTa molecules find a consistent microenvironment within the MOF-5 pores, which is essential for the observed solid solution-like photophysical properties of the composite materials. To learn more about the spatial orientation and rotational freedom of the DiKTa dye molecules within the MOF-5 framework, we performed anisotropy measurements (Figure 11a and Figure S18). For reference, DiKTa dissolved in toluene was also investigated under identical conditions. As expected for a molecular dye in a freely diffusing liquid environment, the measurements in the solution phase, given in Figure 11b, showed no measurable anisotropy, since the unrestricted rotational movement of the DiKTa molecules leads to immediate depolarization of the emitted fluorescence. In contrast, the anisotropy

decay curves recorded for the **DiKTa**@MOF-5 composites showed a significantly slower depolarization behavior, indicating a considerably restricted freedom of rotation of the encapsulated dye molecules. Since the initial anisotropy correlates with the orientation of the crystal, the measurements also show that the projection of the transition dipole moment of DiKTa onto the image plane has a preferred orientation within the MOF pore, which is approximately 45° with respect to the crystal edge.

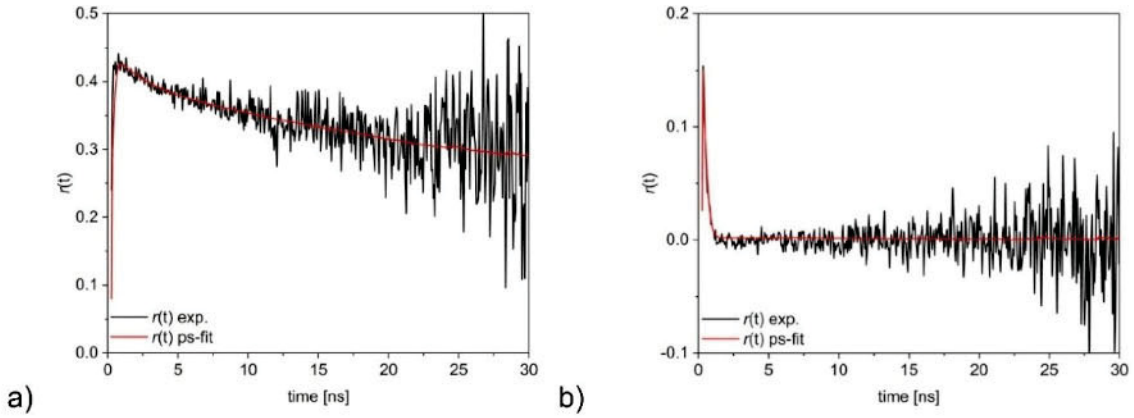


Figure 11. Time-resolved fluorescence anisotropy curves $r(t)$ to resolve the fundamental anisotropy r_0 of a) **DiKTa**@MOF-$5_{0.13}$, b) DiKTa in toluene.

This pronounced difference strongly suggests that DiKTa molecules adopt a spatially defined, preferred orientation within the MOF-5 pore structure and that the rotational movement is sterically hindered by the restriction in the rigid, crystalline framework.
It is noteworthy that even neat MOF-5 showed significant spectral changes under these conditions, with two emission maxima occurring at 380 nm and 506 nm (cf. Figure 9b). To further elucidate the photophysical behavior of DiKTa molecules in the MOF-5 matrix, we performed time-resolved luminescence measurements and compared these with those of a 2 wt% DiKTa-doped PMMA polymer film, which served as a reference. The results are summarized in Table 3 (see Figures S9-S11, Figures S19-S27 and Tables S1 and S6 for more information).

Table 3. Photophysical data for DiKTa polymer film and the **DiKTa**@MOF-5 composites with λ_{exc} = 375 nm or 420 nm for the lifetime measurements at room temperature and 79 K, respectively. The lifetimes are intensity-weighted.

Compound	λ_{exc} **[nm]**[a]	λ_{em} **[nm]**[b]	τ_p **[ns]**[c]	τ_d **[µs]**[d]	τ_p **[ns]**[e]	τ_d **[ms]**[f]
DiKTa solid	330	540 / 534	5.2	0.4	7.2	0.7

2 wt% DiKTa in PMMA	335 / 420	472 / 505	5.7	16	8.1	115
Neat MOF-5	290 / 325	422 / 506	1.2	[g]	1.9	[h]
DiKTa@MOF-$5_{0.03}$	345	487 / 514	3.9	16	3.2	122
DiKTa@MOF-$5_{0.05}$	345	488 / 514	3.1	10	2.9	81
DiKTa@MOF-$5_{0.09}$	345	492 / 515	3.1	18	2.7	41
DiKTa@MOF-$5_{0.13}$	345	494 / 513	3.7	11	4.1	15

[a] Excitation wavelength at room temperature / 79 K. [b] Wavelength of the fluorescence maximum at room temperature / 79 K. [c] Prompt fluorescence decay time, measured at 300 K (λ_{exc} = 375 nm). [d] Delayed fluorescence decay time, measured at 300 K (λ_{exc} = 420 nm). [e] Prompt fluorescence decay time, measured at 79 K (λ_{exc} = 375 nm). [f] Delayed fluorescence decay time, measured at 79 K (λ_{exc} = 420 nm). [g] Due to the emission maximum, we were unable to measure a lifetime. [h] No delayed components could be detected.

In the polymer matrix, both prompt and delayed fluorescence components were resolved at room temperature and 79 K. Under ambient conditions, the prompt emission showed a decay time of 5.7 ns, while the delayed component was recorded with 16 µs. These values are in good agreement with the measurements in polymer film reported in the literature.[75] A similar photophysical behavior was observed for the **DiKTa**@MOF-5 composites, with prompt fluorescence decay times between 3.1 and 3.9 ns. In the delayed fluorescence range, the measured decay times were between 10 and 18 µs, with no consistent trend with respect to the loading amount. These values are in the typical range for prompt and delayed fluorescence of DiKTa at 298 K, confirming that the molecule retains its luminescence properties after incorporation. The intrinsic photophysical behavior of the DiKTa molecules in both polymeric and MOF-based matrices indicate an interaction between dye molecules and the surrounding matrix. These interactions are less pronounced compared to the interactions in the solid state. However, a comparison of the delayed emission of the composite materials and the polymer film with that of solid DiKTa clearly shows that aggregation phenomena significantly influence the photophysical reaction in the solid state. In particular, the delayed fluorescence in the microsecond range characteristic of DiKTa in solution or polymer matrix is completely absent in the solid form. This suggests that strong intermolecular interactions and aggregation-induced quenching occur in neat DiKTa, which have a significant influence on the MR-TADF behavior. At 79 K, solid DiKTa exhibits significant phosphorescence, but the observed delayed emission is characterized by a relatively short decay time of only approximately 0.7 ms. This is in strong contrast to the prolonged delayed fluorescence decay time of

approximately 115 ms measured for DiKTa in a PMMA polymer matrix. A comparative analysis between the 2 wt% DiKTa-doped PMMA film and the **DiKTa**@MOF-5 composites shows that all composites exhibit a significantly delayed luminescence at 79 K. Unlike the findings at room temperature, the duration of the delayed emission is inversely proportional to the dye loading. With increasing loading, the delayed decay component systematically decreases. This trend is good agreement with earlier reports on other loaded MOFs and polymer films. [112-114] The comparison of the photophysical data of polymer films, **DiKTA**@MOF-5 composites, and DiKTa in the solid state supports the conclusion that the DiKTa molecules were successfully embedded in the MOF matrix. The observed emission properties are consistent with those of a polymer film and confirm the assumption of a solid solution. The embedded dye molecules are spatially isolated from each other within the MOF pores. To the best of our knowledge, these results show for the first time that the concept of solid solution can be effectively extended to MR-TADF emitters in MOF environments, enabling their use in solid-state optoelectronics without the typical disadvantages of dye aggregation.

3 Conclusion

In this study, we report the first successful incorporation of the MR-TADF emitter DiKTa into MOF-5 single crystals, providing a detailed investigation of its structural and photophysical properties within a crystalline host. Several independent experimental methods clearly support a successful incorporation into the pores of the MOF instead of simple adsorption of the dye on the surface. Structural characterizations using PXRD and N_2 adsorption measurements demonstrate that the presence of DiKTa leads to a slight expansion of the MOF lattice and a significant reduction in surface area, confirming successful pore occupation and guest-host interactions. Photophysical analysis, including steady-state and time-resolved spectroscopy reveals a distribution of the dye, restricted rotational freedom, and a preferred spatial orientation within the framework.

In parallel, we provide a rigorous theoretical description of the emitter's photophysics, representing first application of QM/MM simulations to DiKTa in explicit solvation using TD-DFT and the DFT/MRCI method. By transcending the limitations of previous vacuum-based or implicit PCM models, our approach accurately reproduces the experimentally observed solvatochromism and quantifies the impact of explicit

intermolecular interactions on the electronic structure. The simulations reveal that both absorption and emission spectra are highly sensitive to the intermolecular interactions with the solvent molecules with significant variations in energies and intensities across the sampling snapshots. As the analysis has already shown (especially the theoretical part), ISC is not actually that strong in DiKTa. For this reason, rISC is already largely suppressed at 80 K, and the prompt and delayed components can still be clearly distinguished from one another even at 300 K. Our approach enables an alternative to solvent-based embedding - now in the solid state - which also increases the loading concentrations. This, in turn, is helpful for overall brightness, since in polymers a higher loading would lead to aggregation again, which is effectively suppressed in the MOF. Overall, the combination of advanced material synthesis and high-level theoretical modeling provides a comprehensive perspective on the behavior of multi-resonant emitters in complex environments, paving the way for the rational design of future optoelectronic materials with higher loadings and thus, potentially higher brightness.

4 Acknowledgements

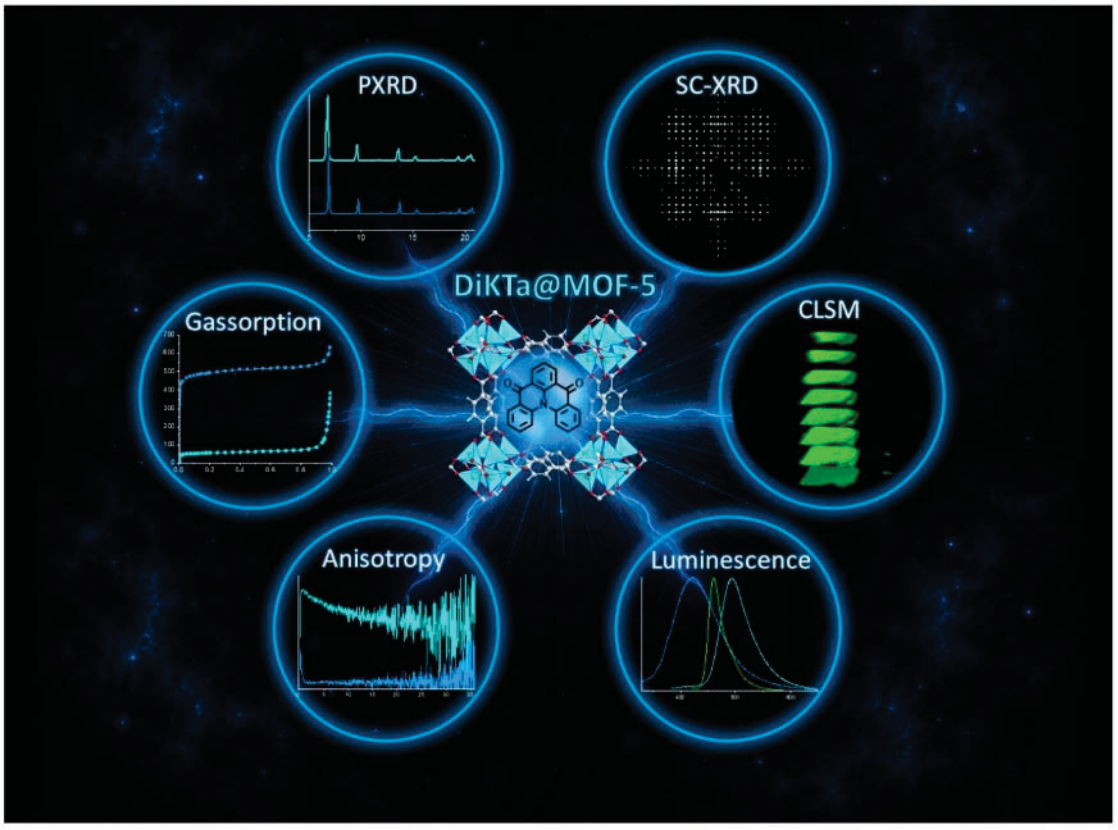
Financial support by the German Research Foundation (DFG, GI 349/6-2, 396890929/GRK 2482 "ModISC" and the grant 440366605 for the Rigaku diffractometer) is gratefully acknowledged. Computational infrastructure and support were provided by the Centre for Information and Media Technology at Heinrich Heine University Düsseldorf. M.S. and C.J. are indebted to generous funding by the German Research Foundation for a Stoe Stadi P powder diffractometer (INST 208/940-1, no. 559318975). The authors thank Dr. Guido Reiß for the SC-XRD measurements and helpful discussions.

Data Availability Statement

The data that supports the findings of this study are available in the supplementary material of this article

Table of Contents text

QM/MM simulations of the multi-resonant TADF emitters DiKTa using TD-DFT and DFT/MRCI methods quantifies the impact of explicit intermolecular interactions on the electronic structure and MOF-5 allowed to orient and stabilize this advanced OLED emitter.



References

[1] C. W. Tang, S. A. Vanslyke, *Appl. Phys. Lett.* **1987**, *51*, 913-915.

[2] G. Mandal, J. Bauri, R. B. Choudhary, *Mater. Sci. Eng. B* **2024**, *303*, 117271.

[3] M. A. Baldo, S. Lamansky, P. E. Burrows, M. E. Thompson, S. R. Forrest, *Appl. Phys. Lett.* **1999**, *75*, 4-6.

[4] M. Cocchi, J. Kalinowski, D. Virgili, J. A. G. Williams, *Appl. Phys. Lett.* **2008**, *92*, 113302.

[5] T. Fleetham, G. J. Li, J. Li, *ACS Appl. Mater. Inter.* **2015**, *7*, 16240-16246.

[6] D. H. Kim, N. S. Cho, H. Y. Oh, J. H. Yang, W. S. Jeon, J. S. Park, M. C. Suh, F. H. Kwon, *Adv. Mater.* **2011**, *23*, 2721-2726.

[7] C. A. Parker, C. G. Hatchard, *Trans. Faraday Soc.* **1961**, *57*, 1894−1904.

[8] A. Maciejewski, M. Szymanski, R. P. Steer, *J. Phys. Chem.* **1986**, *90*, 6314-6318.

[9] A. Endo, M. Ogasawara, A. Takahashi, D. Yokoyama, Y. Kato, C. Adachi, *Adv. Mater.* **2009**, *21*, 4802-4806.

[10] A. Endo, K. Sato, K. Yoshimura, T. Kai, A. Kawada, H. Miyazaki, C. Adachi, *Appl. Phys. Lett.* **2011**, *98*, 083302.

[11] Q. Wei, N. N. Fei, A. Islam, T. Lei, L. Hong, R. X. Peng, X. Fan, L. Chen, P. Q. Gao, Z. Y. Ge, *Adv. Opt. Mater.* **2018**, *6*, 1800512.

[12] G. Mehes, H. Nomura, Q. Zhang, T. Nakagawa, C. Adachi, *Angew. Chem. Int. Ed.* **2012**, *51*, 11311-11315.

[13] H. Nakanotani, Y. Tsuchiya, C. Adachi, *Chem. Lett.* **2021**, *50*, 938-948.

[14] Y. Gao, T. Su, L. Zhao, Y. Geng, Y. Wu, M. Zhang, Z. M. Su, *Org. Electron.* **2017**, *50*, 70-76.

[15] Y. Gao, C. Sun, T. Su, *J. Mol. Struct.* **2023**, *1272*, 134213.

[16] Y. Yuan, Y. Hu, Y. X. Zhang, J. D. Lin, Y. K. Wang, Z. Q. Jiang, L. S. Liao, S. T. Lee, *Adv. Funct. Mater.* **2017**, *27*, 1700986.

[17] H. Uoyama, K. Goushi, K. Shizu, H. Nomura, C. Adachi, *Nature* **2012**, *492*, 234–238.

[18] P. Data, P. Pander, M. Okazaki, Y. Takeda, S. Minakata, A. P. Monkman, *Angew. Chem. Int. Edit.* **2016**, *55*, 5739-5744.

[19] D. Püschel, J. Wiefermann, S. Hédé, T. Heinen, L. Pfeifer, O. Weingart, M. Suta, T. J. J. Müller, C. Janiak, *J. Mater. Chem. C* **2023**, *11*, 8982-8991.

[20] D. Y. Chen, W. Liu, C. J. Zheng, K. Wang, F. Li, S. L. Tao, X. M. Ou, X. H. Zhang, *ACS Appl. Mater. Inter.* **2016**, *8*, 16791-16798.

[21] T. Hatakeyama, K. Shiren, K. Nakajima, S. Nomura, S. Nakatsuka, K. Kinoshita, J. Ni, Y. Ono, T. Ikuta, *Adv. Mater.* **2016**, *28*, 2777-2781.

[22] X. Qiu, G. J. Tian, C. W. Lin, Y. Y. Pan, X. Y. Ye, B. H. Wang, D. G. Ma, D. H. Hu, Y. Luo, Y. G. Ma, *Adv. Opt. Mater.* **2021**, *9*, 2001845.

[23] S. M. Suresh, L. Zhang, D. Hall, C. F. Si, G. Ricci, T. Matulaitis, A. M. Z. Slawin, S. Warriner, Y. Olivier, I. D. W. Samuel, E. Zysman-Colman, *Angew. Chem. Int. Edit.* **2023**, *62*, e202215522.

[24] S. Wu, L. Zhang, J. Wang, A. Kumar Gupta, I. D. W. Samuel, E. Zysman-Colman, *Angew. Chem. Int. Ed.* **2023**, *62*, e202305182.

[25] E. Hamzehpoor, D. F. Perepichka, *Angew. Chem. Int. Edit.* **2020**, *59*, 9977-9981.

[26] X. Liang, Z. P. Yan, H. B. Han, Z. G. Wu, Y. X. Zheng, H. Meng, J. L. Zuo, W. Huang, *Angew. Chem. Int. Edit.* **2018**, *57*, 11316-11320.

[27] S. Nakatsuka, H. Gotoh, K. Kinoshita, N. Yasuda, T. Hatakeyama, *Angew. Chem. Int. Edit.* **2017**, *56*, 5087-5090.

[28] Y. Tsuchiya, Y. Ishikawa, S. H. Lee, X. K. Chen, J. L. Brédas, H. Nakanotani, C. Adachi, *Adv. Opt. Mater.* **2021**, *9*, 2002174.

[29] J. M. Dos Santos, D. Hall, B. Basumatary, M. Bryden, D. Y. Chen, P. Choudhary, T. Comerford, E. Crovini, A. Danos, J. Y. De, S. Diesing, M. Fatahi, M. Griffin, A. K. Gupta, H. Hafeez, L. Hämmerling, E. Hanover, J. Haug, T. Heil, D. Karthik, S. Kumar, O. L. V. Lee, H. Y. Li, F. Lucas, C. F. R. Mackenzie, A. Mariko, T. Matulaitis, F. Millward, Y. Olivier, Q. Qi, I. D. W. Samuel, N. Sharma, C. F. Si, L. Spierling, P. Sudhakar, D. M. Sun, E. Tankelevicute, M. D. Tonet, J. X. Wang, T. Wang, S. Wu, Y. Xu, L. Zhang, E. Zysman-Colman, *Chem. Rev.* **2024**, *124*, 13736-14110.

[30] J. Mei, N. L. C. Leung, R. T. K. Kwok, J. W. Y. Lam, B. Z. Tang, *Chem. Rev.* **2015**, *115*, 11718-11940.

[31] Y. N. Hong, J. W. Y. Lam, B. Z. Tang, *Chem. Soc. Rev.* **2011**, *40*, 5361-5388.

[32] A. P. Deshmukh, N. Geue, N. C. Bradbury, T. L. Atallah, C. R. Chuang, M. Pengshung, J. S. Cao, E. M. Sletten, D. Neuhauser, J. R. Caram, *Chem. Phys. Rev.* **2022**, *3*, 021401.

[33] C. Janiak, J. K. Vieth, *New J. Chem.* **2010**, *34*, 2366-2388.

[34] A. Kirchon, L. Feng, H. F. Drake, E. A. Joseph, H. C. Zhou, *Chem. Soc. Rev.* **2018**, *47*, 8611-8638.

[35] H. C. Zhou, J. R. Long, O. M. Yaghi, *Chem. Rev.* **2012**, *112*, 673-674.

[36] I. M. Hönicke, I. Senkovska, V. Bon, I. A. Baburin, N. Bönisch, S. Raschke, J. D. Evans, S. Kaskel, *Angew. Chem. Int. Edit.* **2018**, *57*, 13780-13783.

[37] J. Lippke, B. Brosent, T. von Zons, E. Virmani, S. Lilienthal, T. Preusse, M. Hulsmann, A. M. Schneider, S. Wuttke, P. Behrens, A. Godt, *Inorg. Chem.* **2017**, *56*, 748-761.

[38] I. Senkovska, F. Hoffmann, M. Fröba, J. Getzschmann, W. Böhlmann, S. Kaskel, *Micropor. Mesopor. Mat.* **2009**, *122*, 93-98.

[39] M. Eddaoudi, J. Kim, N. Rosi, D. Vodak, J. Wachter, M. O'Keeffe, O. M. Yaghi, *Science* **2002**, *295*, 469-472.

[40] J. H. Cavka, S. Jakobsen, U. Olsbye, N. Guillou, C. Lamberti, S. Bordiga, K. P. Lillerud, *J. Am. Chem. Soc.* **2008**, *130*, 13850-13851.

[41] K. S. Park, Z. Ni, A. P. Cote, J. Y. Choi, R. Huang, F. J. Uribe-Romo, H. K. Chae, M. O'Keeffe, O. M. Yaghi, *Proc. Natl. Acad. Sci. U. S. A.* **2006**, *103*, 10186-10191.

[42] W. Gong, H. M. Xie, K. B. Idrees, F. A. Son, Z. J. Chen, F. R. Sha, Y. Liu, Y. Cui, O. K. Farha, *J. Am. Chem. Soc.* **2022**, *144*, 1826-1834.

[43] X. B. Xu, Y. Lu, Y. Yang, F. Nosheen, X. Wang, *Sci. China Mater.* **2015**, *58*, 370-377.

[44] Y. Liu, S. Liu, D. He, N. Li, Y. Ji, Z. Zheng, F. Luo, S. Liu, Z. Shi, C. Hu, *J. Am. Chem. Soc.* **2015**, *137*, 12697-12703.

[45] W. Q. Fan, K. Liang, J. Y. Liang, *J. Mater. Chem. A* **2024**, *12*, 30318-30328.

[46] T. O. Knedel, E. Ricklefs, C. Schlusener, V. B. Urlacher, C. Janiak, *ChemistryOpen* **2019**, *8*, 1337-1344.

[47] Y. L. Weng, R. Chen, Y. Hui, D. Chen, C. X. Zhao, *Chem. Bio. Eng.* **2024**, *1*, 99-112.

[48] S. L. Li, Z. X. Zhou, G. Q. Liu, Q. Zhang, Y. F. Gao, H. Zhu, S. P. Zhu, *Chem. Eng. J.* **2024**, *493*.

[49] X. C. Li, Z. H. Zhang, W. M. Xiao, S. J. Deng, C. Chen, N. Zhang, *J. Mater. Chem. A* **2019**, *7*, 14504-14509.

[50] S. Rojas, F. J. Carmona, C. R. Maldonado, P. Horcajada, T. Hidalgo, C. Serre, J. A. R. Navarro, E. Barea, *Inorg. Chem.* **2016**, *55*, 2650-2663.

[51] H. Q. Zheng, Y. N. Zhang, L. F. Liu, W. Wan, P. Guo, A. M. Nyström, X. D. Zou, *J. Am. Chem. Soc.* **2016**, *138*, 962-968.

[52] C. C. Cao, C. X. Chen, Z. W. Wei, Q. F. Qiu, N. X. Zhu, Y. Y. Xiong, J. J. Jiang, D. W. Wang, C. Y. Su, *J. Am. Chem. Soc.* **2019**, *141*, 2589-2593.

[53] C. Empel, M. N. A. Fetzer, S. Sasmal, T. Strothmann, C. Janiak, R. M. Koenigs, *Chem. Commun.* **2024**, *60*, 7327-7330.

[54] G. Cai, H. L. Jiang, *Angew. Chem. Int. Ed. Engl.* **2017**, *56*, 563-567.

[55] X. Wu, Z. Bao, B. Yuan, J. Wang, Y. Sun, H. Luo, S. Deng, *Micropor. Mesopor. Mat.* **2013**, *180*, 114-122.

[56] J. Dechnik, A. Nuhnen, C. Janiak, *Cryst. Growth Des.* **2017**, *17*, 4090-4099.

[57] F. Wang, Z. Wang, J. J. Yu, S. Han, X. W. Li, Y. Wang, *Sep. Purif. Technol.* **2024**, *333*, 125892.

[58] S. Gökpinar, S. J. Ernst, E. Hastürk, M. Möllers, I. El Aita, R. Wiedey, N. Tannert, S. Niessing, S. Abdpour, A. Schmitz, J. Quodbach, G. Füldner, S. K. Henninger, C. Janiak, *Ind. Eng. Chem. Res.* **2019**, *58*, 21493-21503.

[59] H. Babaei, A. J. H. McGaughey, C. E. Wilmer, *Chem. Sci.* **2017**, *8*, 583-589.

[60] H. Babaei, M. E. DeCoster, M. Jeong , Z. M. Hassan, T. Islamoglu, H. Baumgart, A. J. H. McGaughey, E. Redel, O. K. Farha, P. E. Hopkins, J. A. Malen, C. E. Wilmer, *Nat. Commun.* **2020**, *11*, 4010.

[61] Y. Gao, F. Wang, J. Tang, C. C. Wang, X. H. Yi, Y. W. Wei, G. C. Liu, P. Wang, H. F. Fu, C. Zhao, X. C. Qiu, S. L. Yi, *Chem. Eng. J.* **2024**, *495*, 153651.

[62] N. Prasetya, C. Wöll, *RSC Adv.* **2023**, *13*, 22998-23009.

[63] K. L. Shi, H. H. Su, K. K. Liu, Y. T. Zhang, J. Y. Zhu, *Sep. Purif. Technol.* **2025**, *357*, 130155.

[64] C. Z. Wang, J. Chen, Q. H. Li, G. E. Wang, X. L. Ye, J. Lv, G. Xu, *Angew. Chem. Int. Edit.* **2023**, *62*, e202302996.

[65] M. B. Kanakala, S. A. Bhat, A. Kumar, C. V. Yelamaggad, *ACS Appl. Mater. Interfaces* **2025**, *3*, 1731-1738.

[66] S. L. Z. Jiokeng, T. J. M. M. Ntep, M. N. A. Fetzer, T. Strothmann, C. G. Fotsop, I. K. Tonle, C. Janiak, *ACS Appl. Mater. Interfaces* **2024**, *16*, 2509-2521.

[67] T. O. Knedel, S. Buss, I. Maisuls, C. G. Daniliuc, C. Schlusener, P. Brandt, O. Weingart, A. Vollrath, C. Janiak, C. A. Strassert, *Inorg. Chem.* **2020**, *59*, 7252-7264.

[68] U. Ryu, H. S. Lee, K. S. Park, K. M. Choi, *Polyhedron* **2018**, *154*, 275-294.

[69] Y. J. Cui, T. Song, J. C. Yu, Y. Yang, Z. Y. Wang, G. D. Qian, *Adv. Funct. Mater.* **2015**, *25*, 4796-4802.

[70] C. Y. Sun, X. L. Wang, X. Zhang, C. Qin, P. Li, Z. M. Su, D. X. Zhu, G. G. Shan, K. Z. Shao, H. Wu, J. Li, *Nat. Commun.* **2013**, *4*, 2717.

[71] Y. Tang, W. Q. Cao, L. J. Yao, Y. J. Cui, Y. Yu, G. D. Qian, *J. Mater. Chem. C* **2020**, *8*, 12308-12313.

[72] N. Z. Zhang, D. W. Zhang, J. Zhao, Z. G. Xia, *Dalton T* **2019**, *48*, 6794-6799.

[73] Y. Yuan, X. Tang, X. Y. Du, Y. Hu, Y. J. Yu, Z. Q. Jiang, L. S. Liao, S. T. Lee, *Adv. Opt. Mater.* **2019**, *7*, 1801536.

[74] X. Li, Y. Z. Shi, K. Wang, M. Zhang, C. J. Zheng, D. M. Sun, G. L. Dai, X. C. Fan, D. Q. Wang, W. Liu, Y. Q. Li, J. Yu, X. M. Ou, C. Adachi, X. H. Zhang, *ACS Appl. Mater. Interfaces* **2019**, *11*, 13472-13480.

[75] D. Hall, S. M. Suresh, P. L. dos Santos, E. Duda, S. Bagnich, A. Pershin, P. Rajamalli, D. B. Cordes, A. M. Z. Slawin, D. Beljonne, A. Köhler, I. D. W. Samuel, Y. Olivier, E. Zysman-Colman, *Adv. Opt. Mater.* **2020**, *8*, 1901627.

[76] B. H. Monjezi, T. Kasper, G. Hong, C. F. Si, R. Oestreich, O. Weingart, P. G. Weidler, C. Wöll, E. Zysman-Colman, C. Janiak, S. Bräse, K. Müller-Buschbaum, A. Knebel, *Adv. Sci.* **2026**, *13*, e00068.

[77] F. Huang, K. Wang, Y.-Z. Shi, X.-C. Fan, X. Zhang, J. Yu, C.-S. Lee, X.-H. Zhang, *ACS Appl. Mater. Interfaces* **2021**, *13*, 36089-36097.

[78] S. Wu, W. Li, K. Yoshida, D. Hall, S. Madayanad Suresh, T. Sayner, J. Gong, D. Beljonne, Y. Olivier, I. D. Samuel, *ACS Appl. Mater. Interfaces* **2022**, *14*, 22341-22352.

[79] D. Hall, J. C. Sancho-García, A. Pershin, G. Ricci, D. Beljonne, E. Zysman-Colman, Y. Olivier, *J. Chem. Theory Comput.* **2022**, *18*, 4903-4918.

[80] S. Nathiya, M. Panneerselvam, L. T. Costa, *Phys. Chem. Chem. Phys.* **2025**, *27*, 7265-7278.

[81] A. K. Dhara, S. K. Ghosh, *Phys. Rev. A* **1987**, *35*, 442-442.

[82] E. Runge, E. K. U. Gross, *Phys. Rev. Lett.* **1984**, *52*, 997-997.

[83] S. Grimme, M. Waletzke, *J. Chem. Phys.* **1999**, *111*, 5645-5655.

[84] M. Kleinschmidt, C. M. Marian, M. Waletzke, S. Grimme, *J. Chem. Phys.* **2009**, *130*, 044708-044708.

[85] A. Heil, M. Kleinschmidt, C. M. Marian, *J. Chem. Phys.* **2018**, *149*, 164106-164106.

[86] J. E. Field, D. Venkataraman, *Chem. Mater.* **2002**, *14*, 962-964.

[87] J.-D. Chai, M. Head-Gordon, *Phys. Chem. Chem. Phys.* **2008**, *10*, 6615-6620.

[88] F. Weigend, *Phys. Chem. Chem. Phys.* **2006**, *8*, 1057–1065.

[89] F. Weigend, R. Ahlrichs, *Phys. Chem. Chem. Phys.* **2005**, *7*, 3297–3305.

[90] M. J. Frisch, G. W. Trucks, H. B. Schlegel, G. E. Scuseria, M. A. Robb, J. R. Cheeseman, G. Scalmani, V. Barone, G. A. Petersson, H. Nakatsuji, X. Li, M. Caricato, A. V. Marenich, J. Bloino, B. G. Janesko, R. Gomperts, B. Mennucci, H. P. Hratchian, J. V. Ortiz, A. F. Izmaylov, J. L. Sonnenberg, D. Williams-Young, F. Ding, F. Lipparini, F. Egidi, J. Goings, B. Peng, A. Petrone, T.

Henderson, D. Ranasinghe, V. G. Zakrzewski, J. Gao, N. Rega, G. Zheng, W. Liang, M. Hada, M. Ehara, K. Toyota, R. Fukuda, J. Hasegawa, M. Ishida, T. Nakajima, Y. Honda, O. Kitao, H. Nakai, T. Vreven, K. Throssell, J. J. A. Montgomery, J. E. Peralta, F. Ogliaro, M. J. Bearpark, J. J. Heyd, E. N. Brothers, K. N. Kudin, V. N. Staroverov, T. A. Keith, R. Kobayashi, J. Normand, K. Raghavachari, A. P. Rendell, J. C. Burant, S. S. Iyengar, J. Tomasi, M. Cossi, J. M. Millam, M. Klene, C. Adamo, R. Cammi, J. W. Ochterski, R. L. Martin, K. Morokuma, O. Farkas, J. B. Foresman, D. J. Fox, Gaussian, Inc., W. CT, **2016**.

[91] F. Furche, R. Ahlrichs, C. Hättig, W. Klopper, M. Sierka, F. Weigend, *Wiley Interdiscip. Rev. Comput. Mol. Sci.* **2014**, *4*, 91-100.

[92] W. Humphrey, A. Dalke, K. Schulten, *J. Mol. Graph.* **1996**, *14*, 33-38.

[93] X. He, V. H. Man, W. Yang, T.-S. Lee, J. Wang, *J. Chem. Phys.* **2020**, *153*, 114502.

[94] C. Tian, K. Kasavajhala, K. A. A. Belfon, L. Raguette, H. Huang, A. N. Migues, J. Bickel, Y. Wang, J. Pincay, Q. Wu, C. Simmerling, *J. Chem. Theory Comput.* **2020**, *16*, 528-552.

[95] W. Jorgensen, J. Chandrasekhar, J. Madura, R. Impey, M. Klein, *J. Chem. Phys.* **1983**, *79*, 926-935.

[96] C. I. Bayly, P. Cieplak, W. Cornell, P. A. Kollman, *J. Phys. Chem.* **1993**, *97*, 10269-10280.

[97] J. Wang, W. Wang, P. A. Kollman, D. A. Case, *J. Am. Chem. Soc* **2001**, *222*, 2001.

[98] U. C. Singh, P. A. Kollman, *J. Comput. Chem.* **1984**, *5*, 129-145.

[99] S. V. Shedge, T. J. Zuehlsdorff, A. Khanna, S. Conley, C. M. Isborn, *J. Chem. Phys.* **2021**, *154*, 084116-084116.

[100] M. Bracker, M. K. Kubitz, C. Czekelius, C. M. Marian, M. Kleinschmidt, *ChemPhotoChem* **2022**, *6*, e202200040.

[101] D. A. Case, T. E. Cheatham Iii, T. Darden, H. Gohlke, R. Luo, K. M. Merz Jr, A. Onufriev, C. Simmerling, B. Wang, R. J. Woods, *J. Comput. Chem.* **2005**, *26*, 1668-1688.

[102] T. Darden, D. York, L. Pedersen, *J. Chem. Phys.* **1993**, *98*, 10089-10092.

[103] H. J. C. Berendsen, J. P. M. Postma, W. F. van Gunsteren, A. DiNola, J. R. Haak, *J. Chem. Phys.* **1984**, *81*, 3684-3690.

[104] O. Weingart, A. Nenov, P. Altoè, I. Rivalta, J. Segarra-Martí, I. Dokukina, M. Garavelli, *J. Mol. Mod.* **2018**, *24*, 1–30-31–30.

[105] C. S. Tsao, M. S. Yu, T. Y. Chung, H. C. Wu, C. Y. Wang, K. S. Chang, H. L. Chen, *J. Am. Chem. Soc.* **2007**, *129*, 15997-16004.

[106] S. B. Han, Y. H. Wei, C. Valente, I. Lagzi, J. J. Gassensmith, A. Coskun, J. F. Stoddart, B. A. Grzybowski, *J. Am. Chem. Soc.* **2010**, *132*, 16358-16361.

[107] T. Chokbunpiam, S. Fritzsche, C. Chmelik, J. Caro, W. Janke, S. Hannongbua, *Chem. Phys. Lett.* **2016**, *648*, 178-181.

[108] F. Salles, A. Ghoufi, G. Maurin, R. G. Bell, C. Mellot-Draznieks, G. Ferey, *Angew. Chem. Int. Ed.* **2008**, *47*, 8487-8491.

[109] R. Pallach, J. Keupp, K. Terlinden, L. Frentzel-Beyme, M. Kloss, A. Machalica, J. Kotschy, S. K. Vasa, P. A. Chater, C. Sternemann, M. T. Wharmby, R. Linser, R. Schmid, S. Henke, *Nat. Commun.* **2021**, *12*, 4097.

[110] S. Canossa, *Crystengcomm* **2025**, *27*, 6556-6571.

[111] S. L. Griffin, E. G. Meekel, J. M. Bulled, S. Canossa, A. Wahrhaftig-Lewis, E. M. Schmidt, N. R. Champness, *Nat. Commun.* **2025**, *16*, 3209.

[112] M. H. Ni, M. Gong, X. Li, J. L. Gu, B. Li, Y. Chen, *Appl. Mater. Today* **2021**, *23*, 100982.

[113] V. Glembockyte, M. Frenette, C. Mottillo, A. M. Durantini, J. Gostick, V. Strukil, T. Friscic, G. Cosa, *J. Am. Chem. Soc.* **2018**, *140*, 16882-16887.

[114] R. Luchowski, S. Sabnis, M. Szabelski, P. Sarkar, S. Raut, Z. Gryczynski, J. Borejdo, P. Bojarski, I. Gryczynski, *J. Lumin.* **2010**, *130*, 2446-2451.

Supporting Information

From Aggregation to Isolation: Preserving MR-TADF Emission of DiKTa in MOF-5

Annette Vollrath,‡[a] Marcus N. A. Fetzer,‡[a] Jennifer Kremper,‡[b,c] Benedikt Bendel,[d] Ralf Kühnemuth,[e] Markus Suta,[d] Jan Meisner,*[b] Oliver Weingart,*[c,f] and Christoph Janiak*[a]

[a]Inorganic and Structural Chemistry, Heinrich Heine University Düsseldorf, Universitätsstraße 1, D-40225 Düsseldorf, Germany

[b]Institute for Physical Chemistry, Theory and Simulation of Complex Systems, Heinrich Heine University Düsseldorf, Universitätsstr. 1, 40225 Düsseldorf, Germany

[c]Institute for Theoretical and Computational Chemistry, Photodynamics, Heinrich Heine University Düsseldorf, Universitätsstr. 1, 40225 Düsseldorf, Germany

[d]Inorganic Photoactive Materials, Heinrich Heine University Düsseldorf, Universitätsstraße 1, D-40225 Düsseldorf, Germany

[e]Institute for Molecular Physical Chemistry, Heinrich Heine University Düsseldorf, Universitätsstraße 1, D-40225 Düsseldorf, Germany

[f]Center for Information and Media Technology, Heinrich Heine University, Universitätsstraße 1, 40225 Düsseldorf, Germany.

‡ These authors contributed equally to this work.

* Corresponding authors

Emails: Annette.Vollrath@hhu.de; fetzer@uni-duesseldorf.de; Jennifer.Kremper@hhu.de; Benedikt.Bendel@hhu.de; rakue001@hhu.de; Markus.Suta@hhu.de; meisner@hhu.de; Oliver.Weingart@hhu.de; janiak@hhu.de

Table of Contents

1. General Information
2. Sources of chemicals
3. Synthesis of DiKTa
4. Photophysical properties of DiKTa
5. DiKTa@MOF-5 synthesis and characterization
6. Digestion UV-Vis spectroscopy
7. Calculation of pore filling and the probability p of multiple occupations
8. Photophysical properties of DiKTa@MOF-5 composites
9. Quantum chemical calculations of DiKTa in solvents

S1. General Information

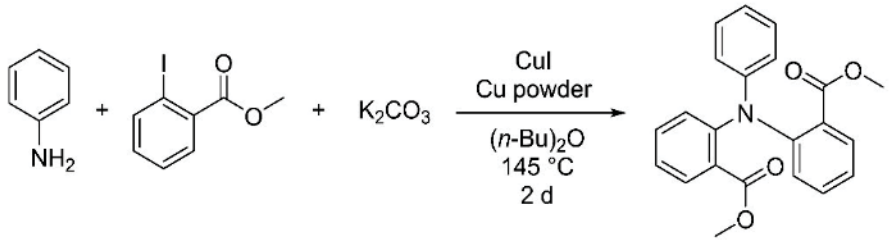
Unless otherwise noted, all commercially available compounds were used as provided without further purification. Solvents used in reactions were p. A. grade. Solvents for ambient pressure column chromatography for the preparative purification of synthesis products were technical grade and distilled prior to use. Column chromatography was performed using silica gel Merck 60 (particle size 0.063 – 0.2 mm). Solvent mixtures are understood as volume/volume. Analytical thin-layer chromatography (TLC) was performed on Macherey-Nagel silica gel aluminium plates with F-254 indicator, visualized by irradiation with UV light (λ_{exc} = 254 or 365 nm). ^{1}H-NMR and ^{13}C-NMR were recorded on a Bruker Avance III 300 MHz NMR spectrometer in $CDCl_3$. Data are reported in the following order: chemical shift (δ) in ppm; multiplicities are indicated s (singlet), d (doublet), t (triplet), q (quartet), m (multiplet). ^{1}H-NMR chemical shifts are referenced to the residual proton solvent signal versus TMS (δ($CHCl_3$ = 7.26)). ^{13}C-NMR chemical shifts are referenced to the carbon solvent signal versus TMS (δ($CHCl_3$ = 77.2)). EI-MS was measured on a JOEL JMS-Q1600GC. HR-ESI-MS was measured on a Bruker Daltonics UHR-QTOF maXis 4G. All measurements were done on positive ion mode. Powder X-ray diffraction (PXRD) analysis was conducted at ambient temperature on a Rigaku Miniflex 600 powder diffractometer using Cu K_α radiation with λ = 1.541 Å (40 kV, 15 mA, 600 W) in the range of 2 θ = 2°– 50° and a flat silicon low background with a small indent. N_2 sorption isotherms were obtained with a Belsorp MAXII high-precision gas/vapor adsorption measurement instrument at 77 K. Single-crystal X-ray diffraction measurements were performed at 150 K using a Rigaku XtaLAB Synergy S diffractometer (Rigaku, Tokyo, Japan) equipped with a PhotonJet Cu K_α radiation source (λ = 1.54184 Å) and a hybrid pixel array detector. Suitable single crystals were selected under a polarized-light Leica M80 microscope (Leica, Wetzlar, Germany) and mounted in oil on a cryo-loop. Unit-cell refinement, data reduction, and absorption correction were carried out using CrysAlisPro 21.5 as part of the data processing procedure. Optical measurements were carried out on a FS5 photoluminescence spectrometer (Edinburgh Instruments) or on a FLS1000 (cf. Figure 2c) photoluminescence spectrometer (Edinburgh Instruments) equipped with a 450 W Xe arc lamp, double grating monochromators (Czerny-Turner) in excitation and emission compartment and a thermoelectrically cooled PMT-980 detector (Hamamatsu). Lifetimes were determined as amplitude weighted average lifetime.

S2. Sources of chemicals

Reagent	Manufacturer
Aniline	ACROS Organics
Methyl 2-iodobenzoate	BLDpharm
Copper(I) iodide	Alfa Aesar
Potassium carbonate	Fisher Chemical
Copper powder	Laboratory stock
Dibutyl ether	Sigma-Aldrich
Dimethyldormamide (DMF)	Fisher Chemical
Magnesium sulfate	VWR Chemicals
Sodium hydroxide	Fisher Chemical
HCl (37%)	Sigma-Aldrich
Thionyl chloride	Thermo Scientific
Aluminium chloride	TCI Chemicals
Dichloromethane (DCM)	Sigma-Aldrich
Diethylformamide (DEF)	TCI Chemicals
Zinc nitrate hexahydrate	Roth
Terephthalic acid (H_2BDC)	Alfa Aesar

S3. Synthesis of DiKTa

S3.1 Synthesis of dimethyl 2,2'-(phenylazanediyl)dibenzoate 1



1 Yield: 76 %

Freshly distilled aniline was used for the synthesis. The synthesis was carried out according to the instructions of J. E. Field *et al.*[1]

In a 100 mL three-necked round-bottom flask equipped with a stirring bar and a reflux condenser, 2.28 mL of aniline (25 mmol), 11.2 mL of methyl 2-iodobenzoate (76.2 mmol), 10.5 g of K_2CO_3 (76.2 mmol), 500 mg of Cu powder (7.87 mmol), and 320 mg of CuI (1.68 mmol) were placed under a nitrogen atmosphere. 40 mL of dibutyl ether were added and the reaction mixture was heated to 145 °C for 48 h. The mixture was filtered through celite and the remaining product was washed from the filter with 500 mL of DCM. The filtrate was concentrated under vacuum. The crude product was purified by column chromatography on silica using a 4:1 mixture of cyclohexane and ethyl acetate as eluent. The resulting solid was washed with hot ethanol to yield 6.87 g (76 %) of pure product.

^{1}H-NMR (300 MHz, $CDCl_3$): δ = 7.65 (dd, *J* = 7.7, 1.2 Hz, 2H, B), 7.41 (ddd, J = 8.1, 7.3, 1.7 Hz, 2H, A), 7.20-7.10 (m, 6H, C), 6.90-6.82 (m, 1H, D), 6.78-6.74 (m, 2H, E), 3.39 (s, 6H, F) ppm (Figure S1).

^{13}C-NMR (75 MHz, $CDCl_3$): δ = 168.0, 148.6, 146.6, 132.8, 131.1, 129.1, 128.8, 128.0, 124.1, 121.9, 120.8, 51.9 ppm (Figure S2).

The data is in accordance with the literature.[1-2]

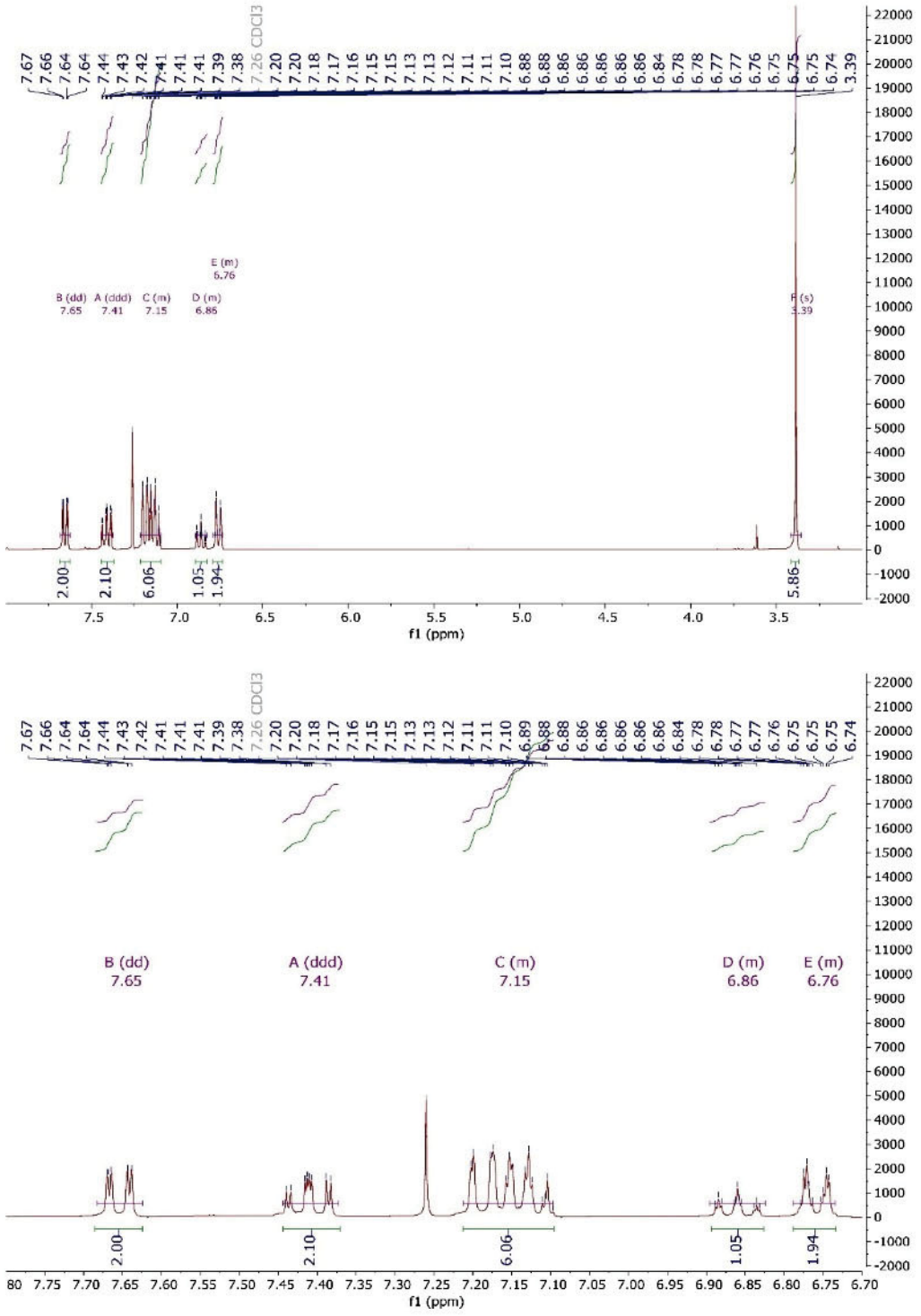


Figure S1. ^{1}H-NMR spectra (300 MHz) of **1** in $CDCl_3$.

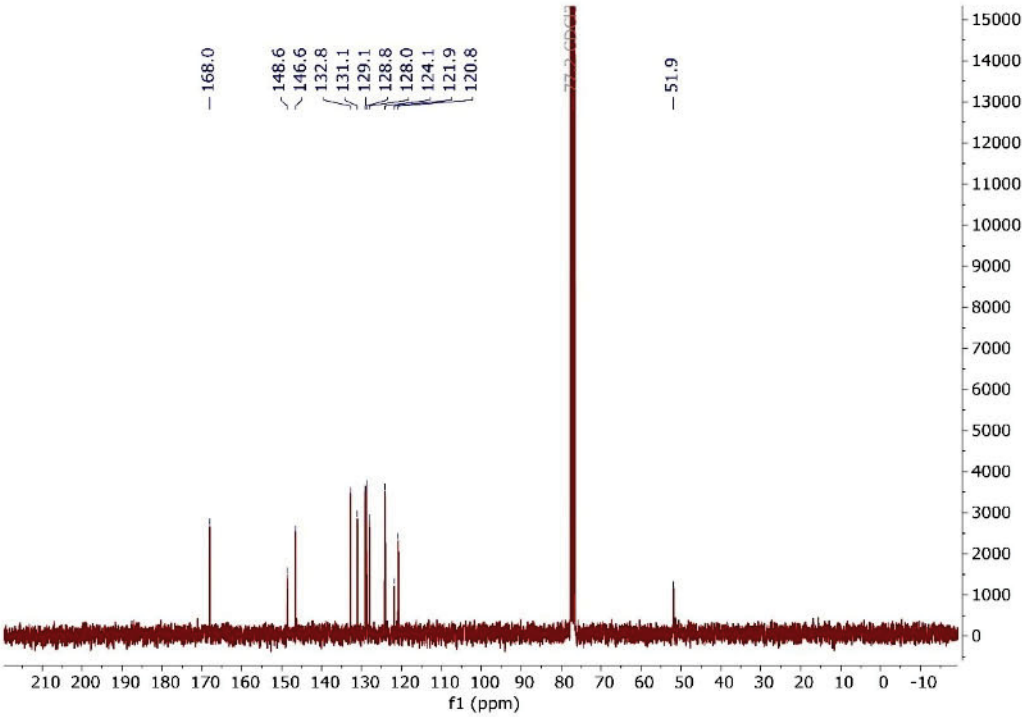
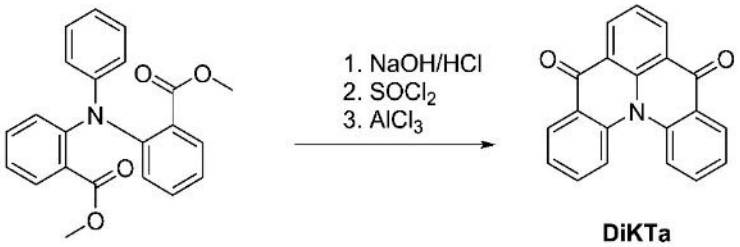


Figure S2. ^{13}C-NMR spectrum (75 MHz) of **1** in $CDCl_3$.

S3.2 Synthesis of DiKTa



DiKTa
Yield: 82 %

The synthesis was carried out according to the instructions of D. Hall *et al.*[2]

Product **1** (5.0 g, 13.8 mmol) was combined with an excess of sodium hydroxide in a mixture of ethanol and water (1:1) with a total volume of 60 mL. The reaction was heated under reflux for 16 hours. After cooling to room temperature, the mixture was acidified with hydrochloric acid to precipitate the diacid. After filtration, the product was washed three times with 25 mL of distilled water and dried overnight in a vacuum oven at 60 °C (4.34 g, 94% yield). The product was used for the next step without further purification or characterization.

Under a nitrogen atmosphere, the diacid (2.0 g, 6 mmol) was dispersed in 50 mL DCM and 1.0 mL of thionyl chloride (13.7 mmol) and 4 drops of DMF were added successively. The reaction mixture was refluxed for 3 hours and then cooled to room temperature. Under a nitrogen counterflow, 8 g of

aluminum chloride (60 mmol) was slowly added and refluxed for another 4 hours. The reaction mixture was then cooled to 0 °C in an ice bath and the reaction was quenched by adding water dropwise under vigorous stirring. The reaction was extracted with 50 mL DCM, the organic phase was washed three times with 50 mL water, and then dried over magnesium sulfate. After removing the excess solvent, the crude product was purified by column chromatography using a 1:1 mixture of cyclohexane and ethyl acetate. The resulting product is a yellow crystalline solid (1.55 g, 87% yield). Yield from product **1**: 82%, overall: 62%.

^{1}H-NMR (300 MHz, $CDCl_3$): δ = 8.74 (d, *J* = 7.6 Hz, 2H, A), 8.49 (dd, *J* = 7.9, 1.2 Hz, 2H, B), 8.14 (d, *J* = 8.0 Hz, 2H, C), 7.74 – 7.61 (m, 3H, D), 7.49 (ddd, *J* = 8.0, 7.1, 1.0 Hz, 2H, E) ppm (Figure S3).

^{13}C-NMR (75 MHz, $CDCl_3$): δ = 178.7, 139.9, 139.4, 133.0, 132.8, 127.9, 126.6, 125.3, 123.7, 120.4 ppm (Figure S4).

EI-MS: m/z = 297 $[M]^+$, 269 $[M\text{-}CO]^+$, 241 $[M\text{-}C_2O_2]^+$ (Figure S5).

HR-ESI-MS: $[M+H]^+$ Calculated ($C_{20}H_{12}NO_2$) 298.0863; Found 298.0859 (Figure S6).

The data is in accordance with the literature.[1-2]

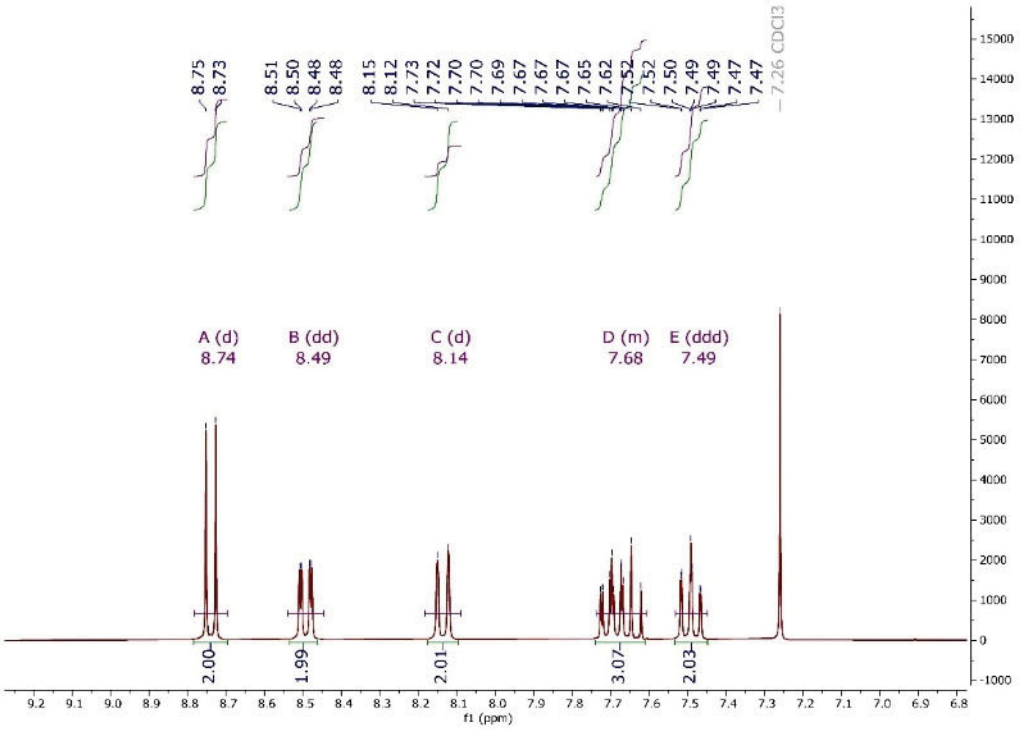


Figure S3. ^{1}H-NMR spectrum (300 MHz) of DiKTa in $CDCl_3$.

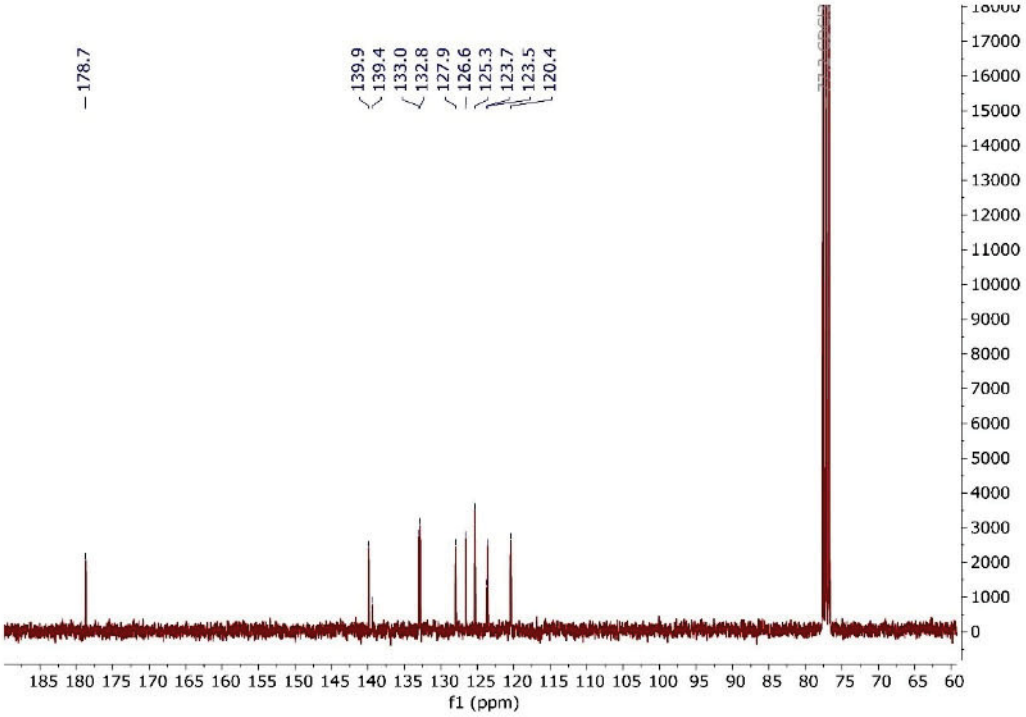


Figure S4. ^{13}C-NMR spectrum (75 MHz) of DiKTa in $CDCl_3$.

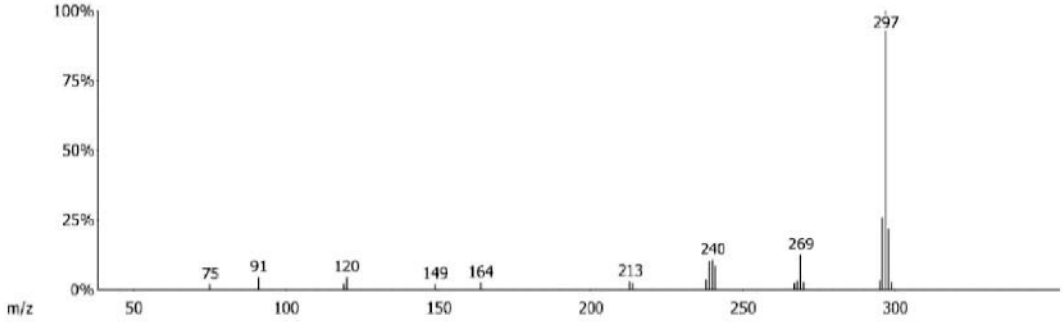


Figure S5. Electron impact-mass spectrum of DiKTa.

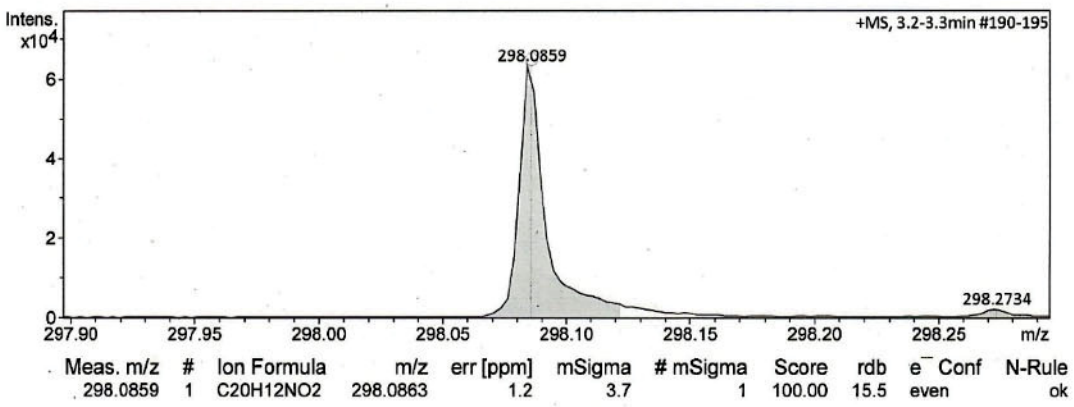


Figure S6. HR-ESI-mass spectrum of DiKTa.

S4. Photophysical properties of DiKTa

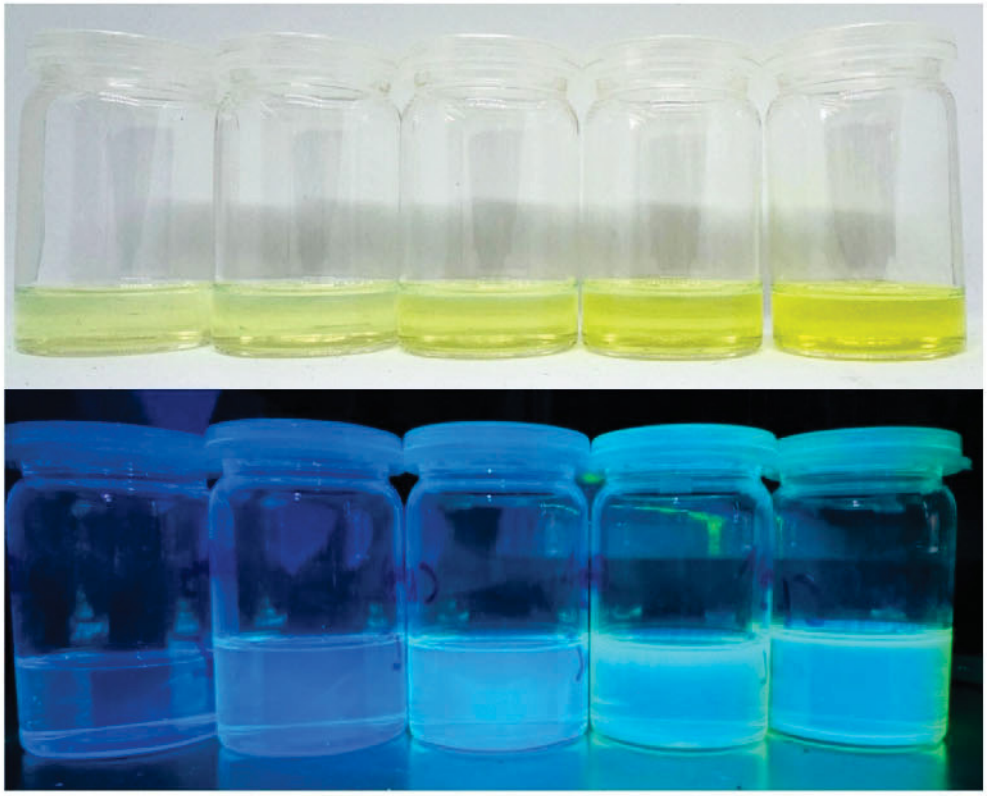
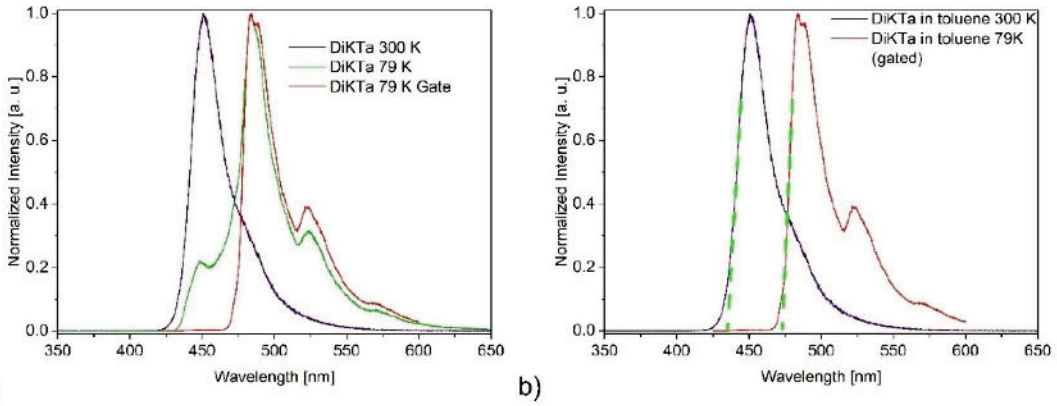
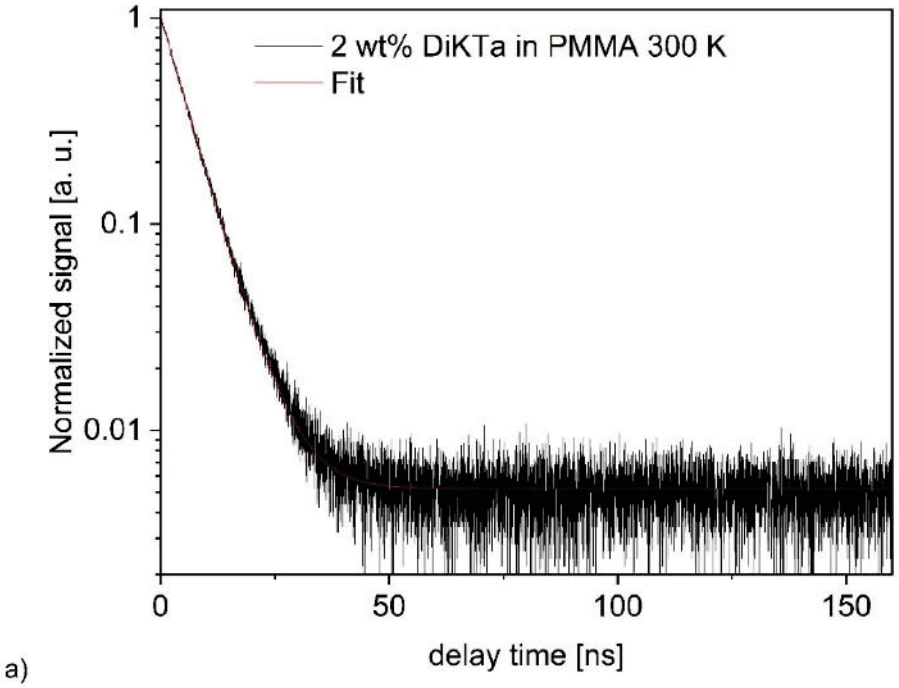


Figure S7. Photographic images of solutions of DiKTa in $CHCl_3$ with increasing concentrations under daylight (top) and UV-light (λ_{exc} = 365 nm, bottom). Concentration from left to right 0.001 g L^{-1}, 0.01 g L^{-1}, 0.1 g L^{-1}, 1 g L^{-1}, and 5 g L^{-1}.

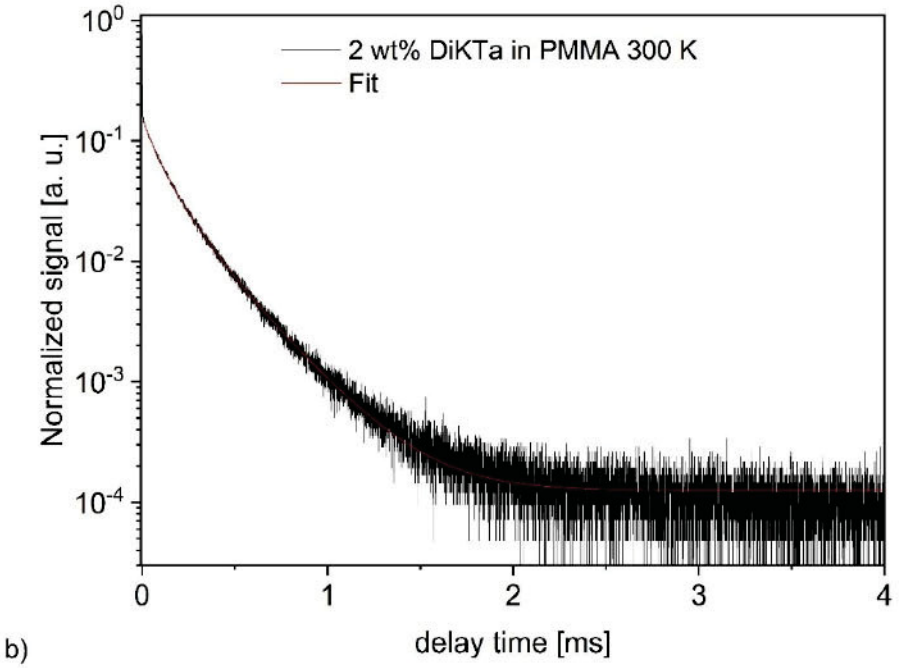


a) b)

Figure S8. Emission spectra of a) DiKTa in toluene at 300 K (λ_{exc} = 335 nm), 79 K (λ_{exc} = 335 nm), and 79 K with a delay of 10 ms and window of 10 ms (λ_{exc} = 420 nm). b) Onset (green dotted line) of the steady state spectrum at 300 K and 79 K for the determination of ΔE_{ST}.

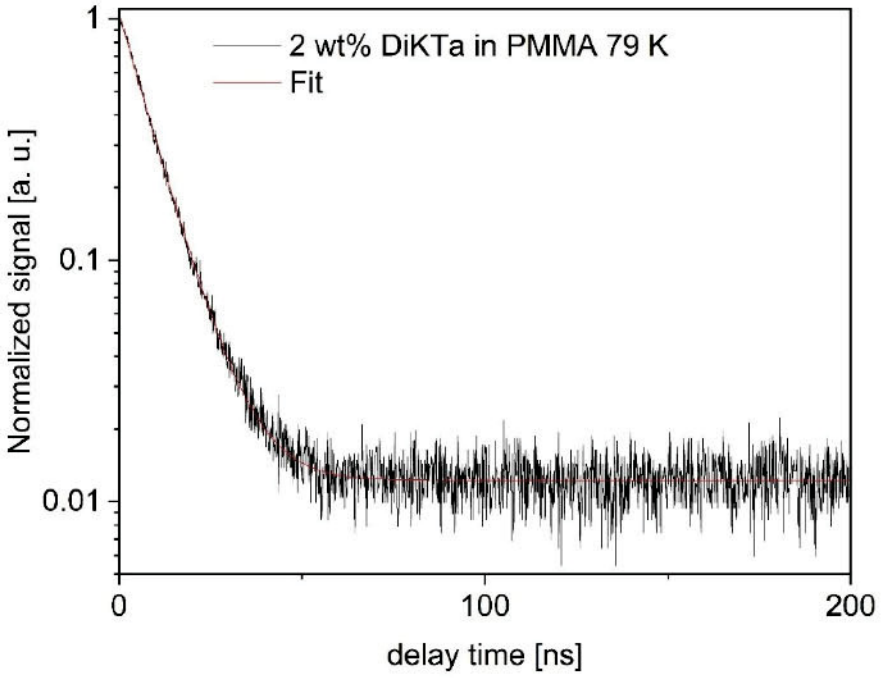


a)

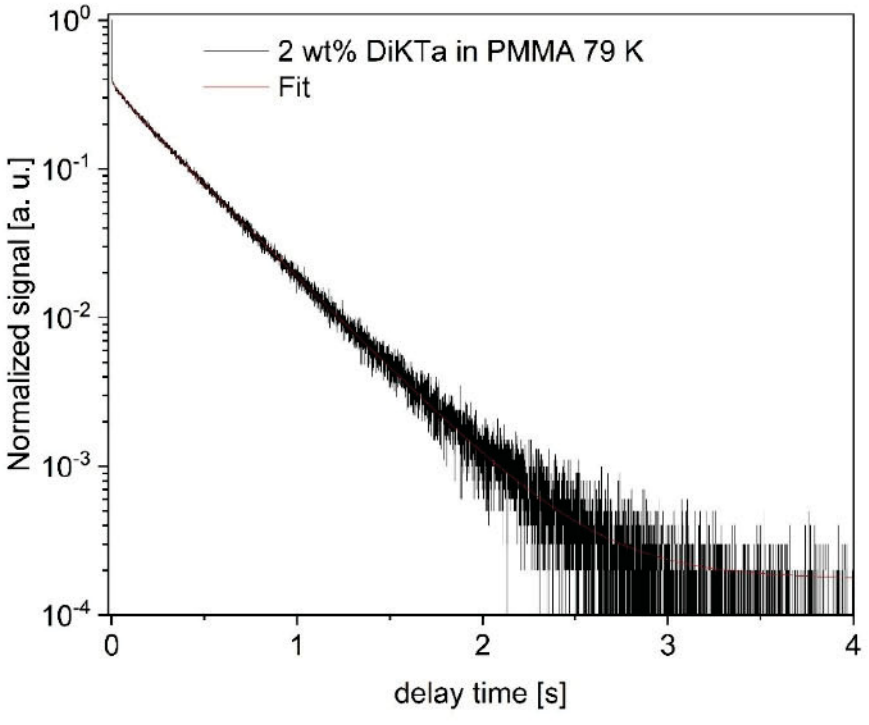


b)

Figure S9. a) Prompt and b) delayed time-resolved photoluminescence decay (black) of DiKTa in PMMA at 300 K.

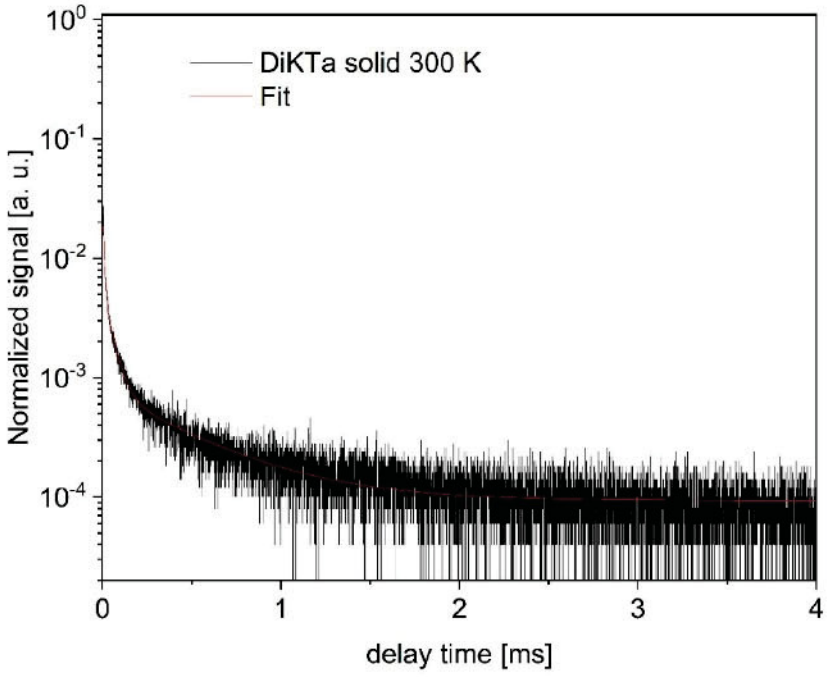


a)

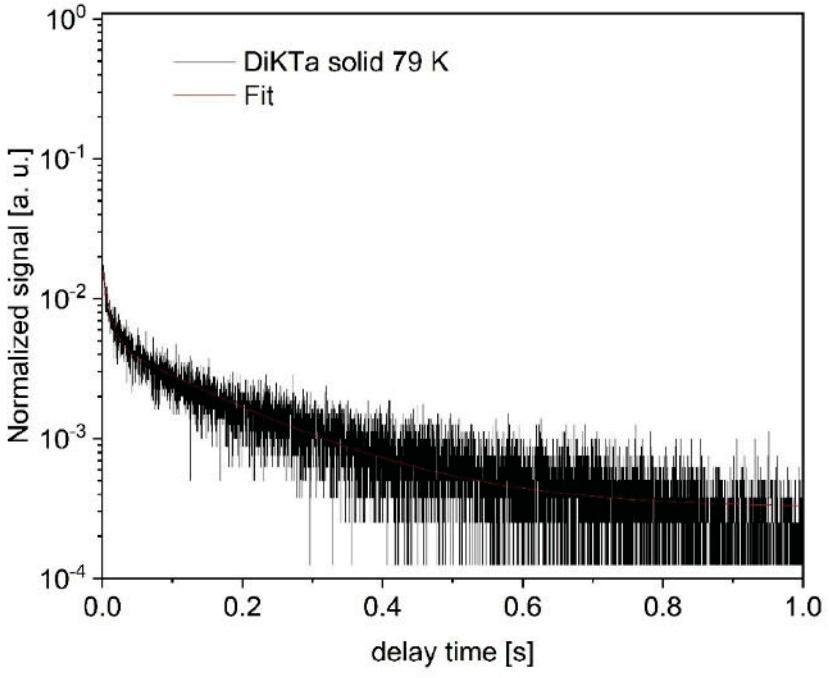


b)

Figure S10. a) Prompt and b) delayed time-resolved photoluminescence decay (black) of the DiKTa in PMMA at 79 K.



a)



b)

Figure S11. Time-resolved photoluminescence decay (black) of solid DiKTa at a) 300 K and b) 79 K.

Table S1. Summary of each decay plot with the respective exponential fitting parameters including pre-exponential factors A*i* and lifetimes *ti* for the DiKTa in PMMA and the solid DiKTa.

Compound	A1	t1	A2	t2	A3	t3
2 wt% DiKTa in PMMA (prompt, 300K)	1.01 ± $4.257 \cdot 10^{-4}$	5.681 ± 0.004				
2 wt% DiKTa in PMMA (delayed, 300K)	0.02	13247.594	0.08673	85827.2762	0.06041	233947.40854
2 wt% DiKTa in PMMA (prompt, 79K)	1.03829	8.139				
2 wt% DiKTa in PMMA (delayed, 79K)	0.024	$1.175 \cdot 10^{7}$	0.044	$1.055 \cdot 10^{8}$	0.33	$3.485 \cdot 10^{8}$
DiKTa solid (prompt, 300K)	0.988 ± 0.002	4.026 ± 0.009	0.052 ± 0.003	12.521 ± 0.33		
DiKTa solid (delayed, 300K)	0.005 ± $5.008 \cdot 10^{-5}$	48642.154 ± 547.386	0.035 ± $2.654 \cdot 10^{-4}$	$6075.9746.951 \cdot 10^{-4}$ ± 45.05	$6.951 \cdot 10^{-4}$ ± $1.206 \cdot 10^{-5}$	475804.527 ± 8812.673
DiKTa solid (prompt, 79K)	0.844 ± 0.009	5.724 ± 0.031	0.113 ± 0.009	12.535 ± 0.362		
DiKTa solid (delayed, 79K)	0.087 ± 0.001	262354.367 ± 3670.564	0.01 ± $1.173 \cdot 10^{-4}$	9963457.747 ± 188944.002	0.005 ± $3.844 \cdot 10^{-5}$	$1.657 \cdot 10^{8}$ ± 2096116.874

S5. DiKTa@MOF-5 – Synthesis and characterization

In this work, we used the optimized synthesis of Han *et al.* for MOF-5 with slight modifications.[3]

8 mL of DEF was placed in a test tube together with 308 mg of $Zn(NO_3)_2 \cdot 6H_2O$ and 58 mg of H_2BDC. The mixture was treated in an ultrasonic bath until all solids were dissolved. The reaction solution was filled into a 16 mL Pyrex tube via a syringe filter (0.2 µm PTFE membrane) and sealed. The tube was stored in an oven at 85 °C for 72 hours and then cooled back to room temperature. The crystals obtained were washed three times with 5 mL DEF and stored in solution. For N_2 adsorption, the crystals were activated super critically with CO_2.

The same synthesis procedure was used for the synthesis of the composites. In this process, pure DEF was gradually replaced by a 0.5 mmol L^{-1} concentrated solution of DiKTa in DEF (see Table S1), resulting in concentrations of DiKTa in the reaction mixtures of 0.06, 0.12, 0.25, and 0.5 mmol L^{-1}. Depending on the increasing concentration, the composite materials

DiKTa@MOF-$5_{0.03}$, **DiKTa**@MOF-$5_{0.05}$, **DiKTa**@MOF-$5_{0.09}$, and **DiKTa**@MOF-$5_{0.13}$ could be produced.

Table S2. Concentration and molar ratio determinations of the prepared DiKTa@MOF-5 composites.

Compound	Volume of DEF solution of DiKTa[a] [mL]	Concentrations of DiKTa in the reaction mixtures [mmol L^{-1}]	Molar ratio DiKTa:Zn:H_2BDC [mmol]
DiKTa@MOF-$5_{0.03}$	1	0.06	0.0005:1.04:0.35
DiKTa@MOF-$5_{0.05}$	2	0.12	0.001:1.04:0.35
DiKTa@MOF-$5_{0.09}$	4	0.25	0.002:1.04:0.35
DiKTa@MOF-$5_{0.13}$	8	0.5	0.004:1.04:0.35

[a] DEF solution of DiKTa with a concentration of 0.5 mmol L^{-1}

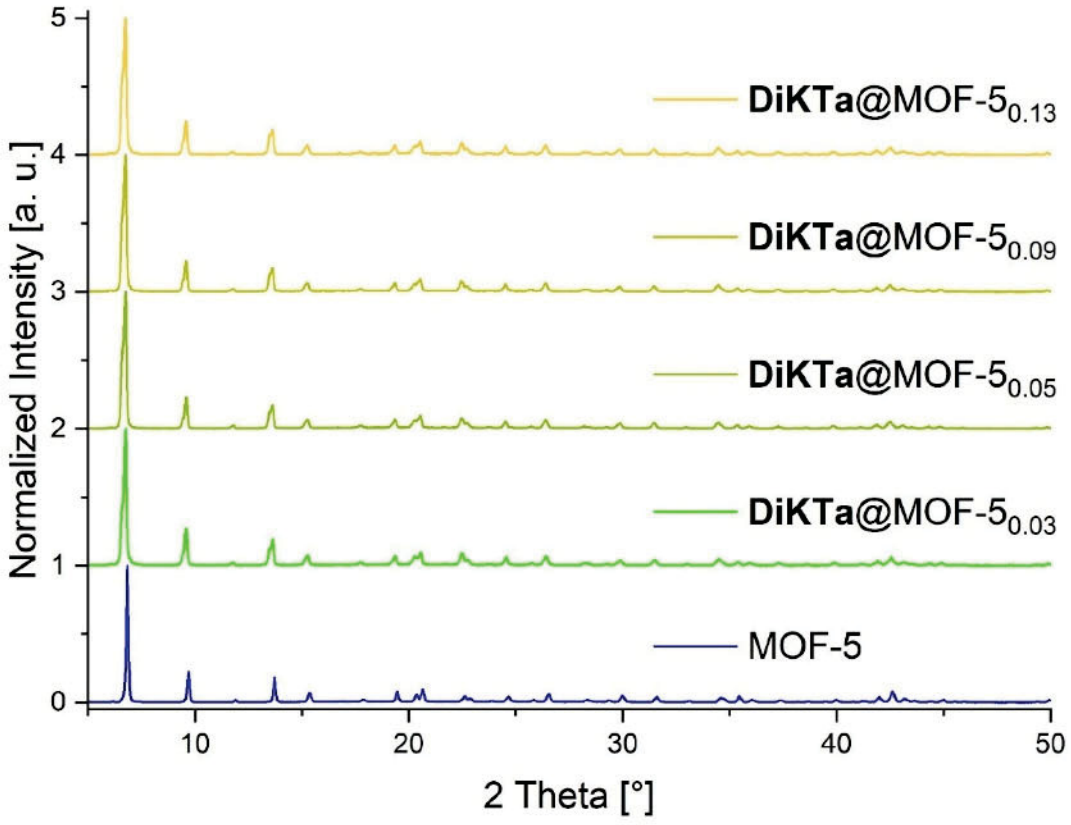


Figure S12. PXRD of MOF-5 and all composites prepared.

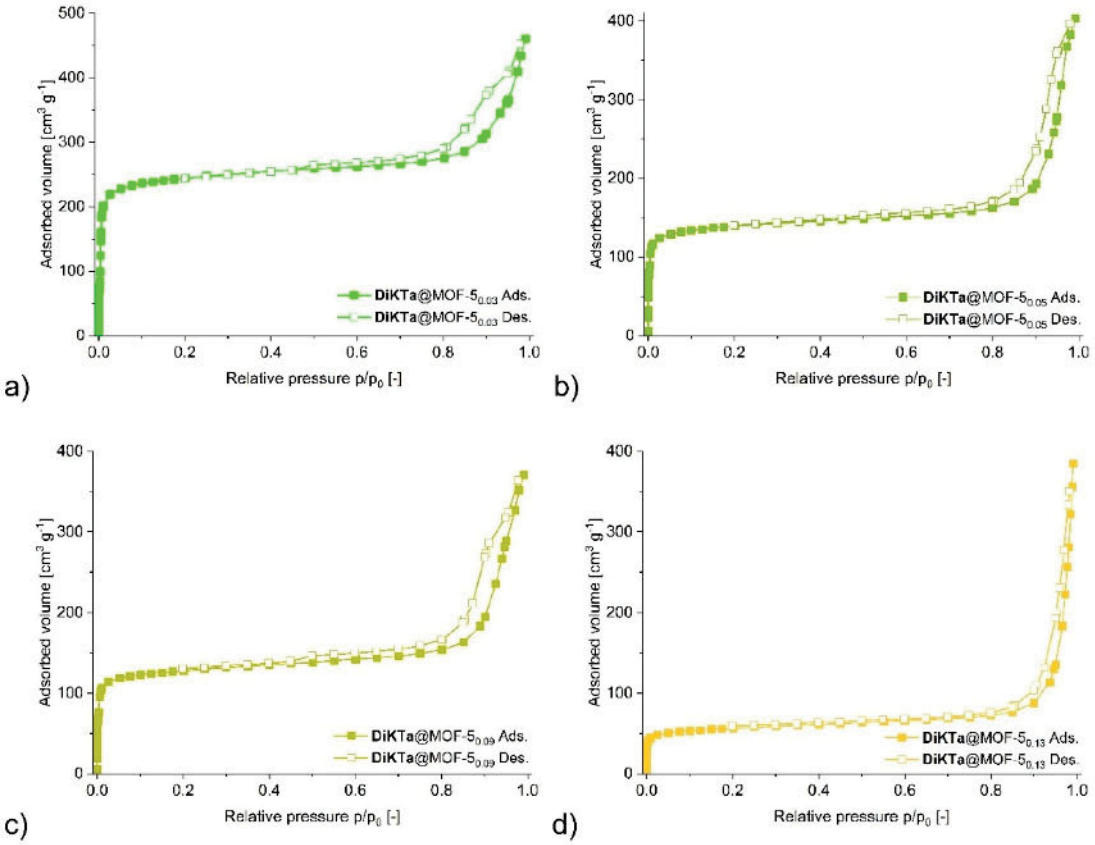
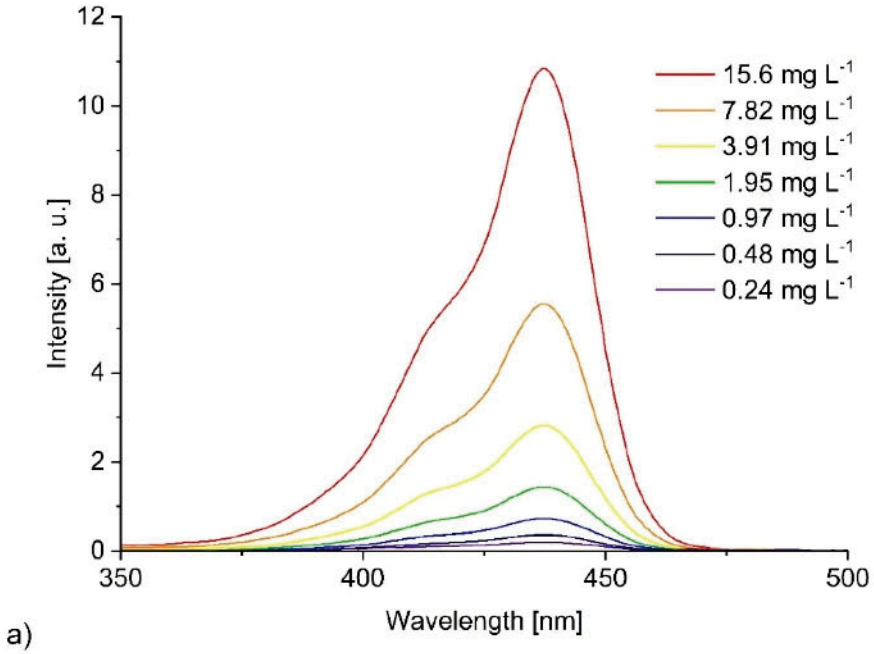


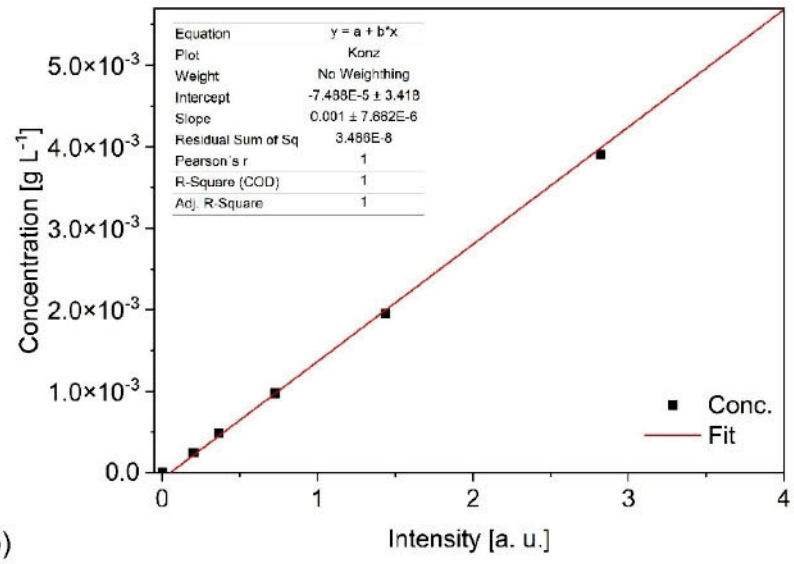
Figure S13. Nitrogen sorption isotherms at 77 K of a) **DiKTa**@MOF-$5_{0.03}$ (965 $m^2 g^{-1}$), b) **DiKTa**@MOF-$5_{0.05}$ (540 $m^2 g^{-1}$), c) **DiKTa**@MOF-$5_{0.09}$ (499 $m^2 g^{-1}$), and d) **DiKTa**@MOF-$5_{0.13}$ (213 $m^2 g^{-1}$) (filled symbols adsorption, empty symbols desorption).

S6. Digestion UV-Vis spectroscopy

All samples were digested under acidic conditions. DiKTa was extracted from the aqueous phase with DCM, the solvent was removed under reduced pressure using a rotary evaporator, the solid residue was dried at high vacuum, and then dissolved in a defined amount of chloroform. The amount of DiKTa in each MOF could be determined using the previously generated calibration curve (Figure S14).



a)



b)

Figure S14. a) UV-Vis spectra of differently concentrated solutions of DiKTa in chloroform. b) Calibration line with fit and R-values. Values were taken at a wavelength of 437 nm.

The weight of incorporated DiKTa can be calculated by multiplying the intensity by the slope of the calibration curve and the amount of chloroform. The loading of DiKTa in MOF-5 could be calculated using the following formula:

$$loading\ (wt\%) = \frac{weight\ of\ incorporated\ \boldsymbol{DiKTa}}{weight\ of\ \boldsymbol{DiKTa}@MOF} \times 100$$

All MOF-5 composites were dissolved with 4 mL chloroform. E. g. for the determination of DiKTa@MOF-$5_{0.13}$: 8.3 mg of composite were digested, resulting in an intensity of 1.873 at $\lambda_{abs.}$ = 437 nm.

$$loading\ (0.13\ wt\%) = \frac{1.873 \times 0.00144 \times 4}{8.3} \times 100$$

Table S3. Determination of the DiKTa loading in the prepared MOF-5 composites using the UV-Vis digestion method.

Name	mg digested	Intensity at λ_{em} = 426 nm	Concentration from UV-Vis	Loading [wt%]
MOF-5	4.2	0	0	0
DiKTa@MOF-$5_{0.03}$	6.5	0.338	0.41 mg L^{-1}	0.03
DiKTa@MOF-$5_{0.05}$	10.1	0.877	1.21 mg L^{-1}	0.05
DiKTa@MOF-$5_{0.09}$	7.1	1.109	1.52 mg L^{-1}	0.09
DiKTa@MOF-$5_{0.13}$	8.3	1.873	2.62 mg L^{-1}	0.13

S7. Calculation of pore filling and the probability p of multiple occupations

We analyzed the crystallographic structure of MOF-5 to calculate the pore loading. The framework consists of cubic pores, each defined by eight SBUs at the corner points. Each SBU contributes one-eighth of its volume to a specific pore. The pore edges are bridged by linker molecules (here BDC), with each link contributing a quarter of its length to the pore structure. This arrangement allows us to directly relate the atomic composition of a single pore to the molecular formula of the MOF-5 repeating unit (see Figure S15). Based on the molecular formulas and the loadings from section S6, the ratio of occupied to unoccupied pores could be calculated. However, it is assumed that there is only one DiKTa molecule in each pore. For this purpose, the molar mass of MOF-5, which corresponds to 769.87 g mol^{-1}, and the molar mass of DiKTa, which corresponds to 297.31 g mol^{-1}, were used. It can be calculated that for a loading of 0.13 wt% **DiKTa**@MOF-5, 0.0013 g DiKTa (4.37 µmol) are contained in 0.9987 g MOF-5 (1.29 mmol). This results in a ratio of 0.0044:1.3. This corresponds to 295 pores per DiKTa molecule or 0.0034 DiKTa molecules per pore for the largest loading. For all composites, see Table S3

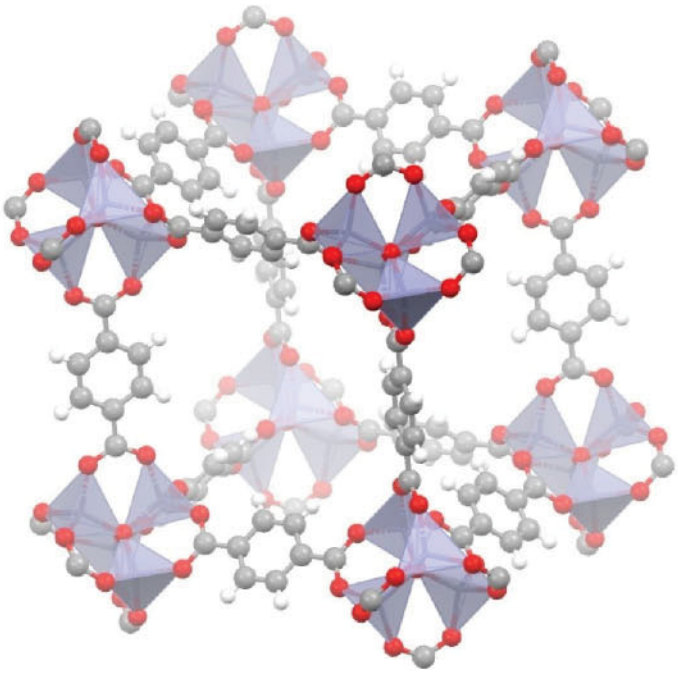


Figure S15. Section of the cubic structure of MOF-5 from CCDC No.256965.[4]

Table S4. Calculations for pore filling

Compound	DiKTa / MOF-5 [g]	DiKTa / MOF-5 [mmol]	Pores per DiKTa ratio	DiKTa per pore ratio
DiKTa@MOF-$5_{0.03}$	0.0003 / 0.9997	0.001 / 1.3	1300	0.0008
DiKTa@MOF-$5_{0.05}$	0.0005 / 0.9995	0.0017 / 1.3	765	0.0013
DiKTa@MOF-$5_{0.09}$	0.0009 / 0.9991	0.003 / 1.3	433	0.0023
DiKTa@MOF-$5_{0.13}$	0.0013 / 0.9987	0.0044 / 1.3	295	0.0034

Based on these results, we were able to calculate the probability p of multiple occupancy. For this, we used a Pearson distribution. The results are listed in Table S4.

$$P(n) = \frac{\alpha^n \times e^{-\alpha}}{n!}$$

$$\alpha = -\ln\left(unoccupied\ pores\right)$$

Table S5. Probability *p* of multiple occupation of DiKTa in a MOF-5 pore.

	DiKTa@MOF-$5_{0.03}$	**DiKTa**@MOF-$5_{0.05}$	**DiKTa**@MOF-$5_{0.09}$	**DiKTa**@MOF-$5_{0.13}$
DiKTa per pore	0.0008	0.0013	0.0023	0.0034
α	0.0008	0.001301	0.002303	0.003405
p (one) [%]	99.96	99.93	99.89	99.83
p (two) [%]	0.04	0.07	0.11	0.17

S8. Photophysical properties of DiKTa@MOF-5 composites

Multi-parameter fluorescence image spectroscopy:

Polarized fluorescence lifetime imaging was done on a FV1000 confocal laser scanning microscope (Olympus, Hamburg, Germany) equipped with single-photon counting electronics and picosecond time resolution (Hydra Harp 400, PicoQuant, Berlin, Germany). The sample was excited by a linearly polarized 440 nm pulsed laser diode (LDH-D-C-440, PicoQuant), operated at 26.7 MHz and focused by a UPlanXApo objective (10x, 0.4 NA, Olympus), The collected fluorescence was split by polarization, directed through a set of

bandpass filters (ET 480/40 M, AHF, Germany) and focussed onto two single photon avalanche diodes. z-stacks were obtained recording 40 frames of size 1.27 mm x 1.27 mm, separated by 8.7 µm. From the polarized fluorescence decays time-resolved anisotropy decays were calculated (Figure S18). The initial anisotropies, r_0, showed a marked correlation with the crystal orientation, exhibiting a maximum around 45° between polarization axis of the laser and the crystal edges.

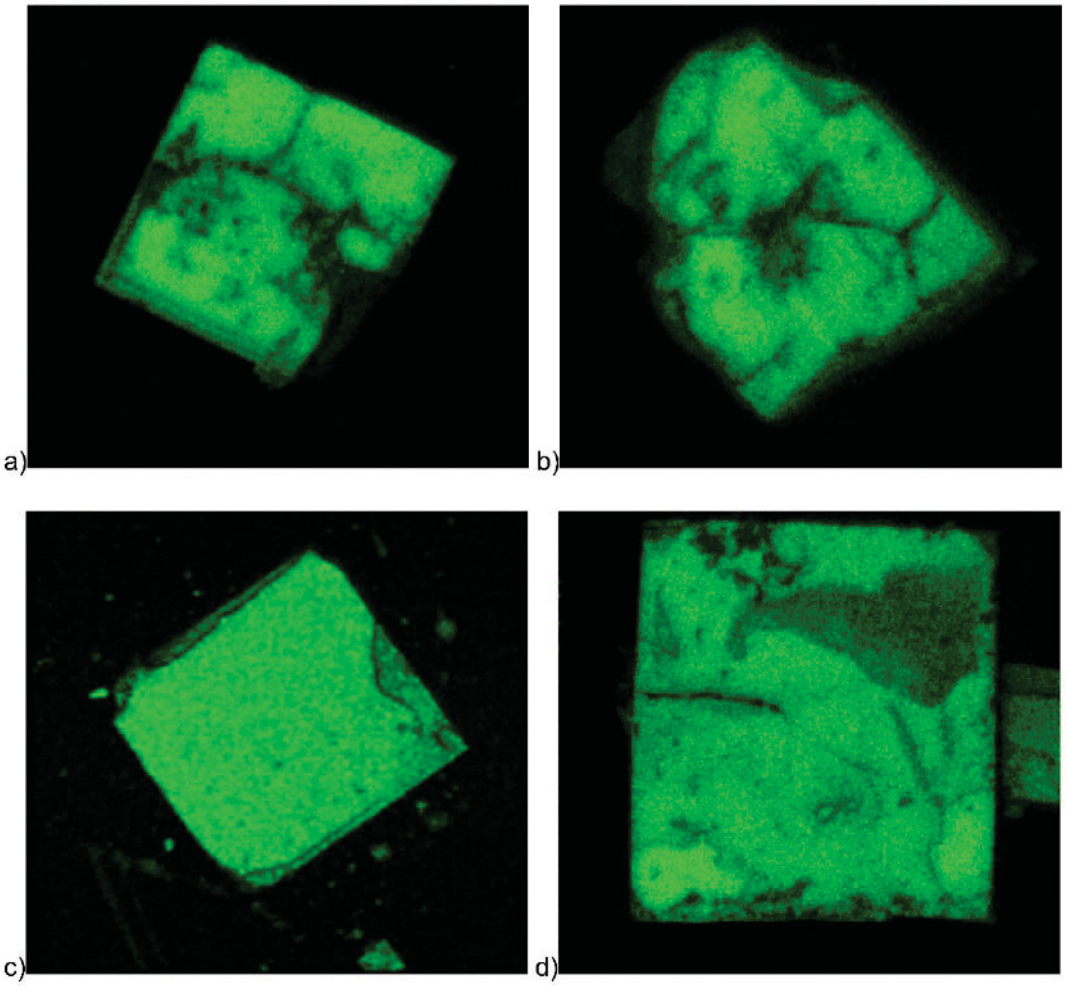


Figure S16. Confocal images of single crystals of all **DiKTa**@MOF-5 composite viewed from above a) **DiKTa**@MOF-$5_{0.03}$, b) **DiKTa**@MOF-$5_{0.05}$, c) **DiKTa**@MOF-$5_{0.09}$, and d) **DiKTa**@MOF-$5_{0.13}$.

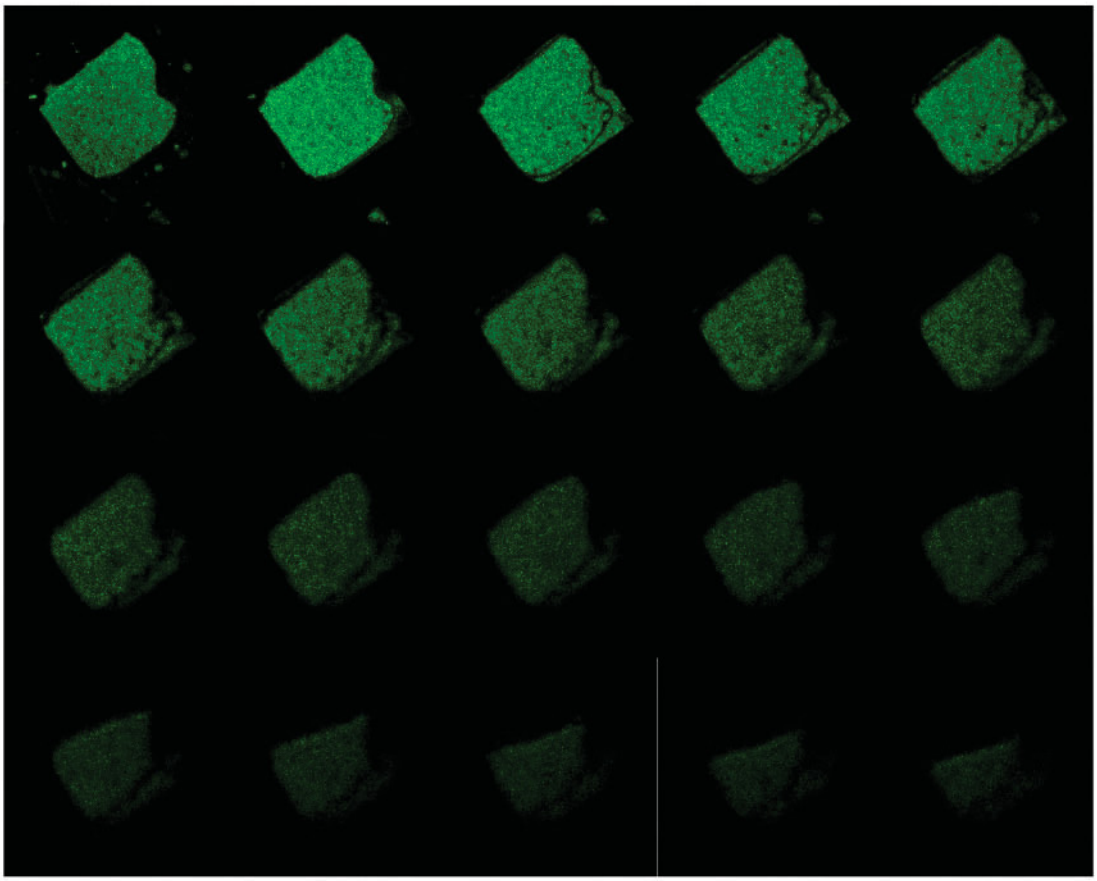


Figure S17. Confocal images of one single crystal of a **DiKTa**@MOF-5 composite. The crystal was scanned in z-direction in steps of 8.7 µm. The obtained images are shown from the bottom of the crystal (top left picture) to the top of the crystal (bottom right picture). λ_{exc} = 440 nm, λ_{em} = 460-500 nm

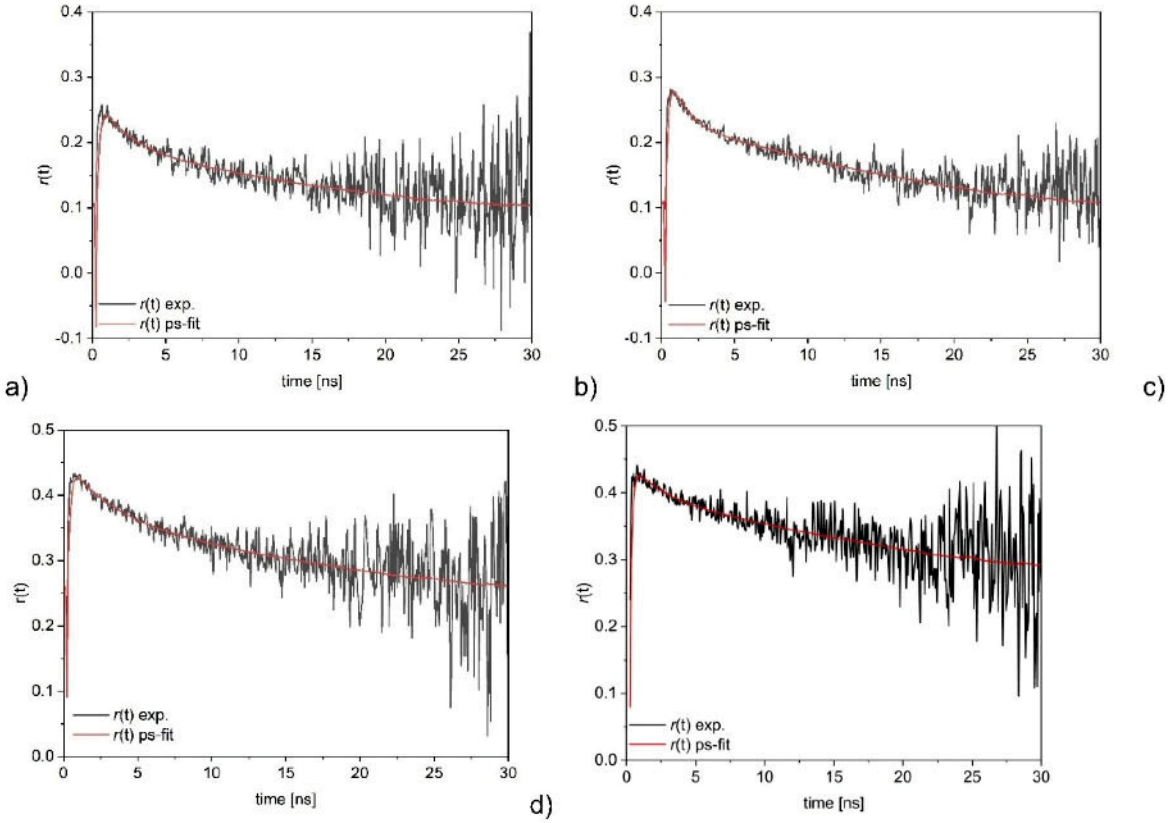
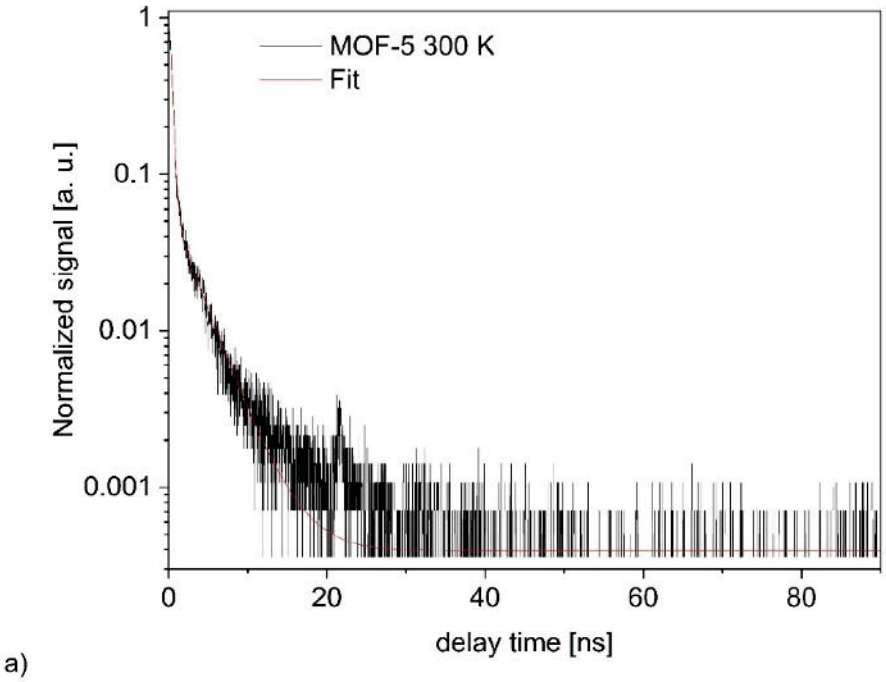
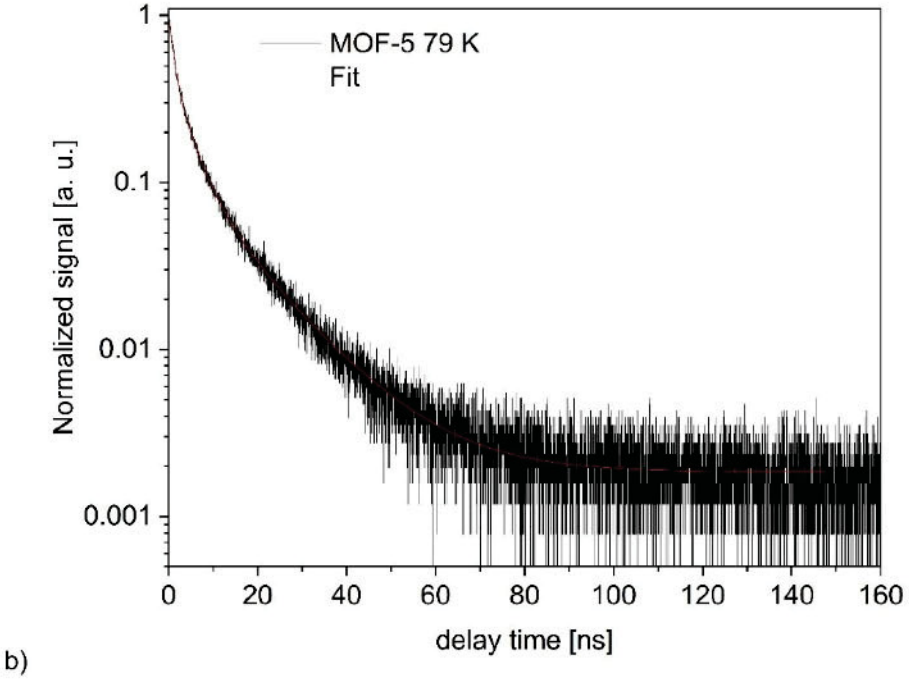


Figure S18. Time-resolved fluorescence anisotropy curves *r*(t) to resolve the fundamental anisotropy r_0 of a) **DiKTa**@MOF-$5_{0.03}$, b) **DiKTa**@MOF-$5_{0.05}$, c) **DiKTa**@MOF-$5_{0.09}$, and d) **DiKTa**@MOF-$5_{0.13}$.

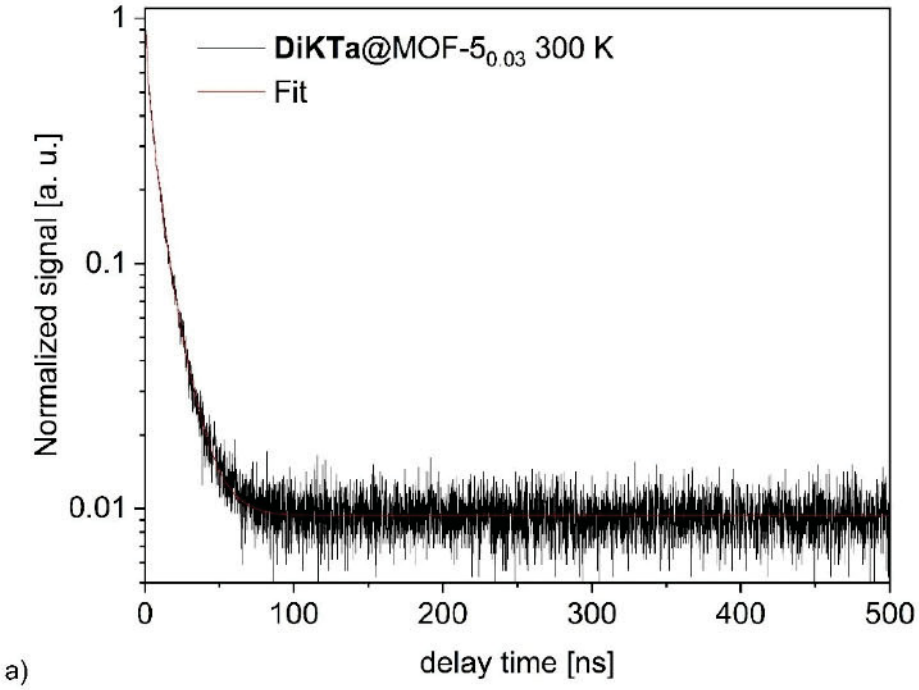


a)

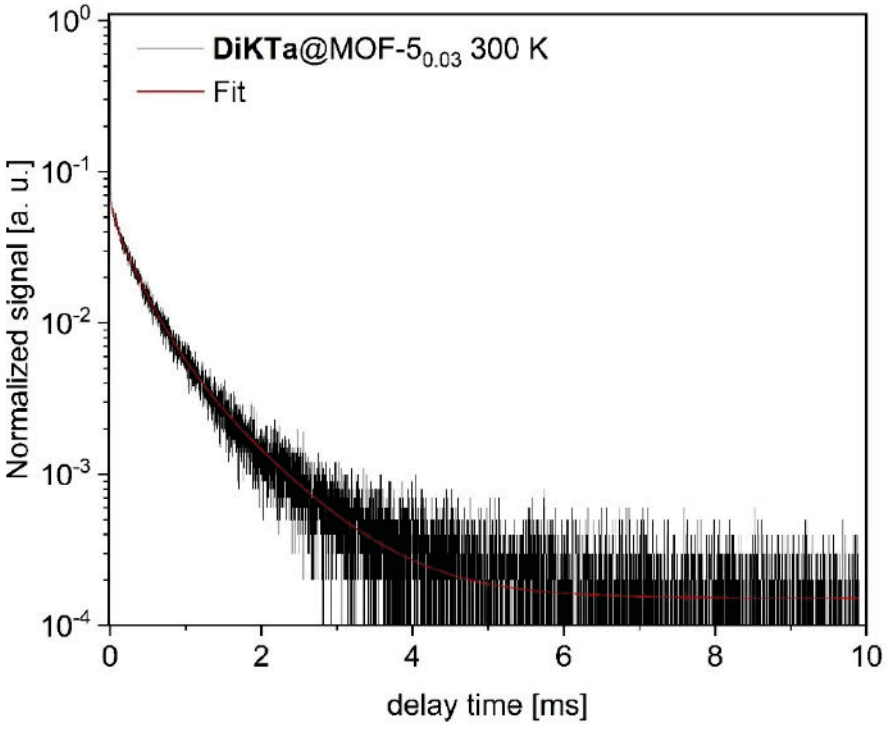


b)

Figure S19. Time-resolved photoluminescence decay (black) of the MOF-5 at a) 300 K and b) 79 K.

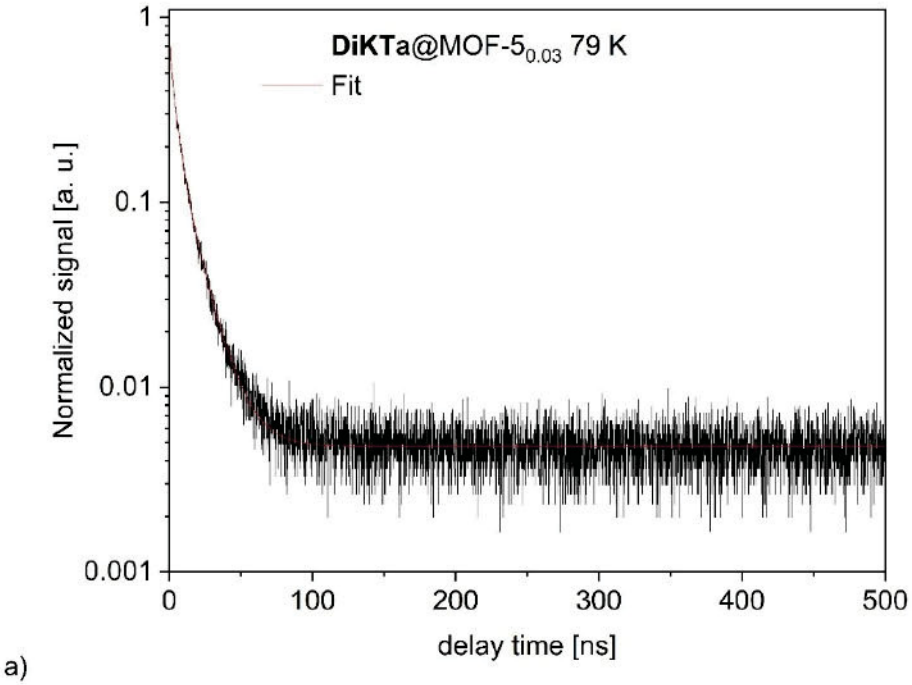


a)

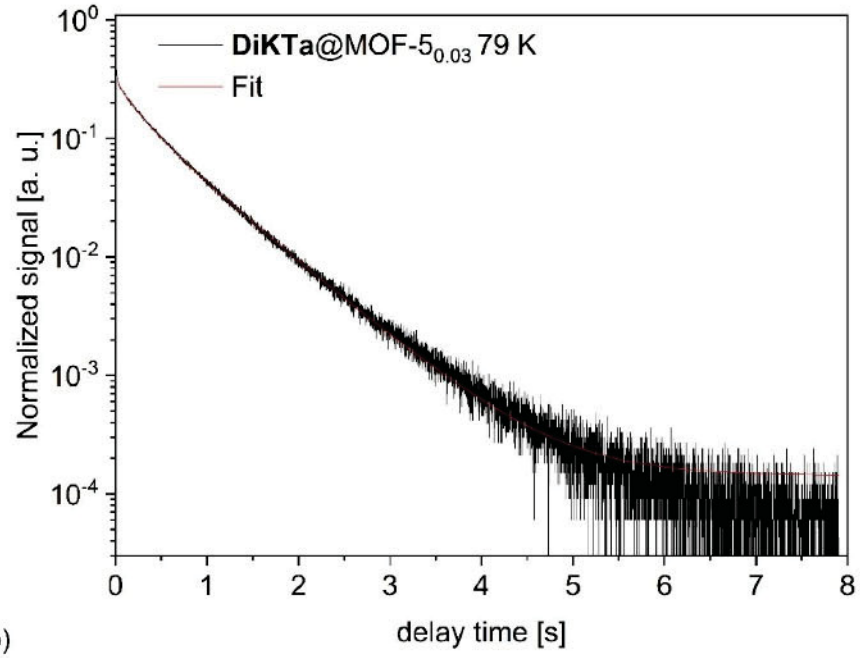


b)

Figure S20. a) Prompt and b) delayed time-resolved photoluminescence decay (black) of **DiKTa**@MOF-5$_{0.03}$ at 300 K.

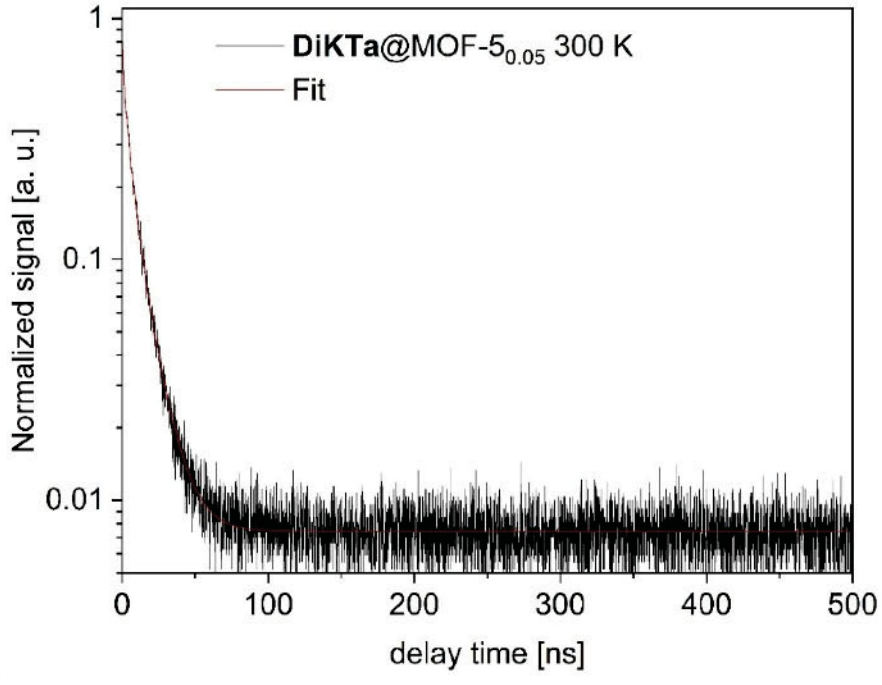


a)

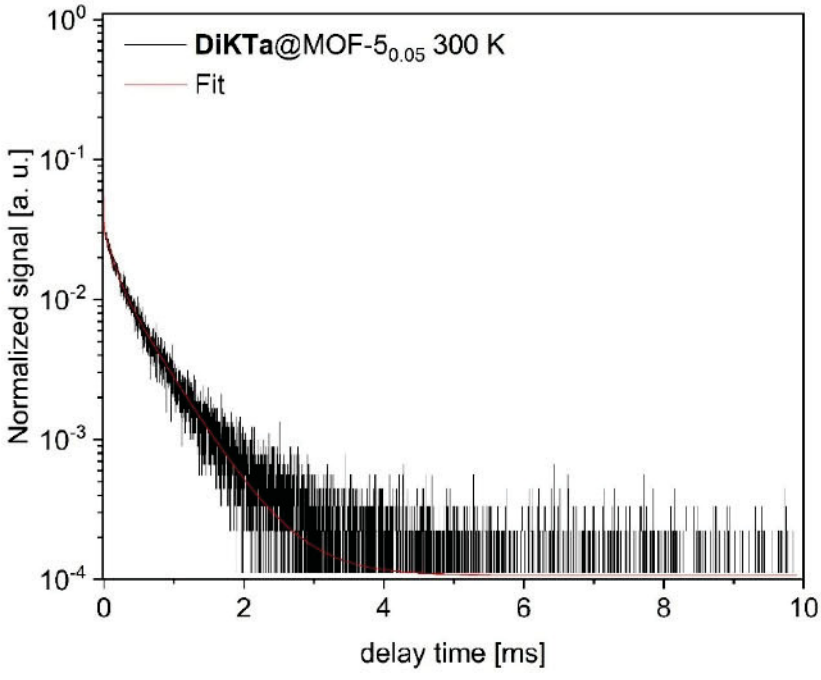


b)

Figure S21. a) Prompt and b) delayed time-resolved photoluminescence decay (black) of **DiKTa**@MOF-5$_{0.03}$ at 79 K.

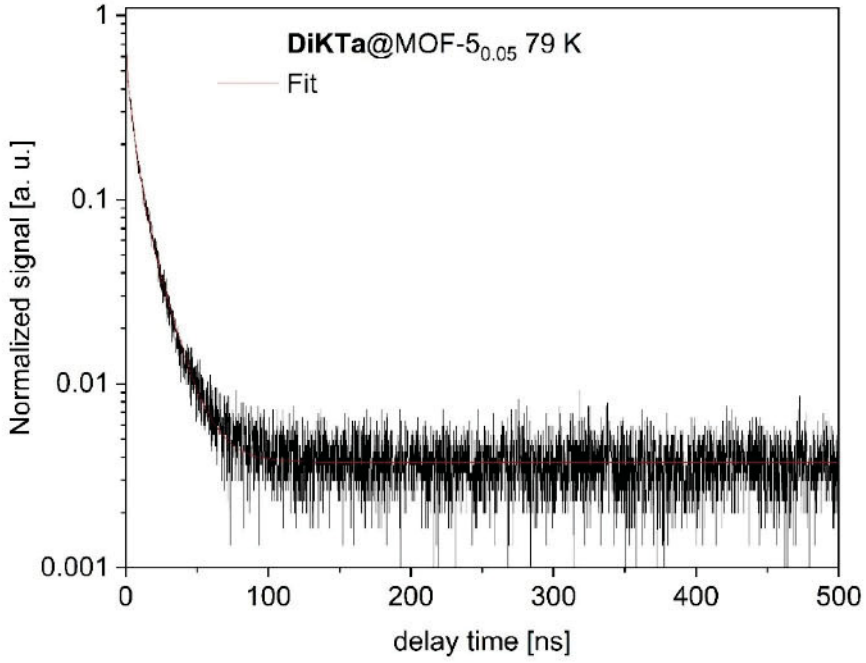


a)

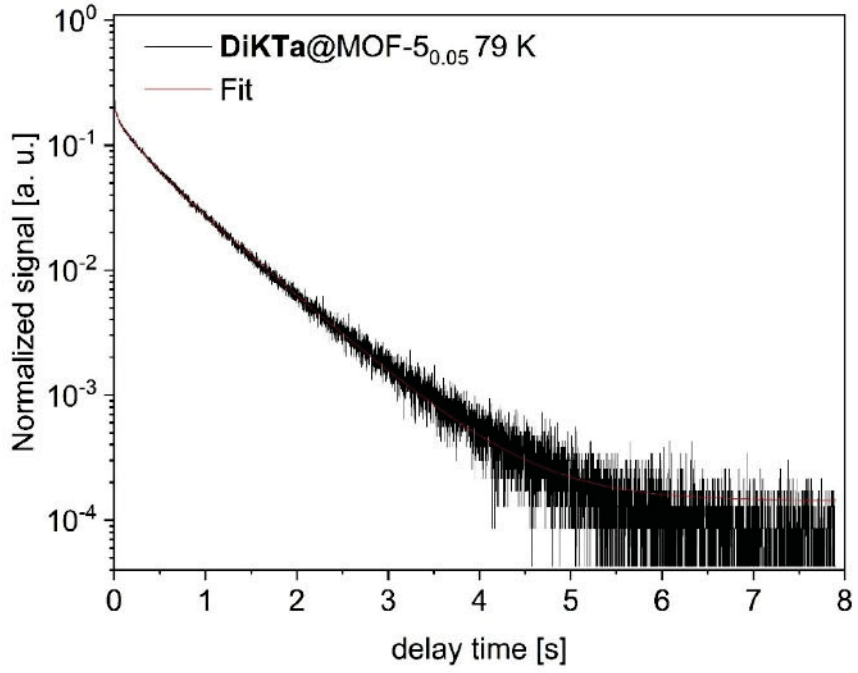


b)

Figure S22. a) Prompt and b) delayed time-resolved photoluminescence decay (black) of **DiKTa**@MOF-5$_{0.05}$ at 300 K.

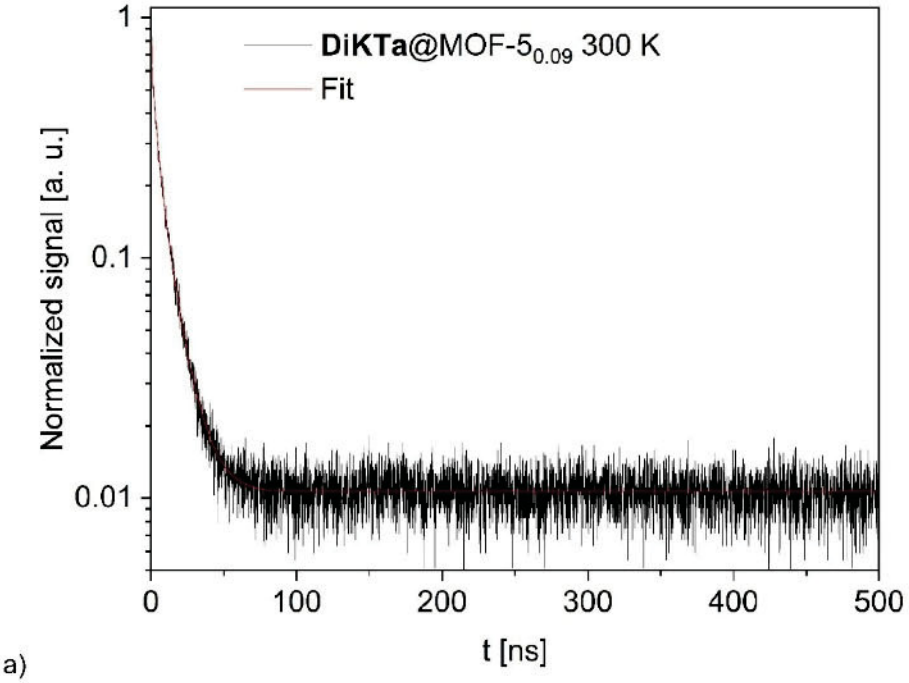


a)

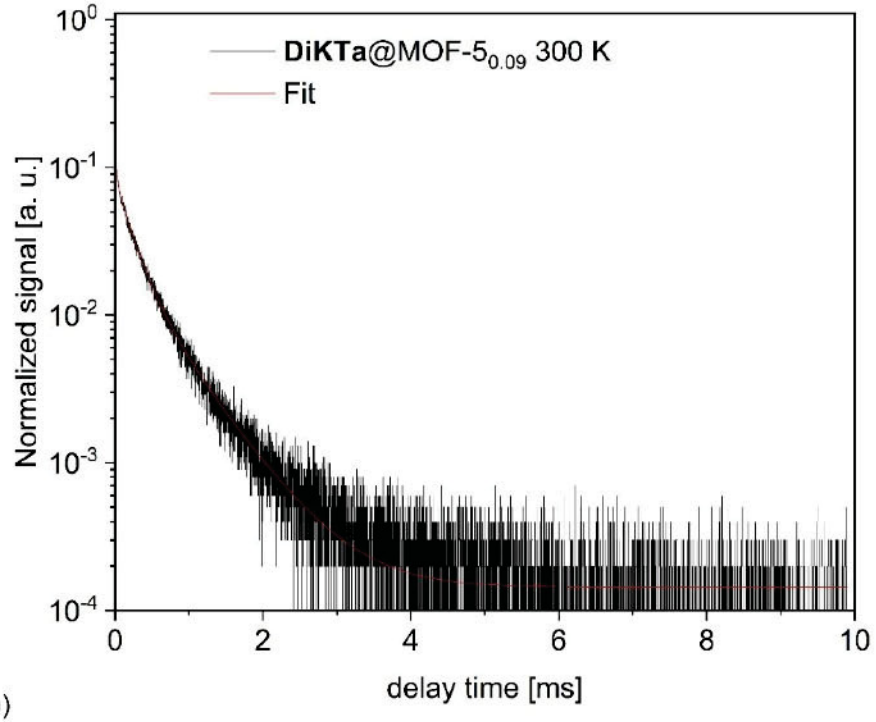


b)

Figure S23. a) Prompt and b) delayed time-resolved photoluminescence decay (black) of **DiKTa**@MOF-5$_{0.05}$ at 79 K.

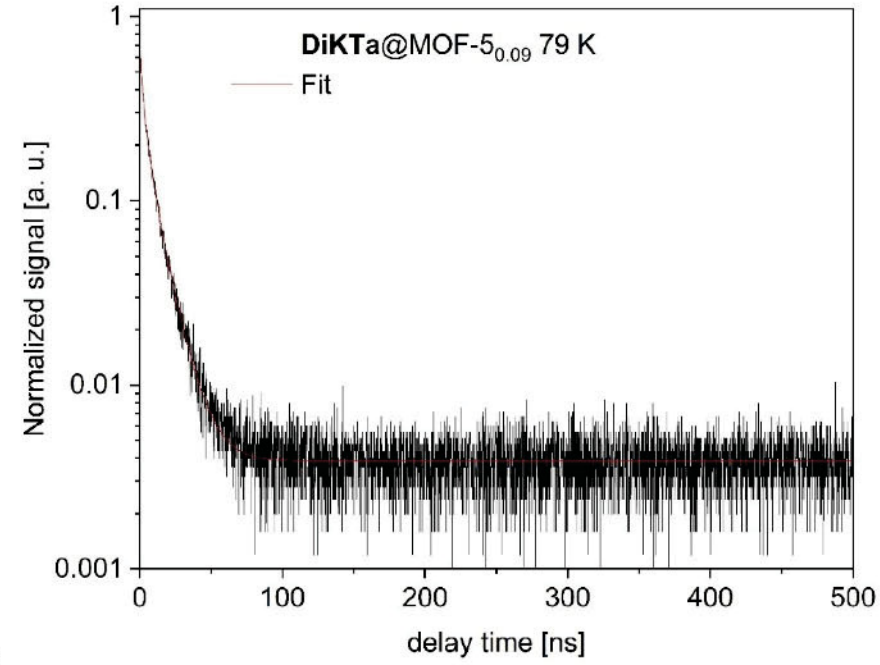


a)

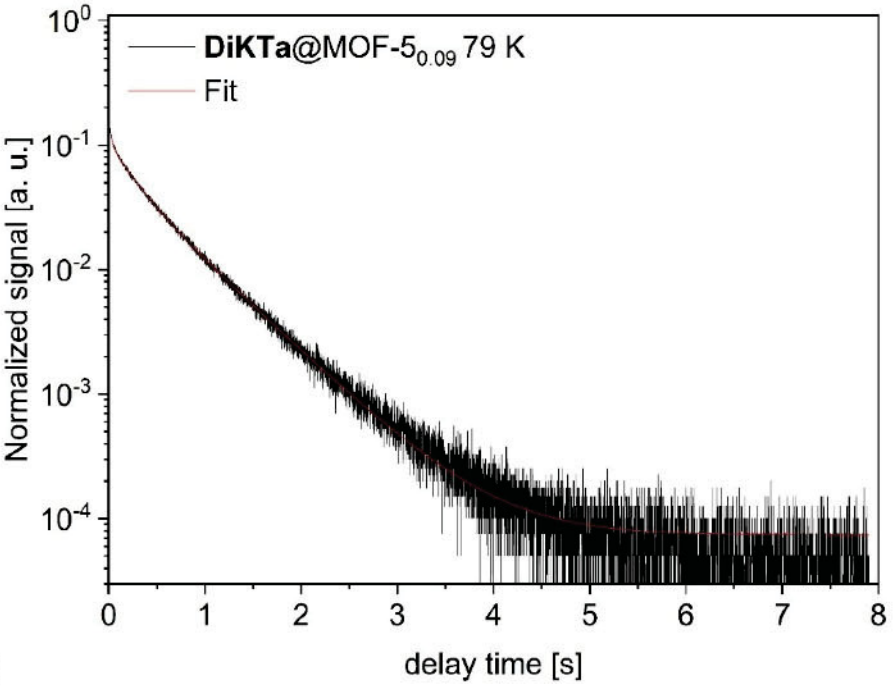


b)

Figure S24. a) Prompt and b) delayed time-resolved photoluminescence decay (black) of **DiKTa**@MOF-5$_{0.09}$ at 300 K.

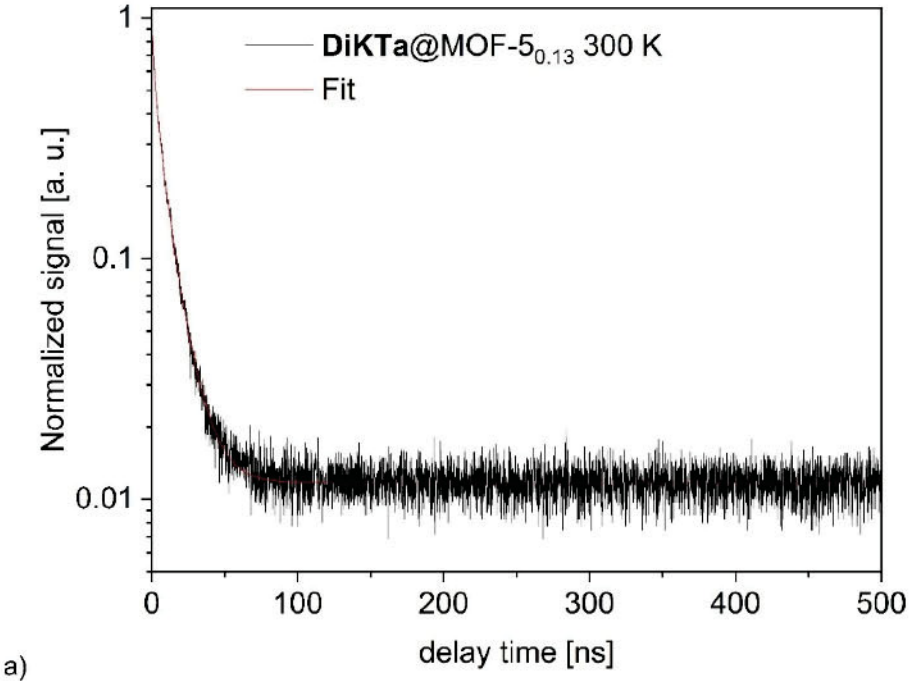


a)

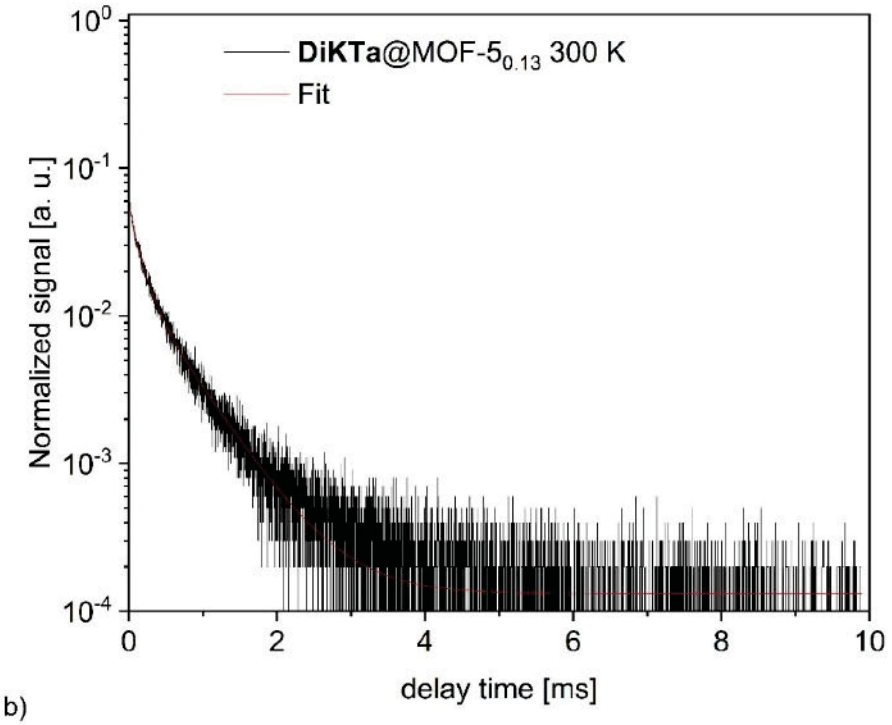


b)

Figure S25. a) Prompt and b) delayed time-resolved photoluminescence decay (black) of **DiKTa**@MOF-5$_{0.09}$ at 79 K.

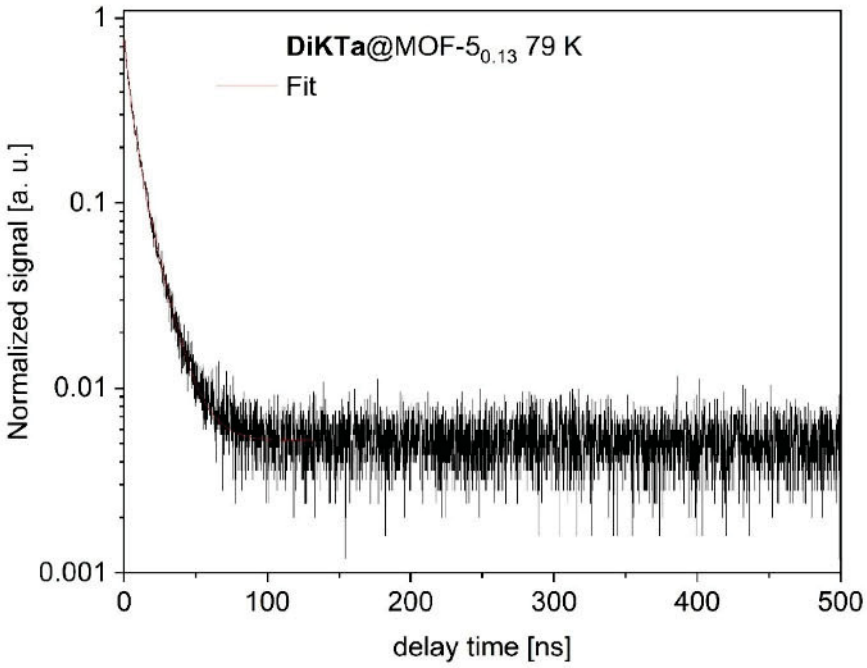


a)

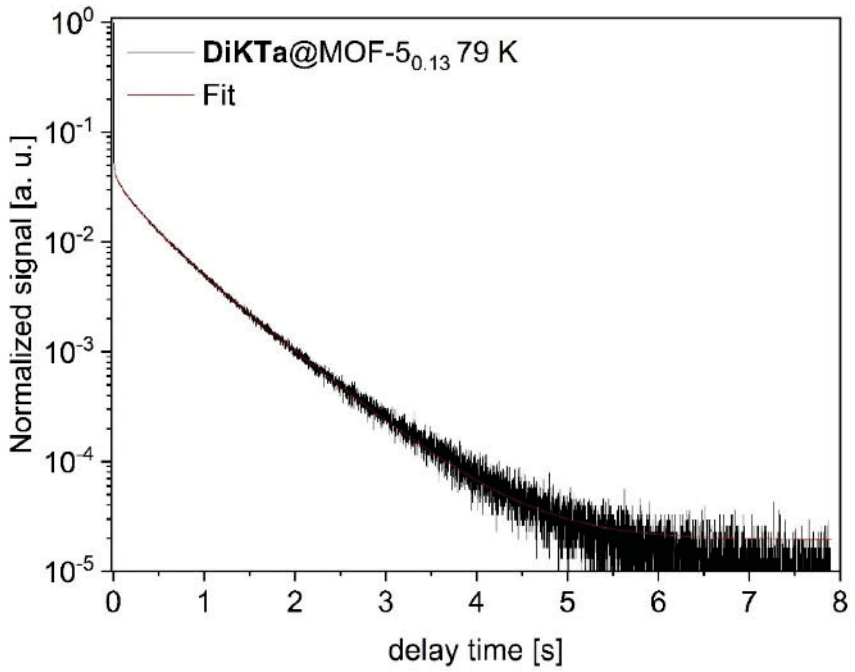


b)

Figure S26. a) Prompt and b) delayed time-resolved photoluminescence decay (black) of **DiKTa**@MOF-5$_{0.13}$ at 300 K.



a)



b)

Figure S27. a) Prompt and b) delayed time-resolved photoluminescence decay (black) of **DiKTa**@MOF-$5_{0.13}$ at 79 K.

Table S6. Summary of each decay plot with the respective exponential fitting parameters including pre-exponential factors A*i* and lifetimes t*i* for the neat MOF-5 and the composites.

Compound	A1	t1	A2	t2	A3	t3
Neat MOF-5 (300 K)	1.511	0.301	0.061	3.264		
Neat MOF-5 (79 K)	0.534	1.162	0.357	4.105	0.119	14.151
DiKTa@MOF-$5_{0.03}$ (prompt, 300 K)	0.267	1.069	0.408	4.474	0.335	11.855
DiKTa@MOF-$5_{0.03}$ (delayed, 300 K)	0.017	40887.28	0.038	277154.304	0.016	785528.434
DiKTa@MOF-$5_{0.03}$ (prompt, 79 K)	0.371	0.554	0.414	4.496	0.228	13.414
DiKTa@MOF-$5_{0.03}$ (delayed, 79 K)	0.059	$4.226 \cdot 10^7$	0.118	$2.849 \cdot 10^8$	0.167	$6.831 \cdot 10^8$
DiKTa@MOF-$5_{0.05}$ (prompt, 300 K)	0.436	0.668	0.342	4.642	0.254	11.892
DiKTa@MOF-$5_{0.05}$ (delayed, 300 K)	0.046	3283.487	0.015	133498.488	0.017	541833.162
DiKTa@MOF-$5_{0.05}$ (prompt, 79 K)	0.46	0.438	0.364	4.501	0.2	13.95
DiKTa@MOF-$5_{0.05}$ (delayed, 79 K)	0.052	$2.543 \cdot 10^7$	0.058	$2.531 \cdot 10^8$	0.112	$6.891 \cdot 10^8$
DiKTa@MOF-$5_{0.09}$ (prompt, 300 K)	0.314	4.15	0.446	0.723	0.278	11.121
DiKTa@MOF-$5_{0.09}$ (delayed, 300 K)	0.031	34763.512	0.058	212750.66	0.023	619159.694
DiKTa@MOF-$5_{0.09}$ (prompt, 79 K)	0.461	0.439	0.32	3.722	0.233	11.575
DiKTa@MOF-$5_{0.09}$ (delayed, 79 K)	0.044	$2.588 \cdot 10^7$	0.041	$2.095 \cdot 10^8$	0.065	$5.869 \cdot 10^8$
DiKTa@MOF-$5_{0.13}$ (prompt, 300 K)	0.302	0.789	0.376	4.659	0.325	11.46
DiKTa@MOF-$5_{0.13}$ (delayed, 300 K)	0.023	17885.01	0.034	147120.527	0.018	577515.019
DiKTa@MOF-$5_{0.13}$ (prompt, 79 K)	0.285	0.609	0.373	4.154	0.356	11.975
DiKTa@MOF-$5_{0.13}$ (delayed, 79 K)	0.01	$4.605 \cdot 10^7$	0.017	$2.812E \cdot 10^8$	0.02	$6.611 \cdot 10^8$

S9. Quantum chemical calculations of DiKTa in different solvents

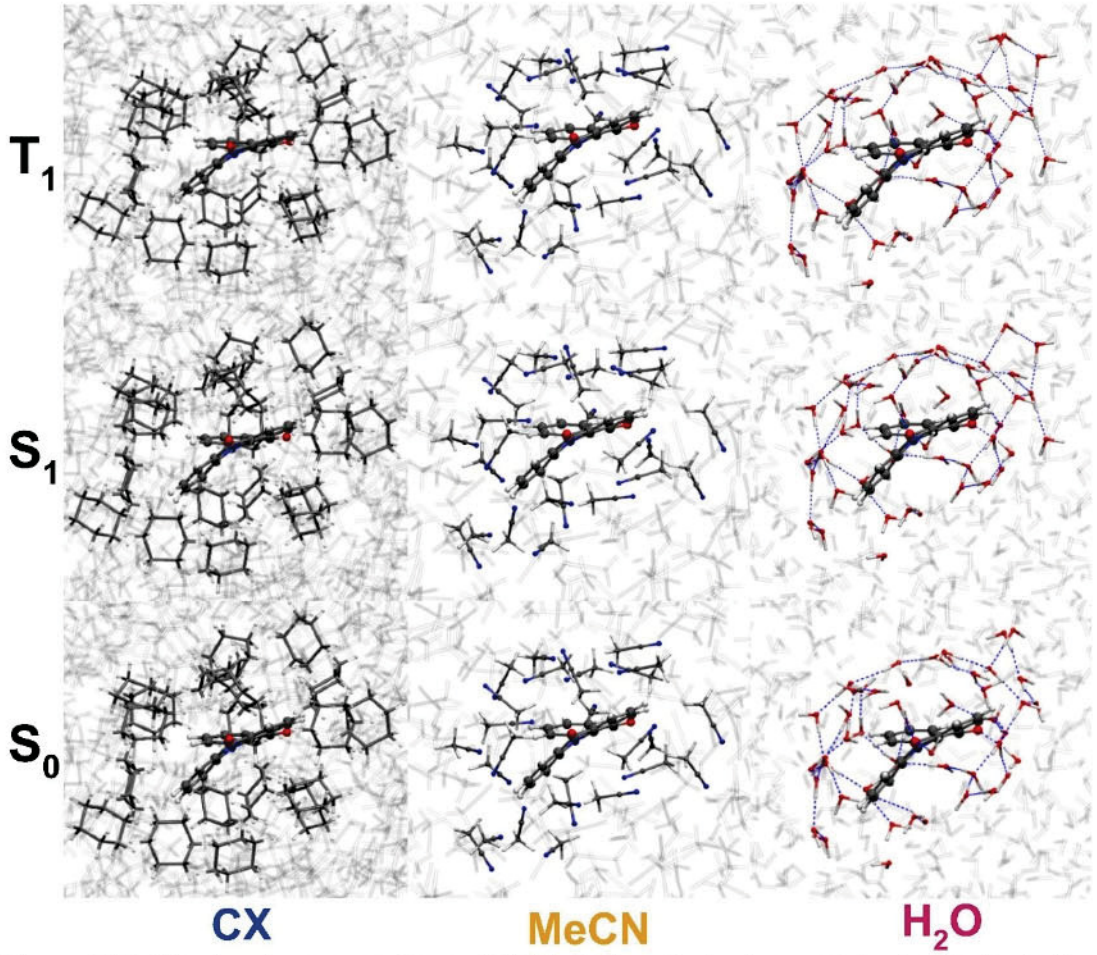


Figure S28. Structural representations of DiKTa in its optimized geometries for the S_0 (bottom), S_1 (middle), and T_1 (top) states, embedded in explicitly modeled solvent environments. The three columns correspond to different solvents: cyclohexane (CX, left, blue), acetonitrile (MeCN, middle, orange), and water (H_2O, right, magenta). DiKTa and surrounding solvent molecules are visualized with VMD.[5]

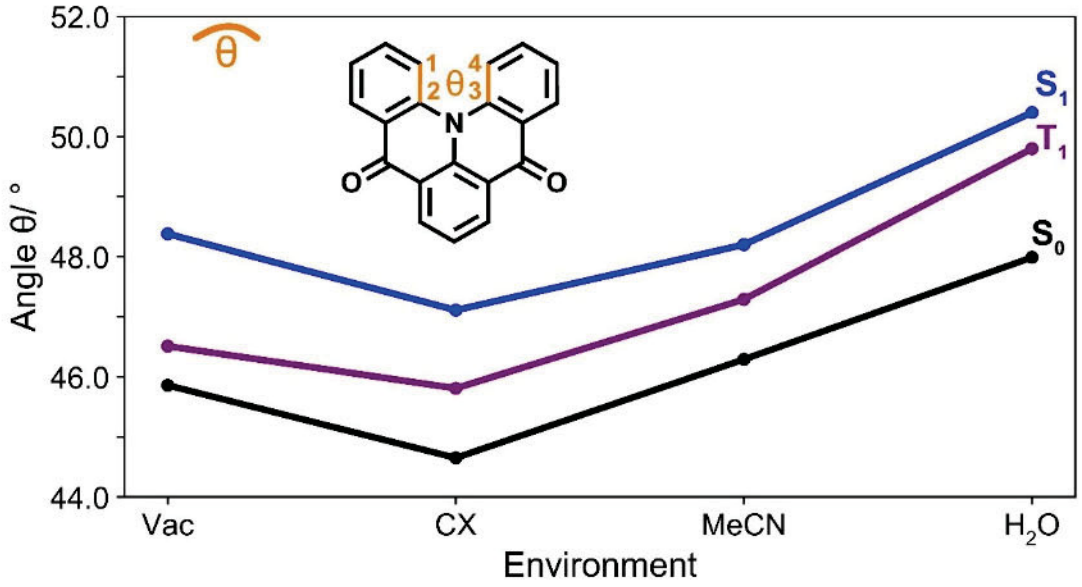


Figure S29. Torsion angle (θ) of DiKTA in the electronic states S_0 (black), S_1 (blue), and T_1 (violet) in vacuum and in different solvents. The torsion angle was measured for the carbon atoms C1-C2-C3-C4, which are marked in orange. Structural representation of DiKTa for the vacuum ground state visualized with VMD.[5]

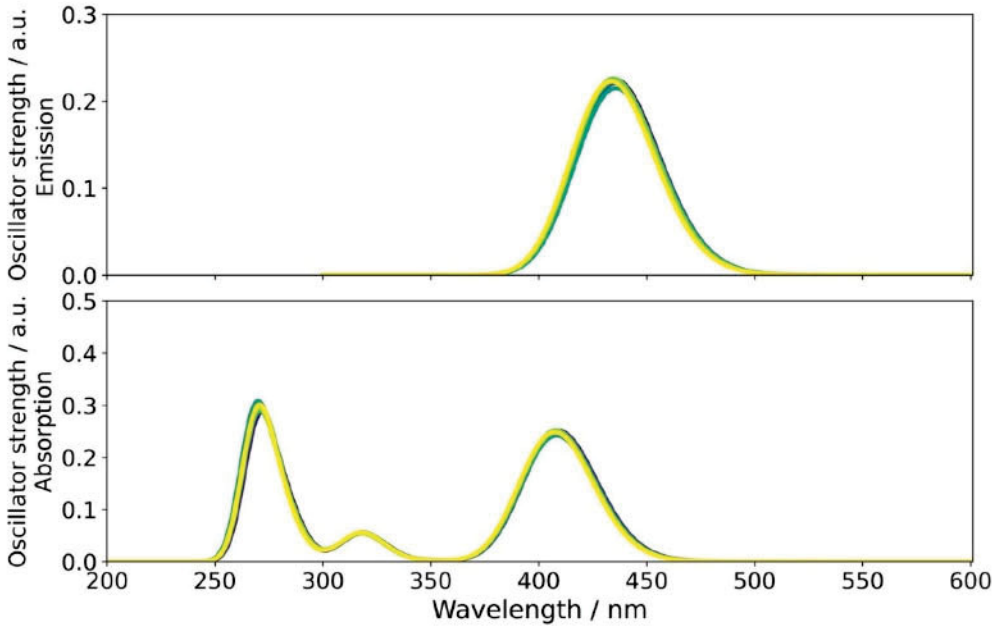


Figure S30. Calculated absorption (bottom) and emission (top) spectra of **DiKTa** in cyclohexane obtained from QM/MM simulations. Each colored line represents a different snapshot from the MM-MD sampling. The spectra were obtained by Gaussian broadening using a FWHM of 0.3 eV.

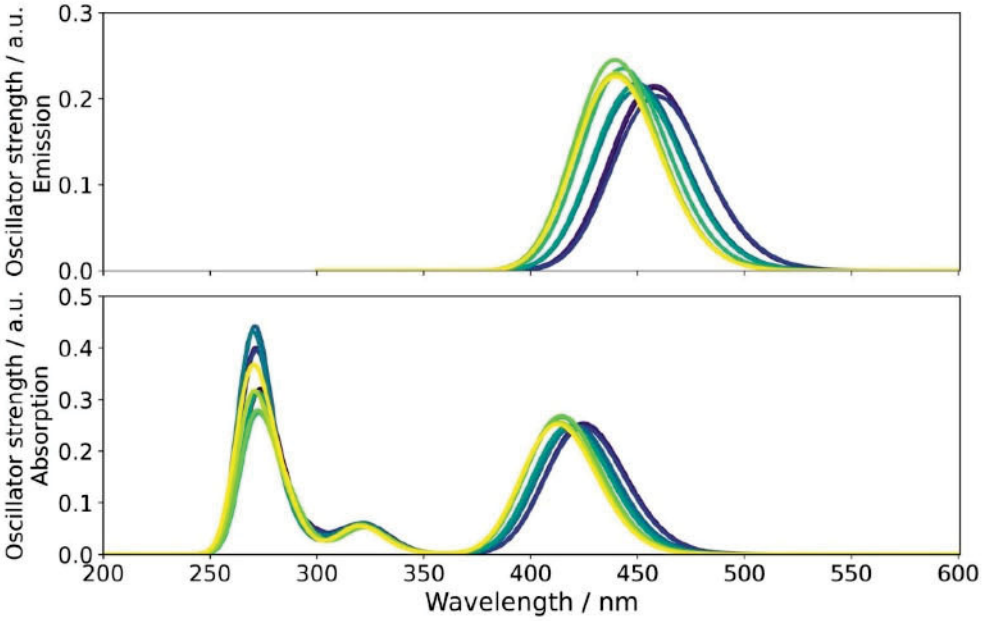


Figure S31. Calculated absorption (bottom) and emission (top) spectra of **DiKTa** in acetonitrile obtained from QM/MM simulations. Each colored line represents a different snapshot from the MM-MD sampling. The spectra were obtained by Gaussian broadening using a FWHM of 0.3 eV.

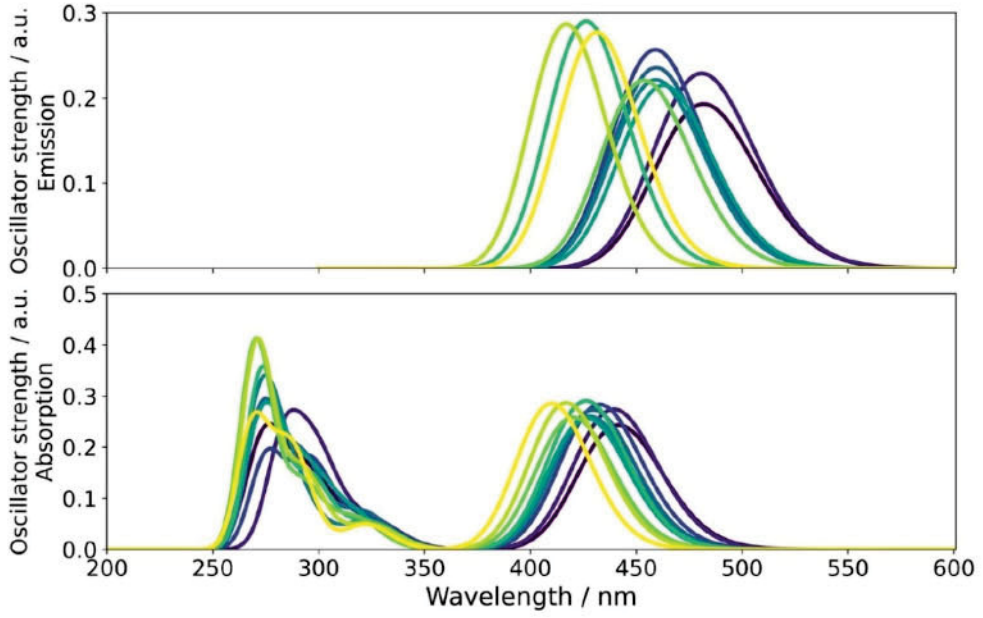


Figure S32. Calculated absorption (bottom) and emission (top) spectra of **DiKTa** in acetonitrile obtained from QM/MM simulations. Each colored line represents a different snapshot from the MM-MD sampling. The spectra were obtained by Gaussian broadening using a FWHM of 0.3 eV.

Table S7. Electronic excited states of DiKTa in Vacuum (Vac), CX, MeCN, and H_2O. The solvent molecules were explicitly included using a QM/MM approach. Shown are the vertical excitation energies, percentage contributions of dominant configurations, and the respective excitation types. All results are shown for DFT/MRCI.

	Geometry	S0								S_1				T_1				
Vac	Vertical excitation	S_0	S_1	S_2		T_1	T_2			S_1	S_2			T_1		T_2		
	Energy / eV	0,0	3,37	3,78		2,97	3,54			3,29	3,76			2,95		3,40		
	Percentage / %	91,29	80,40	59,80	16,50	80,29	57,42		16,56	80,48	61,16	15,71		4,72	71,06	57,56	10,73	6,16
	Excitation	-	H, L	H-6, L	H-7, L+1	H, L	H-6, L		H-7, L+1	H, L	H-6, L	H-7, L+1		H-1, L	H, L	H-5, L	H-5, L+1	H-7, L
	Characters	-	π, π^*	n, π^*	n, π^*	π, π^*	n, π^*		n, π^*	π, π^*	n, π^*	n, π^*		π, π^*	π, π^*	π, π^*	π, π^*	n, π^*
CX	Vertical excitation	S_0	S_1	S_2		T_1	T_2			S_1	S_2			T_1		T_2		
	Energy / eV	0,00	3,03	3,41		2,71	3,25			2,96	3,42			2,69		3,07		
	Percentage / %	91,53	81,36	60,88	14,67	81,69	6,05	12,05	30,47	22,39	81,35	62,24	14,78		74,45		7,23	53,45	9,18
	Excitation	-	H, L	H-5, L	H-7, L+1	H, L	H-4, L	H-5, L	H, L+1	H-2, L	H, L	H-6, L	H-7, L+1		H, L		H-7, L	H-5, L	H-5, L+1
	Characters	-	π, π^*	n, π^*	n, π^*	π, π^*	π, π^*	n, π^*	π, π^*	π, π^*	π, π^*	n, π^*	n, π^*		π, π^*		n, π^*	π, π^*	π, π^*
MeCN	Vertical excitation	S_0	S_1	S_2			T_1	T_2			S_1	S_2			T_1		T_2		
	Energy / eV	0,00	2,95	3,48			2,64	3,24			2,86	3,47			2,54		3,19		
	Percentage / %	91,51	81,63	60,46	8,68	8,24	82,19	11,51	40,33	20,99	81,58	60,30	10,58	6,83	81,14		7,64	38,77	18,06
	Excitation	-	H, L	H-6, L	H-6, L+1	H-7, L+1	H, L	H-2, L	H, L+1	H-5, L	H, L	H-6, L	H-6, L+1	H-7, L+1	H, L		H-2, L	H, L+1	H-5, L
	Characters	-	π, π^*	n, π^*	n, π^*	n, π^*	π, π^*	π, π^*	π, π^*	π, π^*	π, π^*	n, π^*	n, π^*	n, π^*	π, π^*		π, π^*	π, π^*	π, π^*
H_2O	Vertical excitation	S0	S_1	S_2			T_1	T_2			S1	S_2			T_1		T_2		
	Energy / eV	0,00	2,89	3,60			2,59	3,22			2,84	3,65			2,52		3,21		
	Percentage / %	91,71	81,85	58,78	11,26	8,48	82,98	12,54	16,37	48,64	81,77	56,50	14,04	4,51	82,61		8,50	50,41	20,68
	Excitation	-	H, L	H-5, L	H-6, L+1	H-7, L+1	H, L	H-2, L	H-5, L	H, L+1	H, L	H-6, L	H-5, L+1	H-7, L+1	H, L		H-2, L	H, L+1	H-5, L
	Characters	-	π, π^*	n, π^*	n, π^*	n, π^*	π, π^*	n, π^*	n, π^*	π, π^*	π, π^*	n, π^*	n, π^*	n, π^*	π, π^*		π, π^*	n, π^*	π, π^*

Optimal tuning of ωB97X-D

The accuracy of time-dependent density functional theory (TDDFT) excitation energies, especially for charge-transfer states, computed with range-separated functionals such as ωB97X-D critically depends on the proper choice of the range-separation parameter ω[6]. The optimal value of ω is system-specific and must therefore be determined individually. In this work, ω was optimized for the ωB97X-D functional[7] using Koopmans' theorem[8]. The optimal parameter was obtained by minimizing a target function, which is defined by the following equation:

$$J^2 = \sum_{i=0}^{1} \left[\epsilon_{HOMO}^{\omega}(N+i) + IP(N+i)\right]^2 \qquad 1$$

where $\varepsilon_{HOMO}^{\omega}$ denotes the HOMO energy obtained with the range-separation parameter ω. The vertical ionization potentials are given by $IP(N) = E(N-1) - E(N)$ *and* $IP(N+1) = E(N) - E(N+1)$, with $E(N)$ representing the total energy of the system containing N electrons. As a result of the minimization, an optimal range-separation parameter of $\omega = 0.17$ bohr^{-1} is obtained for DiKTa.

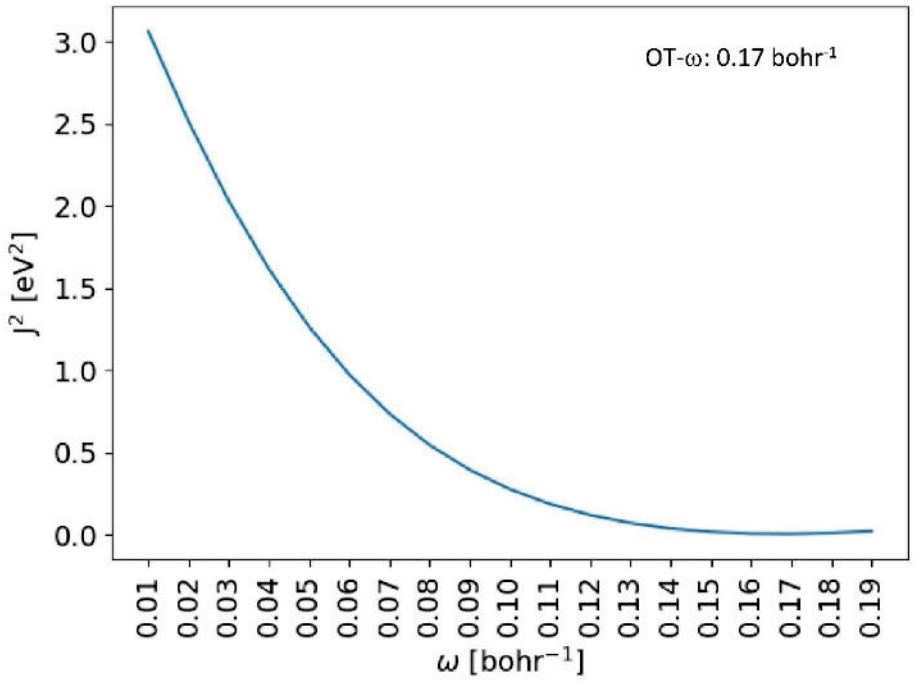


Figure S33. J^2 -plot for the optimal tuning of the ωB97X-D functional and the def2-SVP basis set.

References

[1] J. E. Field, D. Venkataraman, *Chem. Mater.* **2002**, *14*, 962-964.

[2] D. Hall, S. M. Suresh, P. L. dos Santos, E. Duda, S. Bagnich, A. Pershin, P. Rajamalli, D. B. Cordes, A. M. Z. Slawin, D. Beljonne, A. Köhler, I. D. W. Samuel, Y. Olivier, E. Zysman-Colman, *Adv. Opt. Mater.* **2020**, *8*, 1901627.

[3] S. B. Han, Y. H. Wei, C. Valente, I. Lagzi, J. J. Gassensmith, A. Coskun, J. F. Stoddart, B. A. Grzybowski, *J. Am. Chem. Soc.* **2010**, *132*, 16358-16361.

[4] M. Eddaoudi, H. L. Li, T. Reineke, M. Fehr, D. Kelley, T. L. Groy, O. M. Yaghi, *Top. Catal.* **1999**, *9*, 105-111.

[5] W. Humphrey, A. Dalke, K. Schulten, *J. Mol. Graph.* **1996**, *14*, 33-38.

[6] R. Baer, E. Livshits, U. Salzner, *Annual review of physical chemistry* **2010**, *61*, 85-109.

[7] J.-D. Chai, M. Head-Gordon, *Phys. Chem. Chem. Phys.* **2008**, *10*, 6615-6620.

[8] D. Jacquemin, B. Moore, A. Planchat, C. Adamo, J. Autschbach, *Journal of Chemical Theory and Computation* **2014**, *10*, 1677-1685.

3.4 Beiträge an weiteren Veröffentlichungen als Co-Autor

Die in diesem Kapitel aufgelisteten Publikationen werden in derjenigen Reihenfolge vorgestellt, die auch in der Publikationsliste zugrunde gelegt ist. Die aufgeführten Co-Autorenschaften sind das Ergebnis der im Verlauf der Promotion geleisteten wissenschaftlichen Mitarbeit an mehreren Forschungsarbeiten und daraus hervorgegangenen Veröffentlichungen.

Ein wesentlicher Schwerpunkt der eigenen Beiträge lag auf der Durchführung und Auswertung von bildgebenden Untersuchungen mittels Rasterelektronenmikroskopie (REM), einschließlich der Probenpräparation. Ergänzend hierzu wurden Elementanalysen unter Verwendung der energiedispersiven Röntgenspektroskopie (EDX) durchgeführt, die zur chemischen Charakterisierung der untersuchten Materialien beitrugen. Weitere Beiträge umfassten die Durchführung und Auswertung von Pulverröntgendiffraktometrie-Messungen (PXRD), die insbesondere zur strukturellen Analyse und Phasenidentifikation herangezogen wurden.

3.4.1 Encapsulation of Phosphorescent Pt(II) Complexes in Zn-Based Metal-Organic Frameworks toward Oxygen-Sensing Porous Materials

Tim-Oliver Knedel, Stefan Buss, Iván Maisuls, Constantin G. Daniliuc, Carsten Schlüsener, Philipp Brandt, Oliver Weingart, Annette Vollrath, Christoph Janiak, Cristian A. Strassert, *Inorg. Chem.* **2020**, *59*, 7252-7264.

Kurzzusammenfassung

In dieser Arbeit werden die Synthese sowie die strukturelle und photophysikalische Charakterisierung von sechs phosphoreszierenden, wasserlöslichen Pt(II)-Komplexen beschrieben, wobei deren Emissionsmaxima, Photolumineszenz-Quantenausbeuten (Φ_L), Lebensdauern (τ), Aggregationsneigung und Empfindlichkeit gegenüber der Mikroumgebung in Abhängigkeit vom Substitutionsmuster am dreizähnigen Hauptluminophor untersucht wurden. Verschiedene Nebenliganden, nämlich ein trisulfoniertes Phosphan und mit Maltohexaose konjugierte Pyridine (mit oder ohne Amidbrücken), wurden eingeführt und hinsichtlich der Realisierung von Switch-on-

Photolumineszenz-Markern evaluiert, die über die in Biofilmen von $Gram^+$- und $Gram^-$-Modellen, nämlich *Staphylococcus aureus* und *Escherichia coli*, wahrgenommene Mikroumgebung berichten. Mithilfe der konfokalen Lumineszenz-Mikro(spektros)kopie konnten wir beobachten, dass ausgewählte Komplexe spezifisch mit den Biofilmen interagieren, während planktonische Zellen unmarkiert bleiben. Durch den Einsatz der Photolumineszenz-Lebensdauer-Bildmikroskopie wurden die Lebensdauern im angeregten Zustand innerhalb von *S.* aureus-Biofilmen gemessen. Die Photolumineszenzintensitäten wurden drastisch erhöht, und die Lebensdauern der angeregten Zustände verlängerten sich bei der Bindung an die viskose Biofilm-Matrix erheblich, was hauptsächlich auf die Unterdrückung strahlungsloser Deaktivierungswege durch die Abschirmung vor physikalischen Löschprozessen, wie Wechselwirkungen mit Lösungsmittelmolekülen und $^3O_2$, zurückzuführen war. Die besten Leistungen wurden für nicht aggregierende Komplexe mit Maltohexaose-Targeting-Einheiten und ohne Amidbrücken erzielt. Bemerkenswert ist, dass in Abwesenheit von Maltodextrin eine hydrophobe Adamantylgruppe ausreicht, um eine beträchtliche Markierungskapazität zu erreichen. Darüber hinaus zeigten Photolumineszenzstudien, dass ausgewählte Komplexe auch effektiv mit *E. coli*-Biofilmen interagieren können, wobei die Bakterienzellen in der Lage sind, die maltodextrinbasierten Wirkstoffe teilweise aufzunehmen. Zusammenfassend ermöglichen die hier vorgestellten Konzepte die Entwicklung spezifischer Biofilm-Reporter, die sowohl räumliche Auflösung als auch auf Lebensdauer und Spektrum basierende Messwerte liefern. In Anbetracht der Tatsache, dass die meisten bisher beschriebenen theragnostischen Wirkstoffe hauptsächlich auf metabolisch aktive Bakterien an der Oberfläche von Biofilmen abzielen, ohne jedoch tief in die Matrix eingetauchte Zellen zu erreichen, wird eine neue Plattform mit einer klaren Struktur-Eigenschafts-Korrelation für die Früherkennung solcher Bakterienansammlungen bereitgestellt.

Eigenanteil an der Veröffentlichung:

- Literaturrecherche
- Synthese der Metall-organischen Gerüstverbindungen
- Einlagerung der Pt(II)-Komplexe in MOFs
- Quenchingexperimente
- Zusammenfassen und Auswerten der Daten im Rahmen einer Bachelorarbeit

3.4.2 Novel Re(I) Complexes as Potential Selective Theranostic Agents in Cancer Cells and In Vivo in Caenorhabditis elegans Tumoral Strains

Alicia Marco, Pezhman Ashoo, Samanta Hernández-García, Pedro Martínez-Rodríguez, Natalia Cutillas, Annette Vollrath, Dustin Jordan, Christoph Janiak, Fernando Gandía-Herrero, José Ruiz, *J. Med. Chem.* **2024**, *67*, 7891-7910.

Kurzzusammenfassung

Es wurde eine Serie von Rhenium(I)-Komplexen der allgemeinen Struktur fac-$[Re(CO)_3(N^N)L]^{0/+}$ (**Re1–Re9**) hergestellt. Dabei steht N^N für einen zweizähnigen, vom Benzimidazol abgeleiteten Liganden mit Esterfunktionalität, während L entweder ein Chlorid- oder ein Pyridinligand ist. Die neu synthetisierten Verbindungen zeigten eine ausgeprägte Wirksamkeit gegenüber A2780-Ovarialkarzinomzellen. Besonders die Komplexe **Re7–Re9**, die den Liganden 4 NMe_2py enthalten, erwiesen sich als besonders aktiv und zeigten zudem eine bemerkenswerte Wirkung in 3D-HeLa-Sphäroidmodellen. **Re9**, das eine elektronenarme Benzothiazol-Einheit besitzt, weist eine Emission im roten Spektralbereich auf und konnte daher erfolgreich als Werkzeug für Bioimaging-Anwendungen sowohl in vitro als auch in vivo eingesetzt werden. Die biologische Aktivität von **Re9** wurde außerdem an zwei verschiedenen Tumorstämmen von *C. elegans* (JK1466 und MT2124) untersucht, um weitere onkogene Signalwege zu erfassen. Dabei zeigte sich, dass **Re9** das Tumorwachstum in beiden Stämmen durch eine gesteigerte intrazelluläre ROS-Produktion hemmen kann. Bemerkenswert ist zudem die hohe Selektivität der Verbindung gegenüber Krebszellen, da weder die Entwicklung noch die Reproduktion der Nematoden beeinträchtigt wurden.

Eigenanteil an der Veröffentlichung:

- Umkristallisation der Rhenium(I)-Komplexe zur Gewinnung von Einkristallen
- Messungen von PXRDs der Rhenium(I)-Komplexe
- Revision des Manuskripts

3.4.3 Mechanochemical synthesis and application of mixed-metal copper–ruthenium HKUST-1 metal–organic frameworks in the electrocatalytic oxygen evolution reaction

Linda Sondermann, Quentin Smith, Till Strothmann, Annette Vollrath, Thi Hai Yen Beglau, Christoph Janiak, *RSC Mechanochem.* **2024**, *1*, 296-307.

Kurzzusammenfassung

Es werden neuartige Elektrodenmaterialien für die elektrokatalytische Wasserstofferzeugung untersucht, um die Aktivität teurer Edelmetallkomponenten zu steigern. Hier wurden verschiedene Mischmetall-Kupfer-Ruthenium-Kombinationen des metallorganischen Gerüsts (MOF) HKUST-1 (HKUST = Hong Kong University of Science and Technology, mit der Formel $[Cu_3(BTC)_2(H2O)_3]_n$ (BTC = Benzol-1,3,5-tricarboxylat)) als Cu_xRu-BTC mittels einer mechanochemischen Methode synthetisiert. Diese mechanochemische Methode ermöglichte die Synthese der Mischmetall-MOFs im Grammbereich innerhalb einer Stunde. Die Charakterisierung mittels Pulver-Röntgendiffraktometrie (PXRD), N_2-Adsorption, Rasterelektronenmikroskopie (SEM), thermogravimetrischer Analyse (TGA) und Fourier-Transform-Infrarotspektroskopie (FT-IR) bestätigte die Bildung eines MOF mit der HKUST-1-Topologie, wenn auch mit geringerer Porosität im Vergleich zu reinem HKUST-1. Die synthetisierten MOFs wurden als Vorläufermaterialien für Katalysatoren für die Sauerstoffentwicklungsreaktion (OER) getestet und zeigten eine Leistung, die mit dem Industriestandard Rutheniumoxid (RuO_2) vergleichbar war. Es wurden eine Überpotentiale (η) von 314 mV (RuO_2 η = 312 mV) und eine Tafel-Steigung (b) von 55 mV dec^{-1} (RuO_2 b = 47 mV dec^{-1}) erzielt, was in Kombination mit einem Ladungstransferwiderstand (R_{CT}) von 13,6 Ω (RuO_2 R_{CT} = 52,8 Ω) und einer faradayschen Effizienz (FE) von 70 % (RuO_2 FE = 66 %) die Annahme stützt, dass der aus $Cu_{10}Ru$-BTC abgeleitete Katalysator mit einer innigen Mischung aus Kupfer und Ruthenium im Nanobereich für die OER wirksam ist, wobei er einen geringeren Rutheniumgehalt aufweist als RuO_2. Alle aus den Cu_xRu-BTC-Proben und RuO_2 abgeleiteten Katalysatoren zeigten bei einer chronopotentiometrischen Messung über 12 Stunden eine gute Stabilität.

Eigenanteil an der Veröffentlichung:

- Aufnahme von REM-Bildern der jeweiligen Proben
- EDX-Analyse der jeweiligen Proben
- Revision des Manuskripts

3.4.4 Comparison of In Situ and Postsynthetic Formation of MOF-Carbon Composites as Electrocatalysts for the Alkaline Oxygen Evolution Reaction

Linda Sondermann, Laura Maria Voggenauer, Annette Vollrath, Till Strothmann, Christoph Janiak, *Molecules* **2025**, *30*, 208.

Kurzzusammenfassung

Nickel-Eisen-Mischmetall-Materialien (Ni_xFe) finden als kostengünstige, in der Erde reichlich vorhandene Elektrokatalysatoren für die Sauerstoffentwicklungsreaktion (OER) Beachtung. Hier wurden Nickel- und Nickel-Eisen-Mischmetall-Verbundstoffe auf Basis metallorganischer Gerüste (MOF) mit den Kohlenstoffmaterialien Ketjenblack (KB) oder Kohlenstoffnanoröhren (CNT) *in situ* in einer Ein-Topf-Solvothermie-Reaktion synthetisiert. Als direkter Vergleich zu diesen *in situ* synthetisierten Verbundstoffen wurden die reinen MOFs nach der Synthese durch Mahlen mit KB oder CNT gemischt, um physikalische Mischverbundstoffe zu erzeugen. Die *in situ* und nach der Synthese hergestellten MOF/Kohlenstoff-Proben wurden vergleichend als (Vor-)Katalysatoren für die OER getestet, und die meisten von ihnen übertrafen den RuO_2-Benchmark. Je nach Kohlenstoffmaterial und Metallverhältnis zeigten die *in situ* oder nach der Synthese hergestellten Verbundwerkstoffe eine bessere Leistung, was zeigt, dass die Methode zur Herstellung des Verbundwerkstoffs die OER-Aktivität beeinflussen kann. Das beste Material, Ni_5Fe-CNT, wurde *in situ* synthetisiert und erreichte ein Überpotential (η) von 301 mV (RuO_2 η = 354 mV), eine Tafel-Steigung (b) von 58 mV/dec (RuO_2 b = 91 mV/dec), einen Ladungstransferwiderstand (Rct) von 7 Ω (RuO_2 R_{ct} = 39 Ω) sowie eine faradaysche Effizienz (FE) von 95 % (RuO_2 FE = 91 %). Strukturelle Veränderungen in den Materialien konnten durch einen Stabilitätstest im alkalischen

Elektrolyten festgestellt werden, und eine 12-stündige Chronopotentiometrie zeigte, dass die hergestellten Elektrokatalysatoren und RuO_2 eine gute Stabilität aufweisen.

Eigenanteil an der Veröffentlichung:

- Aufnahme von REM-Bildern der jeweiligen Proben
- EDX-Analyse der jeweiligen Proben
- Revision des Manuskripts

3.4.5 Synthesis and characterization of lignin-modified geopolymer composites for aqueous phase sequestration of methyl orange dye in a fixed-bed column

Idriss Kamdem Taquieteu, Hermann Dzoujo Tamaguelon, Victor Shikuku, Sylvain Tome, Donald Kamdem Njouond, Manelle Fouetfack Dongmo, Hanibal Othman, Annette Vollrath, Abdulrahman Mohabbat Christoph Janiak, Charles Banenzouéa, David Joh Daniel Dina, *Mater. Adv.* **2025**, *6*, 5074-5088.

Kurzzusammenfassung

In der vorliegenden Arbeit wurde die Leistungsfähigkeit von Geopolymer-Lignin-Verbundwerkstoffen auf der Basis von Puzzolan und Sägemehl bei der Bindung von Methylorange (MO) in einem Festbett untersucht, was als vielversprechende Strategie zur Verwertung von Sägemehlabfällen angesehen wird. Die Verbundwerkstoffe GP0, GP-CL5 und GP-CL10 wurden durch Alkalisierung hergestellt, wobei Puzzolan durch 0, 5 bzw. 10 % Lignin (CL) ersetzt wurde, das aus Sägemehl extrahiert wurde. Die Verbundstoffe wurden mit Standardmethoden charakterisiert, nämlich Röntgendiffraktometrie (XRD), Fourier-Transform-Infrarotspektroskopie (FTIR), thermogravimetrische Analyse (TGA), Brunauer-Emmett-Teller-Oberflächenanalyse (BET) und Rasterelektronenmikroskopie (SEM). Die spezifischen Oberflächen verringerten sich durch die Zugabe und Erhöhung des CL-Anteils von 53,4 auf 24,9 m^2g^{-1} für GP0 bzw. GP-CL10. Die Einarbeitung von CL führte zu einem Poly(ferro-lignino-sialat)-Einzelnetzwerk. Die Zugabe von CL verlängerte die Durchbruchzeit und die Betriebszeit der Säule. Das Thomas-Modell beschrieb die Durchbruchskurven am besten. Die MO-Sequestrierungsleistung (Q_0) war bei GP-CL10 dreimal besser als bei GP0, wenn die Zufuhrrate erhöht wurde. Der

Bindungsmechanismus des MO umfasst im Wesentlichen externe und interne Diffusion sowie elektrostatische Wechselwirkungen. Die Adsorption wird eher durch die Oberflächenchemie als durch die strukturellen Eigenschaften des Adsorptionsmittels bestimmt. Diese Ergebnisse deuten darauf hin, dass Geopolymer-Lignin-Verbundstoffe potenzielle umweltfreundliche Adsorptionsmittel für die Entfernung von Azofarbstoffen in einem kontinuierlichen Adsorptionssystem sind und einen plausiblen Weg für die Verwertung von Sägemehl aufzeigen.

Eigenanteil an der Veröffentlichung:

- Aufnahme von REM-Bildern der jeweiligen Proben
- Revision des Manuskripts

3.4.6 Eco-friendly energy storage: optimizing alfalfa biomass for advanced supercapacitor materials

Zohreh Asadi Ghare Jeloo, Sakineh Ghasemzadeh, Hassan Hosseini-Monfared, Mehran Javanbakht, Philipp Seiffert, Annette Vollrath, Robert Oestreich, Julia Michalski, Leila Naji, Mitra Najafloo, Christoph Janiak, *Mater. Sci. Eng. B* **2026**, *324*, 118944.

Kurzzusammenfassung

Diese Studie stellt eine umweltfreundliche und kostengünstige Strategie zur Synthese von hierarchisch porösem Kohlenstoff (HPC) aus leicht verfügbarer Luzerne-Biomasse für Elektroden von Hochleistungs-Superkondensatoren (SC) vor. Das Luzerne-HPC-Material wurde durch Karbonisierung und anschließende optimierte KOH-Aktivierung synthetisiert, um eine äußerst vorteilhafte poröse Struktur zu erzielen. Strukturelle, morphologische und elektrochemische Analysen zeigten, dass die Aktivierungstemperatur und die Vorläuferverhältnisse die Porenentwicklung und die vorteilhafte intrinsische Heteroatomdotierung (N, O) maßgeblich beeinflussten. Das resultierende Material verfügt über eine außergewöhnlich hohe spezifische Oberfläche, was den Ionentransport und die Ladungsspeicherung verbessert. Unter den hergestellten Proben zeigte AC-7 die überlegene elektrochemische Leistung und erreichte in einem Dreielektrodensystem eine hohe spezifische Kapazität von 502 F g^{-1}. Bei Einbau in symmetrische Münzzellen mit 6 M KOH-Elektrolyt lieferte

AC-7 eine gravimetrische Kapazität von 97,6 F g^{-1}, was einer bemerkenswerten Energiedichte von 13,56 Wh kg−1 bei einer Leistungsdichte von 125 W kg^{-1} entspricht. Entscheidend ist, dass die Elektrode zudem eine ausgezeichnete Zyklenstabilität zeigte und nach 2000 Zyklen über 92 % ihrer Anfangskapazität beibehielt. Die überragende Leistung von AC-7 wird auf seinen optimalen Mesoporengehalt und die stärkere Dotierung mit Heteroatomen zurückgeführt, die gemeinsam die Ionen-Diffusion und die pseudokapazitive Aktivität verbesserten. Diese Forschungsarbeit belegt erfolgreich, dass reichlich vorhandene landwirtschaftliche Abfälle wie Luzerne als nachhaltiger und kostengünstiger Ausgangsstoff für die Entwicklung von Hochleistungs-Kohlenstoffelektroden der nächsten Generation genutzt werden können.

Eigenanteil an der Veröffentlichung:

- Aufnahme von REM-Bildern der jeweiligen Proben
- EDX-Analyse der jeweiligen Proben
- Revision des Manuskripts

4 Zusammenfassung

Die vorliegende Dissertation befasste sich mit der Entwicklung und Untersuchung funktioneller Metall-organischer Gerüstverbindungen sowie verwandter Koordinationspolymere für Anwendungen in der Lumineszenz, Sensorik und Optoelektronik. Ziel der Arbeit war es, den Einfluss der Struktur poröser Gerüstmaterialien auf die Eigenschaften eingebetteter organischer Chromophore zu untersuchen und neue Materialkonzepte für lumineszente Anwendungen zu entwickeln. Hierzu wurden sowohl neuartige Koordinationspolymere synthetisiert als auch etablierte MOFs gezielt mit funktionellen Farbstoffen modifiziert und hinsichtlich ihrer strukturellen sowie photophysikalischen Eigenschaften umfassend charakterisiert.

Ein erster Schwerpunkt der Arbeit lag auf der Synthese und kristallstrukturellen Untersuchung der neuartigen Kobalt(II)-Koordinationsnetzwerke [Co(pdb)(DMF)] und $[Co_2(pdi)(DMF)_3]\cdot 2DMF\cdot H_2O$ mit Dihydrophenazinbasierten Di- und Tetracarboxylat-Linker. Durch solvothermale Synthesen wurden zwei neue Koordinationspolymere erfolgreich hergestellt und mittels Einkristall-Röntgenstrukturanalyse (SCXRD) charakterisiert. Systematische Untersuchungen verschiedener Metallsalze zeigten, dass ausschließlich Kobalt(II)-nitrat unter den gewählten Reaktionsbedingungen kristalline Produkte lieferte, während entsprechende Reaktionen mit anderen Metallionen oder alternativen Kobalt-Salzen keine oder lediglich amorphe Produkte ergaben. Diese Ergebnisse verdeutlichten den entscheidenden Einfluss sowohl des Metallions als auch des Gegenions auf die Gerüstbildung. Darüber hinaus konnte gezeigt werden, dass die unterschiedliche Konnektivität der eingesetzten Linker zur Ausbildung verschiedener Sekundärbaueinheiten sowie dreidimensionaler Netzwerkstrukturen mit unterschiedlicher Topologie und Interpenetration führte. Für [Co(pdb)(DMF)] wurde ein dreidimensionales Koordinationsnetzwerk erhalten, in dem dinukleare Kobalt-Paddle-Wheel-Einheiten als sekundäre Baueinheiten fungierten und über die vier Carboxylatgruppen der organischen pdb-Linker miteinander verknüpft waren. Das resultierende Gerüst wies eine cds- ($CdSO_4$-)Topologie auf und bildete durch die gegenseitige Durchdringung dreier symmetrisch angeordneter Netzwerke eine dreifach interpenetrierte Struktur.

Im Fall von $[Co_2(pdi)(DMF)_3]\cdot 2DMF\cdot H_2O$ wurde das Gerüst durch zwei kristallographisch unterschiedliche Kobalt(II)-Zentren aufgebaut. Dabei war lediglich eines der beiden Metallzentren mit allen vier Carboxylatgruppen des Tetracarboxylat-Linkers koordiniert und ermöglichte dadurch die Ausbildung des dreidimensionalen Netzwerks. Die Struktur konnte einer inversen pts- (PtS-)Topologie zugeordnet werden, bei der das Co_2-Fragment als tetraedrischer Knoten und der Linker als quadratisch-planarer Vierfachknoten betrachtet wurden. Im Vergleich zu klassischen pts-Netzwerken waren dabei die tetraedrischen und quadratisch-planaren Knoten vertauscht.
Die Untersuchungen lieferten somit grundlegende Erkenntnisse über die Struktur-Eigenschafts-Beziehungen dihydrophenazinbasierter Koordinationspolymere.

Ein weiterer Schwerpunkt der Dissertation lag auf der post-synthetischen Einlagerung des Fluorophors 8-(Dimethylamino)-10-isoalloxazin (DAMI) in die aluminiumbasierten Metall-organischen Gerüstverbindungen DUT-4, DUT-5 und MIL-53. Ziel dieser Untersuchungen war es, die Lumineszenzeigenschaften des Farbstoffs durch seine räumliche Isolation innerhalb der MOF-Poren auch im Festkörper zu erhalten und gleichzeitig neuartige fluoreszenzbasierte Sensormaterialien zu entwickeln. Es konnte nachgewiesen werden, dass DAMI im kristallinen Festkörper nahezu keine Fluoreszenz aufwies, in Lösung und auch nach der Immobilisierung in den Gerüststrukturen jedoch eine intensive Emission zeigte. Die MOFs fungierten dabei als „feste Lösungen“, welche die Aggregation der Farbstoffmoleküle wirksam verhinderten und dadurch ihre Emissionseigenschaften bewahrten. Die erhaltenen Komposite wurden anschließend hinsichtlich ihrer Eignung als Sensoren für flüchtige organische Verbindungen untersucht. Dabei bewirkten elektronenarme Nitroaromaten, vor allem Nitrobenzol, eine ausgeprägte Fluoreszenzlöschung, wohingegen elektronenreiche aromatische Verbindungen, insbesondere Toluol, zu einer Verstärkung der Emission führten. Diese Effekte konnten durch photoinduzierten Elektronentransfer zwischen den Analyten und dem verwendeten Farbstoff erklärt werden. Darüber hinaus zeigte der Vergleich der verschiedenen MOF-Strukturen, dass sowohl die Porengeometrie als auch die strukturelle Flexibilität des Wirtsgerüstes einen entscheidenden Einfluss auf die Diffusion der Analyten, die Wirt-Gast-Wechselwirkungen und damit auf die Sensoreigenschaft der Komposite ausübten.

Der dritte Teil der Dissertation befasste sich mit der erstmaligen Einlagerung des Multi-Resonanz-TADF-Emitters DiKTa in die Poren von MOF-5-Einkristallen. Ziel dieser Untersuchungen war es, die strukturellen und photophysikalischen Eigenschaften des Emitters innerhalb einer definierten porösen Wirtsstruktur zu untersuchen und die Eignung von MOFs als alternative Matrix für MR-TADF-Emitter zu bewerten. Mithilfe der verschiedenen Analysemethoden wie Röntgenpulverdiffraktometrie, Einkristallstrukturmessungen, Stickstoffsorptionsmessungen, stationären und zeitaufgelösten spektroskopischen Untersuchungen konnte nachgewiesen werden, dass sich die DiKTa-Moleküle erfolgreich innerhalb der Poren des Gerüstes befanden und nicht lediglich an der Kristalloberfläche adsorbiert waren. Darüber hinaus lieferten die Ergebnisse der Fluoreszenzanisotropiemessungen Hinweise auf eine bevorzugte Orientierung sowie eine eingeschränkte Rotationsfreiheit der Moleküle innerhalb der MOF-Poren, wodurch deren photophysikalischen Eigenschaften gezielt beeinflusst wurden. Damit erwiesen sich Metall-organische Gerüstverbindungen als eine vielversprechende Plattform zur Immobilisierung von MR-TADF-Emittern und eröffneten neue Möglichkeiten für die Entwicklung lumineszenter Materialien.

Insgesamt lieferten die im Rahmen dieser Dissertation durchgeführten Untersuchungen neue Erkenntnisse über lumineszente Farbstoffe in Metall-organischen Gerüstverbindungen. Es konnte gezeigt werden, dass sowohl die Struktur der Wirtsgerüste als auch die Wirt-Gast-Wechselwirkungen einen entscheidenden Einfluss auf die photophysikalischen Eigenschaften der eingelagerten Farbstoffe ausüben. Die Kombination aus Synthese, Strukturaufklärung und spektroskopischer Charakterisierung ermöglichte ein vertieftes Verständnis dieser Zusammenhänge und zeigte das Potenzial von Metall-organischen Gerüstverbindungen als vielseitige Plattformen zur gezielten Modulation lumineszenter Eigenschaften. Die gewonnenen Ergebnisse bilden eine Grundlage für das rationale Design zukünftiger Hybridmaterialien für Anwendungen in der chemischen Sensorik und der Optoelektronik, insbesondere im Bereich organischer Leuchtdioden.

5 Unveröffentlichte Ergebnisse

Im folgenden Kapitel werden bislang unveröffentlichte Ergebnisse vorgestellt, die im Rahmen einer Bachelorarbeit von Herrn Nikolas Jansen unter wissenschaftlicher Betreuung entstanden sind. Ziel war die Synthese neuer Metall-organischer Gerüstverbindungen auf Basis eines Acridon-Linkers sowie deren strukturelle und photophysikalische Charakterisierung.

Als Linker wurde 10-Methyl-9-oxo-9,10-dihydroacridin-2,6-dicarbonsäure (H_2acr) verwendet (Abbildung 14). Die Verbindung wurde von Herrn Dr. Lennart Bunnemann aus dem Arbeitskreis von Prof. C. Czekelius bereitgestellt. Die Identität wurde mittels ^{1}H- und ^{13}C-NMR-Spektroskopie bestätigt; die Spektren sind im Anhang dargestellt.

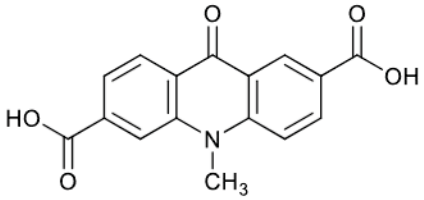


Abbildung 14: Strukturformel von 10-Methyl-9-oxo-9,10-dihydroacridin-2,6-dicarbonsäure (H_2acr).

Löslichkeitsuntersuchungen des Acridon-Linkers

Vor der Synthese von Koordinationsverbindungen wurde die Löslichkeit des Linkers H_2acr in verschiedenen protischen und aprotischen sowie wasserlöslichen und wasserunlöslichen Lösungsmitteln untersucht, um geeignete Reaktionsbedingungen für die solvothermale Synthese zu identifizieren. Hierzu wurden kleine Mengen des Linkers in unterschiedlichen Lösungsmitteln suspendiert und die Löslichkeit durch schrittweise Zugabe weiterer Lösungsmittel sowie Ultraschallbehandlung bewertet.

Insgesamt zeigte H_2acr in allen untersuchten Lösungsmitteln nur eine geringe Löslichkeit. Zwar war in den meisten Ansätzen eine leichte Gelbfärbung der Lösung zu beobachten, der überwiegende Teil des Feststoffes blieb jedoch ungelöst. Dimethylformamid (DMF) erwies sich als das am besten geeignete Lösungsmittel. Durch eine Ultraschallbehandlung konnte der Linker weitgehend dispergiert werden, sodass eine trübe gelbliche Lösung entstand. Aufgrund dieser Ergebnisse wurde DMF für die nachfolgenden Syntheseversuche als Reaktionsmedium ausgewählt.

Syntheseversuche zur Darstellung neuer Koordinationsverbindungen mit H_2acr

Zur Synthese neuer Koordinationsverbindungen auf Basis des Acridon-Linkers H_2acr wurden solvothermale Reaktionen mit verschiedenen Metallsalzen durchgeführt. Hierzu kamen Salze von Zink, Kobalt, Kupfer, Nickel, Aluminium und Zirkonium zum Einsatz. Die Synthesen erfolgten überwiegend in DMF bei 120 °C über einen Zeitraum von drei Tagen. Um den Einfluss der Reaktionsbedingungen auf die Kristallbildung zu untersuchen, wurden zusätzlich verschiedene Metall-Linker-Verhältnisse (2:1, 1:1 und 1:2) sowie die Zugabe von 1,4-Diazabicyclo[2.2.2]octan (DABCO), Salzsäure, Essigsäure oder Trifluoressigsäure (TFA) untersucht. Für ausgewählte Ansätze mit Zink und Kobalt wurden darüber hinaus Mikrowellensynthesen durchgeführt.

Die erhaltenen Produkte wurden mittels Pulverdiffraktometrie (PXRD) hinsichtlich ihrer Kristallinität untersucht. Unter den gewählten Reaktionsbedingungen lieferten die meisten Syntheseansätze amorphe Feststoffe oder Produkte, deren Diffraktogramme mit dem des eingesetzten Linkers übereinstimmten. Reproduzierbare Hinweise auf die Bildung neuer kristalliner Phasen konnten ausschließlich für Zink-haltige Ansätze erhalten werden.

Die Ergebnisse der einzelnen Syntheseversuche mit den Metallsalzen werden nachfolgend zusammengefasst.

Zirkonium, Kupfer, Nickel und Aluminium

Es wurden Zirkonium(IV)-chlorid bzw. Kupfer(II)-chlorid-Monohydrat eingesetzt. Die Reaktionen mit Zirkonium führten überwiegend zu braunen Feststoffen, die sich anhand der PXRD-Messungen als amorph erwiesen. Hinweise auf die Bildung kristalliner Koordinationsverbindungen konnten unter den gewählten Bedingungen nicht erhalten werden.

Die Kupfer-haltigen Ansätze lieferten überwiegend amorphe Produkte beziehungsweise unveränderten Linker. Lediglich bei einem Ansatz mit einem Metall-Linker-Verhältnis von 2:1 unter Zusatz von DABCO wurde ein grünlicher kristalliner Feststoff erhalten. Da sich dieses Produkt trotz mehrfacher Versuche nicht reproduzieren ließ, wurde auf eine weiterführende Charakterisierung verzichtet.

Die Syntheseversuche mit Nickel(II)-nitrat-Hexahydrat und Aluminium(III)-nitrat ergaben ausschließlich gelbe Feststoffe. Die anschließende PXRD-Analyse zeigte entweder amorphe Produkte oder Diffraktogramme, die mit dem des freien Linkers übereinstimmten. Somit konnten unter den gewählten Reaktionsbedingungen keine neuen kristallinen Koordinationsverbindungen erhalten werden.

Zink und Kobalt

Weitere Syntheseversuche wurden mit Zink(II)-nitrat-Hexahydrat und Kobalt(II)-nitrat-Hexahydrat als Metallsalze durchgeführt. Neben unterschiedlichen Metall-Linker-Verhältnissen wurden auch der Einfluss verschiedener Modulatoren (Salzsäure, Essigsäure, Trifluoressigsäure und DABCO) sowie alternative Synthesebedingungen mittels Mikrowellenreaktor untersucht.

Die Synthesen mit Kobalt führten überwiegend zu gelben Feststoffen, deren Pulverdiffraktogramme entweder amorphe Produkte oder unveränderten Linker erkennen ließen. Ein Ansatz im Metall-Linker-Verhältnis 2:1 ergab zwar einen dunkel gefärbten Feststoff, dieser erwies sich jedoch ebenfalls als amorph. Unter Zusatz von Salzsäure wurde ein hellgrüner Feststoff erhalten, dessen Diffraktogramm neue Reflexe aufwies und somit auf die Bildung einer bislang unbekannten kristallinen Phase hindeutete. Trotz mehrfacher Wiederholung konnte dieses Produkt jedoch nicht reproduziert werden. Auch eine Mikrowellensynthese führte zu keinem vergleichbaren Ergebnis. Eine weiterführende Charakterisierung erfolgte daher nicht.

Im Gegensatz dazu lieferten mehrere Zink-haltige Ansätze reproduzierbar kristalline Produkte. Insbesondere bei einem Metall-Linker-Verhältnis von 2:1 wurde ein gelbes Pulver erhalten, dessen Pulverdiffraktogramm deutlich von dem des freien Linkers abwich und auf die Bildung einer neuen kristallinen Verbindung schließen ließ. Die gleichen Reflexe wurden auch bei den Synthesen unter Zusatz von Essigsäure beziehungsweise Trifluoressigsäure beobachtet. Die erhaltene Verbindung wird im Folgenden als Zn(acr) bezeichnet.

Die Synthese von Zn(acr) konnte darüber hinaus erfolgreich mittels Mikrowellensynthese reproduziert werden. Hierzu wurde die Reaktionslösung 30 Minuten bei 140-150 °C erhitzt und anschließend innerhalb von 60 Minuten

kontrolliert auf Raumtemperatur abgekühlt. Im Gegensatz dazu führte die Zugabe von DABCO nicht zur Bildung eines kristallinen Produktes.

Eine Einkristallstrukturanalyse der Verbindung war bislang nicht möglich, da Zn(acr) ausschließlich als feinkristallines Pulver erhalten wurde und keine für eine Einkristallanalyse geeigneten Kristalle gebildet werden konnten. Die weiterführende Charakterisierung erfolgte daher erstmals mittels Pulverdiffraktometrie, Rasterelektronenmikroskopie, Infrarotspektroskopie, Gassorptionsmessungen sowie Fluoreszenzspektroskopie.

Charakterisierung der Koordinationsverbindung Zn(acr)

Unter den untersuchten Reaktionsbedingungen konnte ausschließlich für Zink eine reproduzierbar herstellbare kristalline Verbindung erhalten werden. Das Produkt entstand bei der Umsetzung von Zink(II)-nitrat-Hexahydrat mit H_2acr im Metall-Linker-Verhältnis 2:1 in DMF bei 120 °C über drei Tage als feines gelbes Pulver. Die Zugabe von Essigsäure oder Trifluoressigsäure führte zu Produkten mit identischen Pulverdiffraktogrammen, sodass von der Bildung derselben kristallinen Phase ausgegangen werden kann. Für die weiterführenden Untersuchungen wurden daher die Synthesen ohne Zusatz von Modulatoren ausgewählt.

Mikroskopische Aufnahmen der erhaltenen Probe sind in Abbildung 15 dargestellt. Zur weiteren Untersuchung der Morphologie wurde die Verbindung mittels Rasterelektronenmikroskopie analysiert. Die REM-Aufnahmen (Abbildung 16) zeigen überwiegend blockförmige kristalline Partikel mit einer rauen Oberflächenstruktur sowie kleinere Agglomerate. Die Partikel weisen eine heterogene Größenverteilung auf. Aufgrund der geringen Kristallgröße konnten keine geeigneten Kristalle für eine Einkristallstrukturanalyse isoliert werden, sodass eine strukturelle Aufklärung mittels SCXRD bislang nicht möglich war.

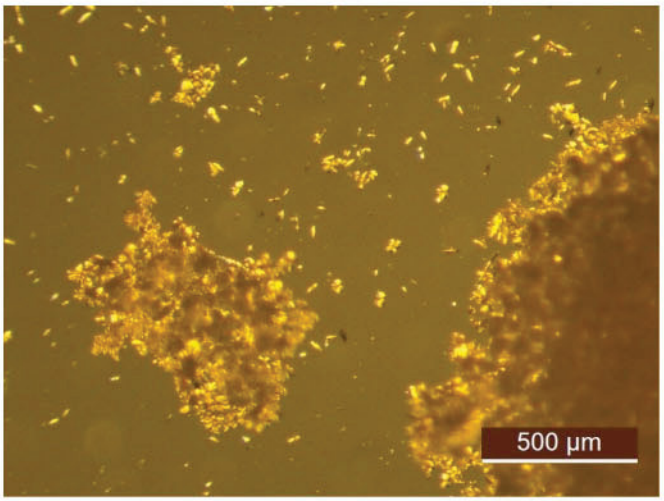


Abbildung 15: Mikroskopische Aufnahme der synthetisierten Koordinationsverbindung Zn(acr).

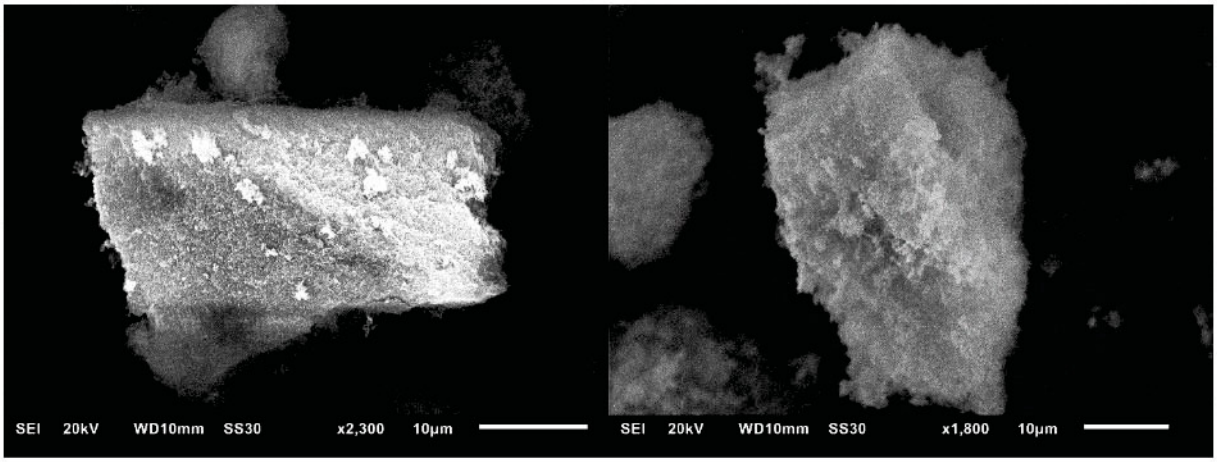


Abbildung 16: REM-Aufnahmen der synthetisierten Koordinationsverbindung Zn(acr).

Zur Überprüfung der Phasenreinheit wurden von Zn(acr) Pulverdiffraktogramme aufgenommen. Die gemessenen Diffraktogramme unterscheiden sich deutlich von dem des freien Linkers H_2acr und weist auf die Bildung einer neuen kristallinen Phase hin (Abbildung 17). Die unter Zusatz von Essigsäure erhaltene Probe zeigt nahezu identische Reflexe, sodass beide Produkte derselben Verbindung zugeordnet werden können. Ein Vergleich mit Literaturdaten ähnlicher Koordinationsverbindungen war nicht möglich, da keine strukturell vergleichbaren Systeme mit Acridon-basierten Linkern gefunden werden konnten.

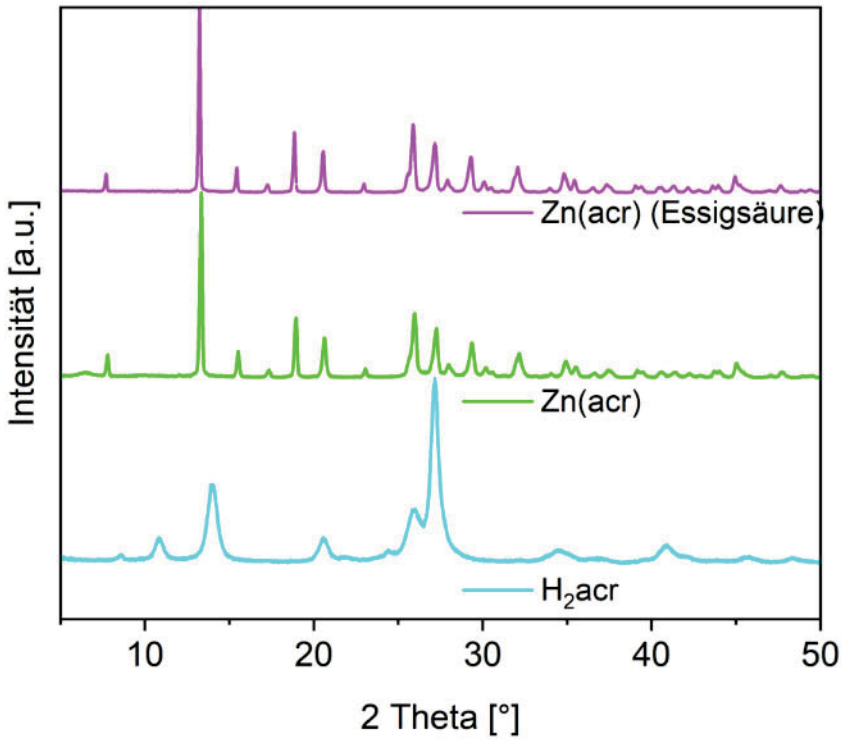


Abbildung 17: Pulverdiffraktogramme der Koordinationsverbindungen Zn(acr) mit (rosa) und ohne (grün) Essigsäure und des freien Linkers H_2acr (hellblau).

Zur weiteren Charakterisierung der Verbindung Zn(acr) wurden die IR-Spektren des freien Linkers H_2acr und der synthetisierten Koordinationsverbindung miteinander verglichen (Abbildung 18).

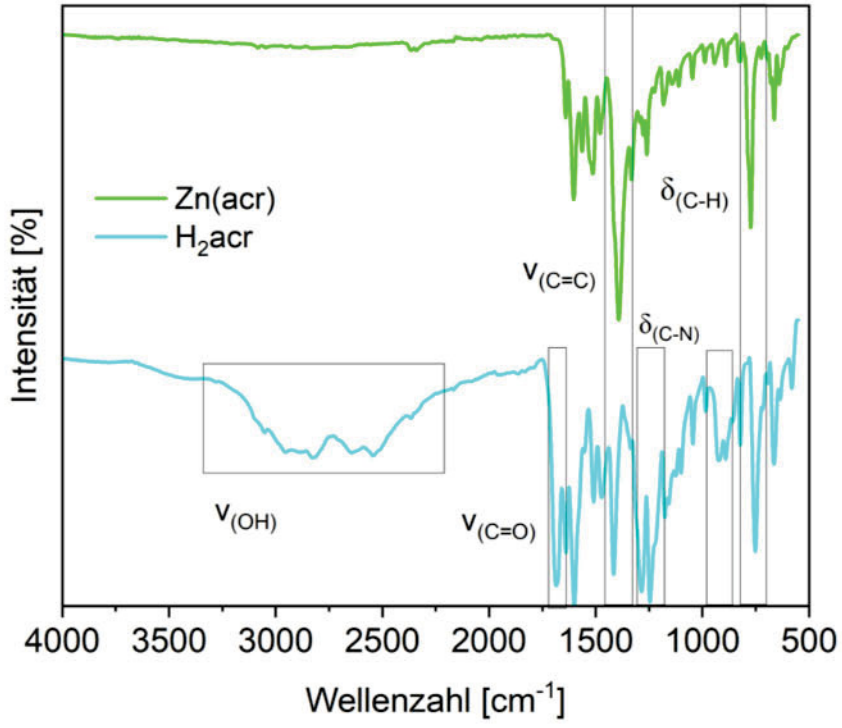


Abbildung 18: IR-Spektren der Koordinationsverbindung Zn(acr) (grün) und des freien Linkers H_2acr (hellblau).

Beide Spektren zeigen mehrere gemeinsame Banden, die den strukturellen Gemeinsamkeiten des organischen Linkers entsprechen. So können die Banden bei etwa 750 cm^{-1} den außerplanaren C–H-Deformationsschwingungen der aromatischen Ringe zugeordnet werden. Die Signale im Bereich von etwa 1350-1400 cm^{-1} sind charakteristisch für C=C-Streckschwingungen des aromatischen Systems und treten aufgrund der veränderten chemischen Umgebung in der Koordinationsverbindung leicht verschoben auf. Darüber hinaus sind im Bereich um 1650 cm^{-1} Banden zu beobachten, die den Carbonylschwingungen zugeordnet werden können.

Deutliche Unterschiede zwischen beiden Spektren zeigen sich insbesondere im Bereich der Carboxylgruppen. Im Spektrum des freien Linkers ist eine intensive Bande bei etwa 1700 cm^{-1} zu erkennen, die der C=O-Valenzschwingung der protonierten Carboxylgruppen zugeordnet werden kann. Diese Bande verschwindet im Spektrum von Zn(acr), was auf eine Deprotonierung der Carboxylgruppen und deren Beteiligung an der Koordination des Zinkions hindeutet. Ebenfalls fehlt die breite Bande im Bereich zwischen etwa 2200 und 3600 cm^{-1}, die dem Wasserstoffbrückenbindungssystem der Carboxylgruppen des freien Linkers zugeschrieben wird. Dies spricht ebenfalls für die Ausbildung koordinativer Bindungen zwischen den Carboxylatgruppen und den Metallzentren.

Darüber hinaus weist die dem C–N-Schwingungsbereich zuzuordnende Bande zwischen etwa 1200 und 1300 cm^{-1} in der Koordinationsverbindung eine deutlich geringere Intensität auf als im freien Linker. Insgesamt belegen die Veränderungen im IR-Spektrum, insbesondere das Verschwinden der für protonierte Carboxylgruppen charakteristischen Schwingungen, die erfolgreiche Koordination des Linkers an die Zinkzentren und stützen damit die Bildung einer neuen Koordinationsverbindung.

Zur Untersuchung der Porosität von Zn(acr) wurden Stickstoffsorptionsmessungen durchgeführt. Vor der Messung wurde die Probe drei Stunden bei 130 °C unter Vakuum aktiviert, um eingelagertes Lösungsmittel zu entfernen. Da das Thermogravimetriegerät zum Zeitpunkt der Untersuchungen nicht zur Verfügung stand, konnte die thermische Stabilität der Verbindung vorab nicht mittels TGA überprüft werden. Zur Kontrolle der Strukturstabilität wurde daher nach der Aktivierung ein Pulverdiffraktogramm aufgenommen. Dieses zeigte keine Veränderungen

gegenüber der unbehandelten Probe, sodass von einer ausreichenden thermischen Stabilität unter den gewählten Aktivierungsbedingungen ausgegangen werden konnte. Die anschließend aufgenommene Stickstoffsorptionsisotherme zeigt keine messbare Stickstoffaufnahme. Demnach weist die Verbindung unter den untersuchten Bedingungen keine zugängliche Porosität auf. Dieses Ergebnis unterscheidet Zn(acr) deutlich von klassischen Metall-organischen Gerüstverbindungen mit permanent zugänglichen Poren und deutet darauf hin, dass entweder keine offenen Poren vorliegen oder diese für Stickstoff bei 77 K nicht zugänglich sind.

Da Acridon-Derivate lumineszente Eigenschaften aufweisen, wurden sowohl der freie Linker H_2acr als auch die synthetisierte Koordinationsverbindung Zn(acr) mittels Fluoreszenzspektroskopie untersucht. Abbildung 19 zeigt die Emissionsspektren des freien Linkers in THF gelöst und als Feststoff sowie der Koordinationsverbindung.

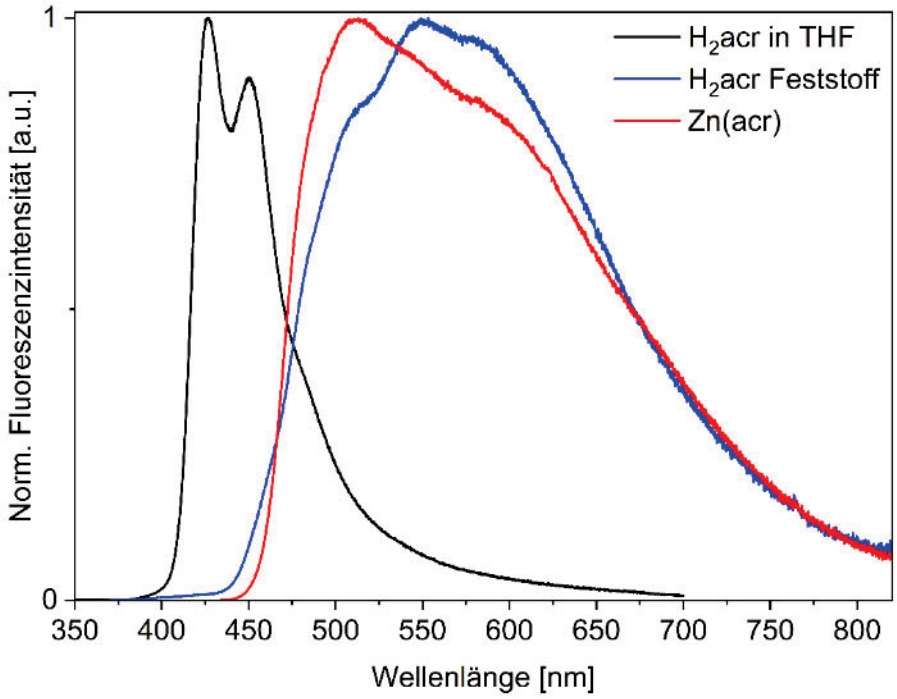


Abbildung 19: Emissionsspektrum des freien Linkers H_2acr in THF (schwarz), als Feststoff (blau) und der synthetisierten Koordinationsverbindung Zn(acr) (rot) (λ_{exc} = 320 nm).

Sowohl der freie Linker im Feststoff als auch Zn(acr) zeigen ein vibronisch strukturiertes Emissionsspektrum mit drei deutlich ausgeprägten Emissionsbanden bzw. einem Maximum mit zwei Schultern. Während das Emissionsmaximum des freien Linkers als Feststoff bei etwa 550 nm liegt, wird für Zn(acr) ein Maximum bei etwa

512 nm beobachtet. Die ähnliche vibronische Struktur der Spektren deutet darauf hin, dass die Emission in beiden Fällen überwiegend ligandenzentriert ist. Die Koordination des Linkers an die Zinkzentren führt somit zu einer Veränderung der relativen Intensitäten und der Lage der Emissionsbanden, ohne den grundlegenden Emissionsmechanismus wesentlich zu verändern.

Die beobachteten Emissionsbanden können den vibronischen Übergängen 0-0, 0-1 und 0-2 zugeordnet werden. Im Spektrum von Zn(acr) weist der 0-0-Übergang die höchste Intensität auf, während beim freien Linker als Feststoff die höheren vibronischen Übergänge vergleichsweise stärker ausgeprägt sind. Dieses Verhalten deutet darauf hin, dass die Koordination an das Zinkzentrum die molekulare Beweglichkeit des Linkers einschränkt und dadurch nichtstrahlende Relaxationsprozesse reduziert. Die erhöhte strukturelle Starrheit der Koordinationsverbindung begünstigt somit die strahlende Desaktivierung des angeregten Zustands.

Der in THF gelöste Linker zeigt dagegen ein deutlich einfacheres Emissionsprofil mit zwei schmalen Emissionsbanden bei kürzeren Wellenlängen. In Lösung sind die einzelnen Linkermoleküle räumlich voneinander getrennt und weisen eine höhere Beweglichkeit als im kristallinen Festkörper auf. Dadurch werden insbesondere die durch eine definierte Kristallpackung hervorgerufenen intermolekularen Wechselwirkungen zwischen benachbarten Linkermolekülen reduziert. Gleichzeitig können Wechselwirkungen mit den umgebenden Lösungsmittelmolekülen sowie, in Abhängigkeit von der Konzentration, zwischen einzelnen Linkermolekülen auftreten. Die Unterschiede zwischen Lösungs- und Festkörperemission können daher auf die veränderte molekulare Umgebung, die Solvatation sowie die unterschiedlichen intermolekularen Wechselwirkungen zurückgeführt werden.

Insgesamt zeigen die Fluoreszenzmessungen, dass die Koordination des Acridon-Linkers an Zink(II) dessen photophysikalische Eigenschaften beeinflusst. Die Veränderungen der Emissionsspektren sprechen für eine erhöhte strukturelle Starrheit des Liganden innerhalb der Koordinationsverbindung bei gleichzeitig überwiegend ligandenzentriertem Emissionscharakter.

Zusammenfassung

Im Rahmen dieser Untersuchungen wurde die Eignung des Acridon-basierten Linkers H_2acr für die Synthese neuer Koordinationsverbindungen mit verschiedenen Metallionen untersucht. Hierzu wurden unterschiedliche Metallsalze, Metall-Linker-Verhältnisse sowie verschiedene Synthesebedingungen und Modulatoren eingesetzt. Während die meisten Ansätze unter den gewählten Reaktionsbedingungen ausschließlich amorphe Produkte oder unveränderten Linker lieferten, konnte mit Zink(II) eine neue Koordinationsverbindung, Zn(acr), reproduzierbar synthetisiert werden.

Die Charakterisierung mittels PXRD und IR-Spektroskopie weist auf die Bildung einer neuen Koordinationsverbindung hin. Aufgrund der ausschließlich pulverförmig erhaltenen Probe war eine Strukturaufklärung mittels Einkristallröntgenstrukturanalyse jedoch bislang nicht möglich. Die Gassorptionsmessungen zeigten keine Stickstoffaufnahme, sodass unter den gewählten Messbedingungen keine permanente Porosität nachgewiesen werden konnte.

Die fluoreszenzspektroskopischen Untersuchungen belegen eine Emission der Koordinationsverbindung, die der des freien Linkers ähnelt. Dies deutet darauf hin, dass die Lumineszenz überwiegend ligandenzentriert ist und die Koordination an das Zinkzentrum den Emissionsmechanismus nicht grundlegend verändert, sondern hauptsächlich die photophysikalischen Eigenschaften des Linkers beeinflusst.

Insgesamt zeigen die Ergebnisse das Potenzial des Acridon-basierten Linkers H_2acr für die Synthese neuer lumineszenter Koordinationsverbindungen. Zukünftige Arbeiten sollten sich insbesondere auf eine Optimierung der Synthesebedingungen oder geeignete Umkristallisationsverfahren konzentrieren, um größere Einkristalle zu erhalten und dadurch eine vollständige Strukturaufklärung mittels SCXRD zu ermöglichen.

6 Experimentalteil

6.1 Chemikalien

Chemikalie	Reinheit	Hersteller
1,4-Diazabicyclo(2.2.2)octan	98 %	Alfa Aesar
Aluminium(III)-Nitrat	≥ 98 %	Roth
N,N-Dimethylformamid (DMF)	≥ 99,5 %	Fisher
Essigsäure	≥ 99.8 %	Aldrich
Ethanol	-	Supelco
Kobalt(II)-nitrat Hexahydrat	≥ 98 %	Roth
Kupfer(II)-chlorid-Hydrat	p.a.	Janssen Chimica
Nickel(II)nitrat-Hexahydrat	98 %	Ferak Berlin
Salzsäure	37 %	VWR Chemicals
Trifluoressigsäure	99.50 %	Acros Organics
Zink(II)nitrat Hexahydrat	≥ 96 %	Roth
Zirkonium(IV)-chlorid	p.a.	Aldrich

6.2 Geräte

NMR-Spektroskopie

Die ^{1}H- und ^{13}C-NMR-Spektren wurden bei 298 K mit einem Bruker Avance III-300 aufgenommen (^{1}H: 300 MHz, ^{13}C: 150 MHz). Die chemischen Verschiebungen sind in parts per million (ppm) angegeben.

Röntgenpulverdiffraktometrie (PXRD)

Die Pulverdiffraktogramme wurden mit einem Rigaku MiniFlex 600 (600 W, 40 kV, 15 mA) unter Verwendung von Cu-Kα-Strahlung (λ = 1,54182 Å) im 2θ-Bereich von 5°

bis 50° aufgenommen. Die Auswertung der Messdaten erfolgte mit den Programmen Match! (Crystal Impact, Version 3.3.0) und Origin.

Infrarot-Spektroskopie (IR)

Die Infrarotspektren wurden mit einem Bruker Tensor 37 FT-IR-Spektrometer in ATR-Technik aufgenommen. Die Spektren wurden in einem Wellenzahlbereich von 4000 bis 500 cm^{-1} aufgezeichnet.

Rasterelektronenmikroskopie (REM)

Vor den REM-Untersuchungen wurden die Proben mit einem JEOL JFC-1200 Fine Coater durch Goldsputtern leitfähig beschichtet. Die Aufnahmen erfolgten mit einem JEOL JSM-6510 Rasterelektronenmikroskop bei einer maximalen Vergrößerung von ×30.000. Die Messungen wurden unter Vakuum mit einer Beschleunigungsspannung von bis zu 20 kV durchgeführt. Als Elektronenquelle diente eine LaB_6-Kathode.

Sorptionsmessung

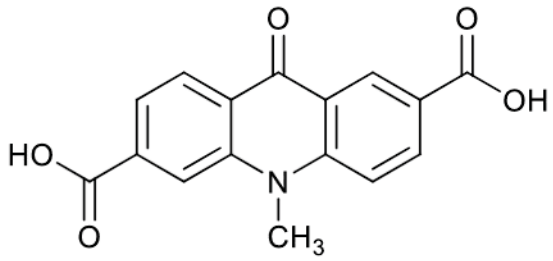
Vor den Sorptionsmessungen wurden die Proben drei Stunden bei 130 °C unter Vakuum aktiviert. Die Stickstoffsorptionsmessungen wurden bei 77 K mit einem BELSORP MAX II durchgeführt.

Fluoreszenzspektroskopie

Die Fluoreszenzspektren wurden mit einem FS5 Spektrofluorometer (Edinburgh Instruments) aufgenommen. Das Gerät ermöglicht Messungen bis zu einer Wellenlänge von 1650 nm sowie zeitaufgelöste Fluoreszenzmessungen mit einer zeitlichen Auflösung bis in den Pikosekundenbereich. Es verfügt über einen Referenzdetektor zur Korrektur von Intensitätsschwankungen der Lichtquelle, einen Transmissionsdetektor zur Absorptionsmessung sowie einen hochempfindlichen Single-Photon-Counting-(SPC)-Detektor zur Detektion der Fluoreszenzemission.

6.3 Synthesevorschriften

Synthese von Zn(acr)



H_2acr

+ $Zn(NO_3)_2 \cdot 6\ H_2O$ $\xrightarrow[100\ °C,\ 72\ h]{DMF}$ Zn(acr)

5 mg H_2acr (0,017 mmol) und 10,01 mg Zink(II)-Nitrat-Hexahydrat (0,034 mmol) wurden unter Verwendung eines Ultraschallbads in 3 ml DMF gelöst. Das Reaktionsgefäß wurde dann verschlossen für 3 Tage in einem Ofen auf 120 °C erhitzt. Das dabei entstandene gelbe Pulver wurde mit DMF und Ethanol gewaschen, zentrifugiert und im Vakuumtrockenschrank bei 60 °C getrocknet.

Ausbeute: 9,9 mg

7 Anhang

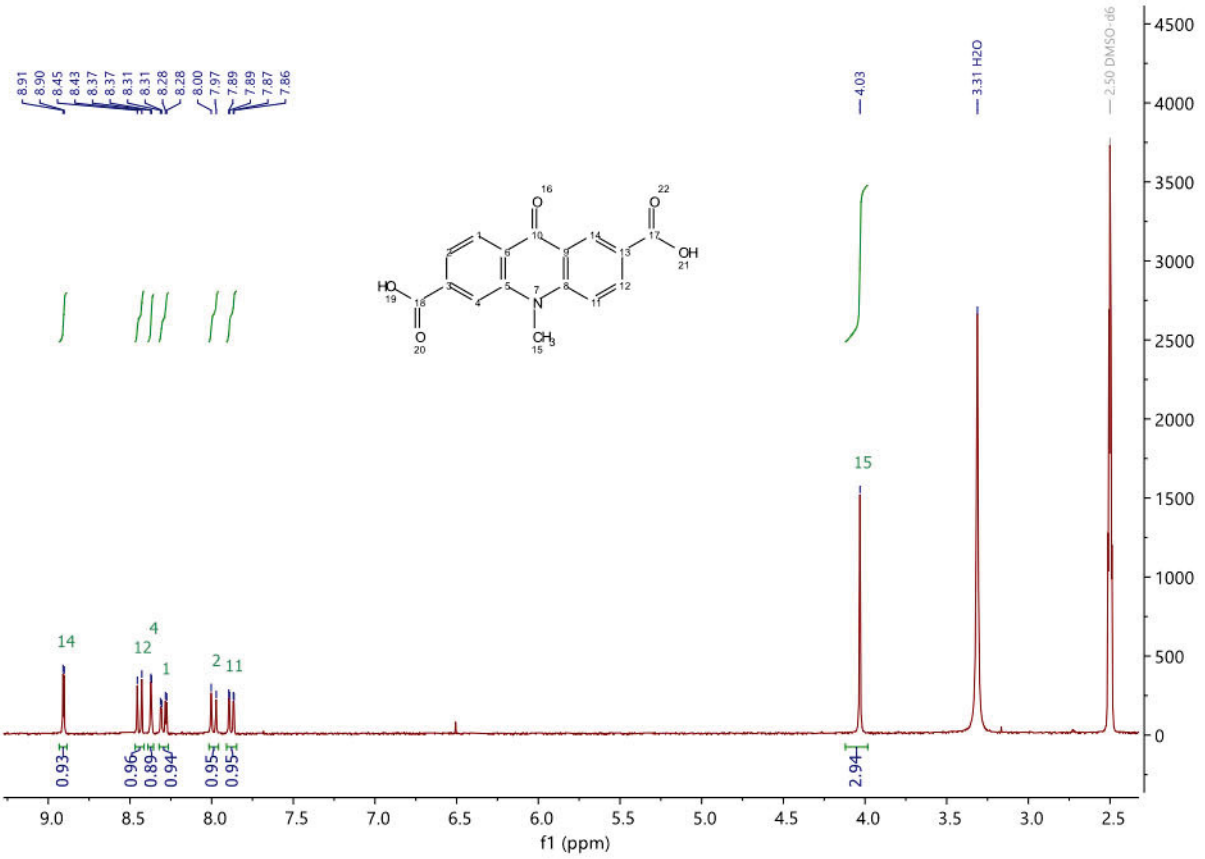


Abbildung 20: ^{1}H-NMR-Spektrum von 10-Methyl-9-oxo-9,10-dihydroacridin-2,6-dicarboxylsäure (300 MHz, DMSO-d6) (zu Kapitel 5 und 6.3).

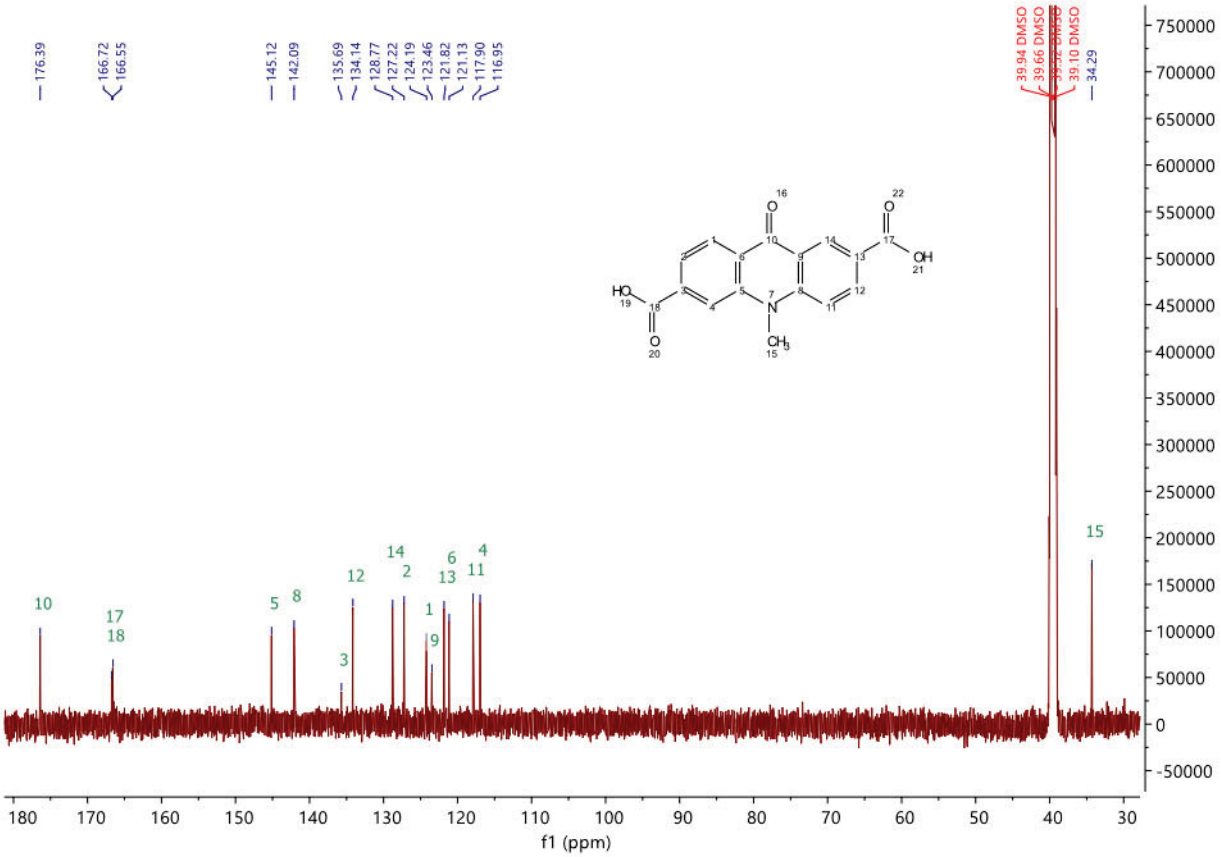


Abbildung 21: ^{13}C-NMR-Spektrum von 10-Methyl-9-oxo-9,10-dihydroacridin-2,6-dicarboxylsäure (150 MHz, DMSO-d_6) (zu Kapitel 5 und 6.3).

8 Literaturverzeichnis

[1] C. Janiak and J. K. Vieth, *New Journal of Chemistry* **2010**, *34*, 2366-2388.

[2] S. Bauer, N. Stock, *Chemie in unserer Zeit* **2008**, *42*, 12-19.

[3] O. K. Farha, I. Eryazici, N. C. Jeong, B. G. Hauser, C. E. Wilmer, A. A. Sarjeant, R. Q. Snurr, S. T. Nguyen, A. Ö. Yazaydin and J. T. Hupp, *Journal of the American Chemical Society* **2012**, *134*, 15016-15021.

[4] S. Brunauer, P. H. Emmett, E. Teller, *Journal of the American Chemical Society* **1938**, *60*, 309-319.

[5] S. R. Batten, N. R. Champness, X. M. Chen, J. Garcia-Martinez, S. Kitagawa, L. Öhrström, M. O'Keeffe, M. P. Suh and J. Reedijk, *Pure and Applied Chemistry* **2013**, *85*, 1715-1724.

[6] B. F. Hoskins and R. Robson, *Journal of the American Chemical Society* **1990**, *112*, 1546-1554.

[7] O. M. Yaghi and H. L. Li, *Journal of the American Chemical Society* **1995**, *117*, 10401-10402.

[8] *Suchergebnisse bei SciFinder® des Chemical Abstracts Service (CAS): https://scifinder-n.cas.org/search/reference/6a79b1b749b78102b13c33d8/1, Seite wurde aufgerufen am 13.08.2026*.

[9] *The Royal Swedish Academy of Sciences, Press Release: Nobel Prize in Chemistry 2025. https://www.nobelprize.org/prizes/chemistry/2025/press-release/, Seite wurde aufgerufen am 04.08.2026*.

[10] A. K. Cheetham, C. N. R. Rao and R. K. Feller, *Chemical Communications* **2006**, 4780-4795.

[11] M. O'Keeffe, *Chemical Society Reviews* **2009**, *38*, 1215-1217.

[12] N. Stock and S. Biswas, *Chemical Reviews* **2012**, *112*, 933-969.

[13] S. Kitagawa, R. Kitaura and S. Noro, *Angewandte Chemie International Edition* **2004**, *43*, 2334-2375.

[14] S. S. Y. Chui, S. M. F. Lo, J. P. H. Charmant, A. G. Orpen and I. D. Williams, *Science* **1999**, *283*, 1148-1150.

[15] H. Li, M. Eddaoudi, M. O'Keeffe and O. M. Yaghi, *Nature* **1999**, *402*, 276-279.

[16] T. Loiseau, C. Serre, C. Huguenard, G. Fink, F. Taulelle, M. Henry, T. Bataille and G. Férey, *Chemistry - A European Journal* **2004**, *10*, 1373-1382.

[17] J. H. Cavka, S. Jakobsen, U. Olsbye, N. Guillou, C. Lamberti, S. Bordiga and K. P. Lillerud, *Journal of the American Chemical Society* **2008**, *130*, 13850-13851.
[18] V. Guillerm, S. Gross, C. Serre, T. Devic, M. Bauer and G. Férey, *Chemical Communications* **2010**, *46*, 767-769.
[19] J. Dong, D. Zhao, Y. Lu and W. Y. Sun, *Journal of Materials Chemistry A* **2019**, *7*, 22744-22767.
[20] Y. J. Cui, Y. F. Yue, G. D. Qian and B. L. Chen, *Chemical Reviews* **2012**, *112*, 1126-1162.
[21] J. Rocha, L. D. Carlos, F. A. A. Paz and D. Ananias, *Chemical Society Reviews* **2011**, *40*, 926-940.
[22] M. D. Allendorf, C. A. Bauer, R. K. Bhakta and R. J. Houk, *Chemical Society Reviews* **2009**, *38*, 1330-1352.
[23] X. Q. Lin, X. Zhang, J. X. Yang, M. L. Sun, J. S. Chen, J. K. Cheng, Y. Y. Qin and Y. G. Yao, *Inorganic Chemistry* **2025**, *64*, 16246-16257.
[24] Y. S. Jiang, W. X. Chang, Z. H. Li, X. Zhou, P. J. Zhang, X. H. Huang, X. Y. Pan, Z. D. He, Y. Wang and Z. Q. Tian, *JACS Au* **2025**, *5*, 1875-1883.
[25] M. N. A. Fetzer, M. Vieten, A. Limon and C. Janiak, *Molecules* **2025**, *30*, 4151.
[26] X. D. Zhu, J. Lü, X. J. Li, S. Y. Gao, G. L. Li, F. X. Xiao and R. Cao, *Crystal Growth & Design* **2008**, *8*, 1897-1901.
[27] H. Furukawa and O. M. Yaghi, *Journal of the American Chemical Society* **2009**, *131*, 8875-8883.
[28] H. B. T. Jeazet, C. Staudt and C. Janiak, *Dalton Transactions* **2012**, *41*, 14003-14027.
[29] I. Senkovska, V. Bon, A. Mosberger, Y. T. Wang and S. Kaskel, *Advanced Materials* **2025**, *37*, 2414724.
[30] T. O. Knedel, S. Buss, I. Maisuls, C. G. Daniliuc, C. Schlüsener, P. Brandt, O. Weingart, A. Vollrath, C. Janiak and C. A. Strassert, *Inorganic Chemistry* **2020**, *59*, 7252-7264.
[31] V. Virender, V. Pandey, G. Singh, P. K. Sharma, P. Bhatia, A. A. Solovev and B. Mohan, *Topics in Current Chemistry* **2024**, *383*, 1-36.
[32] M. T. Khulood, U. S. Jijith, P. P. Naseef, S. M. Kallungal, V. S. Geetha and K. Pramod, *International Journal of Pharmaceutics* **2025**, *673*, 125380.
[33] P. Horcajada, T. Chalati, C. Serre, B. Gillet, C. Sebrie, T. Baati, J. F. Eubank, D. Heurtaux, P. Clayette, C. Kreuz, J. S. Chang, Y. K. Hwang, V. Marsaud, P. N. Bories,

L. Cynober, S. Gil, G. Férey, P. Couvreur and R. Gref, *Nature Materials* **2010**, *9*, 172-178.
[34] L. E. Kreno, K. Leong, O. K. Farha, M. Allendorf, R. P. Van Duyne and J. T. Hupp, *Chemical Reviews* **2012**, *112*, 1105-1125.
[35] R. I. Walton, *Chemical Society Reviews* **2002**, *31*, 230-238.
[36] J. R. Lakowicz, *Principles of Fluorescence Spectroscopy*, Springer: Boston, **2006**, p. 1-4.
[37] M. de Bruin, *Pure and Applied Chemistry* **1982**, *54*, 1533-1554.
[38] R. Vangrieken and M. Debruin, *Pure and Applied Chemistry* **1994**, *66*, 2513-2526.
[39] W. H. Melhuish, *Pure and Applied Chemistry* **2026**, *56*, 231-245.
[40] M. Kasha, *Discussions of the Faraday Society* **1950**, 14-19.
[41] A. Jabłoński, *Zeitschrift für Physik* **1935**, *94*, 38-46.
[42] J. R. Lakowicz, *Principles of Fluorescence Spectroscopy*, Springer: Boston, **2006**, p. 3-5.
[43] S. L. Walden, J. A. Carroll, A. N. Unterreiner and C. Barner-Kowollik, *Advanced Science* **2024**, *11*, 2306014.
[44] H. Yersin, *Highly Efficient OLEDs with Phosphorescent Materials*, Wiley-VCH Verlag GmbH & Co. KGaA, Weinheim, **2008**, p. 1-10.
[45] J. H. Burroughes, D. D. C. Bradley, A. R. Brown, R. N. Marks, K. Mackay, R. H. Friend, P. L. Burn and A. B. Holmes, *Nature* **1990**, *347*, 539-541.
[46] H. Uoyama, K. Goushi, K. Shizu, H. Nomura and C. Adachi, *Nature* **2012**, *492*, 234-238.
[47] M. Pope, P. Magnante and H. P. Kallmann, *Journal of Chemical Physics* **1963**, *38*, 2042-2043.
[48] L. J. Rothberg and A. J. Lovinger, *Journal of Materials Research* **1996**, *11*, 3174-3187.
[49] S. Diesing, L. Zhang, E. Zysman-Colman and I. D. W. Samuel, *Nature* **2024**, *627*, 747-753.
[50] Y. Huang in *Recent research of materials for emissive layer of OLED*, *Vol. 2608* J. Phys.: Conf. Ser., **2023**.
[51] S. X. Gao, Z. Y. Cui and F. Li, *Chemical Society Reviews* **2023**, *52*, 2875-2885.
[52] J. Jayabharathi, V. Thanikachalam and S. Thilagavathy, *Coordination Chemistry Reviews* **2023**, *483*, 215100.

[53] K. A. King, P. J. Spellane and R. J. Watts, *Journal of the American Chemical Society* **1985**, *107*, 1431-1432.
[54] S. Kéna-Cohen and S. R. Forrest, *Physical Review B* **2007**, *76*, 075202.
[55] M. A. Baldo, D. F. O'Brien, Y. You, A. Shoustikov, S. Sibley, M. E. Thompson and S. R. Forrest, *Nature* **1998**, *395*, 151-154.
[56] A. Fathima, V. Moorthy, S. Joshi, L. Sathiyanarayanan, D. Karthik and K. R. Naveen, *Communications Materials* **2026**, *7*, 1-13.
[57] A. Y. Freidzon, A. A. Safonov, A. A. Bagaturyants, D. N. Krasikov, B. V. Potapkin, A. A. Osipov, A. V. Yakubovich and O. Kwon, *Journal of Physical Chemistry C* **2017**, *121*, 22422-22433.
[58] C. A. Parker and C. G. Hatchard, *Transactions of the Faraday Society* **1961**, *57*, 1894-1904.
[59] D. Pelczarski, M. Makowska-Janusik and W. Stampor, *Scientific Reports* **2025**, *15*, 44963.
[60] H. Wang, L. S. Xie, Q. Peng, L. Q. Meng, Y. Wang, Y. P. Yi and P. F. Wang, *Advanced Materials* **2014**, *26*, 5198-5204.
[61] H. Tanaka, K. Shizu, H. Miyazaki and C. Adachi, *Chemical Communications* **2012**, *48*, 11392-11394.
[62] H. J. Kim and T. Yasuda, *Advanced Optical Materials* **2022**, *10*, 2201714.
[63] X. Yin, Y. He, X. Wang, Z. X. Wu, E. B. Pang, J. Xu and J. A. Wang, *Frontiers in Chemistry* **2020**, *8*, 725.
[64] Q. S. Zhang, J. Li, K. Shizu, S. P. Huang, S. Hirata, H. Miyazaki and C. Adachi, *Journal of the American Chemical Society* **2012**, *134*, 14706-14709.
[65] S. M. Suresh, D. Hall, D. Beljonne, Y. Olivier and E. Zysman-Colman, *Advanced Functional Materials* **2020**, *30*, 1908677.
[66] T. Hatakeyama, K. Shiren, K. Nakajima, S. Nomura, S. Nakatsuka, K. Kinoshita, J. P. Ni, Y. Ono and T. Ikuta, *Advanced Materials* **2016**, *28*, 2777-2781.
[67] X. F. Luo, X. W. Xiao and Y. X. Zheng, *Chemical Communications* **2024**, *60*, 1089-1099.
[68] S. S. Kothavale and J. Y. Lee, *Advanced Optical Materials* **2020**, *8*, 2000922.
[69] U. Ryu, H. S. Lee, K. S. Park and K. M. Choi, *Polyhedron* **2018**, *154*, 275-294.
[70] L. S. Luo and R. C. Jin, *iScience* **2021**, *24*, 103206.
[71] D. S. R. Khafaga, M. T. El-Morsy, H. Faried, A. H. Diab, S. Shehab, A. M. Saleh and G. A. M. Ali, *RSC Advances* **2024**, *14*, 30201-30229.

[72] T. O. Knedel, E. Ricklefs, C. Schlüsener, V. B. Urlacher and A. C. Janiak, *ChemistryOpen* **2019**, *8*, 1337-1344.
[73] A. Saura-Sanmartin, A. Martinez-Cuezva, M. Marin-Luna, D. Bautista and J. Berna, *Angewandte Chemie-International Edition* **2021**, *60*, 10814-10819.
[74] D. D. Xu, W. W. Dong, M. K. Li, H. M. Han, J. Zhao, D. S. Li and Q. C. Zhang, *Inorganic Chemistry* **2022**, *61*, 21107-21114.
[75] P. B. So, H. T. Chen and C. H. Lin, *Microporous and Mesoporous Materials* **2020**, *309*, 110495.
[76] B. Singco, L. H. Liu, Y. T. Chen, Y. H. Shih, H. Y. Huang and C. H. Lin, *Microporous and Mesoporous Materials* **2016**, *223*, 254-260.
[77] S. Rojas, I. Colinet, D. Cunha, T. Hidalgo, F. Salles, C. Serre, N. Guillou and P. Horcajada, *ACS Omega* **2018**, *3*, 2994-3003.
[78] J. B. Birks, *Photophysics of Aromatic Molecules*, Wiley, New York, **1970**, p. 1294-1295.
[79] Y. N. Hong, J. W. Y. Lam and B. Z. Tang, *Chemical Communications* **2009**, 4332-4353.
[80] M. Gutiérrez, Y. Zhang and J. C. Tan, *Chemical Reviews* **2022**, *122*, 10438-10483.
[81] A. Reiffers, C. T. Ziegenbein, A. Engelhardt, R. Kühnemuth, P. Gilch and C. Czekelius, *Photochemistry and Photobiology* **2018**, *94*, 667-676.
[82] A. Losi, *Photochemistry and Photobiology* **2007**, *83*, 1283-1300.
[83] M. G. Kotp, J. Lüder, S. W. Kuo and A. F. M. EL-Mahdy, *Materials Advances* **2024**, *5*, 4142-4150.
[84] S. F. Xu, H. C. Dai, S. L. Zhu, Y. C. Wu, M. X. Sun, Y. Chen, K. Fan, C. Y. Zhang, C. L. Wang and W. P. Hu, *eScience* **2021**, *1*, 60-68.
[85] J. Lee, K. Shizu, H. Tanaka, H. Nakanotani, T. Yasuda, H. Kaji and C. Adachi, *Journal of Materials Chemistry C* **2015**, *3*, 2175-2181.
[86] K. Sato, K. Shizu, K. Yoshimura, A. Kawada, H. Miyazaki and C. Adachi, *Physical Review Letters* **2013**, *110*, 247401.
[87] Y. Yuan, X. Tang, X. Y. Du, Y. Hu, Y. J. Yu, Z. Q. Jiang, L. S. Liao and S. T. Lee, *Advanced Optical Materials* **2019**, *7*, 1801536.
[88] D. Hall, S. M. Suresh, P. L. dos Santos, E. Duda, S. Bagnich, A. Pershin, P. Rajamalli, D. B. Cordes, A. M. Z. Slawin, D. Beljonne, A. Köhler, I. D. W. Samuel, Y. Olivier and E. Zysman-Colman, *Advanced Optical Materials* **2020**, *8*, 1901627.

[89] A. Vollrath, X. Liu, N. Jansen, P. Seiffert, D. Geller and C. Janiak, *Crystals* **2026**, *16*, 185.
[90] A. Vollrath, V. Gvilava, P. Seiffert, C. Czekelius and C. Janiak, *Zeitschrift für anorganische und allgemeine Chemie* **2026**, e70183.